UNIVERSITY OF CALIFORNIA,
IRVINE

M-N-C Catalysts for Electrochemical Transformations of N-Species to Ammonia and Beyond

DISSERTATION

submitted in partial satisfaction of the requirements
for the degree of

DOCTOR OF PHILOSOPHY

in Chemical and Biomolecular Engineering

by

Eamonn Murphy

Dissertation Committee:
Professor Plamen Atanassov, Chair
Professor Xiaoqing Pan
Professor Iryna V. Zenyuk

2023

DEDICATION

“If you’re going to try, go all the way. Otherwise, don’t even start” – Charles Bukowski

“Sometimes you climb out of bed in the morning, and you think, I’m not going to make it, but you laugh inside – remembering all the times you’ve felt that way” – Charles Bukowski

This dissertation is dedicated to my mom, dad and brother, Colleen, Mark and Ian Murphy, whose endless support and encouragement made the completion of this journey possible. Always being available when I need to talk prevented me from burning out, allowing me to enjoy the PhD journey.

I also dedicate this dissertation to my friends, Matt Sabin, So-Young Lee, Alvin Ly, Ying Huang and Han Wang for being sources of joy and happiness throughout the PhD. Being both scientific collaborators and sources of great discussions, but also amazing and supportive friends.

TABLE OF CONTENTS

LIST OF FIGURES

ACKNOWLEDGEMENTS

I would like to thank the American Chemical Society for the permission to include Chapter 2 in my dissertation, which was published in *ACS Catalysis*, 12 (11), 6651-6662 (2022). I would like to thank all my co-authors and those who helped with the experiments for the work, including Yuanchao Liu, Ivana Matanovic, Shengyuan Guo, Peter Tieu, Ying Huang, Alvin Ly, Suparna Das, Iryna Zenyuk, Xiaoqing Pan, Erik Spoerke and Plamen Atanassov.

Chapter 3 in my dissertation is currently in the revision approval process with *Nature Communications*. I would like to thank all my co-authors and those who helped with the experiments for the work, including Yuanchao Liu, Ivana Matanovic, Martina Rüscher, Ying Huang, Alvin Ly, Shengyuan Guo, Wenjie Zang, Xingxu Yan, Andrea Martini, Janis Timoshenko, Beatriz Roldán Cuenya, Iryna Zenyuk, Xiaoqing Pan, Erik Spoerke and Plamen Atanassov.

The work in Chapter 4 is ready for submission to *Advanced Energy Materials*. I would like to use this chance to thank all co-authors who contributed to the work, including Baiyu Sun, Martina Rüscher, Yuanchao Liu, Wenjie Zang, Shengyuan Guo, Ying Huang, Alvin Ly, Iryna Zenyuk, Xiaoqing Pan, Janis Timoshenko, Beatriz Roldán Cuenya, Erik Spoerke and Plamen Atanassov.

I had the opportunity to co-lead additional projects that were enabled through materials systems developed in this dissertation and applied to neighboring decarbonization reactions such at the CO_2RR and ORR. Some of this work has been published in ChemElectroChem 9 (17), e202200647, titled “Synergistic Electrocatalytic Syngas Production from Carbon Dioxide by Bi‐Metallic Atomically Dispersed Catalysts”, while the work for the ORR is in the final preparations

for submission and is titled “Electrochemical Trends of a Hybrid Platinum and Metal-Nitrogen-Carbon Catalyst Library for the Oxygen Reduction and Carbon Monoxide Oxidation Reactions”. Although this work is not included in this dissertation, I would like thank the co-authors of this work for their significant contributions. For the CO_2RR work, I would like to thank Laurent Delafontaine, Shengyuan Guo, Yuanchao Liu, Tristan Asset, Ying Huang, Jiazhe Chen, Iryna Zenyuk, Xiaoqing Pan and Plamen Atanassov. For the ORR work, I would like to thank Alvin Ly, Hanson Wang, Tristan Asset, Ying Huang, Yuanchao Liu, Shengyuan Guo, Xiaoqing Pan, Iryna Zenyuk and Plamen Atanassov.

I am very grateful for the opportunity to participate it the Next Generation Electrochemistry 2022 workshop in Chicago and for the chance to do a short research exchange at the Fritz Haber Institute in Berlin. In both experiences, I greatly benefited in both my knowledge of addressing current challenges in electrochemistry, but also in expanding my professional network both locally and internationally.

I would like to thank the Solutions That Scale initiative for providing me a funded research fellowship to investigate work on the decarbonization of ammonia synthesis. I would like to thank Professor Maxx Arguilla and Professor Plamen Atanassov for their support and mentorship in this research.

I would especially like to thank my family for their never-ending support throughout this PhD journey, always giving me support and motivation to keep going in tough times. Thank you to my

friends who are always there to talk, listen and give support in stressful times, it means a lot to me and has helped me tremendously throughout my PhD.

VITA

Eamonn Murphy

2016 B.S. in Chemical Engineering, Colorado School of Mines

2017 MSc. In Advanced Chemical Engineering, Imperial College London

2023 Ph.D. in Chemical and Biomolecular Engineering, University of California, Irvine

FIELD OF STUDY

Chemical and Biomolecular Engineering

PUBLICATIONS

1. ***Murphy, E**., *Liu, Y., Matanovic, I., Huang, Y., Ly, A., Guo, S., Zang, W., Yan, X., Martini, A., Timoshenko, J. and Cuenya, B.R., 2022. Elucidating electrochemical nitrate and nitrite reduction over atomically-dispersed transition metal sites. *chemrxiv*
2. Cosenza, A., Delafontaine, L., Ly, A., Wang, H., **Murphy, E.**, Liu, Y., Specchia, S. and Atanassov, P., 2023. Novel acid-free process intensification for the synthesis of non-precious metal-nitrogen-carbon electrocatalysts for oxygen reduction reaction. *Journal of Power Sources*, *556*, p.232382.

3. Guo, S., Liu, Y., Huang, Y., Wang, H., **Murphy, E.**, Delafontaine, L., Chen, J.L., Zenyuk, I.V. and Atanassov, P., 2023. Promoting Electrolysis of Carbon Monoxide toward Acetate and 1-Propanol in Flow Electrolyzer. *ACS Energy Letters*, *8*, pp.935-942.
4. Delafontaine, L., Cosenza, A., **Murphy, E**., Liu, Y., Chen, J., Sun, B. and Atanassov, P., 2023. Metal–Nitrogen–Carbon Catalysts by Dynamic Template Removal for Highly Efficient and Selective Electroreduction of CO2. *ACS Applied Energy Materials*.
5. Cabana, J, … ,**Murphy, E**., NGenE 2022: Electrochemistry for Decarbonization. *ACS Energy Letters*, 8, 1, pp740-747.
6. Guo, S., Liu, Y., **Murphy, E.**, Ly, A., Xu, M., Matanovic, I., Pan, X. and Atanassov, P., 2022. Robust palladium hydride catalyst for electrocatalytic formate formation with high CO tolerance. *Applied Catalysis B: Environmental*, *316*, p.121659.
7. *Delafontaine, L., ***Murphy, E.**, Guo, S., Liu, Y., Asset, T., Huang, Y., Chen, J., Zenyuk, I.V., Pan, X. and Atanassov, P., 2022. Synergistic Electrocatalytic Syngas Production from Carbon Dioxide by Bi-Metallic Atomically Dispersed Catalysts. *ChemElectroChem*, *9*(17), p.e202200647.
8. ***Murphy, E.**, *Liu, Y., Matanovic, I., Guo, S., Tieu, P., Huang, Y., Ly, A., Das, S., Zenyuk, I., Pan, X. and Spoerke, E., 2022. Highly durable and selective Fe-and Mo-based atomically dispersed electrocatalysts for nitrate reduction to ammonia via distinct and synergized NO2– pathways. *ACS Catalysis*, *12*(11), pp.6651-6662.
9. Chen, Y., Huang, Y., Xu, M., Asset, T., Yan, X., Artyushkova, K., Kodali, M., **Murphy, E.**, Ly, A., Pan, X. and Zenyuk, I.V., 2022. Catalysts by pyrolysis: Direct observation of transformations during re-pyrolysis of transition metal-nitrogen-carbon materials leading to state-of-the-art platinum group metal-free electrocatalyst. *Materials Today*, *53*, pp.58-70.

10. Liu, Y., **Murphy, E**., Potma, E.O., Matanovic, I., Fishman, D.A. and Atanassov, P., 2021. Protocol for rapid ammonia detection via surface-enhanced Raman spectroscopy. *STAR protocols*, *2*(2), p.100599.
11. **Murphy, E.C**., Dumont, J.H., Park, C.H., Kestell, G., Lee, K.S. and Labouriau, A., 2020. Tailoring properties and processing of Sylgard 184: Curing time, adhesion, and water affinity. *Journal of Applied Polymer Science*, *137*(14), p.48530.
12. Liu, Y., Asset, T., Chen, Y., **Murphy, E**., Potma, E.O., Matanovic, I., Fishman, D.A. and Atanassov, P., 2020. Facile all-optical method for in situ detection of low amounts of ammonia. *Iscience*, *23*(11), p.101757.
13. Dumont, J.H., **Murphy, E**., Geller, D., Lee, K.S. and Labouriau, A., 2019. Effects of thermal aging and ionizing radiation on sPVC and aromatic polyether urethane used to store nuclear materials. *Polymer Testing*, *78*, p.105960.

ABSTRACT OF THE DISSERTATION

M-N-C Catalysts for Electrochemical Transformation of N-Species to Ammonia and Beyond

by

Eamonn Murphy

Doctor of Philosophy in Chemical and Biomolecular Engineering

University of California, Irvine, 2023

Professor Plamen Atanassov, Chair

Ammonia (NH_3) is a critically important molecule, necessary to produce fertilizers and is also used in a variety of household chemical and as a precursor in pharmaceuticals. Additionally, NH_3 has a relatively large energy density and can be liquified at mild conditions, making it appealing as not only a chemical feedstock but also as an energy storage vector. Unfortunately, the now century old Haber Bosch (HB) process remains the only way to produce NH_3 on a large scale. The HB process is one of the most energy intensive and carbon dioxide emitting processes and is therefore essential to decarbonize as we transition into a greener future.

The electrochemical transformation of reactive nitrogen-species is a promising, carbon neutral pathway for NH_3 synthesis. Typical approaches utilize di-nitrogen (N_2) as a reactant; however, the success of these systems remains unproven. Utilizing a more oxidized form of nitrogen, nitrate (NO_3^-), presents several advantages such as increased solubility in aqueous electrolytes and favorable adsorption energies, helping to increase the NO_3^- to NH_3 selectivity. The electrochemical nitrate reduction reaction (NO_3RR) is a complex $8e^-$ transfer reaction, where the

reaction pathway and participation of reaction intermediates is largely unknown. This dissertation addresses these issues by fundamental studies partitioning the reaction pathway over distinct catalytic sites in a bi-metallic system. Then moving to develop a series of physically relevant NO_3/NO_2RR activity descriptors. Finally, the knowledge gained from the fundamental studies is applied to create an active particle-active support catalyst system, achieving the NO_3RR to NH_3 at industrial current densities. Specifically, the studies are outlined below.

i) Highly durable and selective Fe-and Mo-based atomically dispersed electrocatalysts for nitrate reduction to ammonia via distinct and synergized NO_2^-pathways

An atomically dispersed bi-metallic FeMo-N-C catalyst was developed and was shown computationally and experimentally that the Fe-N_x sites favor NO_2^- to NH_3 conversion, while the Mo-N_x sites favor NO_3^- to NO_2^- conversion. These sites were synergized to achieve a NO_3- to NH_3 efficiency of 94%. Additionally, DFT uniquely demonstrated that over highly oxyphilic sites, such as Mo-N_x the real active site during the reaction is *O-Mo-N_x and can simultaneously adsorb multiple intermediates.

ii) Elucidating electrochemical nitrate and nitrite reduction over atomically dispersed transition metal sites

A library of 3*d*, 4*d*, 5*d* and *f*-metal atomically dispersed Metal-Nitrogen-Carbon catalysts were synthesized and extensively characterized for their atomically dispersed nature and M-N_x coordination. Electrochemical NO_3RR and NO_2RR were performed to obtain experimental activity descriptors. DFT was used to generate a series of computational activity descriptors. The experimental and computational activity descriptors were correlated to develop a set of physically relevant computational descriptors, such that the

NO_3/NO_2RR activity of M-N-C catalysts could be accurately predicted with a simple descriptor. Additionally, isotopic doping experiments revealed the complex NO_2^- production consumption mechanism over the M-N-C catalysts, confirming the $2e^- + 6e^-$ transfer pathway rather than the commonly assumed direct $8e^-$ pathway.

iii) Synergizing γ-Fe_2O_3 nanoparticles on single atom Fe-N-C for nitrate reduction to ammonia at industrial current densities

An active particle-active support catalyst system was synthesized by reducing γ-Fe_2O_3 nanoparticles onto an atomically dispersed Fe-N-C support. The catalyst system was characterized electrochemically to demonstrate the increase in NO_3RR performance of the γ-Fe_2O_3/Fe-N-C system over a γ-Fe_2O_3/XC72 system. Uniquely, the γ-Fe_2O_3/Fe-N-C system showed potential independent behavior on the FE_{NH3}, allowing for a reductive potential up to -1.2 V *vs.* RHE, while maintaining a 100% FE_{NH3} and a high $Yield_{NH3}$ over 9 mmol hr^{-1} cm^{-2}. An economic analysis invesitagting the levelized cost of NH3 revealed it is more beneficial to reduce the levelized cost of NH_3 to operate at a higher over potential of -1.0V at a lower energy efficiency, with a very high NH_3 partial current density (1.3 A/cm^2). Post-mortem XPS revealed that during the pre-reduction activation step, a surface layer of Fe^{2+}/Fe^0 is formed, resulting in the ultra-high NO_3RR activity observed.

Chapter 1

INTRODUCTION

1.1 Motivation

Synthetic ammonia via the nitrogen reduction reaction (NRR) is of critical significance to the global population and human activity as a key precursor for agricultural fertilizer. With an annual production of ~175 Mt worldwide accounting for ~70 billion USD market value, the industrial ammonia manufacturing, also called Haber-Bosch (H-B) process, is so important that more than 50% of the nitrogen atoms present in the human body originate from this process.[1] However, the H-B process is energy intensive due to an over 400 ^{o}C and 200 bar reaction condition, consuming 1-2% of global energy and being ranked as the 2nd most energy intensive chemical manufacturing process, right after ethylene and co-products. [2,3] Additionally, the needed stoichiometric hydrogen ($3H_2 + N_2 = 2NH_3$) is currently produced from steam reformation of natural gas that emits ~332 Mt carbon dioxide ($3CO_2$ per $8NH_3$), making the H-B process the 3rd largest CO_2 emitting manufacturing process (1st cement and 2nd iron ore). [4] Moreover, owning to the harsh reaction conditions and the need for steam reformation, the H-B process requires centralized infrastructure with a high capital cost and complex product distribution. Therefore, a sustainable, energy efficient, carbon neutral and decentralized ammonia synthesis pathway is essential for future energy utilization and chemical manufacturing.

Inspired by the biological enzyme, nitrogenase that utilizes protons (H^+) from water to synthesize ammonia at ambient conditions [5], electrocatalysis, particularly in aqueous media, is seen as a promising approach for green and distributed ammonia synthesis on a large scale. However, the electrocatalytic nitrogen reduction reaction (N_2RR) is extremely challenging, given the low

solubility of N_2 gas, its robust triple N≡N bond and the prevalent competing hydrogen evolution reaction (HER), as shown in Figure 1-1. Furthermore, the optimization of such low N_2RR activity is theoretically limited by the 'linear scaling relationships' between the adsorption energies of different surface intermediates [6], such that the parasitic HER dominates the catalytic activity over the entire potential range (Figure 1-1c).[7] Therefore, novel catalyst design is critical to realize such a kinetically and thermodynamically unfavorable process. Atomically dispersed catalysts, also named as single-atom catalysts (SACs), show unique electronic structure and catalytic activity as compared to their bulk and nanoparticle counterparts. [8] For example, single-atom transition metal nitrogen doped carbon (M-N-C) catalysts have long been studied as non-precious metal catalysts for the oxygen reduction reaction (ORR). [9,10] Recently, SACs have been utilized for the carbon dioxide reduction reaction (CO_2RR) to produce syngas[11] and other value-added products [12,13]. M-N-C catalysts were also reported to have nitrogen affinity in nitric oxide reduction. [14] Meanwhile, in the past three years, SACs supported by a carbonaceous matrix have been increasingly proposed and reported for their N_2RR activities in aqueous electrolyte.

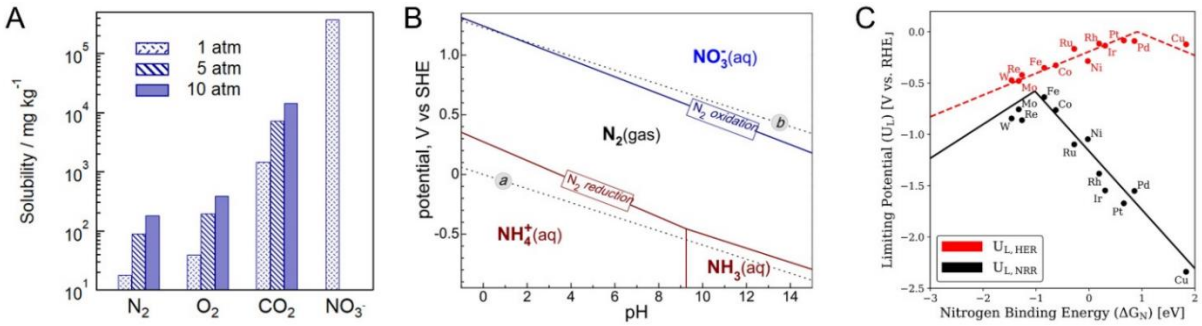

Figure 1-1. Kinetic and thermodynamic challenges of N_2RR. (A) Pressure dependence of dinitrogen solubility in water as compared to oxygen (O_2), carbon dioxide (CO_2) and nitrate (NO_3^-). (B) Pourbaix diagram of N_2RR and HER in an aqueous system. (C) Computation-based volcano plot of nitrogen adsorption energy on a transition metal terrace and rate determining potential of N_2RR and HER. Figures were adopted from References [7,15].

Due to the sluggish kinetics and low selectivity of N_2RR, especially in protic media, the benchmark of ammonia yield is extremely sensitive to exogenous contaminations in the form of either ammonia (NH_3) or the oxidized species of nitrogen (NO_x). In fact, ammonia is ubiquitous in our daily life and lab environment [16], which can easily introduce false positives to the N_2RR system. Since 2019, several impactful papers have been published, highlighting the immediate need for rigorous control in N_2RR systems. [16–21] Chorkendorf and coworkers proposed that regardless of Ar or OCV controls, multi-point quantitative isotopic analysis was indispensable.[22] In this work, by utilizing a multipoint quantitative isotopic analysis under a purified $^{15}N_2$ gas feed, all metal surfaces (Rh, Ru, etc.) failed to show N_2RR activity in a static H-cell. [16] Although later publications often presented a series of control experiments and occasionally included nuclear magnetic resonance (NMR) results for $^{15}NH_3$, a clear and convincing report was still absent. For example, very few papers reported whether the Ar or OCV control was performed independently or as a sequential test with same electrode, electrolyte and cell. Another example is the local bubble build-up on static electrodes (e.g., carbon papers), rendering the commonly reported plots of LSV showing a gap in the current density under Ar and N_2 atmospheres, claiming NRR activity, meaningless. [23]

Moreover, the contamination of NO_x species in catalysts and gas feeds creates a significant challenge on conducting effective and rigorous N_2RR. Furthermore, the adventitious NO_x species are also present in the labelled $^{15}N_2$ gas [24], creating ambiguity even in isotopic analysis. In 2020, Wenzhen Li and coworkers reported a widespread existence of NO_x in commercial catalysts [20], which was related to the retraction of a 2014 *Science* paper on electrocatalytic ammonia synthesis in molten salt [25]. Nitrogen can exist in multiple oxidation states from N_2 (0^+) to NO_3^- (5^+), in which the more oxidized forms can be more easily reduced to NH_3, Figure 1-2. More

recently, Simonov and coworkers published a critical work on the NO_x purification and verification in both standard and isotopic analysis for N_2RR.[21] That is, instead of simply claiming the purification of feed gases ($^{14}N_2$ and $^{15}N_2$), the NO_x level in the N_2 gas and electrolyte must be quantitatively verified and reported throughout the whole electrocatalytic process or at key steps. In the over 100 papers being explicitly evaluated by Simonov, only the lithium-mediated approach in aprotic media was satisfactory based on their three criteria in terms of reliable yield, multi-point quantitative isotopic analysis and the quantitative verification and reporting of NO_x species in the N_2RR system.

One promising work was reported by Duan and coworkers, wherein a unique high pressure reactor was used to enhance the kinetics and thermodynamics of N_2RR on single-atom (Rh, Ru, Co) sites on a graphdiyne matrix (SA-GDY).[26] Under a pressure of 55 atm in an electrolyte composed of 5 mM H_2SO_4 and 0.1 M K_2SO_4 (Figure 1-2), an ammonia yield rate of ~1.7 nmol s^{-1} cm^{-2} and FE of 20.36% were achieved at the cathodic potential of -0.2 V *vs.* RHE. But the non-verified NO_x species in this work failed to strictly meet the rigorous criteria set forth by Simonov et al. Nonetheless, this work demonstrated a promising systems optimization approach, utilizing increased N_2 pressure and thus favorable kinetics in an attempt to increase N_2RR activity.

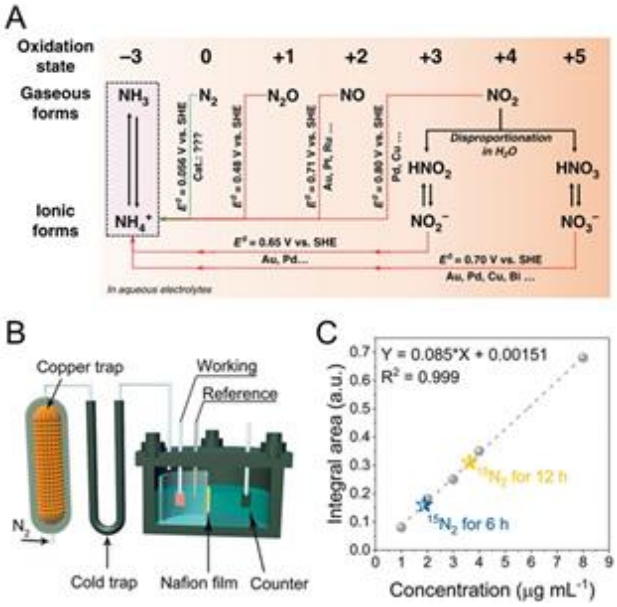

Figure 1-2. (A) Electrocatalytic pathways towards ammonia via the reduction of dinitrogen, gaseous NO_x molecules and ionic NO_x species. (B) High pressure reactor for N_2RR in aqueous electrolyte. (C) Time course study of ammonia yield via isotopic analysis with $^{15}N_2$ gas feed. Figures were adopt from references [21,27].

Several recent works have synthesized catalysts inspired by the biological enzyme nitrogenase, which consists of Mo and Fe cofactors, however, it should be noted that, not only for nitrogenase, Mo and Fe atoms are also the cofactor centers of natural nitrate/nitrite reductase. [28] Our recent work on nitrate reduction showed significant activity of Fe- and Mo-based SACs towards the electrocatalytic conversion of NO_3^-/NO_2^- to ammonia with high Faradic efficiency. However, when dinitrogen gas (N_2) was fed, in the absence of any NO_x species, no detectable ammonia was observed at potentials between 0 V and -0.7 V in a static H-cell filled with PBS, KOH, HCl or H_2SO_4 electrolyte. Therefore, following the rigorous benchmarked protocol is essential to demonstrate unambiguous N_2RR activity of all proposed catalysts. As mentioned in Simonov's work [21], N_2RR is such a kinetically and thermodynamically difficult process and thus it is not reasonable to see that such a variety of catalysts, including SACs, can effectively

promote N_2RR. After carefully reviewing the most recent and influential papers for single-atom N_2RR catalysts, we believe it does not enrich the discussion to make a typical comparison table with faradaic efficiency (FE) and ammonia yield for these catalysts.

As an alternative route to circumvent the significant challenges faces in the electrochemical reduction of N_2, a more oxidized form, nitrate (NO_3^-) presents a promising pathway. Although the reduction of NO_3^- to NH_3 is an $8e^-$ transfer process, 5 more e^- per NH_3 molecule than N_2 (Figure 1-3), there are several advantages to the nitrate reduction reaction (NO_3RR). In direct contrast to N_2, NO_3^- has a solubility in aqueous electrolytes 5 orders of magnitude higher as shown in Figure 1-1. The NO_3^- molecule only has a N=O double bond, making the activation and cleaving of this bond much easier than the highly stable N≡N bond. Additionally, it has been shown that the adsorption energies of NO_3^- on atomically dispersed M-N_x sites is more favorable over competing H^+. Both advantages allow the NO_3^- reactant to easily reach the catalytic active site and compete against the HER. A unique advantage of atomically dispersed catalysts for the NO_3RR is the isolation of M-N_x sites, which prevent the coupling of N-N intermediates (N_2), favoring the formation of mono-nitrogen products (NH_3).

NO_3^- is an environmental pollutant often found in wastewater runoffs, largely due to overfertilization practices and in industrial waste streams at concentrations up to 2M.[29] For wastewater reutilization, NO_3^- must be reduced and is typically done so though enzymatic denitrification treatments, reducing the NO_3^- to benign N_2. By employing the NO_3RR, the waste NO_3^- can not only be reduced for water remediation purposes, but a value added NH_3 is generated, providing dual benefits, while enhancing the efficiency of the nitrogen cycle. Importantly, the origin of the nitrogen in NO_3^-, is from the HB process, creating an NH_3 molecule used in the production of nitrogen-based fertilizers. Therefore, the NO_3RR through

waste streams is not independent of the HB process but does allow for a more efficient use and recycling of nonutilized NH_3. To create a NH_3 synthesis pathway fully decoupled from the HB process, low temperature plasma methods to oxidize N_2 into NO_x (NO_3^-) species is gaining interest. Currently the limiting factor of this technology is the high energy cost in the overall process of N_2 plasma oxidation and subsequent electrochemical NO_3^- reduction. However, current state of the art techniques places this green NH_3 pathway at an equivalent energy cost as Li-mediated pathways, highlighting its technical feasibility.

NO_3^- not only enables an electrochemical pathway to NH_3 synthesis, but also provides an opportunity for electrochemical carbon-nitrogen bond formation. Electrochemical C-N bond formation is an extremely new field, which is quickly gaining attention, for the high value chemicals which could theoretically by synthesized. NO_3^- is an ideal nitrogen reactant due to its high solubility in aqueous electrolytes, while its carbon-based reactant counterpart carbon dioxide / carbon monoxide with low solubility can be present in the gas phase. By employing a gas diffusion electrode (GDE), gaseous CO_2/CO can directly reach the solid surface of the catalyst, where the aqueous phase NO_3^- reactant is simultaneously present, at the triple phase boundary. Electrochemical C-N formation enables the direct synthesis of urea. Typically, 80% of produced NH_3 undergoes a second energy intensive, thermal reaction with NH_3 and CO_2 to produce urea ($CO(NH_2)_2$). The direct electrochemical synthesis eliminates emissions from both the HB process and secondary intensive reactions, decentralizing the synthesis of urea. The electrochemical synthesis of urea from NO_3^- is a complex multi proton electron transfer process ($16e^-$) as seen in Figure 1-3. Ideally, CO_2 and N_2 could be coupled, drastically reducing the required e^- ($6e^-$), however, to date success has only been confirmed when utilizing NO_3^-.

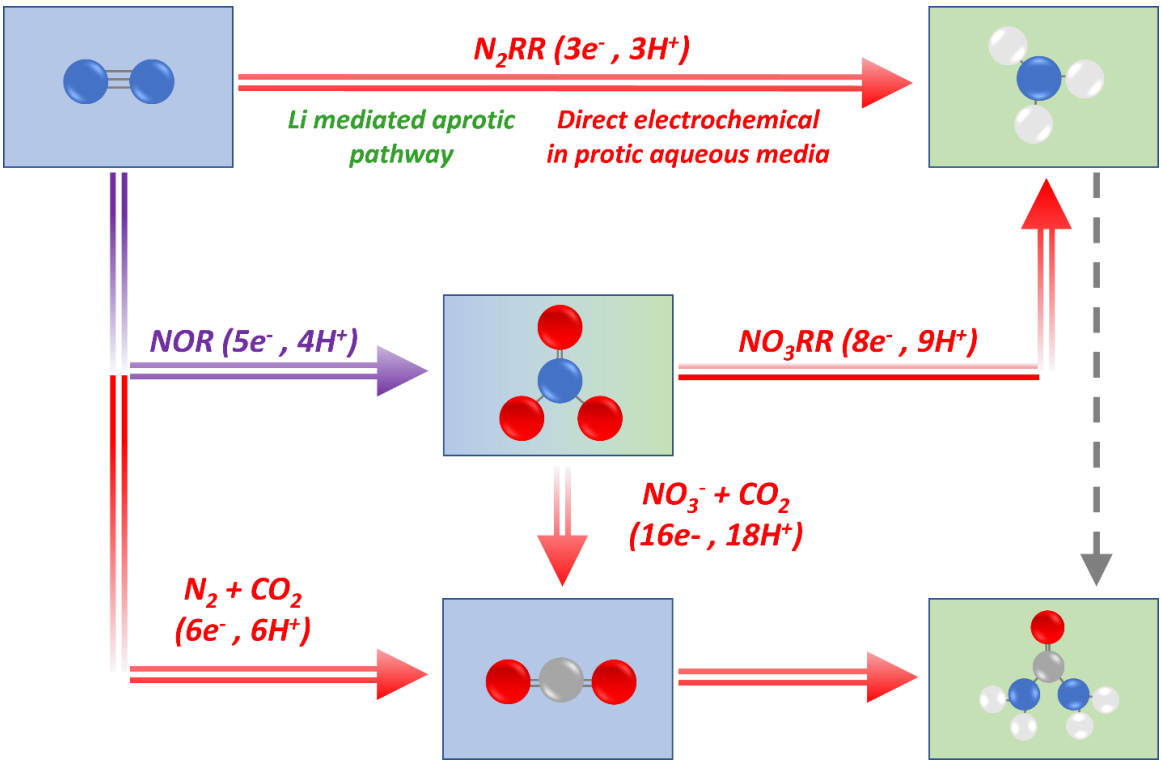

Figure 1-3. Landscape of electrochemical N-transformation pathways with N_2 and NO_3^- to NH_3 and coupling of carbon and nitrogen species for urea synthesis.

1.2 Dissertation focus

The electrochemical nitrate reduction reaction is a complex reaction with numerous (desorbable) intermediates. Only recently has interest been resurging for the NO_3RR, where most studies investigate extended metal surfaces, leaving atomically dispersed catalyst largely unexplored. This dissertation utilizes experimental and computational efforts to investigate the NO_3RR reaction mechanism and reveals role of the NO_2^- intermediate, following a complex $2e^- + 6e^-$ transfer pathway.

In chapter 2 a novel bio-inspired atomically dispersed FeMo-N-C catalysts is synthesized and it is demonstrated computationally and experimentally that the Mo-N_x sites follow a dissociative adsorption pathway, dissociating NO_3^- to NO_2^-, while the Fe-N_x sites follow an associative

adsorption pathway for NO_3^- to NH_3. The Fe-N_x sites also demonstrate extreme activity to the $6e^-$ reduction of NO_2^- to NH_3. Therefore, by synergizing the Mo-N_x and Fe-N_x sites, a cascade pathway for NO_3^- to NH_3 at high efficiency is demonstrated. Additionally, in this work it is revealed that the Mo-N_x sites cyclically generate NO_2^- by simultaneously adsorbing reaction intermediates (yielding a *O-Mo-N_x active site).

In Chapter 3, aiming to address the lack of experimentally supported NO_3RR activity descriptors in the literature, a library of 3*d*, 4*d*, 5*d* and *f*-metal atomically dispersed M-N-C catalysts were synthesized and extensively characterized. Experimental activity descriptors such as the reaction onset potential, NO_3RR and NO_2RR descriptors are extracted, while DFT was used to create a series of computational activity descriptors. The experimental and computational descriptors are then correlated to find the most relevant. Throughout this work, isotopic $^{15}NO_2^-$ doping experiments revealed the complex $2e^- + 6e^-$ transfer pathway over all M-N-C catalysts, demonstrating the difficulty in claiming a direct $8e^-$ pathway, even when little to NO_2^- is detected in the bulk electrolyte. Lastly, correlating the experimental and computational data revealed that over highly oxyphilic active sites, the true active site which must be considered for the NO_3RR is the oxo-form, where oxygen is bound as a fifth ligand (*O-M-N_x).

Chapter 4 extends beyond a mechanistic study to achieve the highest possible NO_3RR performance in terms of NH_3 partial current density (at maximum FE_{NH3}). A novel active particle-active support system (γ-Fe_2O_3/Fe-N-C) is synthesized and characterized. Through highly localized and bulk measurements, electronic interactions between the nanoparticles and single atom support are evaluated. Optimized NO_3RR performance reaches 1.95 A/cm^2 at near 100% FE_{NH3}. An economic analysis evaluating the tradeoff between energy efficiency (applied potential) and partial current density is performed, demonstrating an optimal operating potential

at -1.0 V *vs.* RHE. The high durability of the γ-Fe_2O_3/Fe-N-C catalyst is shown over 24 hours at -1.0 V *vs.* RHE, maintaining 100% FE and a current of 1.3 A/cm^2. Additionally, post-mortem XPS reveal the importance of the pre-reduction activation step, where surface Fe^{3+} is reduced to highly active Fe^{2+}/Fe^0, resulting in the ultra-high NO_3RR performance.

Chapter 5 closes by discussing the existing challenges of the NO_3RR which must be addressed in transitioning this technology forward to realize green NH_3 synthesis through electrochemical pathways. Additional comments on the progression of N_2RR are discussed. The catalytic systems developed in this dissertation were applied to neighboring CO_2 reduction and O_2 reactions and is briefly mentioned. Finally, the outlook of NO_3^- as a reactant for the electrochemical C-N bond formation is discussed.

Chapter 2

Highly durable and selective Fe- and Mo-based atomically dispersed electrocatalysts for nitrate reduction to ammonia via distinct and synergized NO_2^- pathways

2.1 Overview

Production of ammonia (NH_3).[30,31] NH_3 is critical to produce N-based fertilizers and shows promise as an energy vector and carbon free liquid fuel.[30,32–34] Currently, the near century old Haber-Bosch (H-B) process is the only industrial NH_3 manufacturing approach. However, the H-B process operates at high temperatures and pressures and utilizes grey hydrogen.[35] As a result, the process consumes 1-2% of global energy and produces 1-2% global CO_2 emissions.[34,36] Electrochemical methods offer carbon-neutral pathways for NH_3 synthesis, at ambient conditions and in a distributed manner. To date, the electrocatalytic nitrogen reduction reaction (N_2RR) from dinitrogen gas, is the most heavily researched. However, N_2RR faces several challenges such as low solubility in aqueous electrolytes, competition from the more facile hydrogen evolution reaction (HER) and large thermodynamic activation barriers.[37–39] As a result, the faradaic efficiencies (FE) and yields of NH_3 in aqueous systems remains low – even proving difficult for reliable analytical detection.[16,20,21]

To circumvent these challenges, oxidized nitrogen species, such as nitrate (NO_3^-) can be utilized as feedstock for efficient electrocatalytic NH_3 production. NO_3^- is the second most abundant form of nitrogen as an environmental pollutant present in industrial waste streams and water runoff at concentrations up to 2 M.[40–42] Nitrate's appeal is owed to its large solubility in aqueous electrolytes and relatively low bond dissociation energy (204 kJ/mol), facilitating significantly more favorable

kinetics compared to N_2RR processes.[43–45] The electrocatalytic nitrate reduction reaction (NO_3RR) has been studied extensively for denitrification and water purification.[43,44,46] Early NO_3RR research focused on selective reduction of NO_3^- to ½N_2 via a $5e^-$ transfer pathway (E^0 = 1.25 V vs. RHE)[45,47] and has been validated on a variety of bulk metals, heterogeneous catalysts (Ru, Rh, Pd, Ir, Pt, Cu, Ag and Au) and their alloys.[48–56]

Recently, significant attention has been shifted to selectively reducing NO_3^- to NH_3 via an $8e^-$ transfer pathway (E^0 = 0.82 V vs. RHE). The $8e^-$ transfer pathway is highly complex, involving many potential reaction intermediates (NO_2, NO_2^-, NO, N_2O, N_2, NH_3, NH_2OH and N_2H_4, etc.). The initial $2e^-$ transfer reduction of adsorbed $*NO_3^-$ to $*NO_2^-$ is thought to be universal in the NO_3RR pathways and is regarded as the rate limiting step.[57–59] Further reduction to *NO is regarded as the selectivity determining step on extended catalyst lattice surfaces. From *NO, the reaction pathways diverge selectively towards NH_3 or N_2, depending on electrolyte conditions and intermediates' adsorption strength on catalyst surfaces. Several recent computational studies have examined the selectivity of the *NO to subsequent reaction products (N_2, NH_2OH and NH_3) over a variety of transition metal surfaces.[60–62] By contrast, single atom catalysts (SAC) provide an intrinsic advantage favoring NH_3 production over N_2 products. By creating isolated single atom active sites, the possibility for two mono-nitrogen moieties to be activated on adjacent sites and form coupled N_2 products (N_2O, N_2, N_2H_4) is minimized, narrowing product selectivity largely to NH_3.[63] Recent work reported the feasibility of Fe-based SACs for NO_3RR and some theoretical work indicated that single atom active sites preferentially adsorb NO_3^- over H^+, reducing competition from the HER.[63–67] Although good progress has been made in the field of nitrate reduction for NH_3 production, developing well-established reaction mechanisms and electrocatalysts with long-term operational stability remain a significant challenge.[29]

In nature, the NO_3RR pathway is carried by enzymatic cascades, wherein the conversion of NO_3^- to NO_2^- and subsequent reduction of NO_2^- to NH_3 are catalyzed by the nitrate reductase Mo-cofactor and the nitrite reductase Fe-cofactor, respectively.[68,69] Analogously, in this work, we demonstrate a highly efficient synthetic electrocatalytic cascade utilizing chemical dissociation of the NO_3^- ion to NO_2^- over single-atom Mo sites. Followed by a kinetically fast $6e^-$ transfer reduction of NO_2^- to NH_3 at 100% FE over single-atom Fe sites.

Enzymatic NO_3RR:

$$NO_3^- \xrightarrow{\text{Mo-cofactor}} NO_2^- \xrightarrow{\text{Fe-cofactor}} NH_3$$

FeMo-N-C NO_3RR:

$$\text{Catalytic cascade: } NO_3^- \xrightarrow[\text{Chemical dissociation}]{\text{Mo-N-C}} NO_2^- \xrightarrow[\text{Fast } 6e^-]{\text{Fe-N-C}} NH_3$$

This biological process indicates the unique role of different metal elements for nitrogen transformation. Herein, we report for the first time, an in-depth study of atomically dispersed mono- and bi-metallic Fe- and Mo-based electrocatalysts for the NO_3RR. Distinct NO_3^- to $*NO_2/NO_2^-$ intermediate pathways were identified both computationally and experimentally. The initial NO_3^- adsorption was found to be dissociative on Mo sites and associative on Fe sites, showing great biological similarity. By integrating both Mo and Fe sites on a bi-metallic catalyst, the two reaction mechanisms were synergized, and the synthetic catalytic cascade achieved a NO_3RR faradaic efficiency (FE) for NH_3 of 94% and a yield of 18.0 μmol cm^{-2} hr^{-1} (153 μg_{NH3} mg^{-1}_{cat} hr^{-1}). Moreover, durability studies showed a well-maintained faradic efficiency above

90% over a 60-hour electrolysis. These findings pave the road for synergizing distinct reaction pathways on atomically dispersed electrocatalyst for highly selective and efficient NH_3 synthesis

2.2 Methods

2.2.1 Synthesis of Fe/Mo/FeMo-N-C SAC

The Fe, Mo and FeMo catalysts are synthesized via the sacrificial support method (SSM). Details of this method are reported in detail in previous work.[70,71] Iron nitrate nonahydrate and ammonium molybdenum tetrahydrate are selected as the iron and molybdenum precursors, selectively. First, a calculated amount of metal nitrate precursor (Fe-N-C precursor = 0.6 g, Mo-N-C precursor = 0.26 g) is combined with a silica of varying surface area, consisting of inhouse Stöber spheres, LM-150 and OX-50 (0.5 g, 1.25 g and 1.25 g, respectively). Nicarbazin (6.25 g) is added to the precursor mixture. For the molybdenum containing catalysts, a calculated amount of urea was added to assist in reducing the molybdenum precursor. The amount of metallic precursor is calculated such that the number of metal atoms between the mono- and bi-metallic catalysts is constant. Next, MilliQ water was added to the precursor ratio and sonicated for 30 min. The viscous mixture was then set at 45 ˚C under constant stirring until dry. The material is then ground and ball-milled for 1 hr at 45 Hz. A first pyrolysis is performed at 650 ˚C for 45 min under a reductive 7% H_2 - 93% Ar atmosphere. The material is then etched 4 days in a 40 wt% hydrofluoric acid mixture (2:1) HF/H_2O. The material is then washed until a neutral pH, before being dried and again ball milled. Next the material undergoes a second pyrolysis at 650 ˚C for 30 min under a 10% NH_3 – 90% Ar atmosphere, followed by a final ball-milling.

2.2.2 Scanning Transmission Electron Microscopy & Energy-Dispersive X-ray Spectroscopy

The surface morphology, nanostructure, and atomic distribution of the catalysts were analyzed by aberration-corrected scanning transmission electron microscopy and energy-dispersive X-ray spectroscopy (EDS) using a JEOL ARM300CF at an accelerating voltage of 300 kV.

2.2.3 Scanning Electron Microscopy

The surface morphology was further examined by scanning electron microscopy (SEM) on an FEI Magellan 400 XHR SEM.

2.2.4 X-ray Diffraction (XRD)

XRD patterns were collected on a Rigaku powder X-ray diffractometer.

2.2.5 X-ray Photoelectron Spectroscopy (XPS)

The surface valence and chemical bonds of the catalysts were analyzed by X-ray photoelectron spectroscopy (XPS) performed on a Kratos AXIS Supra spectrometer with a monochromatic Al Kα source. CasaXPS software was used to analyze the XPS data. An asymmetric 50% Gaussian/50% Lorentzian setup was applied for sp2 carbon. A 70% Gaussian/ 30% Lorentzian setup was used for all other data.

2.2.6 Inductively Coupled Plasma Mass Spectrometry (ICP-MS)

The metal content in each catalyst was quantified by inductively coupled plasma mass spectrometry (ICP-MS) on an Agilent 5110 (Appendix A.1).

2.2.7 Nitrogen Physisorption

N2 adsorption−desorption isotherms were recorded on a Micromeritics 3Flex Analyzer at 77 K, with a low-pressure dosing mode (5 cm^3 /g). The surface area was calculated by the

Brunauer−Emmett−Teller (BET) method, and pore size distribution was obtained using the nonlocal density functional theory model (NLDFT)

2.2.8 Raman Spectroscopy

Raman spectra were taken using an InVia Renishaw Corp., U.K., system to quantify the graphitic and amorphous carbon content.

2.2.9 Electrochemical Measurements

The working electrode was a carbon paper (AvCarb MGL 370, Fuel Cell Store) cut to a geometric surface area of 0.45 cm^2. The carbon paper was pre-treated to increase the hydrophilicity of the paper with an oxygen plasma treatment, followed by acid washing in 0.5 M H_2SO_4 and finally washed with MilliQ water. The catalyst ink was prepared by dispersing 5 mg of the M-N-C catalyst in 300 μL of MilliQ water, 670 μL of isopropanol and 30 μL of a 5 wt% Nafion solution and ultrasonicated for 1 hour. 100 μL of the catalyst ink was drop cast onto the carbon paper for a total catalyst loading of 0.5 mg/cm^2 and dried in a vacuum oven at 60 ˚C overnight.

2.2.10 Nitrate Reduction Reaction (NO_3RR)

Electrochemical nitrate reduction measurements were carried out in a customized glass H-cell, separated by a Nafion 211 membrane (Fuel Cell Store) at ambient conditions. Before the electrochemical test, the membrane was pretreated by boiling in 5% H_2O_2 for 1 hour, followed by boiling in H_2O for 1 hour and then 0.5 M H_2SO_4 and finally washed with Millipore water. Electrochemical measurements were recorded using a Biologic VMP3 potentiostat. A standard three-electrode system was used with a reversible hydrogen electrode and a graphite rod as the reference and counter electrode, respectively. The electrolyte used for all nitrate reduction experiments is 0.05 M phosphate buffer solution (PBS) with a concentration of 0.16 M NO_3^-

(KNO_3), providing a pseudo infinite, but industrially practical concentration of NO_3^- in the bulk throughout all experiments in this study. Prior to electrochemical test, N_2 gas (research grade 99.9995% - PraxAir) is purged in both the working and counter chambers for 30 min at 80 sccm, which contain 30 mL and 25 mL of electrolyte, respectively. Potentiostatic tests are performed for 4 hours under constant stirring at a constant N_2 gas flow rate of 30 sccm to the working chamber. Potentiostatic tests were performed at potentials of -0.2, -0.35, -0.45, -0.55 and -0.70 V *vs.* RHE. Time-course tests are performed at -0.45 V *vs.* RHE for 24 hours at identical conditions. Similarly, consecutive long-term stability tests are performed at -0.45 V *vs.* RHE for 12-hour periods, after which the electrolyte is refreshed and another cycle is performed. LSV was performed at a rate of 10 mV/s, also under constant stirring and a gas flow rate of 30 sccm to the working chamber.

2.2.11 Nitrite Reduction Reaction (NO_2RR)

Electrochemical nitrite reduction experiments were performed analogously to nitrate reduction experiments, utilizing the same H-cell and three electrode system. The electrolyte is 0.05 M PBS with a concentration of 0.01 M NO_2^- (KNO_2), giving a concentration of NO_2^- in the bulk on the same order of magnitude as that observed in the NO_3RR experiments. Potentiostatic tests were performed for 30 min and LSV was obtained at a scan rate of 10 mV/s. Potentiostatic tests were performed at potentials of -0.2, -0.35, -0.45, -0.55 and -0.70 V *vs.* RHE.

2.2.12 Isotopic Doping Experiments

To verify that the source of the electrochemically synthesized NH_3 originates from the NO_3^- feed, several control experiments were performed. The first control removed the driving force for catalysis, nitrate electrolysis was performed analogously to typical nitrate reduction experiments as described above, however, without an applied potential. After 4 hours at open circuit voltage

(OCV), the electrolyte was sampled, and no ammonia was found as shown in Appendix A.2. The next control experiment is to perform the nitrate reduction without the addition of an NO_3^- source. 4-hour nitrate reduction electrolysis was performed using standard 0.05M PBS electrolyte. In the absence of a NO_3^- source, the sampled electrolyte showed no ammonia produced, as shown in Appendix A.2. Furthermore, isotopically labeled experiments were conducted as described in detail below.

Isotopic ^{15}N labeling experiments were performed by using $K^{15}NO_3$ (99% - Cambridge Isotopes) as the isotopic nitrate source, utilizing analogous experimental procedures to the nitrate reduction tests. The electrolyte used for the isotopic labeling experiments is 0.05 M PBS with 0.16 M isotopically labeled potassium nitrate. Potentiostatic tests were performed at -0.45 V *vs.* RHE for 6 hours, under constant stirring and a N_2 gas flow of 30 sccm to the working chamber. The electrolyte was collected at the start of the test, after 1 hour, 2 hours, 4 hours, and 6 hours and the $^{15}NH_3$ is quantified by ^{1}HNMR.

2.2.13 Yield and Faradaic efficiency calculations

The nitrate (NO_3^-) and nitrite (NO_2^-) reduction to ammonia yield rate was calculated by Eq.1.

$$Yield_{NH_3} = \frac{c_{NH_3} * V}{Mw_{NH_3} * t * A_{electrode}} \quad (1)$$

The nitrate (NO_3^-) and nitrite (NO_2^-) reduction to ammonia Faradaic efficiency was calculated by Eq. 2.

$$FE_{NH_3} = \frac{n * F * c_{NH_3} * V}{Mw_{NH_3} * Q} \quad (2)$$

The nitrate (NO_3^-) to nitrite (NO_2^-) reduction Faradaic efficiency was calculated by Eq. 3.

$$FE_{NO_2^-} = \frac{n * F * c_{NO_2^-} * V}{Mw_{NO_2^-} * Q} \quad (3)$$

Where c_{NH_3} is the concentration of $NH_{3(aq)}$ (μg / mL), V is the volume of the electrolyte (mL), Mw_{NH_3} is the molar mass of NH_3 (17.031 g / mol), t is the electrolysis duration (hr), $A_{electrode}$ is the geometric surface area of the working electrode (0.45 cm^2), n is the number of electrons transferred (n = 8 for nitrate reduction to ammonia, n = 6 for nitrite reduction to ammonia and n = 2 for nitrate reduction to nitrite), F is the Faraday constant (96485 C / mol), $c_{NO_2^-}$ is the concentration of NO_2^- (μg / mL), Q is the total charge passed during the electrolysis and $Mw_{NO_2^-}$ is the molecular mass of nitrite (46.005 g / mol)

The turnover frequency (TOF) was estimated using Eq. 4.

$$TOF = \frac{Yield_{NH3}}{SD} \quad (4)$$

Where $Yield_{NH3}$ is the yield rate of NH_3 (μmol / cm^2 s^1) and SD is the site density of metal per geometric area of the working electrode (μmol metal / cm^2).

2.2.14 Product Detection

For typical, non-isotopically labeled nitrate and nitrite reduction experiments, products were detected and quantified using an ultraviolet-visible (UV-Vis) spectrophotometer (Shimadzu, UV-2600). *Ammonia was detected by the spectrophotometer using the indophenol blue method.*[72] Due to the large concentration of ammonia produced, working electrolyte solution was diluted such that the colorimetric result would fall within the range of the calibration curve. Specifically, 2 mL

of the electrolyte (or diluted electrolyte if needed) was placed in a vial. To this, 2 mL of a 1 M NaOH solution that contains 5 wt% salicylic acid, and 5 wt% sodium citrate was added. Then, 1 mL of a 0.05 M NaClO and 0.2 mL of a 1 wt% $C_5FeN_6Na_2O$ (sodium nitroferricyanide) was added to the solution. The solution was incubated in the dark at room temperature for 1 hr and then then UV-Vis spectra were taken. The concentration of NH_3 is determined using the maximum absorbance at a 655 nm wavelength. Standard UV-Vis calibration curves and linear calibration is provided in Appendix A.3.

Nitrite concentration was detected by the spectrophotometer using a commercial nitrate assay kit (Spectroquant), based on the Griess test. Due to the large concentration of nitrite produced, working electrolyte solution was diluted such that the colorimetric result would fall within the range of the calibration curve. Specifically, 2 mL of the electrolyte (or diluted electrolyte if needed) was placed in a vial. To this, 22 mg of the assay reagent was added to the electrolyte and incubated in the dark for 10 min. After incubation, the UV-Vis spectra were taken, and the concentration of nitrite was determined at a maximum absorbance of 540 nm. Standard UV-Vis calibration curves and linear calibration is provided in Appendix A.4.

Nuclear magnetic resonance (NMR) spectroscopy was used to detect and quantify the ammonia produced from NO_3RR and NO_2RR experiments. Dimethylsulfoxide-d6 (DMSO) and 3-(trimethylsilyl)-1-propanesulfonic acid sodium salt (DSS) were used as the locking solvent and internal standard, respectively. The NMR test solution was composed of a mixture of 580 μL of the electrolysis electrolyte, 25 μL of DMSO, 20 μL of 3 M H_2SO_4, and 75 μL of 6 mM DSS (made with Millipore water). The NMR spectrum was obtained on a Bruker CRYO 500 MHz spectrometer. The signal from H_2O was restrained for better accuracy by applying the solvent suppression method during acquisition. Topspin 4.0.8 software was used to process the NMR data.

Standard UV-Vis calibration curves and linear calibration for normal $^{14}NH_3$ and isotopically labeled $^{15}NH_3$ are shown in Appendix A.5 and Appendix A.6, respectively.

2.2.15 Computational Details

All the density functional theory (DFT) calculations were performed using a generalized gradient approximation approach and projector augmented-wave pseudopotentials[73,74] as implemented in the Vienna Ab initio Simulation Package[75–77]. An optB86b-vdW functional was used to account for the van der Waals forces[78–81] with a gamma centered 8x8x1 *k*-mesh and Fermi-smearing; sigma was set to 0.03. In all cases, the plane-wave basis cutoff was set to 400 eV. Fe-N-C and Mo-N-C catalysts were modeled using 4x4 orthorhombic single-layer graphene cells with the dimensions of 9.84 x 8.52 Å and a vacuum region of 15 Å. Active sites were modeled by removing two adjacent C atoms in the cell and filling the internal edges with 4 N atoms after which the resulting structure was coordinated to Fe and Mo atom creating a M-N_4 structure. Computational models for these sites are extensively tested in our previous work.[82–85] All structures were then optimized by allowing all atoms to relax, but the lattice was kept fixed at the DFT optimized value for graphene. The criteria for the convergence of the electronic energy were set to 1×10^{-5} eV, while the forces were converged to 0.01 eV/Å. For details regarding the calculations of the associative and dissociative adsorption over Fe-N_4 and Mo-N_4 sites, see the Appendix A.27 and Table 1.

2.3 Distinct *NO_2/NO_2^- intermediate pathways over Fe and Mo active sites

In biological NO_3^- reduction pathways, Mo-based active centers reduce NO_3^- to NO_2^- and Fe-based active centers further reduce NO_2^- to NH_3 (or N_2). To evaluate the catalytic activity of atomically dispersed Fe and Mo sites towards the NO_3RR to NH_3, a series of atomically dispersed M-N-C (M = Fe, Mo and FeMo) electrocatalysts were employed.

Density Functional Theory (DFT) and experimental NO_3^- reduction time-course studies predicted and confirmed two different reaction mechanisms over the M-N_4 sites. As shown in Figure 2-1a, over exclusively Fe sites, associative NO_3^- adsorption is favorable with a Gibbs free adsorption energy calculated at -0.39 eV. Namely, Fe sites can stabilize the adsorbed NO_3^- regardless of the orientation NO_3^- binds to the active sites, through either one or two oxygen atoms. This determined the basis of a direct $8e^-$ transfer pathway from $*NO_3$ to NH_3, which was supported by its electrocatalytic time-course study as shown in Figure 2-1d, wherein the NO_2^- concentration observed was negligible and constant, throughout the entire 24-hour electrolysis, while the concentration of NH_3 steadily increased. The detected minute amount of NO_2^- ions might be from the low-probability of $*NO_3$ dissociation over the Fe sites, which will be discussed in a following section. In contrast, over exclusively Mo sites (Figure 2-1b), DFT calculations predicted the reaction initiates via a highly favorable dissociative-adsorption pathway ($\Delta_r G$ = -4.2 eV), spontaneously breaking the O-N bond of the NO_3^- molecule to form a surface *O intermediate and NO_2^- ion. The corresponding experimental time-course study supports this hypothesis (Figure 2-1e), highlighting a significant NO_2^- evolution over NH_3 through the entire 24-hour electrolysis. In this case, the complete NO_3^- to NH_3 process follows a $2e^- + 6e^-$ transfer pathway.

Interestingly, by integrating both Mo and Fe sites in a bi-metallic catalyst (Table 2. ICP-MS of Fe-N-C, Mo-N-C and FeMo-N-C electrocatalysts.), a synergized pathway was proposed to optimize the NH_3 production with a catalytic cascade as shown in Figure 2-1c. That is, NO_3^- was dissociated to NO_2^- on Mo sites, and NO_2^- can be subsequently associatively-adsorbed over Fe sites and further reduced to NH_3. In the corresponding time-course study (Figure 2-1f), the

synergistic effect was confirmed by observing improved NH_3 yield and a largely suppressed NO_2^- concentration as compared to the Mo-N-C case, indicating the additional Fe sites readily converted the NO_2^- to NH_3.

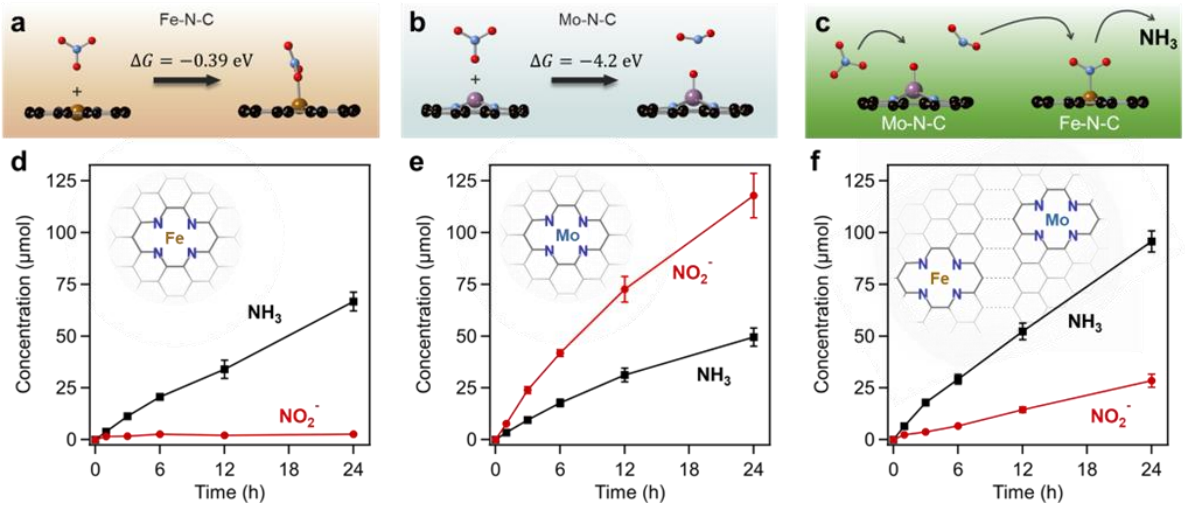

Figure 2-1. Elucidation of distinct NO_3^- to NO_2^- pathways in the electrochemical nitrate reduction (NO_3RR) for NH_3 synthesis over Fe- and Mo-based M-N_4 sites. (a) Associative adsorption of NO_3^- on Fe-N_4 sites as predicted by DFT calculations. (b) Dissociative adsorption of NO_3^- into *O and NO_2^- on Mo-N_4 sites. (c) Proposed catalytic cascade for synergized NO_3^- reduction over Mo-N_4 and Fe-N_4 sites. (d-e) The evolution of NH_3 and NO_2^- concentrations over a 24-hour NO_3RR electrolysis catalyzed by (d) mono-metallic Fe-N-C catalyst, (e) mono-metallic Mo-N-C catalyst and (f) bi-metallic FeMo-N-C catalyst. Insets show top-down view of corresponding active sites. The electrolysis was performed at -0.45 V (vs. RHE) in 0.05M PBS + 0.16M NO_3^- electrolyte. The errors were calculated from three independent electrolysis. UV-Vis absorption curves for the detection of NH_3 and NO_2^- over the 24-hour electrolysis for the Fe-N-C, Mo-N-C and FeMo-N-C are shown in Appendix A.7, Appendix A.8 and Appendix A.9. (C – black, N – blue, O – red, Fe – gold, Mo – purple).

2.4 Electrochemical Nitrite and Nitrate Reduction

By mimicking biological pathways and synergizing Mo and Fe sites, the activity of the bi-metallic catalyst for the NO_3RR was significantly increased compared with its mono-metallic counterparts. To further explore the catalyst activity and reaction mechanism, detailed potential dependent studies were performed for the nitrite reduction reaction (NO_2RR) and NO_3RR processes.

The cathodic current and reaction onset potential were first evaluated by linear sweep voltammetry (LSV) in a standard 0.05 M phosphate buffer solution (PBS) electrolyte. Employing the bio-inspired bi-metallic FeMo-N-C as an example, the LSV curves in Figure 2-2a show that the HER had a delayed onset potential below -0.5 V (*vs.* RHE), indicating the suppression of the parasitic reaction, a characteristic of many atomically dispersed active sites for the NO_3RR.[63–65,86] This is also confirmed by our DFT calculations (Appendix A.10), which show that due to the larger Gibbs free energy of adsorption for NO_3^- and NO_2^- *vs* H adatom (-0.39 and -1.07 eV *vs*. +0.52 eV for Fe-N_4 and -2.72 and -2.24 eV *vs*. -0.18 eV on Mo-N_4 sites at pH=6.3), HER should be pushed to -0.6 V and -1.1 V *vs* RHE on Fe- and Mo-containing sites. The addition of 0.01 M NO_2^- shifts the onset potential over Fe-N_x sites to 0.12 V, observed in both the Fe-N-C (Appendix A.11) and FeMo-N-C (Figure 2-1a) catalysts, indicating the high activity of the Fe sites toward the NO_2RR at low overpotentials. Particularly, when compared with the Mo-N-C catalyst, the Fe-containing catalysts showed a steep NO_2RR current increase at potentials between 0 V and -0.2 V (Appendix A.11). Similarly, the addition of 0.16 M NO_3^- also positively shifted the onset potential to -0.20 V and increased current densities. Interestingly, the positive shift in the onset potential in NO_3^- to -0.09 V, was most significant in the FeMo-N-C catalyst (Appendix A.11), likely due to the cascade

pathway with Mo sites chemically converting NO_3^- to NO_2^- and Fe sites electrochemically reducing the NO_2^- to NH_3 at low overpotentials.

The $6e^-$ transfer reduction of NO_2^- ions or *NOOH intermediate to NH_3 is a critical step in the NO_3RR and the key in synergizing the dissociative and associative reaction mechanisms as shown in Figure1c ($2e^- + 6e^-$ transfer pathway). Therefore, the activity and selectivity of nitrite reduction were first studied as shown in Figure 2-2 b and c. The potential-dependent studies show that both the mono- and bi-metallic electrocatalysts reduced NO_2^- to NH_3 at yields and FEs greater than those for nitrate reduction even under a 16-fold concentration of NO_3^- (Figure 2-2 d and e), demonstrating the downstream $6e^-$ steps from NO_2^- to NH_3 are not rate limiting in the NO_3RR. This is also partially supported by previous experimental and theoretical works.[57,63,87] Additionally, it was revealed that the Fe sites were particularly active for the NO_2RR, in that the its FE was consistently around 100% at all potentials, and the yields were as high as 50.6 μmol cm^{-2} hr^{-1} (865 μg_{NH3} mg^{-1}_{cat} hr^{-1}) at -0.7 V. While less active than Fe sites, mono-metallic Mo sites still maintained a FE above 60% below -0.35 V and reached a maximum yield of 18.3 μmol cm^{-2} hr^{-1} (177 μg_{NH3} mg^{-1}_{cat} hr^{-1}) at -0.7 V. This also explains the moderate NH_3 evolution, compared to the dominant NO_2^- production, of the Mo-N-C in the 24-hour time-course study shown in Figure 2-1e. Interestingly, the difference in nitrite reduction efficacy between Fe and Mo sites mirrors the behavior seen in biological systems, where Mo-based reductases preferentially convert NO_3^- to NO_2^- and Fe-based reductases preferentially convert NO_2^- to NH_3.

Based on the understanding of the NO_2RR activities, the more complex electrochemical nitrate (NO_3^-) reduction was investigated. Figure 2-2d shows the FE for NH_3 and NO_2^-, with the balance being undetected gas phase products, likely H_2 or NO species since N_2 is unlikely to form on

single-atom active sites. The corresponding NH_3 yields as a function of potential are shown in Figure 2-2e.

In agreement with Figure 2-1 d and e, the NH_3 and NO_2^- FEs confirmed distinct reaction mechanisms for Fe and Mo sites. NO_3RR over exclusively Mo sites resulted in a large portion of cathodic current going to the kinetically facile NO_3^- to NO_2^- reduction via the dissociative-adsorption mechanism, resulting in a FE_{NO2-} up to 33% (~60% molar percent) at -0.45 V. Meanwhile, the FE_{NH3} was 66% at -0.45 V with a corresponding yield of 5.6 μmol cm^{-2} hr^{-1} (48 μg_{NH3} mg^{-1}_{cat} hr^{-1}). Although decreasing the electrode potential from -0.2 V to -0.7 V increased the NH_3 yield (Figure 2-2e), its FEs failed to surpass 70% and a 1.5-fold FE_{NO2-} was observed at -0.7 V. In contrast, the NO_3RR over Fe sites demonstrates a highly selective and efficient reduction of NO_3^- to NH_3 (rather than NO_2^-) via a direct $8e^-$ pathway, resulting in a FE_{NH3} up to 84% and a yield of 10.1 μmol cm^{-2} hr^{-1} (86 μg_{NH3} mg^{-1}_{cat} hr^{-1}) at -0.45 V. Although the NO_3RR became slightly favorable to NO_2^- at more cathodic conditions, the FE_{NH3} was well maintained above 80% and the NH_3 yield over Fe active sites was consistently higher than that of Mo active sites. Given Fe-N-C's excellent NO_2RR activity (Figure 2-2 b and c), the first $2e^-$ transfer process is likely the rate limiting step for the NO_3RR.

These results inform a clear catalytic strategy. By integrating heterogenous Mo sites, which readily reduce NO_3^- to NO_2^-, with and Fe sites, which are limited by NO_3^- to NO_2^- reduction, into a single *bi-metallic* catalyst (FeMo-N-C), a synergistic catalyst system can be employed to optimize this multistage NO_3NRR chemistry. As shown in Figure 2-2d, the bimetallic FeMo-N-C catalyst showed an increased FE_{NH3} up to 94% at -0.45 V, a value among the highest selectivity

reported for NO_3^- reduction to NH_3 (Table 3. Comparison of Literature of the NO_3RR for NH_3 synthesis.) (The remaining 6% FE came from NO_2^-). Additionally, the NH_3 yields were significantly improved to 18.0 μmol cm^{-2} hr^{-1} (153 μg_{NH3} mg^{-1}_{cat} hr^{-1}), which was 1.8-fold greater than Fe-N-C and 3.5-fold greater than Mo-N-C at -0.45 V. As compared to the NO_2RR, where Fe-N-C showed the largest NH_3 yield over FeMo-N-C and Mo-N-C (Figure 2-2c), the bi-metallic catalyst showed a dominating NH_3 yield in the NO_3RR at all potentials (Figure 2-2e), strongly supporting the synergy of the Mo sites (NO_3^- to NO_2^-) and Fe sites (NO_2^- to NH_3) in the NO_3RR via a cascade reaction for optimized ammonia synthesis.

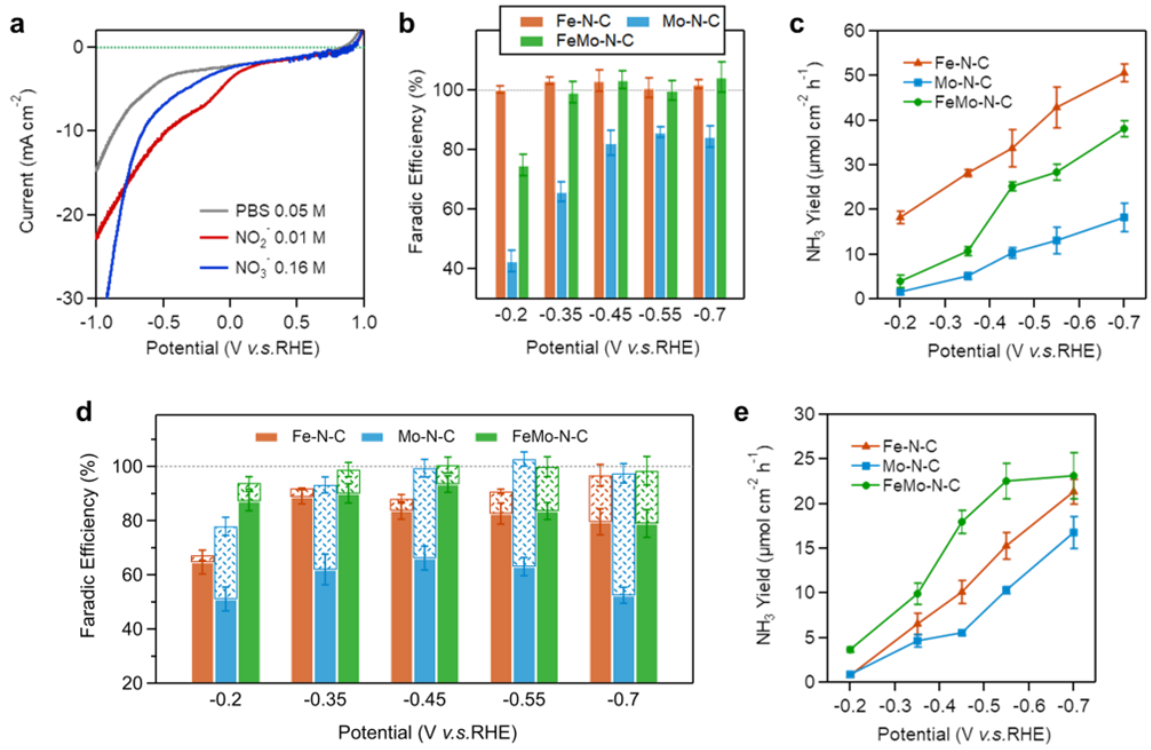

Figure 2-2. Electrocatalytic performance of NO_2^- and NO_3^- reduction for atomically dispersed Fe-N-C, Mo-N-C and FeMo-N-C catalysts. (a) Linear Sweep Voltammetry at a scan rate of 10 mV s^{-1} for the FeMo-N-C catalyst in 0.05M PBS and 0.05M PBS doped with either 0.01M NO_2^- or 0.16M NO_3^-. (b-c) Potential dependent NO_2RR (0.5 hour) for the three catalysts at a NO_2^-

concentration of 0.01M, specifying b) NH_3 Faradic Efficiency (FE) and c) NH_3 yield rate. The NO_2RR chronoamperometry plots and UV-Vis detection for NH_3 are shown in Appendix A.12 and Appendix A.13, respectively. Note, FE's over 100% are a result of electrolyte dilution to bring the concentration of NH_3 into the detection calibration range. Potential dependent NO_3RR (4 hours) for the three catalysts at a NO_3^- concentration of 0.16M. (d) FE for NH_3 (solid bars) and NO_2^- (dashed bars) at varying potentials, with the dotted line indicating 100% FE. (e) Yield rates for NH_3. All errors were calculated from three independent electrolysis. Corresponding TOF calculations are given in Table 4. The NO_3RR chronoamperometry plots and UV-Vis detection for NH_3 and NO_2^- are shown in Appendix A.14, Appendix A.15, Appendix A.16 and Appendix A.17.

2.5 NO_3RR Stability and Reliability

A recent review by Koper and co-workers highlighted that long-term durability studies are an immediate need for the future development of ammonia synthesis via the NO_3RR.[29] Usually, durability has been claimed from single or several cycles of short-term electrolysis (0.5 – 4 hours). For example, titanium electrodes were reported to achieve a FE of 82% for the first 2 hours, after which, the FE dropped to 40%, showing change of catalytic performance over long-term electrolysis.[88] Here, durability studies were performed on the FeMo-N-C catalyst at -0.45 V for a total operation time of 60 hours, broken into five 12-hour segments, each with a refreshed electrolyte (Figure 2-3a). After the first 12 hours, the yield decreased from 13.8 μmol cm^{-2} hr^{-1} to 9.3 μmol cm^{-2} hr^{-1} then remained steady. However, the FE_{NH3} was well maintained above 90% over the 60 hours, demonstrating the robustness of the electrocatalyst for selective NO_3^- reduction to NH_3.

Isotopic analysis is essential to confirm the electrochemical transformation of N-species to NH_3, especially with N-doped catalysts. A 6-hour electrolysis was conducted at -0.45 V with a $^{15}NO_3^-$ feed at the same concentration. Figure 2-3b shows only the characteristic doublet of $^{15}NH_3$ in the ^{1}H-NMR spectrum, wherein the peak intensity steadily increased throughout the 6-hour experiment, showing good linearity between the NH_3 concentration and reaction time (Figure 2-3c). Consequently, the NH_3 production from the labeled $^{15}NO_3^-$ and standard $^{14}NO_3^-$ showed good consistency in terms of both FE_{NH3} 92% vs. 94% and yields 16.5 μmol cm^{-2} hr^{-1} vs. 18.0 μmol cm^{-2} hr^{-1} (Figure 2-3d), confirming the reliability of NO_3^- conversion to NH_3.

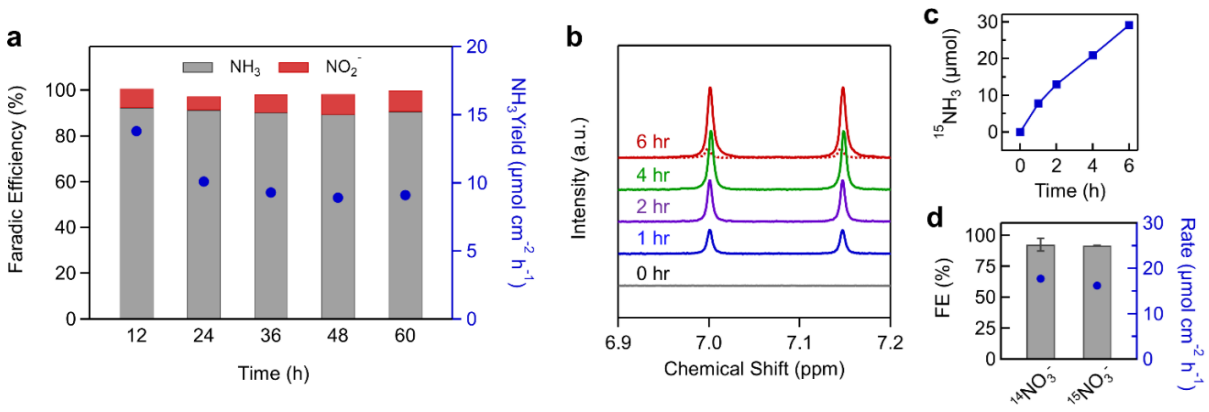

Figure 2-3. NO_3RR stability test and isotopic analysis for the FeMo-N-C catalyst. (a) 60-hour electrolysis at -0.45 V (*vs.* RHE) in 0.05M PBS + 0.16M NO_3^-. Every 12 hours, the electrolyte was sampled for NH_3 and NO_2^- quantification, and then refreshed for the next cycle. (b-d) $^{15}NO_3$RR electrolysis at -0.45 V with isotopically labeled $^{15}NO_3^-$ (0.16 M). (b) ^{1}H-NMR spectra of the electrolyte at varying time intervals. The dashed line at the 6-hour point indicates $^{15}NH_3$ detected in counter chamber due to the NH_3 crossing over the membrane. (c) Concentration of $^{15}NH_3$ as a function of the electrolysis time. (d) Comparison of the NH_3 FE and yield rate from $^{14}NO_3^-$ and $^{15}NO_3^-$ feeds, over 6-hours of electrolysis.

2.6 Physical structure of the Fe, Mo and FeMo-N-C SACs

The atomically dispersed mono- and bi-metallic catalysts in this work were synthesized using the well-established sacrificial support method (SSM).[89,71] The SSM class of M-N-C catalysts have been widely studied due to their good activity and stability for the oxygen reduction reaction (ORR)[9,91], where the oxidative cathodic potentials (0.6 V to 1 V) are even more harsh for carbon corrosion as compared to the reductive potentials in NO_3RR (-0.8 V to -0.2 V). The outstanding ORR performance for the SSM M-N-C was largely attributed to its high degree of graphitization and robust M-N_x sites[92], which also greatly contributed to the excellent stability of the FeMo-N-C for NO_3RR in this work (Figure 2-3a).

Specifically, ICP-MS results showed a metal loading of 0.73 wt% for Fe-N-C and 1.36 wt% for Mo-N-C, while the bi-metallic FeMo-N-C preserved 0.38 wt% Fe and 0.77 wt% Mo, as shown in Table 2. Raman spectroscopy showed the three electrocatalysts have a similar degree of graphitization (Appendix A.18). The resulting carbon matrix exhibited a hierarchical porous structure with leading mesoporosity around 20 nm and 100 nm, as shown by the nitrogen physisorption results and SEM images (Appendix A.19 and Appendix A.20). The N_2 sorption isotherm also confirmed a large amount of micropores that contributed to a BET surface area of *ca.* 600 m^2/g for all catalysts. The hierarchical pore structure was favorable for promoting mass transport of the electrolyte to the active sites. X-ray diffraction (XRD) patterns for the mono- and bi-metallic catalysts (Figure 2-4a), show only two peaks, characteristic of the (002) and (100) graphitic planes. The absence of any Fe or Mo crystalline peaks supports the formation of only atomically dispersed metal sites. The aberration corrected high angle annular dark field (AC-

HAADF) image for the FeMo-N-C catalyst in Figure 2-4b again shows the well-defined porous structure and the absence of any metallic nanoparticles. The high mag AC-HAADF image in Figure 2-4c reveals distinct bright spots, indicating the abundance of atomically dispersed Fe and Mo atoms. Energy dispersive X-ray spectroscopy (EDS) maps (Figure 2-4d) reveal a homogenous distribution of C, N, Mo, and Fe elements. Low and high mag AC-HAADF images and EDS mapping for the mono-metallic Fe-N-C and Mo-N-C catalysts are shown in Appendix A.21 and Appendix A.22, respectively. Fe 2p X-ray photoelectron spectroscopy (XPS) spectra (Figure 2-4e) reveals the presence of N-coordinated Fe-N_x moieties (708.5 eV). Mo 3d XPS spectra (Figure 2-4f) similarly indicates the formation of N-coordinated Mo-N_x moieties (229 eV). N 1s XPS spectra (Figure 2-4g) shows the presence of several N-moieties, assigned to be pyridinic (398 eV), pyrrolic (401 eV), quaternary (401.5 eV) and graphitic (403 eV).[84,89] Furthermore, a strong peak for M-N_x (399 eV) moieties is also observed, indicating the formation of N-coordinated metal active sites. Complete XPS characterization of M-N-C electrocatalysts is given in Appendix A.23, Appendix A.24 and Appendix A.25, with C 1s, O 1s and N 1s and their atomic concentrations given in Table 5.

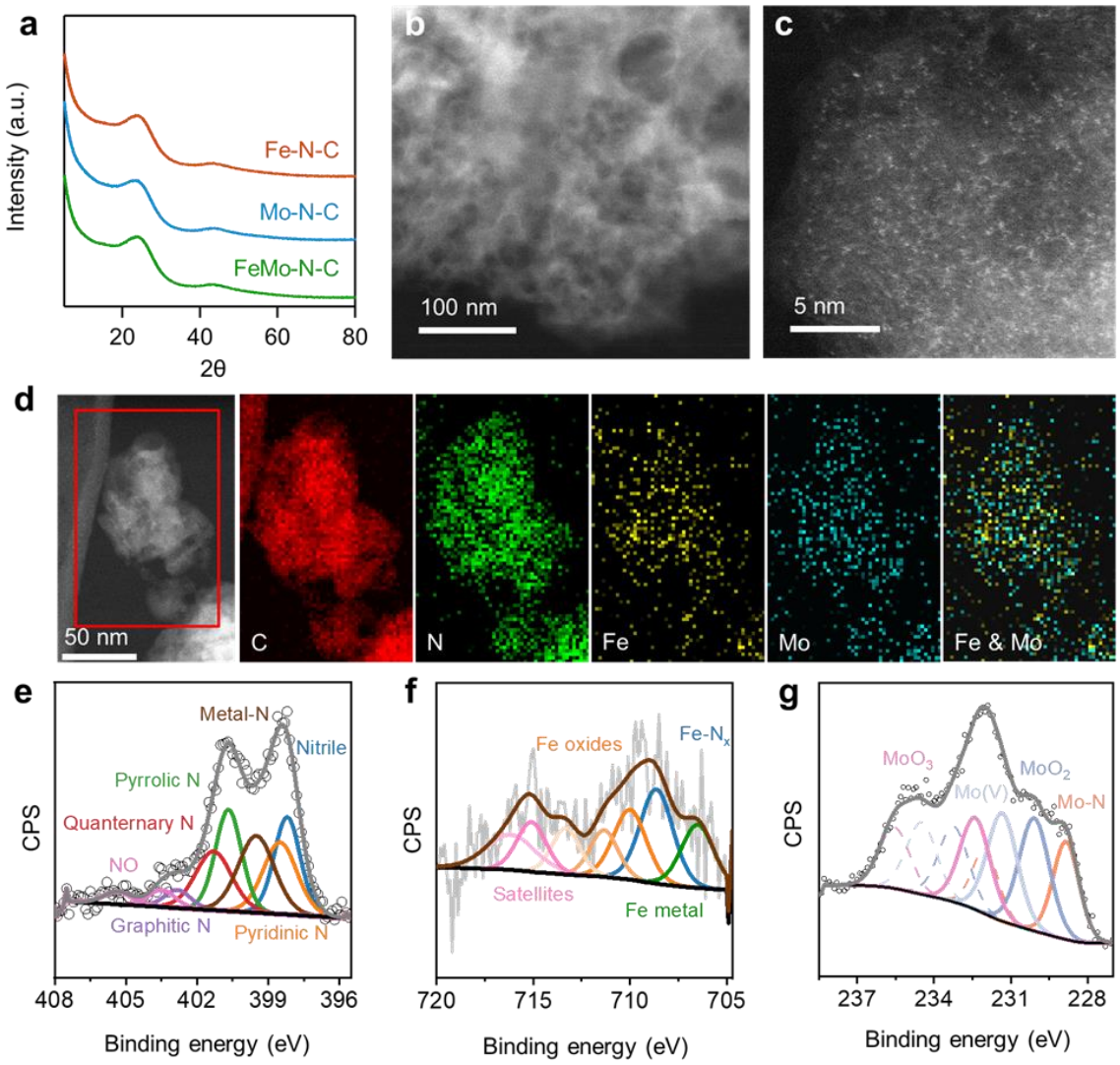

Figure 2-4. Physical characterization of the atomically dispersed catalysts. (a) XRD pattern of the mono- and bi-metallic Fe-N-C, Mo-N-C and FeMo-N-C catalysts. (b) Low magnification AC-HAADF STEM image of the FeMo-N-C catalyst. (c) Atomic resolution AC-HAADF STEM image, bright spots indicate atomically dispersed Fe and Mo sites. (d) AC-HAADF image and EDS mapping of the FeMo-N-C catalyst. XPS spectra of the FeMo-N-C catalyst (e) N 1s spectra confirming the formation of M-N_x moieties. (f) Fe 2p spectra indicating the presence of Fe-N_x sites. (g) Mo 3d spectra indicating the presence of Mo-N_x sites.

2.7 Associative and Dissociative Reaction Mechanisms

DFT was further used to study the mechanism of NO_3^- conversion to NO_2^- and $*NO_2$ on the M-N_4 centers of the Fe-N-C and Mo-N-C catalysts (Figure 2-5 a and b). Theoretically, the initial $2e^-$ transfer of the NO_3RR, reducing NO_3^- to $NO_2^-/*NO_2$, is complex and encompasses distinct dissociative- and associative-adsorption mechanisms. The subsequent $6e^-$ transfer process of $NO_2^-/*NO_2$ to NH_3 has been shown experimentally in this study, through NO_2RR experiments (Figure 2-2 a-c), to be kinetically fast and not involved in the rate determining steps. Other DFT-based computational work also support this finding, showing the facile reduction of $*NO_2$ to NH_3 on single atom catalysts.

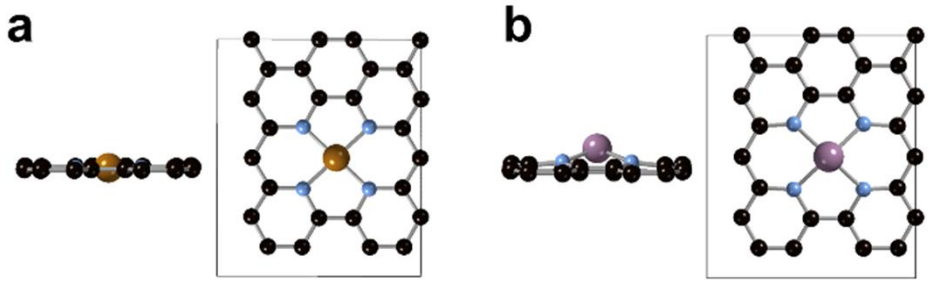

Figure 2-5. DFT optimized structures of the a) Fe-N_4 and b) Mo-N_4 centers (side and top view). Only atoms belonging to one unit cell are shown (C – black, N – blue, Fe – gold, Mo – purple).

In this work, both associative and dissociative adsorption of NO_3^- molecules were considered as the initial step of the NO_3RR (Figure 2-6 a and b, Appendix A.27). Specifically, we have found that the Fe-N_4 sites can stabilize adsorbed NO_3^- molecule regardless of molecular conformation, either through one or two O-atoms. A Gibbs free energy of -0.39 eV was achieved when two O-atoms were coordinated by the Fe site, making associative-adsorption a favorable pathway. The

following protonation step from $*NO_3$ to $*HNO_3$ is slightly endergonic, +0.37 eV, followed by an exergonic, -1.62 eV, step for $*NO_2$ intermediate formation. Further protonation of $*NO_2$ to $*HNO_2$ (+0.19 eV), was more favorable than the desorption of NO_2* into the bulk (+1.07 eV), facilitating direct $8e^-$ pathway for the NO_3RR to NH_3 process.

In contrast, the Mo-N_4 sites showed a very strong oxygen affinity, such that when the NO_3^- molecule was coordinated on the Mo site through a single O-atom, the N-O bond was chemically cleaved (-4.2 eV), leading to an oxygen atom adsorbed (*O) on Mo site and a desorbed NO_2^- ion, as shown in Figure 2-1b. Although the $*NO_3$ intermediate could be stabilized when two O-atoms were coordinated to the Mo site (-2.72 eV), the subsequent dissociative-adsorption pathway was thermodynamically more favorable by an energy downhill of -1.48 eV as depicted $*O+NO_2^-$ in Figure 2-6b. Furthermore, during the optimization of NO_3^- on the Mo site, the N-O bond spontaneously dissociated when coordinated with one O-atom, indicating a small or zero kinetic barrier for the dissociative-adsorption pathway. However, the regeneration of Mo site, through the reduction of the *O to H_2O was not realistic given the Gibbs free energy penalties of +1.39 eV and +2.24 eV in the sequential electron-transfer steps. Although the associative-adsorption pathway could be an option, it is expected to have low selectivity over the $*O+NO_2^-$ step and faces a large energy barrier of +1.35 eV for the protonation of the $*NO_2$ surface intermediate. Therefore, the bare Mo sites inevitably would end being populated by *O species, denoted as the *O-Mo site.

Interestingly, further investigation showed that due to the strong O affinity of the Mo active site, high coordination number and orientation of its *4d*-orbitals, the oxygenated *O-Mo site can simultaneously bind an additional NO_3^- molecule (Figure 2-6c) or NO_2^- molecule (Appendix A.26). For example, with the coordination of a secondary NO_3^- molecule, the strong *O-Mo interaction was split between the *O and $*NO_3$, substantially reducing the energy barrier to

+0.12 eV for the *O protonation (*O+*NO_3 to *OH+*NO_3 in Figure 2-6c) as compared to +1.39 eV on the monocoordinated *O-Mo site (*O+NO_2^- to *OH+NO_2^- in Figure 2-6b). Similarly, the energy barrier for the subsequent protonation of the *OH intermediate was also reduced from +2.24 eV to +0.81 eV (Figure 2-6 b-c) but remained large enough that it is unlikely to be made energetically downhill by applying an electrochemical potential. Then, the remaining *NO_3 was reoriented on the Mo site and subsequently dissociated, releasing a NO_2^- molecule and regenerating the *O-Mo site (grey pathway). It was highlighted that the more energetically favorable pathway (red pathway) occurs through the dissociation of the adsorbed *NO_3 on *O-Mo site, releasing a NO_2^- molecule into the bulk and thus leaving two O-atoms on the Mo site, as shown by the *OO+NO_2^- step in Figure 2-6c. Due to the binding energy being shared between the two O-atoms, the subsequent reduction of one *O intermediate to H_2O was more energetically facile, resulting in an energy barrier of only +0.22 eV. After the release of H_2O via two protonation steps, the *O-Mo site was regenerated and ready to coordinate and dissociate another NO_3^-, restarting the catalytic cycle for NO_2^- generation. This ostensible mechanism agrees well with the continuously increasing NO_2^- concentration observed throughout the entire 24-hour electrolysis in Figure 2-1e.

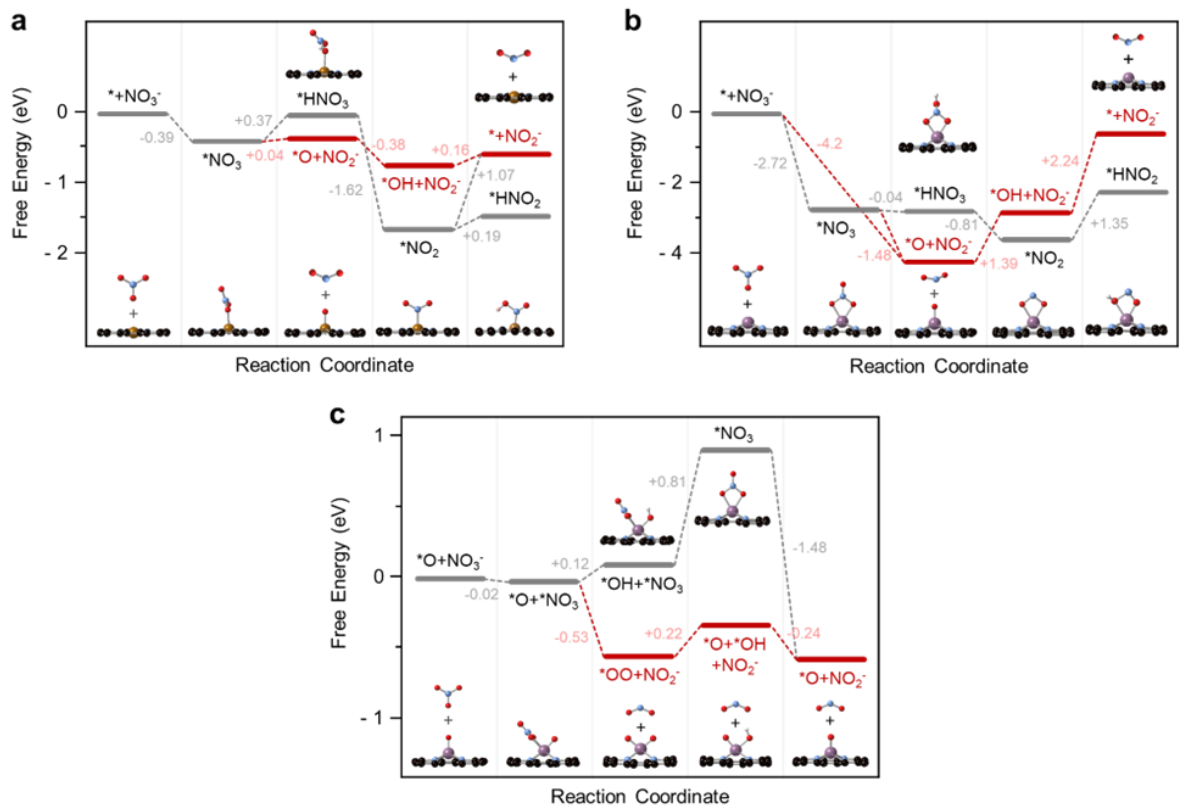

Figure 2-6. Gibbs free energy landscape and intermediate geometries for the conversion of NO_3^- to $*NO_2/NO_2^-$ on a) Fe-N_4 sites and b) Mo-N_4 sites. c) Gibbs free energy landscape and intermediate geometries for the cyclic conversion of NO_3^- to NO_2^- over oxygenated Mo-N_4 sites (*O-Mo). The associative adsorption pathways are marked in grey, while dissociative adsorption and dissociation steps are marked in red. A cathodic potential of 0 V and pH of 6.3 were used to estimate the Gibbs free energy levels. (H – white, C – black, N – blue, O – red, Fe – gold, Mo – purple).

In our calculations, the dissociative-adsorption pathway was also found to be thermodynamically plausible over Fe sites as shown by Figure 2-6a (red pathway). Furthermore, the active site regeneration from *O-Fe is only slightly endergonic at 0 V and can become exergonic at reductive

potentials. Fe sites are less oxophilic than Mo sites and are widely recognized as active non-platinum group metal (PGM) oxygen reduction catalysts[9,85,93]. However, during the experimental time-course study, it was observed that the associative-adsorption, $8e^-$ transfer pathway generating NH_3 was the dominant path, with only a negligible and constant NO_2^- concentration being observed. The dominance of the associative-adsorption pathway could be due to the smaller kinetic barrier for the protonation of $*NO_3$ ($*NO_3$ to $*HNO_3$). Additionally, it must be emphasized that the free energy diagrams were calculated at the experimental pH=6.3. As the dissociation step is not pH dependent, while the associative step is pH dependent, any local increase in H^+ concentration will make the associative step more favorable. Furthermore, the solvent effect by $(H_3O)(H_2O)_n^+$ species could also additionally downshift the energy level of $*HNO_3$.[6]

As mentioned before, the experimental results gave strong evidence of the excellent NO_2^- reduction capability of Fe-N-C catalyst, good NO_2^- generation capability of Mo-N-C catalysts and synergistic effect of bi-metallic FeMo-N-C catalysts (Figure 2-2d). It should be noted that when comparing the energy landscapes in Figure 2-6 a and c, the first 2-electron transfer step (NO_3^- to $*NO_2$) on Fe-N-C showed a maximum energy barrier of +0.37 eV, while the potential determining step on *O-Mo sites showed an energy barrier of +0.22 eV for the completed catalytic cycle of NO_2^- generation. Therefore, the Mo sites are more efficient in the first $2e^-$ transfer step in NO_3RR, producing NO_2^- molecules that can be reduced by Fe sites. This provides strong support for the bi-metallic FeMo-N-C's synergistic effect on the increased ammonia yield rate (Figure 2-2e).

2.8 Conclusions

In summary, taking inspiration from the cascade mechanism of biological nitrate/nitrite reductase enzymes, distinct NO_3RR mechanisms were identified for single atom Mo-N_4 and Fe-N_4 active sites, where Mo sites preferentially followed a dissociative-adsorption pathway, spontaneously breaking the N-O bond, releasing NO_2^- into the bulk and creating the *O-Mo active site for the continuous catalytic cycle of NO_2^- generation. Then, the NO_2^- molecules could be re-adsorbed and further reduced to NH_3, following a $2e^- + 6e^-$ process. Over Fe sites, an associated-adsorption and direct $8e^-$ transfer pathway was favorable in which NO_3^- adsorbs and was directly reduced to NH_3. Additionally, independent NO_2RR electrolysis revealed the ability of the Fe sites to reduce NO_2^- to NH_3 at 100% FE_{NH3} and high yields. DFT results further revealed that the Mo-N-C catalyst was more efficient in the first $2e^-$ transfer step than its Fe-N-C counterpart, which enables the synergistic effect of the bi-metallic FeMo-N-C catalysts in terms of both NH_3 selectivity and yield rate. Specifically, the cascade NO_3RR synergized the favorable dissociation of NO_3^- to NO_2^- over Mo sites with the fast kinetics of Fe sites in reducing NO_2^- to NH_3. As a result, selective NO_3RR to NH_3 at a high FE_{NH3} of 94% was achieved at -0.45 V, outperforming either of the Fe-N-C or Mo-N-C mono-metallic catalysts. Additionally, long-term durability tests over 60 hours demonstrated the robustness of the FeMo-N-C catalyst, maintaining a FE_{NH3} over 90%. This study presents a novel approach in which heterogeneous single atom sites, utilizing distinct reaction pathways can be synergized on a single electrocatalyst to achieve highly selective and efficient NO_3^- reduction to NH_3. This cascade design is partially unconstrained by the linear scaling relationships of the reaction intermediates and sheds light on the future development of sustainable ammonia synthesis.

Chapter 3

Elucidating electrochemical nitrate and nitrite reduction over atomically-dispersed transition metal sites

3.1 Overview

Recently, significant effort has been focused to decarbonize the production of chemicals and fuels.[94,95] Among these, the decarbonization of ammonia (NH_3) synthesis from the traditionally energy intensive and environmentally damaging Haber-Bosch (H-B) process remains a grand challenge.[1,96] The electrochemical synthesis of NH_3, can ideally utilize renewable energy, reactive N-species and protons from water to generate NH_3. The reduction of di-nitrogen (N_2) in aqueous protic electrolytes remains the most heavily researched green pathway for NH_3 synthesis.[31] However, due to the high bond dissociation energy of N_2 (945 kJ mol^{-1}), ultra-low solubility in aqueous electrolytes and competition from the hydrogen evolution reaction (HER), the current Faradaic efficiencies (FE) and NH_3 yield rates ($Yield_{NH3}$) remain prohibitively low.[39,96] Given the total lack of reproducibility and the difficulties of ubiquitous NH_3 contamination in electrochemical systems, direct N_2 reduction remains unproven in aqueous protic electrolytes.[21]

To circumvent the challenges of N_2 reduction, there is a renewed interest in closing the N-cycle by recycling the reactive, more oxidized N-species (nitrate-NO_3, nitrite-NO_2 and nitric oxide-NO) to NH_3.[29,97–99] The electrochemical NO_3^- reduction reaction (NO_3RR) is of particular interest due to its weaker N=O bond (204 kJ mol^{-1}), large solubility in aqueous electrolytes and widespread availability. NO_3^- is an environmental pollutant found in industrial waste streams and agricultural runoffs, due to the heavy overfertilization practices currently utilized.[29] While the

NO_3RR to NH_3 provides a pathway for efficient recycling of NH_3/NO_3^- (originating from the H-B process), additional efforts are focusing on low energy plasma techniques to produce NO_3^- from air, but such processes are to date, not energy efficient. [100–102]

The electrochemical NO_3RR to NH_3 is a complex $8e^-$ ($9H^+$) transfer process, involving several desorbable and non-desorbable surface intermediates, creating a challenge for tailoring the catalytic surface for favorable adsorption of specific intermediates due to scaling relations.[103–105] Previous attempts were made to tune the intermediate adsorption binding energies by modulating the electronic structure on extended metal surfaces through alloys such as CuNi, PdAu and PtRu.[106–108] These attempts achieved improved FE_{NH3} and $Yield_{NH3}$ compared to mono-metallic counterparts, however, these approaches are still constrained by scaling relations and combat this by utilizing strongly alkaline or acidic environments with large concentrations of NO_3^-.

In the biological NO_3RR, the reaction is partitioned as an enzymatic cascade, where the initial $2e^-$ reduction of NO_3^- to NO_2^- is catalyzed over a Mo-cofactor in nitrate-reductase and the further reduction of NO_2^- to NH_3/N_2 is catalyzed over an Fe- or Cu-cofactor in nitrite-reductase.[28,68,109] Inspired by the enzymatic pathway, recent work demonstrated that an atomically dispersed bi-metallic FeMo-N-C catalyst could successfully partition the NO_3RR into the NO_3^--to-NO_2^- and NO_2^--to-NH_3 constituents, outperforming its mono-metallic Mo-N-C or Fe-N-C counterparts. The atomically dispersed Mo-N_x sites facilitated dissociative adsorption of NO_3^-, releasing NO_2^-, which is subsequently re-adsorbed and reduced to NH_3 over Fe-N_x sites at 100% FE.[110] Additionally, other approaches to partition the NO_3RR are emerging in the field for example, employing heterogenous metal sites, where each metal is tailored to efficiently catalyze a segment of the reaction. A recent study demonstrated potential dependent phase transitions of a Cu-Co (3-5 nm) binary metal sulfide catalyst, in which the inner Cu/CuO_x phases efficiently

reduce NO_3^--to-NO_2^-, while the outer Co/CoO phases selectively reduce the NO_2^--to-NH_3. The latter results in a NO_3RR cascade to NH_3, reaching a high FE of 90.6%.[111] A recent complementary work examining a series extended of transition metal surfaces by Carvalho et al. described NO_3RR catalyst design parameters by linking the electronic structure to experimentally observed NO_3RR performance.[112] These design parameters are derived from microkinetic models that described the $2e^-$ transfer rate limiting step (NO_3^- to NO_2^-) and further the NO_3RR FE_{NH3}, identifying a competitive adsorption between H^+ and NO_3^-, that was described by the material-dependent property ($\Delta G_{H^*} - \Delta G_{NO_3^-*}$). The study found that increasing FE_{NH3} correlates with NO* binding and subsequent dissociation into N* and O* as the d-band energy approaches the Fermi energy, resulting in the Co-foil showing the highest ammonium selectivity.

Atomically dispersed metal-nitrogen-carbon (M-N-C) catalysts have been extensively studied in neighboring electrocatalytic reactions (carbon dioxide reduction-CO_2RR[70,113,114], oxygen reduction-ORR[115,116]), demonstrating excellent catalytic activities and unique reaction pathways. Recently, atomically dispersed Fe-N-C catalysts were shown to be very selective for the NO_3RR to NH_3,[63,64] owing to their maximized atomic utilization and favorable NO_3^- adsorption over H^+. Additionally, isolated active sites provide an unfavorable environment for coupling adsorbed N-molecules, enabling mono N-based products (e.g., NH_3) to be selectively produced.

The current understanding of atomically dispersed M-N-C catalysts for the complex NO_3RR is very limited, with only M = Fe, Mo, and Cu being explored at varying conditions. Herein, we identified key transition metals and rare earth elements, important for electrocatalytic reactions and synthesized a set of 13 atomically dispersed M-N-C catalysts (M = Cr, Mn, Fe, Co, Ni, Cu, Mo, Ru, Rh, Pd, W, La, and Ce). Electrochemical descriptors were derived experimentally

through the reaction onset potential (HER, NO_3RR and NO_2RR), the NO_3RR selectivity to both NO_2^- and NH_3 and the NO_2RR selectivity to NH_3. Isotopically doped $^{15}NO_2^-$ in the NO_3RR elucidated the complex production/consumption mechanism of the NO_2^- intermediate. Density functional theory (DFT) was employed to evaluate the Gibbs free energy for the NO_3RR and NO_2RR following either the dissociative adsorption or associative adsorption pathway. By relating the experimentally determined and computationally determined activity descriptors, strong correlations were observed for the NO_2RR (R=0.72) and the NO_3RR (R=0.73) selectivity to NH_3. This work bridges the gap between computation and experiment for the NO_3^- and NO_2^- reduction reactions over atomically dispersed M-N-C catalysts by providing a powerful set of activity descriptors that correlate strongly with the experimentally observed activity. These descriptors can be utilized to guide future atomically dispersed M-N_x catalyst development, for highly active and efficient NO_3^- reduction to NH_3.

3.2 Methods

3.2.1 Materials

Nicarbazin (Sigma-Aldrich), CAB-O-SIL® LM-150 fumed silica (Cabot), Aerosil® OX-50 (Evonik), iron(III) nitrate nonahydrate (Sigma-Aldrich), chromium(III) acetylacetonate (Sigma-Aldrich), manganese(II) nitrate tetrahydrate (Sigma-Aldrich), cobalt(II) nitrate hexahydrate (Sigma-Aldrich), nickel(II) nitrate hexahydrate (Sigma-Aldrich), copper(II) nitrate hemi pentahydrate (Sigma-Aldrich), ammonium molybdate tetrahydrate (Sigma-Aldrich), ruthenium(III) nitrosylnitrate (Alfa Aesar), rhodium(III) nitrate hydrate (Sigma-Aldrich), palladium(II) nitrate dihydrate (Sigma-Aldrich), lanthanum(III) nitrate hexahydrate (Alfa Aesar),

cerium(III) nitrate hexahydrate (Fisher Scientific) and ammonium paratungstate (Sigma-Aldrich), potassium nitrate (Sigma-Aldrich), potassium nitrite (Sigma-Aldrich), isotopic potassium nitrate (^{15}N, 99% - Cambridge Isotope Laboratories), isotopic sodium nitrite (^{15}N, 98%$^{+}$ - Cambridge Isotope Laboratories).

3.2.2 Synthesis of Atomically Dispersed M-N-C Catalysts

All catalysts were synthesized following the well-established sacrificial support method, with the metal precursor loading, pyrolysis temperature, pyrolysis atmosphere and etching environment being tuned to maintain atomically dispersed metal sites between the different metals (Table 6. Summary of optimized synthesis conditions to obtain atomically dispersed metal sites with a variety of M-N-C catalysts. See supplementary note 2 for a discussion on tuning the synthesis parameters to maintain an atomic dispersion of the metal species.).

Synthesis of Mn, Fe, Co, Ni, Cu, Mo and W-N-C catalysts. First a slurry of a carbon-nitrogen containing precursor, Nicarbazin (6.25 g), the silica sacrificial support, LM-150 (Cabot, 1.25 g), OX-50 (Evonik, 1.25 g) and Stöber spheres (made in house, 0.5 g) and the corresponding metal salt precursor (Mn = 0.266 g, Fe = 0.60 g, Co = 0.272 g, Ni = 0.271 g, Cu = 0.345 g, Mo = 0.262 g and W = 0.095 g), in 50 mL of MilliQ water was created. Next, the slurry was sonicated for 30 minutes before being dried overnight at 45 ˚C, under constant stirring. The mixture was then further dried in an oven at 45 ˚C for 24 hours. The resulting powder was then ball milled at 45 Hz for 1 hour. The catalyst powder is then pyrolyzed at 975 ˚C (with a ramp rate of 15 ˚C / min) under a reductive H_2 / Ar (7% / 93%) atmosphere for 45 min. The pyrolyzed powder is then ball milled a second time at 45 Hz for 1 hour. The silicate template is then etched in a hydrofluoric acid (15M) solution for 96 hours. The catalyst is then recovered by filtration and washed to neutral pH,

followed by drying at 60 ˚C overnight. The catalyst undergoes a second pyrolysis in a reductive NH_3 / N_2 (10% / 90%) atmosphere at 950 ˚C for 30 min (with a ramp rate of 20 ˚C / min). The catalyst is then ball milled a final time at 45 Hz for 1 hour.

Synthesis of Cr-N-C catalyst. The synthesis is identical to the previous procedure, with only the pyrolysis temperatures being reduced to 650 ˚C in both the first and second pyrolysis, to maintain an atomic dispersion of the Cr metal. The metal salt precursor loading of Cr = 0.519 g.

Synthesis of Ru-N-C catalyst. The synthesis is identical to the previous procedure, with the pyrolysis temperatures being reduced to 650 ˚C and an inert argon pyrolysis atmosphere, to maintain an atomic dispersion of the Ru metal. The metal salt precursor loading of Ru = 0.235 g

Synthesis of Rh and Pd-N-C catalysts. The synthesis is identical to the previous procedure, with the high pyrolysis temperatures of 975 ˚C and 950 ˚C for the first and second pyrolysis, respectively, however the pyrolysis is performed in an inert argon atmosphere, to maintain an atomic dispersion of the Rh and Pd metals. The metal salt precursor loading of Rh = 0.215 g and for Pd = 0.198 g.

Synthesis of the La and Ce-N-C catalysts. The synthesis is identical to the previous procedure, with the pyrolysis temperatures being reduced to 650 ˚C under an inert argon pyrolysis atmosphere. Furthermore, the etching of the silica template was performed in an alkaline 4M NaOH environment at 80 ˚C for 96 hours. If etched using a hydrofluoric acid environment, the La and Ce

readily form LaF_3 and CeF_3 nanoparticles. The metal salt precursor loading of La = 0.060 g and Ce = 0.061 g.

3.2.3 Electrochemical Measurements

Preparation of the working electrode

A catalyst ink was created by mixing 10 mg of catalyst in a solution of 680 µL IPA, 300 µL MilliQ water and 20 µL of a 5 wt% Nafion solution and sonicated for 1 hour. For linear sweep voltammetry (LSV) experiments, 12.35 µL of catalyst ink was drop casted on a glassy carbon electrode (0.247 cm^2) for a catalyst loading of 0.5 mg/cm^2. For chronoamperometry experiments an AvCarb MGL370 carbon paper was used as the working electrode. The carbon paper was pre-treated by plasma cleaning for 15 min to remove the PTFE layer and then subsequently washed in 3M H_2SO_4 and MilliQ water to create a hydrophilic surface. After the pretreatment, 12.5 µL of catalyst ink was drop casted on the carbon paper with a 0.25 cm^2 geometric working area for a catalyst loading of 0.5 mg/cm^2.

Linear sweep voltammetry

Note that the applied potential for all electrochemical tests is not iR corrected. From PEIS measurements, the solution and contact resistances are small at 13.5 Ω, aided by the high concentration of KNO_3, which dissociates into K^+ and NO_3^- ions, creating a strong electrolyte with a high conductivity. To evaluate the onset potentials for the HER, NO_2RR and NO_3RR, LSV was performed. All LSV measurements were obtained on a Biologic potentiostat, using a rotating disk electrode in a single compartment cell. A glassy carbon electrode (0.247 cm^2), graphite rod and reversible hydrogen electrode are used as the working, counter, and reference electrodes, respectively. To evaluate the HER onset potential, a 0.05M PBS electrolyte was used. For the

NO_2RR onset potential LSV was performed in a 0.05M PBS + 0.01M KNO_2 electrolyte. For the NO_3RR onset potential LSV was performed in a 0.05M PBS + 0.16M KNO_3 electrolyte. LSV curves were obtain by sweeping reductively from 1V to -1V *vs.* RHE at 5 mV/s at a rotation speed of 1600 rpm. The reaction onset potential was determined to be the potential at which a current density of 0.4 mA/cm^2 was reached.

Electrocatalytic nitrate reduction

Electrochemical nitrate reduction measurements were carried out in a customized two compartment H-cell, separated by a Celgard 3401 porous polypropylene membrane (used without pre-treatment). Electrochemical measurements were recorded using an AutoLab potentiostat. A standard three-electrode system was used with a reversible hydrogen electrode (HydroFlex®) and a graphite rod as the reference and counter electrode, respectively. The electrolyte used for all nitrate reduction experiments is a 0.05M phosphate buffer solution (PBS) (pH 6.3) and with 0.16M NO_3^- (KNO_3). Prior to electrochemical tests, N_2 gas (research grade 99.9995% - PraxAir) is purged in both the working and counter chambers for 30 min at 80 sccm, which contain 30 mL and 25 mL of electrolyte, respectively. To assess if saturating the electrolyte with N_2 or Ar has an impact on the equilibrium potentials of the NO_3RR processes, open circuit voltage measurements were performed under N_2 or Ar saturation and showed negligible differences as shown in Appendix B.1. Potentiostatic tests are performed for 2 hours under constant stirring at a constant N_2 gas flow rate of 20 sccm to the working chamber. Potentiostatic tests were performed at potentials of -0.20, -0.40, -0.60 and -0.80 V *vs.* RHE. After the electrolysis, the electrolyte in both the working and counter chambers was sampled and tested for NH_3 and NO_2^-. Note that at the pH = 6.3 conditions utilized in this work, the pKa of ammonia has not been reached (pKa 9.2), therefore the ammonia

produced is in the protonated from ammonium (NH_4^+). However, in the alkaline conditions present during the Berthelot method for detection, the NH_3/NH_4^+ is present in the NH_3 form. Therefore, the discussion in this manuscript is for the detected product ammonia (NH_3). Note our previous work has demonstrated that these atomically dispersed M-N-C catalysts have been shown to be inactive for the reduction of N_2 under these conditions.[110]

NO_3RR tests in alkaline media (pH = 14) were performed using a 1M KOH + 0.16M KNO_3 electrolyte. Due to the extremely high NH_3 yield rate, potentiostatic tests were performed for 15 min at potentials of -0.20, -0.40, -0.60 and -0.80 V *vs.* RHE.

Electrocatalytic nitrite reduction

Electrochemical nitrite reduction experiments were performed analogously to nitrate reduction experiments. The electrolyte is 0.05M PBS and 0.01M NO_2^- (KNO_2) (pH 6.3). Due to the higher NH_3 yield rates of the more active NO_2RR, potentiostatic tests were performed for 30 min. Potentiostatic tests were performed at potentials of -0.20, -0.40, -0.60 and -0.80 V *vs.* RHE. After each electrolysis, the electrolyte in the working chamber was sampled and tested for NH_3 detection.

Isotope-labeling experiments

Isotopic nitrate $^{15}NO_3^-$ labelling

Isotopic $^{15}NO_3^-$ labeling experiments were performed by using $K^{15}NO_3$ (99% - Cambridge Isotopes) as the isotopic nitrate source with a 0.05M PBS + 0.16M $K^{15}NO_3^-$ electrolyte (pH 6.3). Isotopic $^{15}NO_3^-$ experiments were performed using a metal free N-C catalyst. Using a metal free N-C catalyst simultaneously allows the source of the N in the produced NH_3 to be confirmed, while

also demonstrating that the even the metal free N-moieties in the N-C catalysts can catalyze the NO_3RR (and is not from N-originating from catalyst decomposition).Electrolysis was performed at -0.40 V for 4 hours, after which the electrolyte in the working chamber was samples and the produced $^{15}NH_3$ was quantified by ^1H NMR.

Isotopic nitrite $^{15}NO_2^-$ labelling

Isotopic $^{15}NO_2^-$ labeling experiments were performed by using $Na^{15}NO_3$ (98%$^+$ - Cambridge Isotopes) as the isotopic nitrite source. Isotopically labeled $^{15}NO_2^-$ at concentrations of 100, 10 and 1 ppm were doped into the 0.05M PBS + 0.16M KNO_3 (10,000 ppm NO_3^-) electrolyte. Potentiostatic tests were performed at -0.40 V *vs.* RHE for 6 hours, under constant stirring and a N_2 gas flow of 20 sccm to the working chamber. The electrolyte was sampled at 2-, 4- and 6-hour time intervals and the $^{15}NH_3$ was quantified by ^1H NMR.

Calculation of the yield and faradaic efficiency

Note that all error bars in this work are determined from triplicate experiments on independently prepared electrodes and are then calculated using a 90% confidence interval.

For the nitrate (NO_3^-) and nitrite (NO_2^-) reduction reactions, the NH_3 yield rate was calculated by Eq.1.

$$Yield_{NH_3} = \frac{c_{NH_3} * V}{Mw_{NH_3} * t * A_{electrode}} \quad (1)$$

For the nitrate (NO_3^-) and nitrite (NO_2^-) reduction reactions, the NH_3 Faradaic efficiency was calculated by Eq. 2.

$$FE_{NH_3} = \frac{n * F * c_{NH_3} * V}{Mw_{NH_3} * Q} \quad (2)$$

In the NO_3RR, the nitrate (NO_3^-) to nitrite (NO_2^-) reduction Faradaic efficiency was calculated by Eq. 3.

$$FE_{NO_2^-} = \frac{n * F * c_{NO_2^-} * V}{Mw_{NO_2^-} * Q} \quad (3)$$

Where c_{NH_3} is the concentration of $NH_{3(aq)}$ (μg / mL), V is the volume of the electrolyte (mL), Mw_{NH_3} is the molar mass of NH_3 (17.031 g / mol), t is the duration of the chronoamperometric measurement (hr), the surface area of the working electrode, $A_{electrode}$ is 0.45 cm^2. The number of electrons transferred, n, for NO_3^- to NO_2^- is n = 2 and for NO_3^- to NH_3 is n = 8. F is Faraday's constant (96,485 C / mol), the concentration of NO_2^- (μg/ mL), C_{NO2-}, where the molar mass of NO_2^-, Mw_{NO2-} is (46.005 g / mol) and the charge during the chronoamperometric measurement, Q.

Product detection

For typical, non-isotopically labeled NO_3RR and NO_2RR electrolysis, products were quantified using an ultraviolet-visible (UV-Vis) spectrophotometer (Shimadzu, UV-2600).

Determination of ammonia

Ammonia was quantified by UV-Vis using the Berthelot reaction. In cases producing large concentrations of NH_3, the working electrolyte solution was diluted such that the absorbance would fall within the range of the calibration curve. Specifically, 2 mL of the electrolyte (or diluted electrolyte if needed) was pipetted into a vial. To this, 2 mL of a 1 M NaOH solution that contains

5 wt% salicylic acid, and 5 wt% sodium citrate was added. Next, 1 mL of a 0.05 M NaClO and 0.2 mL of a 1 wt% $C_5FeN_6Na_2O$ (sodium nitroferricyanide) was added to the solution. The solution was incubated in the dark at ambient condition for 1 hour, then UV-Vis spectra were recorded. The concentration of NH_3 is determined using the maximum absorbance at a 655 nm wavelength, when compared to the generated calibration curves, Appendix B.2 and Appendix B.3.

Determination of nitrite:

Nitrite was quantified by UV-Vis using a commercial NO_2^- assay kit (Spectroquant), based on the Griess test. In cases producing large concentrations of NO_2^-, the working electrolyte solution was diluted such that the absorbance would fall within the range of the calibration curve. Specifically, 2 mL of the electrolyte (or diluted electrolyte if needed) was placed in a vial. To this, 22 mg of the assay reagent was added to the electrolyte and incubated in the dark at ambient conditions for 10 min. After incubation, the UV-Vis spectra were taken, and the concentration of nitrite was determined at a maximum absorbance of 540 nm wavelength, when compared to the generated calibration curves, Appendix B.4.

NMR determination of ammonia

For isotopic labelling experiments, nuclear magnetic resonance (NMR) spectroscopy was used to detect and quantify both $^{14}NH_3$ and $^{15}NH_3$. Dimethylsulfoxide-d6 (DMSO) and 3-(trimethylsilyl)-1-propanesulfonic acid sodium salt (DSS) were used as the locking solvent and internal standard, respectively. For the NMR test solution, 580 μL of the electrolysis electrolyte, 25 μL of DMSO, 20 μL of 3 M H_2SO_4, and 75 μL of 6 mM DSS (made with Millipore water) are mixed. The NMR spectrum was obtained on a Bruker CRYO 500 MHz spectrometer. The signal from H_2O was

restrained for better accuracy by applying the solvent suppression method during acquisition. Topspin 4.0.8 software was used to process the NMR data. Standard NMR calibration curves for standard $^{14}NH_3$ and isotopically labeled $^{15}NH_3$ are shown in Appendix B.5.

Computational Details

All the density functional theory (DFT) calculations were performed with the generalized gradient approximation approach and projector augmented-wave pseudopotentials[73,74] using the Vienna Ab initio Simulation Package[75–77]. To account for the van der Waals interactions, an optB86b-vdW functional was used[78–81] with a gamma centered 8x8x1 (M-N_4 sites, pyridinic N, graphitic N) or 3x3x1 *k*-mesh (pyrrolic NH) and Fermi-smearing. Sigma and the plane-wave basis cutoff was set to 0.03 and 400 eV, respectively. M-N_4, pyridinic N, and graphitic N sites were modeled using 4x4 orthorhombic single-layer graphene cell with the dimensions of 9.84 x 8.52 Å. Pyrrolic NH defect was modeled using a hexagonal single layer 17.04 x 17.04 Å unit cell. Structures of all the unit cells used for the DFT calculations are shown on Figure S68. A vacuum region of 20 Å was applied in all cases. All structures were optimized by allowing all atoms to relax (including adsorbents) while the cell parameters were kept fixed at the DFT optimized value for graphene. The criteria for the convergence of the electronic energy were set to 1×10^{-5} eV. The forces were converged to 0.01 eV/Å. All calculations were performed as spin polarized calculations. The computational approach for the calculation of Gibbs free energy of reactions and considered steps in the NO_3RR and NO_2RR mechanism are explained in details recent work.[110] However, it must be emphasized that all the Gibbs free energies were calculated at experimental pH of 6.3.

3.2.4 X-ray Photoelectron Spectroscopy Characterization

The metal valence state and quantification of nitrogen-moieties of the M-N-C catalysts were analyzed by X-ray photo electron spectroscopy (XPS). The XPS was performed on a Kratos AXIS Supra spectrometer with a monochromatic Al Kα source (with an emission current of 15 mA and X-ray power of 225 W, while for the high-resolution spectra the emission current and power are 20 mA and 300 W, respectively). No charge neutralization was employed as all these samples are highly conductive, carbon-based catalysts. Survey spectra were obtained at a pass energy of 160 eV from 1400 eV to 5 eV at a step size of 1 eV. The High-resolution C 1s, N 1s and O 1s spectra were obtained at a pass energy of 20 eV with a 0.1 eV step size. The metal spectra were obtained at a pass energy of 40 eV with a 0.1 eV step size. A C 1s spectra was also obtained at a pass energy of 40 eV for calibration. CasaXPS software was used to analyze and fit all spectra and all spectra were calibrated based on the sp^2 carbon (284 eV). A Linear background was employed for the C *1s* and N *1s* spectra, while a Shirley background was used for the O *1s* and metal spectra. The sp^2 carbon in the C *1s* spectra was fit with a 80% Gaussian / 20% Lorentzian function and all other spectra were fit using a 70% Gaussian / 30% Lorentzian function. All fitting parameters employed in this work are based on previous fittings from our group that are reported in the literature references here for this class of M-N-C catalysts.[83,84,117,118]

3.2.5 Electron Microscopy Characterization

The physical structure and atomically dispersed nature of the catalysts were analyzed by aberration-corrected scanning transmission electron microscopy (AC-STEM) and energy dispersive X-ray spectroscopy (EDS) using a JEOL ARM300CF at an accelerating voltage of 300 kV. The coordination environment and valence state of the atomically dispersed sites were examined through atomic resolution electron energy loss spectroscopy (EELS) on a Nion

UltraSTEM200 microscope equipped with a cold FEG, a C3/C5 aberration correction and a high-energy resolution monochromated EELS system (HERMES). To mitigate the beam damage on the coordination between single metal atoms and nitrogen-carbon support, the EELS was collected at a low voltage of 60 kV. During acquisition, the energy dispersion was set as 0.16~0.3 eV/channel with an exposure time of 2~4 s/nm^2. The background in each spectrum was removed by a power-law function and the de-noising of the spectra was performed by the multivariate weighted principal component analysis (PCA) routine in the Digital Micrograph software.

The hierarchical pore structure of the catalyst was examined by scanning electron microscopy (SEM) on an FEI Magellan 400 XHR SEM.

3.2.6 X-ray Absorbance Spectroscopy (XAS)

The electronic structure and local bonding environment of the metal sites were analyzed by ex-situ X-ray Absorption Spectroscopy (XAS) collected on several beamlines. Rh K-edge was measured on the SAMBA beamline at SOLEIL synchrotron radiation facility, Paris, France. The sample was measured in fluorescence mode and references in transmission mode using a Si (220) monochromator for the energy selection. Ionization chambers to measure the X-ray intensity before and after the sample were filled with a mixture of Ar/N_2 (I_0) or pure Ar (I_1 / I_2)

The La L_3-edge was measured on the XAFS beamline at ELETTRA synchrotron radiation facility, Triest, Italy. The sample was measured in transmission mode using a Si (111) 20% detuned monochromator for the energy selection. Simultaneously, a vanadium reference foil was measured for the energy calibration. Ionization chambers to measure the X-ray intensity before and after the sample were filled with a mixture of N_2/He (I_0, I_1, I_2).

The Fe K-edge was measured on the lab-based easyXAFS300 at the Fritz Haber Institute, Berlin, Germany (measured in transmission mode). Using a Ge (620) crystal for the energy selection and a Si drift detector (AXAS-M assembly from KETEK GmbH). A W-ProtoXRD X-ray tube was used.

The Ce L_3-edge, Cr, Mn, Co, Ni and Cu K-edge were measured on the KMC-3 beamline at the Bessy synchrotron radiation facility, Berlin, Germany. Cr-N-C in transmission mode, Cu-, Co-, Ni-, Mn- and Ce-N-C in fluorescence mode using a Si (111) monochromator for the energy selection. The ionization chamber for the measurement of the X-ray intensity before the sample was filled with 100 mbar air (I_0). Either a 13 element Si drift detector was used (fluorescence) or PIPS detector (transmission). Note that the energy resolution of the XAS spectra measured at the KMC-3 beamline is compromised due to technical issues involving the optics/mirrors at the KMC-3 beamline. However, the samples and corresponding reference foils and compounds were measured for energy calibration and comparison of features. Note Mo-N-C and Pd-N-C were measured on the 10-BM beamline of the Advanced Photon Source at Argonne National Laboratory. The ATHENA software was used for data alignment and XAS spectra extraction.[119] A set of in-house built Wolfram Mathematica scripts were used for the XANES analysis. Fitting of the EXAFS spectra was done using FEFFIT scripts.[119] The photoelectron amplitudes and phases were calculated by the FEFF8 code.[120] The EXAFS R-space fitting parameters and results are given in Table 7. If the M-N-C sample and corresponding reference material were not measured at the same beamline (Cr-, La- and Ce-N-C) the S_0^2 factor multiplied by the coordination number is reported.

3.2.7 Other Physical Characterization

X-ray diffraction (XRD) patterns were collected on a Rigaku Ultima-III powder X-ray diffractometer. Inductively coupled plasma mass spectrometry (ICP-MS) on an Aligent 5110 was performed to accurately quantify the low metal content of the M-N-C catalysts. N_2 physisorption was recorded on a Micromeritics 3Flex Analyzer at 77 K, using a low-pressure dosing mode (5 cm^3/g). The surface area and pore size distribution were obtained using the Brunauer-Emmett-Teller (BET) method and the non-local density functional theory model (NLDFT), respectively. Raman spectra were obtained with a 633 nm laser and 600 g.mm grating, using a Horiba LabRAM-HR.

3.3 Structural environment of single-atom metal centers

Atomically dispersed M-N-C catalysts were synthesized through the well-established sacrificial support method (SSM) originally developed by our group.[90,121,122] The SSM has been extensively applied for atomically dispersed Fe-N-C catalysts for the ORR and CO_2RR.[9,70] Here, extending beyond Fe-N-C to a variety of 3*d*-, 4*d*-, 5*d*- and *f*-block metals, a set of atomically dispersed M-N-C catalysts (M = Cr, Mn, Fe, Co, Ni, Cu, Mo, Ru, Rh, Pd, La, Ce, and W) were synthesized, as shown in Figure 3-1a. The metallic centers ideally have a first coordination shell of 4-nitrogen atoms and are coordinated in either an in-plane or out-of-plane configuration as shown in Figure 3-1b. With the synthesis conditions being adjusted to maintain the atomically dispersed nature for each metal element (Table 6), the resulting catalysts showed consistent porosity and pore size distribution (Appendix B.6), degree of graphitization (Appendix B.7) and a well-maintained metal loading at 0.5 – 1.5 wt% (Appendix B.8).

X-ray diffraction (XRD) shows only the characteristic (002) and (100) peaks for carbon, confirming the absence of bulk-like ordered metallic phases (Appendix B.9). Figure 3-1c-e shows representative aberration corrected high-angle annular dark-field scanning transmission electron

microscopy (AC-HAADF-STEM) images for the Fe, Rh, and La-N-C, where atomically dispersed metal sites are clearly observed through the high contrast points. Energy dispersive X-ray spectroscopy (EDS) maps confirm the homogenous distribution of carbon, nitrogen, and the relevant metal throughout the catalyst, Figure 3-1c-e (see other M-N-Cs in Appendix B.10, Appendix B.11, Appendix B.12 and Appendix B.13). Throughout the main text physical characterization of the Fe-, Rh- and La-N-C are shown as a 3*d*, 4*d* and *f*-metal representative for the set of M-N-C catalysts. Complete characterization for the remaining M-N-Cs is found in Appendix B as noted.

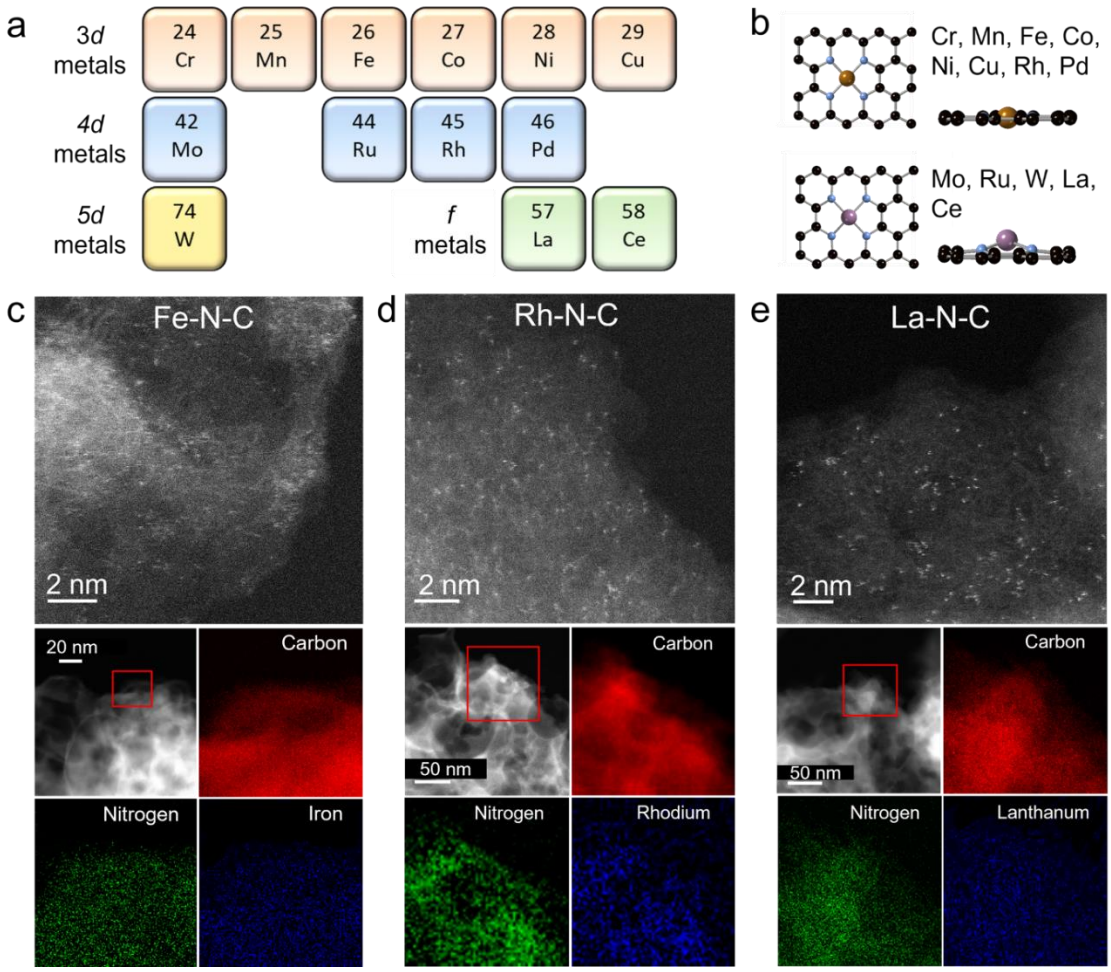

Figure 3-1. Physical structure of the atomically dispersed transition-metal catalysts. (a) Selection of 3*d*, 4*d*, 5*d* and *f* metals synthesized via the sacrificial support method. (b) Schematic of the nitrogen coordinated metal active site ($M\text{-}N_4$) on a prototype carbon matrix, illustrating in-plane and out-of-plane configurations. (c - e) Representative atomic resolution HAADF STEM images for the Fe-N-C, Rh-N-C and La-N-C catalysts. High contrast points indicate atomically dispersed metal sites. Corresponding EDS mapping of the M-N-C is given below.

The electron energy loss spectroscopy (EELS) in Figure 3-2 a-c shows the EELS spectra of small sample regions containing single atoms of Fe, Rh, and La, respectively. The EELS point spectra

show the co-existence of the N K-edge and the corresponding metal-edge (Fe-$L_{3,2}$, Rh-M_3, La-$M_{5,4}$), supporting the bond formation between the singe metal atom and supporting nitrogen atoms (M-N_x). X-ray absorption spectroscopy (XAS) was used to further investigate the chemical state and coordination environment of the catalysts, including X-ray absorption near-edge structure (XANES) and extended X-ray absorption fine structure (EXAFS). The XANES edge position and features (e.g., the intensity of the while line) of the Fe K-edge (7,112 eV), Rh K-edge (23,219.9 eV) and La L_3-edge (5,890.6 eV) as compared to their corresponding reference foil and oxide compounds indicate oxidation states of *ca.* Fe^{2+}, Rh^{3+} and La^{3+}, in agreement with the Fe 2*p*, Rh 3*d* and La 3*d* X-ray photoelectron spectroscopy (XPS) analysis (Appendix B.14). Interestingly, for Cr-N-C, evaluated to be one of the most selective M-N_x sites for the conversion of NO_3^- to NH_3 (Figure 3-2d), the XANES analysis reveals a relatively high Cr oxidation sate, comprising a mixture Cr^{6+} (20-30%) and Cr^{3+} (70-80%). Analogously for other M-N-C catalysts, the chemical state of the metal center is assessed by their respective XANES and XPS spectra (Appendix B.15 - Appendix B.21). Furthermore, the EELS valence state analysis for Fe-N-C and La-N-C, evaluating the intensity ratio and separation distance between the Fe L_3/L_2 and La M_5/M_4 edges further supports the oxidation state of Fe (between Fe^{2+} and Fe^{3+}) and La (La^{3+}) (Appendix B.22). However, the Rh K-edge EELS signal is too weak to perform quantitative analysis. EXAFS provides structural information of the metal centers inner coordination spheres, confirming the presence of shorter bonds (M-C / M-N / M-O) rather than longer metallic M-M bonds. From comparison with complementary techniques (EELS and XPS) the formation of M-N bonds is supported. Fourier transformed (FT) EXAFS spectra for the Fe K-edge, Rh K-edge and La L_3-edge, respectively are shown in Figure 3-2 d-f. In the Fe-N-C and Rh-N-C spectra, a single sharp peak was observed at a bond distance of ca. 1.5 Å (phase uncorrected) for both, characteristic of

the Fe-N and Rh-N coordination in the first shell. While for La-N-C, an *f*-metal with a complex coordination environment (shown to sit out of plane during the modelling of the active site, Figure 3-1b) a peak was observed at higher distances between 1-2.5 Å (phase uncorrected). A similar peak can also be observed in the FT-EXAFS of amorphous La_2O_3. Therefore, we assume that in our La-N-C sample a strongly disordered local environment around the single atom site, including the possible formation of small metal oxide-clusters. For the Ce-N-C catalyst, a more complex peak split feature was observed indicating the complex nature of *f*-metal M-N-C catalysts (Appendix B.23). To deconvolute minor contributions to the EXAFS spectra at larger bond distances, wavelet transforms of the EXAFS oscillations, providing high resolution information in both k-space and R-space are shown in Figure 3-2 g-I. For Fe-N-C and Rh-N-C, in addition to the high intensity Fe-N, Rh-N and La-N peak, a low intensity peak is observed at ca. 3.5 Å, 3.2 Å and 3.7 Å (at low k-space values), respectively which we attribute to Fe-C, Rh-C and La-C interactions in the second coordination shell. The lack of peaks in wavelet-transformed EXAFS spectra at higher values of wavenumber k indicates the absence of metal-metal bonds in the M-N-C catalysts, and, hence, absence of metallic or large oxide clusters. FT-EXAFS and WT-EXAFS for the M-N-C and corresponding metal oxide standards are given for Fe-, Rh- and La-N-C in Appendix B.24, while complete XANES, EXAFS and FT-EXAFS spectra are provided for all M-N-C's in Appendix B.15, Appendix B.16 and Appendix B.17, with fitting parameters provided in Table 7 and fitting results plotted in R-space found in Appendix B.25, respectively.

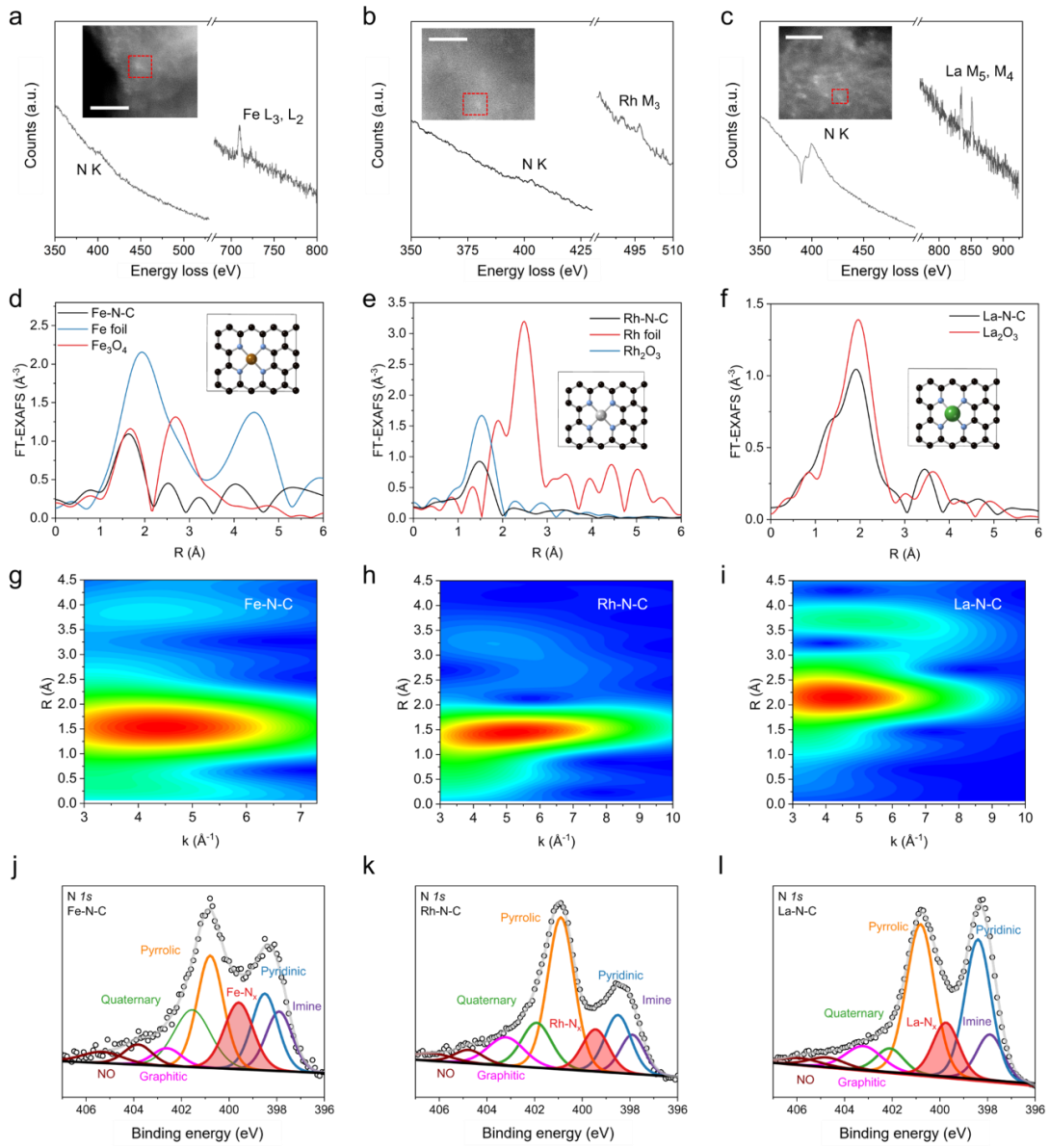

Figure 3-2. Coordination environment of the single-atom metal centers. (a - c) Atomic resolution EELS point spectra of the N K-edge and corresponding metal-edge of Fe ($L_{3,2}$), Rh (M_3) and La ($M_{5,4}$), in the M-N-C catalysts, indicating nitrogen coordination of the single atom M-N_x site. All scale bars are 2 nm. (d - f) FT EXAFS spectra of the Fe, Rh and La-N-C catalysts, with the corresponding metallic foil and metal oxide standards, demonstrating the presence of M-N_x sites. (g - i) WT-EXAFS of the Fe K-edge of Fe-N-C, Rh K-edge of Rh-N-C and La L_3-edge of La-N-

C. (j - l) N *1s* XPS spectra for the Fe, Rh and La-N-C catalysts, confirming the presence of M-N_x moieties.

XPS was used to further examine the metal-nitrogen coordination and other nitrogen moieties present. The representative N 1s spectra for the Fe-, Rh-, and La-N-C catalysts in Figure 3-2 j-l, reveals the presence of metal-nitrogen moieties (M-N_x). N 1s XPS spectra for the remaining M-N-C catalysts is shown in Appendix B.26 - Appendix B.29, all of which demonstrate the formation of M-N_x moieties. The deconvoluted high resolution N 1s XPS spectra showed a variation in the N-content and N-moiety percentage (e.g., pyridinic, pyrrolic, graphitic metal-N_x), as shown in Table 8. Summary of total nitrogen and oxygen content for all metal free N-C catalysts.

In summary, 13 atomically dispersed M-N-C catalysts have been synthesized using the SSM. By combining AC-STEM, EELS, XAS and XPS, the atomically dispersed nature of each metal site has been comprehensively visualized and confirmed to be in a M-N_x coordination. Critically, the well-deciphered coordination environment of the metal center allows us to elucidate the intrinsic activity of the different M-N_x moieties towards the electrocatalytic transformation of reactive N-species.

3.4 Electrochemical performance

The NO_3RR is somewhat universal in that even metal-free nitrogen-doped-carbon (N-C) showed limited but observable activity towards the generation of NH_3 and NO_2^- under an isotopically labeled $^{15}NO_3^-$ feed in neutral electrolyte (pH=6.3) at -0.4 (V *vs.* RHE) (Appendix B.30).

Comparatively, with the addition of nitrogen-coordinated metal sites Cr-N-C as an example, the FE_{NH3} increased from *ca.* 10% (metal free N-C) to 91.2%. While the introduction of Fe-N_x sites boosted the FE_{NH3} to 99 % (again at -0.4 V *vs.* RHE) and the corresponding $Yield_{NH3}$ increased from 1.3 to 10.0 μmol h^{-1} cm^{-2}.

It should be noted that, for the NO_3RR activity, as compared to measurements performed in neutral media, the current density and NH_3 yield rate could be significantly enhanced under alkaline conditions, while maintaining a high FE_{NH3}. Given Fe-N-C as an example, Appendix B.31 shows that when using a 1M KOH electrolyte (pH=14), the NH_3 partial current density increased from 2 mA cm^{-2} (11.4 μmol h^{-1} cm^{-2}) to 35 mA cm^{-2} (156.5 μmol h^{-1} cm^{-2}) at -0.4 V and further to 175 mA cm^{-2} (750.4 μmol h^{-1} cm^{-2}) at -0.6 V, both with a FE_{NH3} above 95%. Other work on alkaline NO_3RR also found similar trends.[64,106,123] However, as a fundamental study, this work focused on neutral pH (pH 6.3) to evaluate the intrinsic activity of the M-N_x sites toward the electrocatalytic NO_3RR and NO_2RR.

Regardless of the NO_3RR pathways[65,124,125], the surface intermediates *NO_2 and *NOOH are inevitable before the reaction pathway diverges to its several possible products. The NO_2^- molecule is also the first desorbable reaction intermediate, playing a key role in the NO_3RR via a cascade pathway.[46,110] For the set of M-N-C catalysts in this work, the NO_2RR displayed an earlier activation than the NO_3RR by linear sweep voltammetry (LSV), as shown in Figure 3-3a, indicating that the $6e^-$ transfer from NO_2^-/*NOOH to NH_3, in the NO_3RR was more facile than the initial $2e^-$ transfer from *NO_3^- to *NO_2^-/*NOOH, which is the rate limiting step and thus the focus of the computational work in the following discussion. Representative LSV for the metal free N-C and a variety of 3*d* and 4*d* metals demonstrates the range of NO_3RR (Figure 3-3b), and NO_2RR (Figure 3-3c) activities, with Cu-N_x being the most active NO_3RR site and Fe-N_x being

the most active NO_2RR site. As a unique nitrate-to-nitrite electrocatalyst[110], Mo-N-C was even more inert than the metal free N-C. A full analysis of the reaction onset potentials (Appendix B.32) clearly visualizes the range of onset potentials for the diverse M-N_x sites.

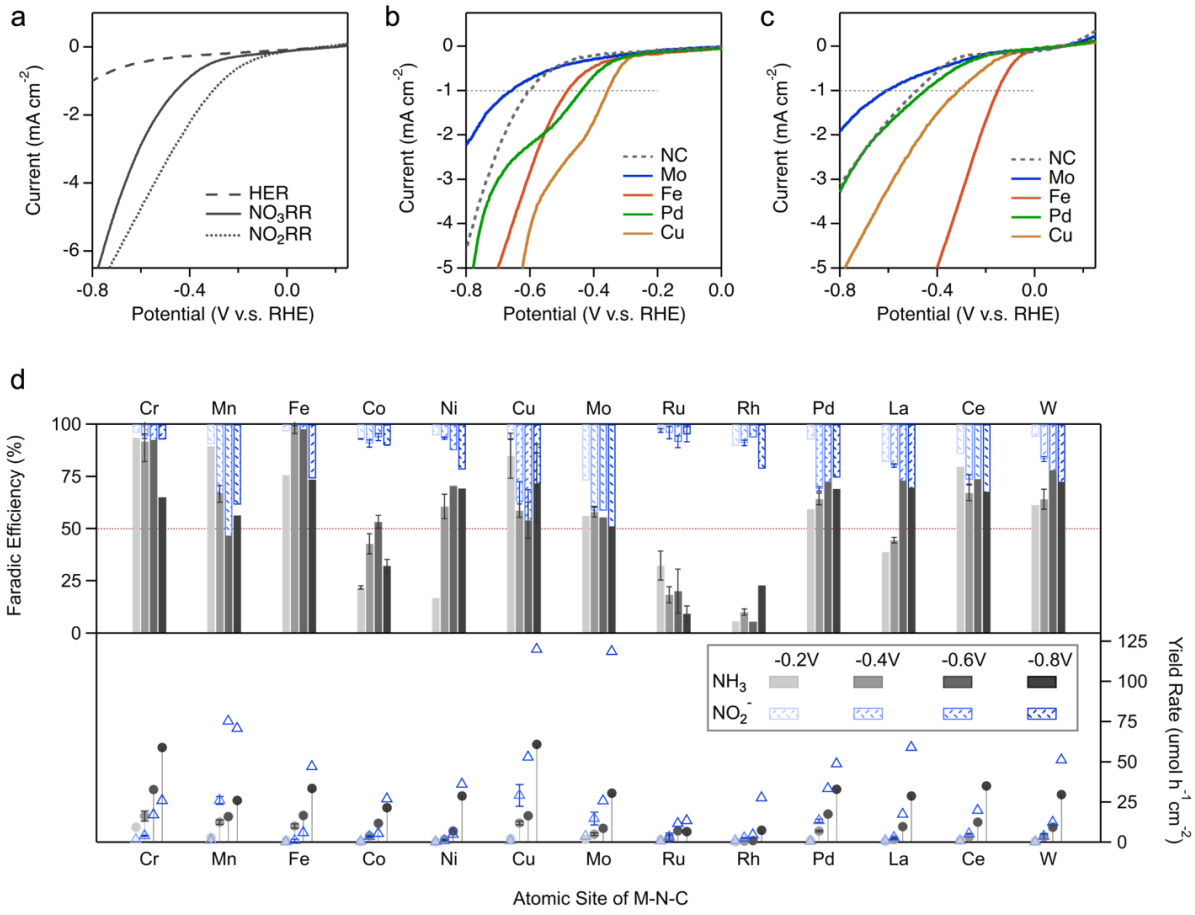

Figure 3-3. Electrochemical activation, selectivity, and activity for the NO_3RR and NO_2RR. (a) Example of a linear sweep voltammetry (LSV) curve for the Cr-N-C catalyst in electrolytes of 0.05M PBS (HER), 0.05M PBS + 0.01M KNO_2 (NO_2RR) and 0.05M PBS + 0.16M KNO_3 (NO_3RR). (b) Representative LSV over the metal free N-C and a variety of 3*d* and 4*d* metals for the NO_3RR and (c) NO_2RR. Complete LSV for all examined M-N-C and metal free catalysts are given in Appendix B.33. (d) *Gap analysis plot (GAP)* for the electrochemical NO_3RR for all M-N-C catalysts in 0.05M PBS + 0.16M KNO_3 for 2 hours. The top section of the figure shows the

Faradaic efficiency for NO_2^- (blue; top-down) and NH_3 (gray; bottom-up) as a function of the applied potentials between -0.2 V and -0.8 V *vs.* RHE. A horizontal line is set at 50% FE to guide the eye. The bottom section of the figure shows the corresponding yield rate (μmol h^{-1} cm^{-2}) for NO_2^- (blue; triangle) and NH_3 (gray; circle) as a function of the applied potentials. The corresponding NO_3RR chronoamperometry plots and UV-Vis detection for NO_2^- and NH_3 concentrations are shown in Appendix B.34 - Appendix B.43. Error bars are determined from replicate trials at -0.40 V *vs.* RHE. The GAP for the metal free N-C catalysts is shown in Appendix B.44.

To investigate the NO_3RR activity and selectivity towards NH_3 and NO_2^-, a series of 2-hour potential holds were performed at potentials between -0.2 V and -0.8 V. A gap analysis plot (GAP) was constructed in Figure 3-3d to visualize the nitrogen conversion landscape. Collectively, as the cathodic potential decreased, the yield rate of NH_3 and NO_2^- increased for all catalysts, but the selectivity varied. Specifically, both Fe-N-C and Cr-N-C showed the highest NH_3 selectivity (FE_{NH3} 92% - 100%) at -0.4 V and -0.6 V. In contrast, Mo-N-C showed comparable, consistent, and somewhat potential-independent selectivity for NO_2^- (40% - 50% FE_{NO2-}) and NH_3 (50% - 55% FE_{NH3}), as expected given that Mo-N_x sites were shown in our previous work, as an active nitrate-to-nitrite converter via dissociative adsorption (chemical process).[110] Similarly, the Mn-, Pd-, W-, La-, and Ce-N-C showed moderate NO_2^- and NH_3 selectivity at high overpotentials (~70% FE_{NH3} *vs.* ~30% FE_{NO2-}) and the FE for nitrogen conversion (FE_{NH3} + FE_{NO2-}) was maintained at 100%. Other early transition metals (Co-, Ni- and Cu-N-C) showed irregular potential dependence on selectivity, wherein Co-N-C showed a volcano trend for FE_{NH3} but consistent FE_{NO2-} and the nitrogen conversion was far below 100%

FE through the entire potential range. For an easier comparison, the NO_3RR electrolysis results ($FE_{NH3/NO2-}$ and $Yield_{NH3/NO2-}$) have been separated based on the applied potential in Appendix B.45, where its clearly observed that Cr-N-C was leading the other catalysts between -0.2 V and -0.6 V, being exceptional at -0.2 V (9.33 μmol h^{-1} cm^{-2} and 94% FE_{NH3}). However, Ni-N-C and Cu-N-C showed a strong potential dependence on the $Yield_{NH3}$, where Cu-N-C outperformed Cr-N-C at -0.8 V (61 *vs.* 59 μmol h^{-1} cm^{-2}). Particularly, Cu-N-C maintained 100% FE for NH_3 + NO_2^- (FE_{NH3} = 72%) at -0.8 V, indicating that no current is wasted on the parasitic HER. Two distinct exceptions were Ru-N-C and Rh-N-C, albeit their early activation indicated by LSV (Appendix B.32), both of which showed inferior NH_3 and NO_2^- activity (Figure 3-3d), displaying unique and significant gaps between the NH_3 and NO_2^- FE bars. This gap in FE is likely due to insoluble, undetected gas phase products (Appendix B.46), likely from the HER, as the isolated active sites present in atomically dispersed catalysts are unfavorable for the coupling of N-N bonds for N_2.

For the role of potential nitrite (as by-product or intermediate), previous reports usually considered the NO_3RR as a direct $8e^-$ transfer pathway with certain irreversible NO_2^- desorption or leaching.[63,64,87] Here, doping of isotopic $^{15}NO_2^-$ in the NO_3RR, schematically shown in Figure 3-4a, revealed that trace amounts (e.g., 1 ppm) of $^{15}NO_2^-$ could be easily reduced to $^{15}NH_3$ even under a concentrated $^{14}NO_3^-$ environment (10,000 ppm), which applied to both M-N_x sites and metal-free N-C sites (Appendix B.47 and Appendix B.48). Figure 3-4b, shows the NMR spectra for a time course electrolysis over Fe-N-C, wherein even at a concentration ratio of 1,000:1 ($^{14}NO_3^-$: $^{15}NO_2^-$), the $^{15}NO_2^-$ competed for an active site, yielding comparable $^{15}NH_3$. NMR spectra for the other M-N-C catalysts is shown in Appendix B.49, where a similar trend is observed for most metals with the no exception of Co- and Ni-N-C, where significantly more

isotopic $^{15}NH_3$ is generated than standard $^{14}NH_3$, in support of Figure 3-3d, suggesting their poor activity towards NO_3^- but high activity towards NO_2^-, which will be addressed in the following section. As the concentration ratio is reduced to 100:1 ($^{14}NO_3^-$: $^{15}NO_2^-$), the $^{15}NO_2^-$ outcompeted $^{14}NO_3^-$, yielding significantly more $^{15}NH_3$ than $^{14}NH_3$ over the 6-hour electrolysis (Figure 3-4c). This indicates that for the nitrogenous products in the NO_3RR, the potential participation of bulk NO_2^- or locally channeled NO_2^-, significantly complicates the mechanism of NH_3 production (e.g., $2e^- + 6e^-$ *vs.* $8e^-$).[110,126] Therefore, unambiguously identifying whether the underlying reaction mechanism is a direct $8e^-$ pathway, a (rapid) $2e^- + 6e^-$ pathway with a bulk/channeled NO_2^- intermediate, or a combination thereof, is of great significance for the design and optimization of NO_3RR systems and even more complex nitrate-involving reactions.[127,128]

Figure 3-4d (and shown individually by applied potential in Appendix B.50 and Appendix B.51) shows the NO_2RR electrolysis for all M-N-C catalyst under a 0.01M NO_2^- feed, a concentration mimicking the bulk NO_2^- concentrations in the NO_3RR electrolysis (Figure 3-4d). Obviously, both the NH_3 selectivity and activity of the NO_2RR were significantly higher than that of the NO_3RR (Figure 3-4d) for all catalysts. Specifically, Fe-, Co-, and La-N-C showed 100% FE_{NH3} over the whole potential range and Cr-, Ni-, Cu-, Pd-, and W-N-C showed increasing FE_{NH3} as the cathodic potentials decreased, reaching 100% at -0.8 V. Again, Mo-N-C showed a unique and potential-independent FE_{NH3} around 75%. Similar to the NO_3RR, the NO_2RR for Ru-N-C and Rh-N-C showed a distinct decreasing trend on the FE_{NH3} and consistent $Yield_{NH3}$ over the entire potential range, likely being outcompeted by the HER as the cathodic potential decreased.

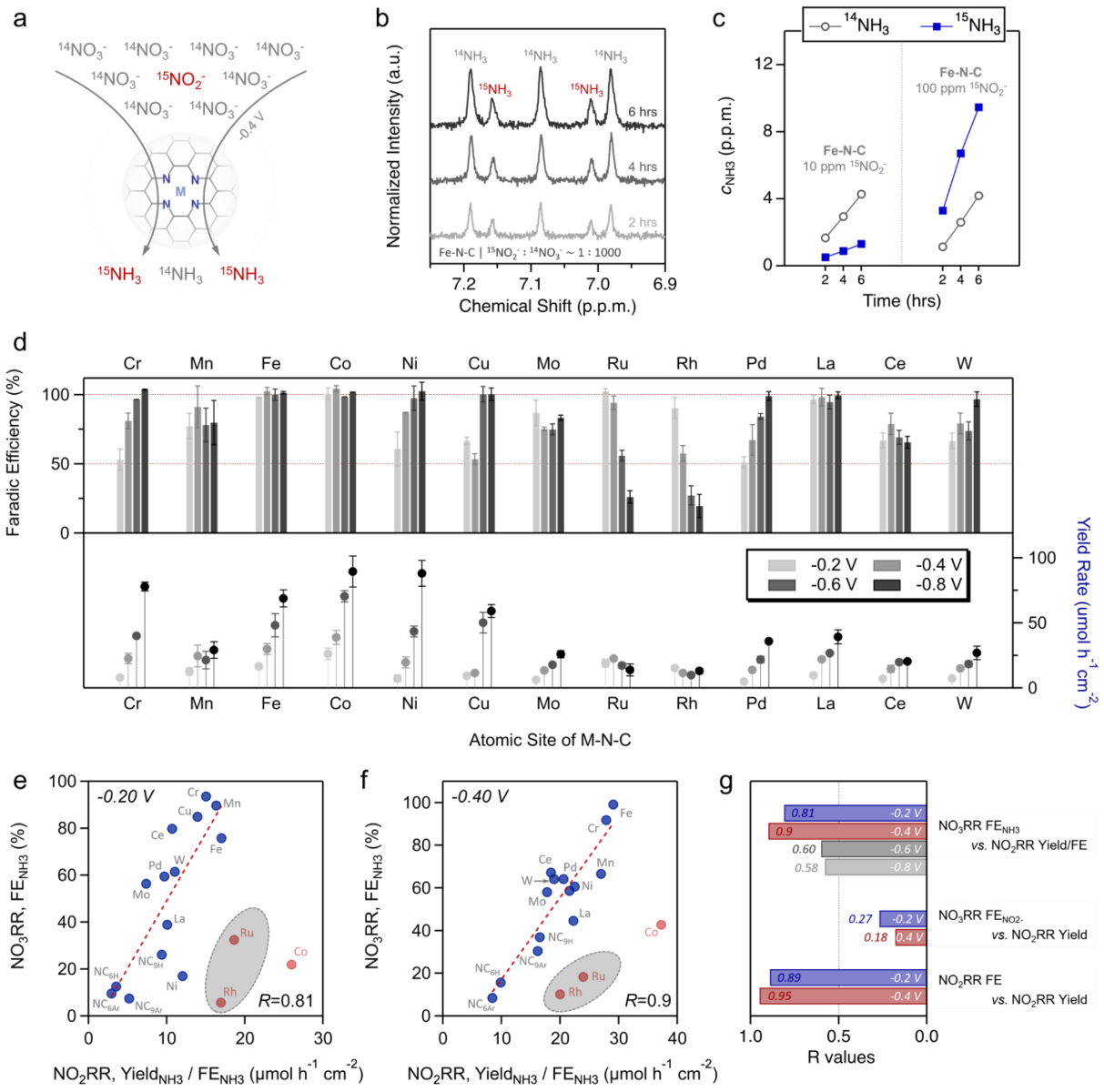

Figure 3-4. Mechanistic analysis of the NO_3RR via a NO_2^- intermediate (a-c) Isotopic analysis of competing NO_3RR and NO_2RR reactions at -0.4 V *vs.* RHE. a) Experimental schematic for NO_3RR electrolysis in which small amounts of $^{15}NO_2^-$ are doped in 0.16M $^{14}NO_3^-$. b) NMR spectra for the electrolysis with 10 ppm of $^{15}NO_2^-$ doped in 0.16M $^{14}NO_3^-$ (10,000 ppm), sampled at 2, 4, and 6 hours. c) Time course analysis of $^{14}NH_3$ and $^{15}NH_3$ concentration at 2, 4, and 6 hours for the NO_3RR with 10 ppm $^{15}NO_2^-$ (left) and 100 ppm $^{15}NO_2^-$ (right) in 0.16M $^{14}NO_3^-$

(10,000 ppm). d) Electrochemical NO_2RR for all M-N-C catalysts in 0.05M PBS + 0.01M KNO_2 for 0.5 hours. Faradaic efficiency for NH_3 as a function of the applied potential between -0.2 V and -0.8 V (top). Bottom section shows the corresponding NH_3 yield rate (μmol h^{-1} cm^{-2}). The chronoamperometry plots and UV-Vis detection curves for NH_3 are shown in Appendix B.52 - Appendix B.58. Note, FE's over 100% are a result of electrolyte dilution to bring the concentration of NH_3 into the UV-vis detection calibrated range. (e-f) Correlations between the NO_3RR Faradaic efficiency for NH_3 in Figure 3-4d. (y-axis) and the dividend of the NH_3 yield rate and Faradaic efficiency of the NO_2RR in Figure 3-4d at (e) -0.20 V and (f) -0.40 V *vs.* RHE. The NO_2RR, $Yield_{NH3}$ / FE_{NH3} is represented as the NO_2RR total current (NO_2RR, j_{total}). The correlation between the NO_2RR, $Yield_{NH3}$ and NO_3RR, FE_{NH3} is shown in Appendix B.59. The Ru and Rh outliers in gray shades were excluded from the linear fit due to the dominant NO_3RR gaseous products as shown in Appendix B.46 as well as Co-N-C. (g) Summary of the goodness of fit, R values, for varying experimental NO_3RR-NO_2RR correlations. All other correlations not shown in Figure 3-4 e-f, are shown graphically in Appendix B.60, Appendix B.61 and Appendix B.62.

To examine the relationship between the NO_2RR and NO_3RR, Figure 3-4 e and f correlates the activity of NO_2RR (FE_{NH3} / $Yield_{NH3}$) with the selectivity of NO_3RR (FE_{NH3}), revealing a linear relationship at -0.20 V and -0.40 V. This linear relationship suggests a major contribution from the bulk or locally channeled NO_2^- towards NH_3 ($2e^-$ + $6e^-$ pathway). Meanwhile, the correlation between the FE_{NO2-} in the NO_3RR and the $Yield_{NH3}$ in the NO_2RR, has a poor linear fit (Appendix B.61), highlighting the complex reaction mechanism. In contrast, the poor correlations between the NO_3RR FE_{NO2-} and NO_2RR $Yield_{NH3}$ (Figure 3-4g), confirmed that in

the NO_3RR the bulk NO_2^- species were in a complex production-consumption process rather than an irreversibly desorbed final by-product.

3.5 Computational descriptors for the NO_3RR and NO_2RR

As discussed above, the first $2e^-$ transfer is the rate limiting step in the NO_3RR, therefore DFT was used to study the energetics of key intermediates in the conversion of NO_3^--to-NO_2^- on various catalytic active sites (Appendix B.63). This included the $*NO_3$ surface intermediate formed by oxidative associative adsorption of NO_3^-, the *O surface intermediate formed by neutral dissociative adsorption of NO_3^-,[110] and the $*NO_2$ surface species formed in the reductive adsorption of NO_3^-, these result in four thermodynamic reaction descriptors, as shown in Figure 3-5a.

Figure 3-5a shows that the Mo-N_4, La-N_4, Ce-N_4 and W-N_4 sites could strongly adsorb NO_3^- ($\Delta_r G$ ~ -4eV) in a dissociative manner, forming an *O surface species and a free NO_2^- molecule. For these oxyphilic metals, upon exposure to NO_3^- molecules, the single-atom sites are oxygenated with a fifth ligand and the new active site (O-M-N_4) can still coordinate a NO_3^-/NO_2^- molecule for further reduction.[110] Appendix B.64 shows that the O-M-N_4 sites had a weaker interaction with NO_3^- but could stabilize the $*NO_3$/$*NO_2$ surface intermediates. For the Cr-N_4, Mn-N_4, Fe-N_4 and Ru-N_4 sites, associative and dissociative adsorption of NO_3^- is likely a competitive process that also depends on the cell potential. Namely, while the associative adsorption of NO_3^- is potential dependent, dissociative adsorption is not as no electrons are involved in this process. Co-N_4, Ni-N_4, Cu-N_4, Pd-N_4, and La-N_4 sites adsorb NO_3^- associatively and produce NH_3 via a $*NO_2$

intermediate. Additionally, our DFT descriptors suggest limited NO_3RR activity over Rh-N4 sites, being only favorable via the reductive adsorption of NO_3^-, while in other computational based works, Rh-N_4 sites suffer some competition between *H and *NO_3, in agreement with the poor NO_3RR activity observed in our experimental observations.[86,129]

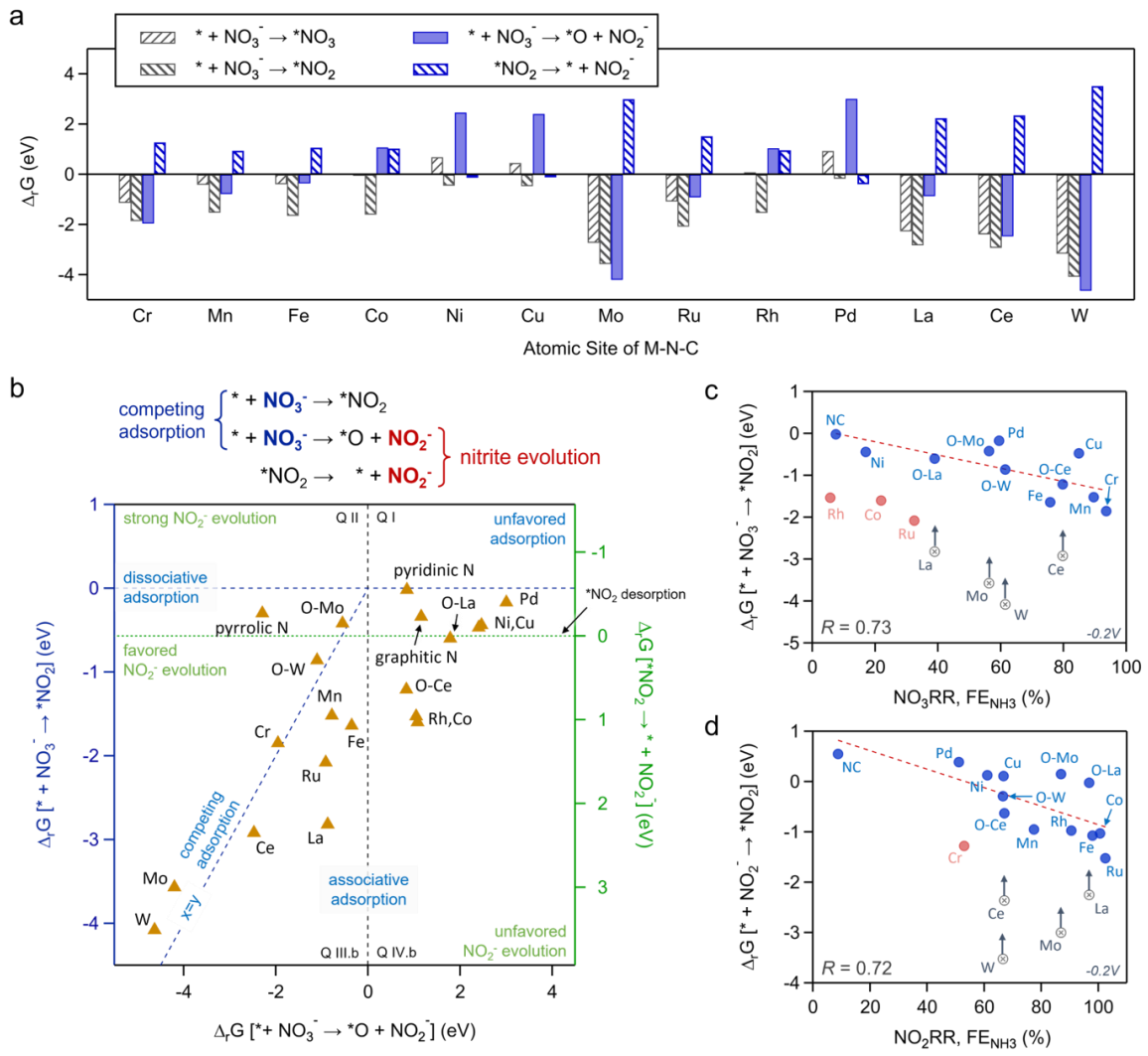

Figure 3-5. Computational NO_3RR descriptors as calculated by using DFT with optB86b-vdW functional. (a) Gibbs free energies (Δ_rG) of the reaction for the first two electron transfer steps in the NO_3RR. Processes that generate NO_2^- in the bulk electrolyte are shown in blue. Note solid bars indicate no electron transfer, uphill gradient stripes indicate a reductive e^- transfer and

downhill gradient stripes indicate an oxidative/reverse electron transfer. (b) Quadrant plot of the $\Delta_r G$ for associative adsorption [$^* + NO_3^- \rightarrow {}^*NO_2$] (Y_1-axis), dissociative adsorption [$^* + NO_3^- \rightarrow {}^*O + NO_2^-$] (X-axis) and *NO_2 desorption [$^*NO_2 \rightarrow {}^* + NO_2^-$] (Y_2-axis), forming sectors where certain reaction pathways are thermodynamically favored. The main quadrants were determined by the X-axis and Y_1-axis. Quadrants III and IV were further divided by the Y_2-axis into III.a, III.b, IV.a and IV.b sub-sections. The three reaction coordinates determined two types of NO_3^- adsorptions and two types of NO_2^- evolutions as shown by the diagram above the figure. For simplified plots correlating two descriptors at a time, see Appendix B.65. (c) Correlation between DFT-derived $\Delta_r G$ [$^* + NO_3^- \rightarrow {}^*NO_2$] and experiment-derived NO_3RR FE_{NH3} at -0.2 V *vs.* RHE. (d) Correlation between DFT-derived $\Delta_r G$ [$^* + NO_2^- \rightarrow {}^*NO_2$] and experiment-derived NO_2RR FE_{NH3} at -0.2 V *vs.* RHE. Oxygenated active sites (O-M) were included for the oxyphilic elements (Mo, La, Ce and W).

The quadrant plot in Figure 3-5b graphically shows the correlations between the DFT-derived descriptors, mapping out the competitive NO_3^- adsorption and sources for NO_2^- evolution. Specifically, the far ends of Quadrant I, Quadrant II and Quadrant IV.b represent unfavored NO_3^- adsorption, exclusive NO_2^- evolution and unfavored NO_2^- evolution, respectively. These three blank sectors explain the above-mentioned universal NO_3RR activity for all M-N-C and metal free N-C catalysts (Appendix B.66), as well as the variant but non-dominant FE_{NO2-} in the NO_3RR. The diagonal of Quadrant III (x=y) indicates competitive associative and dissociative adsorption of NO_3^-. The largest NO_2^- producing catalyst, Mo-N-C (O-Mo-N_4 and Mo-N_4 sites), is located at the diagonal, indicating comparable associative and dissociative adsorption. Several metal centers (e.g., Mn, Fe, Ru, La and Ce) fall below the diagonal in Quadrant III.b and upper Quadrant IV.b, suggesting a favored associative NO_3^- adsorption for high NH_3 selectivity in NO_3RR electrolysis

(Figure 3-5d). Quadrant IV.b (Co, Rh, O-Ce and O-La) marks the region where a solely direct $8e^-$ pathway to NH_3 is feasible, with formation of the $*NO_2$ intermediate being favored, while both descriptors for the generation/desorption of NO_2^- are unfavored. Quadrant IV.a (Ni, Cu and Pd, pyridinic-N and graphitic-N) shows a weak stabilization of the $*NO_2$ intermediate, while simultaneously showing activity for the desorption of $*NO_2$ for NO_2^- evolution. It should be noted that Mo-N-C is the only metal center favoring NO_2^- evolution through both the dissociative NO_3^- adsorption and $*NO_2$ desorption paths, explaining the unique selectivity of Mo-N-C in the NO_3RR (Figure 3-5d). The DFT calculated Gibbs free energy changes for these descriptors are given in Table 12.

To evaluate the practical relevance of these computational descriptors, a set of correlations were developed between the DFT-derived free energies ($\Delta_r G$) in Figure 3-5a and the electrocatalytic performance in Figure 3-3d and Figure 3-4d. Specifically, Figure 3-5c shows the correlation between the adsorption energy of NO_3^- ($\Delta_r G\ [\ ^* + NO_3^- \rightarrow\ ^*NO_2\ ]$) and the NO_3RR NH_3 selectivity (FE_{NH3}), wherein a linear correlation (R=0.73) is observed at -0.2 V. This result highlights the importance of a stable $*NO_2$ intermediate for high NH_3 selectivity in both the $8e^-$ pathway or the $2e^- + 6e^-$ pathway (which requires the re-adsorption of NO_2^-). It should be noted that Ru, Rh were excluded as the outliers due to the ease at which they are outcompeted by the HER, as shown in the NO_3RR electrolysis (Figure 3-3d), while Co is indicated as an outlier due to its unique NO_3RR performance showing strong activity towards the reduction of NO_2^-, while showing poor activity towards NO_3^-, as evidenced by the $^{15}NO_2^-$ doping experiments in Appendix B.49, being a unique metal center showing a dominating concentration of $^{15}NH_3$ over $^{14}NH_3$ (at a 10,000 ppm $K^{14}NO_3^-$ and 10 ppm $K^{15}NO_2^-$). Additionally, the involvement of the

oxo-form for the highly oxyphilic elements (O-Mo, O-W, O-La, O-Ce) shifts them back onto the trend line as compared to their bare M-N_4 counterparts. These results confirmed the distinct active sites/reaction mechanism of early transition 4*d*-, 5*d*- and *f*-metal-based M-N-C catalysts in neutral environments and is attributed to the oxophilicity and large coordination number of these metals that allow simultaneous coordination of multiple intermediates.[130] Similarly, Figure 3-5d shows a comparable correlation (R=0.72) between the adsorption energy of NO_2^- ($\Delta_r G\ [\ ^* + NO_2^- \rightarrow\ ^*NO_2\ ]$) and the NO_2RR ammonia selectivity (FE_{NH3}), indicating that the stabilization of the $^*NO_2$ intermediate also plays a key role in the NO_2RR as well as the downstream $6e^-$ transfer in the NO_3RR.

However, the NO_3RR FE_{NO2-} showed minimum correlations with either $\Delta_r G\ [\ ^*NO_2 \rightarrow\ ^* + NO_2^-\ ]$ or $\Delta_r G\ [\ ^* +\ NO_3^- \rightarrow\ ^*O + NO_2^-\ ]$, as shown in Appendix B.67. This agrees well with the above-mentioned poor correlation between the NO_3RR FE_{NO2-} and NO_2RR $Yield_{NH3}$ (Figure 3-4g and Appendix B.61), wherein the bulk NO_2^- species in the NO_3RR were in an active but and complex production-consumption process, making it difficult to deconvolute the NO_2^- production and consumption rates from its net yield.

3.6 Conclusions

In summary, a rich set of atomically dispersed 3*d*-, 4*d*-, 5*d*- and *f*-block M-N-C catalysts with a well-established M-N_x coordination was synthesized. The gap analysis plot revealed diverse NO_3RR performance, wherein Cr-N-C and Fe-N-C were the most NH_3 selective catalysts, achieving near 100% FE_{NH3}, while Mn-, Cu- and Mo-N-C were highly selective for NO_2^-. For the NO_2RR, several elements including Cr-, Fe-, Co-, Ni-, Cu- and La-N-C achieved a FE_{NH3} of

100% at high overpotentials, with Fe and Co-N-C showing 100% FE_{NH3} over the entire potential range. Isotopically doped $^{15}NO_2^-$ in concentrated $^{14}NO_3^-$, demonstrated the ease at which minute concentrations of NO_2^- in the bulk electrolyte can preferentially reduce to NH_3, convoluting the possibility of a direct $8e^-$ pathway or a $2e^- + 6e^-$ cascade pathway with NO_2^- as transient intermediate for the NO_3RR. The correlation between experimental NO_3RR ammonia selectivity and experimental NO_2RR activity suggested a universal contribution of the NO_2^- intermediate in NO_3RR ($2e^- + 6e^-$). The DFT-derived thermodynamic descriptors theoretically explain the electrocatalytic selectivity for each metal center. Furthermore, these computational descriptors showed strong correlations with the experimental performances, such that a simple computationally evaluated descriptor can be utilized to estimate the activity of M-N-C catalysts for the NO_3RR and NO_2RR. While these computational-experimental activity descriptors provide strong correlations for the NO_3RR and NO_2RR activity, these correlations are limited when the H^+ adsorption is a competing factor leading to the HER over NO_3RR (Ru- and Rh-N-C) and when there is poor NO_3^- activation in contrast with significant NO_2^- activation (Co-N-C). Importantly, these computational-experimental activity descriptors are based on the $M\text{-}N_x$ active site and have strong predictive NO_3/NO_2RR ability at low potentials, where the intrinsic nature of the $M\text{-}N_x$ site is observed. However, the effectiveness of these activity descriptors decreases as the overpotential increases, forcibly driving the reaction and possibly inducing structural changes to the $M\text{-}N_x$ sites, convoluting the intrinsic activity of the atomically dispersed metal center. This work deciphered the unique fundamentals of the NO_3RR over atomically dispersed M-N-C catalysts to create a set of experimentally driven computational descriptors for the NO_3/NO_2RR activity, paving the road for the design of tandem NO_3RR systems and nitrate-

containing systems composed of either multi-metallic M-N-C catalysts or extended catalytic surfaces supported by synergistic M-N-C supports.

Chapter 4 Synergizing γ-Fe_2O_3 Nanoparticles on Single Atom Fe-N-C for Nitrate Reduction to Ammonia at Industrial Current Densities

4.1 Overview

The synthesis of ammonia (NH_3) based fertilizers is essential to support the growing global food demands and due to its current thermochemical synthesis, via the Haber Bosch (HB) process accounts for approximately of 2% of global energy usage and 1.4% of global CO_2 emissions.[1,39,96] The reduction of di-nitrogen (N_2) is a theoretically promising NH_3 synthesis pathway, however, activation of the highly stable and insoluble (in water-based electrolytes) N_2 molecule remains unproven.[16,21] As a replacement for the inert N_2 molecule, recently there has been a revitalized interest in the more oxidized N-form, nitrate (NO_3^-). Nitrate is an environmental pollutant present in ground water runoffs due to heavy overfertilization practices and in industrial waste streams at varying concentrations (0.001 – 2M).[29,131] The reduction of NO_3^- to NH_3 is appealing to reutilize waste nitrogen into value added NH_3, alleviating demand on the HB process, while also serving as an alternative to traditional denitrification techniques, providing dual benefits for the nitrate reduction reaction (NO_3RR). It is important to note, the NO_3RR alone is not a replacement for the HB process as typically, the N-molecule in the NO_3^- originates a HB produced NH_3, but the NO_3RR can help to enhance the efficiency of the N-cycle.[100]

The NO_3RR is a complex $8e^-$ transfer reaction, consisting of several possible soluble and insoluble intermediates (NO_2, NO_2^-, NO, N_2, N_2O, NH_2OH, NH_3, and N_2H_4) and competes directly with the hydrogen evolution reaction (HER).[57] Aiming at industrial relevance, it is essential to optimize catalyst activity and selectivity towards a singular product, in this

discussion NH_3. The use of an alkaline media (pH 13-14) has been shown to enhance the activity of the NO_3RR (over most metals) and significantly suppresses the formation of the common $2e^-$ side product, nitrite (NO_2^-), often reporting the highest NH_3 Faradaic efficiencies (FE_{NH3}) and yield rates ($Yield_{NH3}$) as shown in Table 15.[64,123,132]

When targeting industrially relevant current densities there is a competing compromise between the energy efficiency and NH_3 partial current density (j_{NH3}), both of which are influenced by the corresponding FE_{NH3} and applied reductive potential. In alkaline media, the standard reduction potential for the NO_3RR to NH_3 (equation 1) is 0.69V *vs.* RHE.[64,133]

$$NO_3^- + 6H_2O + 8e^- \rightarrow NH_3 + 9OH^- \ (E^0 = 0.69\,V\ vs.\,RHE;\ pH = 14) \qquad (1)$$

Currently, several reports achieve high FE_{NH3} pushing upwards of 90%, some at mildly reductive potentials, resulting in relatively high cathodic energy efficiencies (almost 40%).[10,14–17] However, most of these reports suffer from limited j_{NH3} (0.5 – 80 mA/cm^2), resulting in the need for largely scaled up devices or stacks, increasing capital costs these systems. In contrast, other reports show higher j_{NH3} (80 < X mA/cm^2), at more cathodic potentials suffering from reduced energy efficiencies.[136–138] Establishing a tradeoff between energy efficiency and j_{NH3} remains ambiguous, although, a recent economic analysis quantifying the levelized cost of NH_3, suggests that the j_{NH3} (production rate) has a more significant influence than the cell voltage or electricity price in reducing the levelized cost of NH_3.[138]

One strategy to achieve both higher cathodic energy efficiencies and increased j_{NH3} is to utilize platinum-group-metals (PGMs) and their alloys as these metals often have earlier (closer to the thermodynamic) reaction onset potentials.[123,139] However, due to their scarcity and price, large scale systems based on these catalysts are not economically promising. Alternatively, cost

efficient PGM-free metals typically require more cathodic reduction potentials to achieve a desirable j_{NH3}. Interestingly, a strategy currently being investigated for the neighboring oxygen reduction rection (ORR) is the use of active supports to increase the activity and durability of the catalyst systems.[140–142] Where a typical inert carbon support (Vulcan / carbon black) is replaced with an ORR active, atomically dispersed metal-nitrogen-carbon (M-N-C) support, often Fe-N-C or Co-N-C. It's speculated that possible electron donation between the platinum nanoparticles and the M-N-C can create more favorable intermediate adsorption energies, increasing the activity of the catalyst system. Additionally, it's thought the $M\text{-}N_4$ active site can modify the electronic structure of the neighboring carbon, increasing the stability of the nanoparticles.

It has been shown in our previous works and supported by other studies that atomically dispersed Fe-N-C is highly active for the NO_3RR, achieving a FE_{NH3} greater than 90%.[63,64,110,143] In this work, we build upon our previous work with atomically dispersed Fe-N-C and utilize an active-catalyst/active-support system, synthesizing a $\gamma\text{-}Fe_2O_3$/Fe-N-C catalyst for ultra-high NO_3RR to NH_3 performance. Where the $\gamma\text{-}Fe_2O_3$/Fe-N-C catalyst exhibits a potential independent behavior on the FE_{NH3} (~100%) between -0.4 to -1.2 V *vs.* RHE, while increasing the j_{NH3} up to nearly 2 A/cm^2 (at a $Yield_{NH3}$ of more than 9 $mmol_{NH3}\ hr^{-1}\ cm^{-2}$). An economic analysis reveals that operating under a strongly reductive potential with a high j_{NH3} is more beneficial for reducing the levelized cost of NH_3, as opposed to a mildly reductive potential with higher energy efficiency but significantly reduced j_{NH3}. Post-mortem XPS revealed that the pre-reduction activation step is critical in achieving the ultra-high NO_3RR performance, generating highly active, exposed Fe^{2+}/Fe^0 sites. A durability test showed that the optimized $\gamma\text{-}Fe_2O_3$/Fe-N-C catalyst could maintain a FE_{NH3} between 90-100% at a current of 1.3 A/cm^2 for over 24-hours. Demonstrating the effectiveness of utilizing an active-catalyst/active-support system.

4.2 Methods

4.2.1 Synthesis of γ-*Fe_2O_3, Co_3O_4 and RuO_x supported on XC72*

The Fe, Co and Ru nanoparticle catalysts were synthesized using an organic solvent synthesis. Taking γ-Fe_2O_3 as an example. First, 44.8 mg of XC72 carbon and 0.2 mmol of $Fe(acac)_2$ was dispersed by sonication for 30 min in 40 mL of benzyl ether. Next the mixture was deaerated by purging N_2 for 30 min. The mixture was then heated to 100 ˚C and then 400 μL of oleylamine and 200 μL of oleic acid were added and the temperature was held for 10 min. Next, the mixture was heated to 180 ˚C and 1 mL of tert-Butyllithium was added and the temperature was held for 10 min. The catalyst mixture was then heated to 210 ˚C and held for 45 min. The catalyst mixture was then centrifuged and washed by ethanol before drying.

The Co and Ru based particle synthesis is identical, with the 0.2 mmol of $Co(acac)_2$ and $Ru(acac)_2$ being added.

4.2.2 Synthesis of Fe-N-C

The atomically dispersed Fe-N-C active support was synthesized using the sacrificial support method (SSM). First, a catalyst mixture of 6.25 g of nicarbazin, 1.25 g of OX-50 (Evonik), 1.25 g of LM150 (Cabot), 0.5 g of stöber spheres (made in house) and 0.6 g of iron (III) nitrate were added and dispersed by sonication for 30 min in water. The catalyst slurry was then dried for 24 hrs at 45 ˚C under continuous stirring. The partially dried slurry was then transferred to an oven for 24 hrs for complete drying at 45 ˚C. The catalyst mixture is then ball milled at 45 Hz for 60 min. Next, the milled catalyst power undergoes pyrolysis in a 5% H_2 / 95% Ar atmosphere for 45 min at 975 ˚C. The pyrolyzed catalyst is then ball milled a second time at 45 Hz for 1 hr before being etched in a concentrated HF (18M) solution for 96 hours to remove the silica support and

any nanoparticles. The etched catalyst is then washed with DI water and filtered until neutral pH before drying. A second pyrolysis under a 10% NH_3 / 90% N_2 atmosphere is performed at 950 ˚C for 30 min. The catalyst is then ball milled a third time at 45 Hz for 1 hr.

4.2.3 Synthesis of γ-*Fe_2O_3/Fe-N-C*

The γ-*Fe_2O_3* nanoparticles supported on atomically dispersed Fe-N-C (γ-Fe_2O_3/Fe-N-C*)* was synthesized analogously to the nanoparticle catalyst supported on XC72, with the carbon support being switched for the active Fe-N-C support.

4.2.4 Physical Characterization

Transmission electron microscopy (TEM) was performed on a JOEL JEM-2100F. To obtain atomic resolution images, aberration-corrected scanning transmission electron microscopy (AC-STEM) and energy dispersive X-ray spectroscopy (EDX) was performed on a JEOL ARM300CF (at 300 keV accelerating voltage). The valence state of the γ-Fe_2O_3 nanoparticles and atomically dispersed Fe sites were examined through atomic resolution electron energy loss spectroscopy (EELS) on a Nion UltraSTEM200 microscope equipped with a cold FEG, a C3/C5 aberration correction and a high-energy resolution monochromated EELS system (HERMES). To suppress beam damage on the atomically dispersed metal-nitrogen coordination, a lower accelerating voltage of 60 keV was used to collect the EELS spectra. For the spectra acquisition, the energy dispersion was set as 0.29 eV/channel at an exposure time of 500 ms/pixel. Background subtraction in the spectrum was achieved by a power-law function and the de-noising of the spectra was performed by the multivariate weighted principal component analysis (PCA) routine in the Digital Micrograph software. The smoothing of the spectra was achieved by a Savitzky-Golay method with points of window of 15 using the Origin software. For energy loss near edge structure

(ELNES) analysis on Fe valence state, the spectra collected from different Fe SA locations were summed up and then averaged to improve the signal to noise ratio.

The surface valence and chemical bonds of the catalysts were analyzed by X-ray photoelectron spectroscopy (XPS) performed using a Kratos AXIS Supra spectrometer with a monochromatic Al Kα source. A pass energy of 160 eV from 1400 eV to 5 eV at a step size of 1 eV was used to obtain the survey spectra. No charge neutralization was employed. CasaXPS software was used to analyze the XPS data with the spectrum being calibrated by C *1s* sp^3 peak at (284.8 eV). For analyzing the data, two backgrounds were used, with a linear background being employed for the C *1s* and N *1s* spectrum, while a Shirley background was used for the N *1s* and Fe *2p* spectrum. For analysis of the sp^2 carbon, an asymmetric 50% Gaussian / 50% Lorentzian was applied. While for all other data, a 70% Gaussian / 30% Lorentzian was applied.

To examine the crystal phase of the catalysts, X-ray diffraction (XRD) patterns were obtained using a Rigaku Ultima-III powder X-ray diffractometer. The iron metal content the catalysts was quantified by thermogravimetric analysis (TGA) performed on a Netzsch TG 209 F1 Libra. To quantify the graphitic and amorphous content in the two catalyst supports (XC72 and Fe-N-C), Raman spectra were taken on an InVia, Renishaw Corp., UK system

4.2.5 Electrochemical Measurements

Preparation of the working electrode

A carbon paper electrode (AvCarb MGL 370, Fuel Cell Store) was used as the working electrode and was cut to a geometric surface area of 0.25 cm^2 (0.5 x 0.5 cm). An oxygen plasma and acid treatment (0.5 M H_2SO_4) were employed to remove the PTFE layer on the electrode and increase the hydrophilicity. A catalyst ink comprised of 5 mg of catalyst, 680 μL of isopropanol, 300 μL of MilliQ water and 20 μL of a 5 wt% Nafion (probe sonicated for 1 min, followed by 30 min in a

sonication bath) was drop cast on the electrode. Catalyst loading on the electrode was optimized during the study, by varying the amount of catalyst ink drop cast.

Electrochemical nitrate reduction

Electrochemical tests were performed in a customized glass H-cell (Adams & Chittenden), separated by a Celgard 3401 membrane (used as received). A three-electrode system comprising a carbon paper with catalyst, reversible hydrogen electrode (Gaskatel) and graphite rod were used as the working, reference and counter electrodes, respectively. An alkaline electrolyte, 1M potassium hydroxide (KOH) with 0.16M potassium nitrate (KNO_3) was used for the NO_3RR tests. Prior to electrochemical testing, the electrochemical cell was purged with N_2 gas (research grade 99.9995% - PraxAir) for 30 min at 80 sscm. During the NO_3RR, N_2 gas was continuously purged at 30 sccm. Control experiments with only 1M KOH + N_2 gas demonstrate that the catalyst is not active for N_2 reduction to ammonia, allowing N_2 to be an inert gas in this system (Figure Sx). For the NO_3RR, the working and counter electrolyte volumes are 30 mL and 25 mL, respectively. Chronoamperometric (CA) tests were performed for 15 min under vigorous stirring. Prior to CA measurements, the electrode was activated by a pre-reduction step at -1.5 V *vs.* RHE for 90 seconds. Linear sweep voltammetry was performed by cathodically sweeping from 0.5 to -1.0 V *vs.* RHE as a scan rate of 5 mV/s. Electrochemically active surface area (ECSA) was determined by varying the scan rate between 20 – 100 mV/s between 0.60 – 0.75 V *vs.* RHE. For the 24-hour durability test, which was segmented into eight, 3-hour sections, an electrolyte reservoir of 250 mL was connected to the cathodic chamber of the h-cell using peristaltic pumps and was continually circulated throughout the electrolysis. The large circulating reservoir prevents the buildup of produced NH_3 from becoming too high in the cell. After a 3-hour segment, all

electrolyte was pumped back into the external reservoir, sampled, and then refreshed for the next 3-hour segment.

Isotopic ($K^{15}NO_3$) nitrate reduction

To confirm the N in the detected NH_3 originated from the KNO_3 feed and not from the N-doped catalyst support, the N_2 gas or other sources of contamination, NO_3RR with isotopically doped $K^{15}NO_3$ was performed. A 1M KOH + 0.16M $K^{15}NO_3$ electrolyte was used. Isotopically labelled $^{15}NO_3RR$ was performed at -1.0 V *vs.* RHE for 15 min, after which the electrolyte was sampled and quantified by ^1H NMR. Where isotopically doped $^{15}NH_3$ yields a doublet and standard $^{14}NH_3$ results in a triplet.

Calculation of the yield and faradaic efficiency

The yield rate of ammonia ($Yield_{NH3}$) from the NO_3RR is calculated from Eq. 1.

$$Yield_{NH_3} = \frac{c_{NH_3} * V}{Mw_{NH_3} * t * A_{electrode}} \quad (1)$$

The Faradaic efficiency for NH_3, FE_{NH3}, is calculated from Eq. 2

$$FE_{NH_3} = \frac{n * F * c_{NH_3} * V}{Mw_{NH_3} * Q} \quad (2)$$

Where c_{NH3} is the concentration of NH_3 in the working chamber (mg/mL), V is the volume of the working chamber (30 mL), the molar mass of ammonia, Mw_{NH3} is 17.031 g/mol, t is the electrolysis time (0.25 hours) and $A_{electode}$ is the area of the working electrode (0.25 cm^2). n is the number of

electrons transferred ($8e^-$ for NO_3^- to NH_3), *F* is Faradays constant (96,485 C) and *Q* is the charge passed during the electrolysis (C).

The cathodic energy efficiency (CEE) is energy efficiency for the cathodic reaction (NO_3RR), assuming no over potential for the anodic oxygen evolution reaction (OER), and is calculated using equation 3.

$$CEE = \frac{(E^0_{O2} - E^0_{NO3RR}) * FE_{NH3}}{E_{O2} - E_{NO3RR}} \quad 3$$

Where E^0_{O2} and E^0_{NO3RR} are the standard potentials for the anodic (1.23 V *vs.* RHE) and cathodic reactions (0.69 V *vs.* RHE), respectively. FE_{NH3} (%) is the Faradic efficiency for NH_3 from the NO_3RR and E_{O2} and E_{NO3RR} are the applied anodic and cathodic potentials, where here, the E_{O2} is assumed to the standard potential.

4.2.6 Product Detection

For typical NO_3RR tests, the detection and quantification of NH_3 is achieved using a ultraviolet-visible (UV-Vis) spectrophotometer (Shimadzu, UV-2600). NH_3 was detected using the indophenol blue method in which 2 mL of electrolyte (or diluted electrolyte) is mixed with 2 mL of solution A (1M NaOH, 5 wt% salicylic acid and 5 wt% sodium citrate), 1 mL of solution B (0.05M NaClO) and solution C (1 wt% sodium nitroferricyanide). After incubating the dark at room temperature for 1 hour, the maximum absorbance is taken at ca. 655 nm and quantified with respective calibration curves. Calibration curves with 1M KOH and varying concentrations of NO_3^- are provided in Figure S_x. For the detection of isotopic ammonia ($^{15}NH_3$), ^1H NMR is used. 3-(trimethylsilyl)-1-propanesulfonic acid sodium salt (DSS) is selected as an internal standard and Dimethylsulfoxide-d6 (DMSO) is used as the locking solvent. The NMR spectra of a solution of 580 μL of electrolyte, 25 μL of DMSO, 20 μL of 3M H_2SO_4, and 75 μL of 6 mM DSS is obtained

on a Bruker CRYO 500 MHz spectrometer. A solvent suppression method was applied to reduce the signal of H_2O, allowing for better resolution. The spectrum was processed using the Topspin 4.0.8 software.

4.2.7 Economic Analysis – Levelized Cost of Ammonia

To evaluate the tradeoff between energy efficiency and ammonia partial current density, the levelized cost of ammonia (LC_{NH3}) was employed as a metric. The LC_{NH3} is calculated analogously to Daiyan et al. and as is determined by equation 4.[138]

$$LC_{NH3} = \frac{R_f * CAPEX + OPEX}{Yield_{NH3}} \quad (4)$$

Where R_f is the capital recovery factor and is set at 0.08 %. $CAPEX$ is the capital cost and is solely attributed to the cost of the electrolyzer stack (in $). OPEX is the operational cost and constitutes costs associated with electricity, nitrate feed and water consumption (all in units of $). $Yield_{NH3}$ is the yield of ammonia (kg), giving a LC_{NH3} in $/kg$_{NH3}$. The $Yield_{NH3}$ is calculated based as a function of the current density and electrolyzer area (with $8e^-$ transferred per NH_3). The electrolyzer stack cost and details of the OPEX parameters are detailed below.

The electrolyzer stack cost is based on parameters in analogous economic calculations and analysis provided in a National Renewable Energy Laboratory report with a cost of \$342 kW^{-1} operating at a cell voltage of 1.9 V and current density of 2 A/cm^2, which yields an assumed NO_3RR electrolyzer stack cost of 12,996 $/$m^2$.[138,144] In the idealized case where the stack cost can be significantly reduced, a cost of \$143 kWh^{-1} is assumed, resulting in an electrolyzer cost of 5,434 $/$m^2$. For the OPEX costs, the cost of the NO_3^- (NO_x) input is assumed to be \$315 per metric ton, as estimated in work by Jiang et al.[138,145] The cost of water is assumed to be \$0.02 L and the cost

of electricity from the grid is assumed to be \$70 MWh^{-1} and electricity generated from renewable sources is assumed to be \$30 MWh^{-1}. The required electrolyzer area required is calculated from equation 5.

$$A_{electrolyzer} = \frac{I_{total}}{j} \quad (5)$$

Where I_{total} is current passing through the electrode (A) and j is current density of the NO3RR system. I_{total} is determined by dividing the applied power to the stack (assumed here as 1 MW) by the cell voltage (assumed here as 1.9 V). Therefore, assuming a system current density of 1.3 A/cm^2 (the performance demonstrated in the 24-hr electrolysis), the total required electrolyzer area is 37.6 m^2.

4.3 γ-Fe_2O_3/Fe-N-C synthesis and characterization

γ-Fe_2O_3 nanoparticles supported on atomically dispersed Fe-N-C (γ-Fe_2O_3/Fe-N-C) were synthesized by utilizing the sacrificial support method (SSM) for the Fe-N-C in combination with an organic solvent synthesis method for the γ-Fe_2O_3 nanoparticles. The SSM is a robust technique developed by our group for the synthesis of atomically dispersed M-N-C catalysts.[143] Schematically, the SSM is shown in Figure 4-1, where a catalyst slurry of a carbon-nitrogen precursor is mixed with nano porous silica and an iron-nitrate salt. The precursor mixture then undergoes a series of ball milling, pyrolyzing and acid etching steps, yielding an exclusively atomically dispersed Fe-N-C support.[143] The γ-Fe_2O_3 nanoparticles are synthesized utilizing an organic solvent method, where iron(III) acetylacetonate and the Fe-N-C support are dispersed by sonication in benzyl ether. After deaerating the system with N_2, the mixture is heated to 100 ˚C after which, oleyl amine and oleic acid are added. After heating to 150 ˚C, the reducing agent,

tertbutyl lithium is added and the catalyst mixture is further heated to 210 ˚C for a 45 min hold. After an ethanol wash and filtration, the final γ-Fe_2O_3/Fe-N-C catalyst is obtained. The synthesis of γ-Fe_2O_3 on XC-72R Vulcan carbon (XC72) is analogous, with the Fe-N-C being replaced for XC72 (γ-Fe_2O_3/XC72). The homogenous dispersion of the γ-Fe_2O_3 and well-controlled sub-5 nm particle size nanoparticles is observed by the HAADF-STEM image in Figure 4-1b and TEM images in Appendix C.1. Additionally, the corresponding elemental mapping is shown in Figure 4-1b, for the γ-Fe_2O_3/XC72 catalyst with a homogenous distribution of Fe, O and C. The γ-Fe_2O_3 nanoparticles have a spinel structure as observed in the aberration corrected (AC) HAADF-STEM image in Figure 4-1c. A schematic of the γ-Fe_2O_3 spinel crystal structure is given in Figure 1d. The high mag STEM image and EDS mapping in Figure 4-1e, verifies the atomic dispersion of Fe and N-doping in the Fe-N-C support. After reducing the γ-Fe_2O_3 nanoparticles on to the Fe-N-C support, Figure 4-1f confirms that the Fe-N-C support retains its atomic dispersion, as single atom Fe-N_x sites and γ-Fe_2O_3 nanoparticles are observed simultaneously. The corresponding EDS mapping of the γ-Fe_2O_3/Fe-N-C catalyst in Figure 4-1g, confirms the presence of nitrogen from the Fe-N-C support. The crystal structure of the catalyst was examined by X-ray diffraction (XRD), confirming the formation of Fe_2O_3 in the γ phase, γ-Fe_2O_3 (Appendix C.2). As a comparison to the Fe_2O_3 catalyst, a Co_2O_3 and RuO_x were also synthesized analogously and characterized using TEM and XRD (Appendix C.3-4) Furthermore, Raman spectroscopy was performed on Fe-N-C and XC72, showing similar graphitic content between the catalyst supports, Appendix C.5.

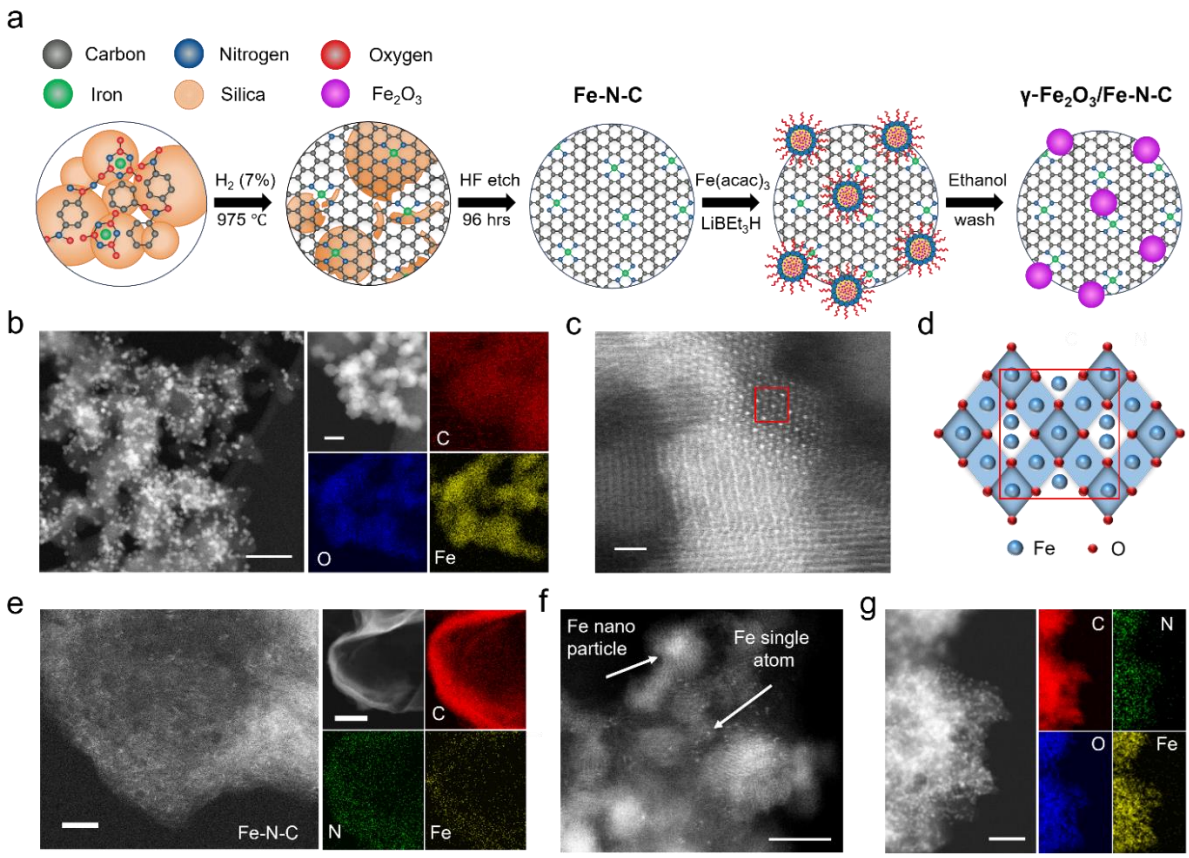

Figure 4-1. Synthesis and AC-HAADF-STEM images of the γ-Fe_2O_3 based catalysts. (a) Synthesis schematic, utilizing the sacrificial support method and an organic solvent synthesis to deposit γ-Fe_2O_3 nanoparticles on the atomically dispersed Fe-N-C. (b) STEM of the γ-Fe_2O_3 catalyst supported on XC72 carbon scale bar is 50 nm, with its corresponding EDS mapping scale bar is 5 nm. (c) Atomic resolution STEM showing the γ-Fe_2O_3 spinel structure, scale bar is 2 nm. (d) Schematic representation of the γ-Fe_2O_3 spinel crystal structure. (e) Atomic resolution STEM image of the atomically dispersed Fe-N-C catalyst support, with its corresponding EDS mapping, scale bar is 2 nm. (f) Atomic resolution STEM image showing the γ-Fe_2O_3 nanoparticles supported on the atomically dispersed Fe-N-C, scale bar is 5 nm. (g) EDS mapping of the γ-Fe_2O_3/Fe-N-C catalyst, scale bar is 50 nm.

To evaluate the chemical state of the γ-Fe_2O_3/Fe-N-C catalyst and evaluate possible changes in the electronic structure of the γ-Fe_2O_3/Fe-N-C catalyst due interactions from the Fe-N_x sites with the γ-Fe_2O_3 nanoparticles, atomic resolution electron energy loss spectroscopy (EELS), X-ray absorption spectroscopy (XAS) and X-ray photoelectron spectroscopy (XPS) was utilized. EELS was used to probe the valence state of the single atom Fe and the γ-Fe_2O_3 sites. Figure 4-2a shows the location where EELS spectra are taken for a γ-Fe_2O_3 particle (locations 1 and 2) and a single atom Fe site (locations 3 and 4). Both spectra show the Fe-$L_{3,2}$ edges, however, there is an L_3, L_2 excitation edge shift to lower energy loss and reduced L_3/L_2 white line ratio for single atom Fe (peak spacing of 12.4 eV), compared to γ-Fe_2O_3 (13.2 eV) in Figure 4-2b. This energy shift and quantitative analysis of the Fe- L_3/L_2 edges suggest the single atom Fe to be in an oxidation state lower than Fe^{3+}, in agreement with our previous work where Fe-N-C has an oxidation state *ca.* $Fe^{2.6+}$.[143] While analysis for the γ-Fe_2O_3 nanoparticles indicated an oxidation state of Fe^{3+}, in agreement with the XPS results in Appendix C.6.[143] Atomic resolution EELS was further applied for a highly localized evaluation of possible γ-Fe_2O_3 and Fe-N_x interactions affecting the electronic structure of the nanoparticles. Comparing the Fe-$L_{3,2}$ edges of the γ-Fe_2O_3 nanoparticles supported on Fe-N-C and XC72 reveals a 0.1 eV shift in the energy loss, Figure 4-2c. Such small shifts in energy loss can arise due to experimental conditions and inaccuracies in the selected method for spectra processing (something which requires extreme care and is system dependent).[146] Therefore, further complementary techniques are employed to evaluate possible nanoparticle-single atom interactions.

X-ray absorption near edge structure (XANES) of the Fe K-edge (*ca.* 7120 eV) was employed to investigate the chemical state of the Fe in both the Fe-N-C support and γ-Fe_2O_3 nanoparticles, shown in Figure 4-2d. From our previous work, the Fe K-edge XANES spectra for the Fe-N-C

falls in between the FeO and Fe_3O_4 standards, closer to FeO, suggesting an Fe oxidation state close to Fe^{2+}.[143] In this work, the γ-Fe_2O_3, the XANES spectra matches the γ-Fe_2O_3 standard, confirming a Fe^{3+} oxidation state and formation of Fe nanoparticles in the γ-phase. Again, to evaluate possible γ-Fe_2O_3 and Fe-N_x interactions, the rising edge and pre-edge of the γ-Fe_2O_3 supported on Fe-N-C and XC72 were compared, however, no meaningful shifts in the energy were observed. Fourier transformed extended X-ray adsorption fine structure (FT-EXAFS) in Figure 4-2e looks at the local coordination of the Fe species compared to several standards. For the γ-Fe_2O_3, regardless of the catalyst support, two dominating peaks are observed. One at a low bond distance (*ca.* 1.5 Å), corresponding to the expected Fe-O (and Fe-N from the support) coordination and one a larger bond distance (*ca.* 2.6 Å), which corresponds to the Fe-Fe coordination in γ-Fe_2O_3.

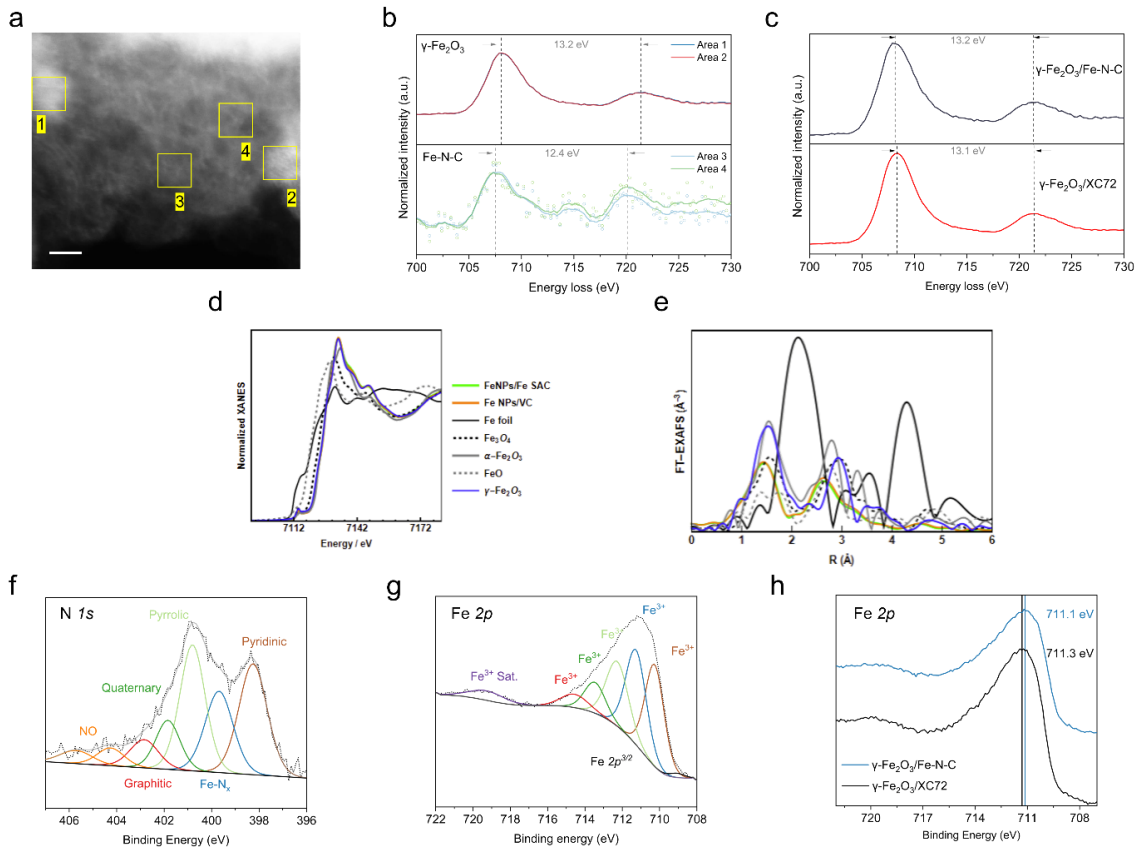

Figure 4-2. Local chemical and coordination environment of the γ-Fe_2O_3 nanoparticle catalysts. (a) AC-STEM image and EELS spectra locations on the γ-Fe_2O_3/Fe-N-C catalysts, scale bar is 2 nm. (b) EELS spectra of the Fe-$L_{3,2}$ edges of the γ-Fe_2O_3 nanoparticle (top) and atomically dispersed Fe-N_x sites (bottom). (c) EELS spectra comparing the energy loss of the Fe-$L_{3,2}$ edge of the γ-Fe_2O_3 supported on Fe-N-C or XC72. XAS data for the γ-Fe_2O_3 catalysts supported on both Fe-N-C and XC72 (d) XANES spectra and (e) EXAFS spectra with the corresponding references. (f) N 1s spectra and (g) Fe 2p XPS spectra. (h) Comparison of the Fe 2p XPS spectra for the γ-Fe_2O_3 catalyst supported on Fe-N-C or XC72.

To further investigate the chemical environment and coordination of the Fe species, XPS was performed. Figure 4-2f shows the N *1s* spectra for the γ-Fe_2O_3/Fe-N-C catalyst, confirming the Fe-N_x coordination, along with the pyridinic and pyrrolic N-moieties, characteristic of the Fe-N-C support (XPS for the Fe-N-C support is given in Appendix C.7). From the deconvoluted Fe *2p* spectra in Figure 4-2g, the oxidation state for the γ-Fe_2O_3 is Fe^{3+}, regardless of the support used, further corroborating the EELS and XANES analysis. Full XPS deconvolution of the C *1s*, O *1s*, N *1s* and Fe *2p* spectra for γ-Fe_2O_3/Fe-N-C and γ-Fe_2O_3/XC72 are shown in Appendix C.6 and Appendix C.8, respectively. Comparing the Fe *2p* spectra between the γ-Fe_2O_3 supported on Fe-N-C and XC72, Figure 4-2h, a binding energy shift of *ca.* 0.2 eV is observed, comparable to that of recent nanoparticle-single atom reports in the literature.[147–149] However, binding energy shifts during the processing and calibration (commonly to features in C *1s* spectrum), can easily induce binding energy shifts on the level of 0.2 eV, especially when the complex nature of the carbon is changing in the compared catalyst supports.[150]

It should be noted that as the popularity of nanoparticle/single atom support systems increases, extreme care must be taken in the interpretation of chemical state characterizations. Often nanoparticle/single atom support electronic interactions are being claimed exclusively through ambiguous shifts in the XPS spectra, and subsequently used as the foundation for computational models and reactions mechanisms, and attributed to any increased activity and stability. In this work, after rigorously investigating the electronic structure of the γ-Fe_2O_3 supported on atomically dispersed Fe-N-C and XC72 supports, with highly localized and more bulk techniques, no spectroscopically detected (EELS, XAS and XPS) interactions were observed.

Here we have synthesized and robustly characterized a γ-Fe_2O_3/Fe-N-C catalyst. While the possibility that electronic interactions between the γ-Fe_2O_3 nanoparticles and Fe-N_x sites exist

enhancing NO_3RR performance, has not been ruled out, such interactions were not detected spectroscopically. These interactions likely need to be probed through electrochemical processes, where the nanoparticle is active, while M-N_x site is inert, allowing changes in onset potentials or peak shapes to reflect interactions between the nanoparticle and M-N_x site (*ie.* ambient temperature CO stripping on Pt/M-N-C). Regardless, at a minimum, the γ-Fe_2O_3/Fe-N-C catalyst contains a multitude of highly active NO_3RR sites at both the nanoparticle and single atom scales, which are synergized, enhancing the NO_3RR performance.

4.4 Electrochemical NO_3RR Performance

Linear sweep voltammetry (LSV) was performed in 1M KOH + 0.16M KNO_3 electrolyte to assess the NO_3RR activity of the blank carbon paper, XC72 and Fe-N-C catalyst supports, and the γ-Fe_2O_3 nanoparticles supported on both XC72 and Fe-N-C as shown in Figure 4-3a. From the LSV there is a slight positive shift in the reaction onset potential (-0.59 V *vs.* RHE) in comparison to the blank carbon paper electrode, when using the XC72 carbon support, indicating even the metal-free carbon support has limited NO_3RR performance. Note in this work all potentials are reported versus the reversible hydrogen electrode, RHE. Employing the Fe-N-C catalyst support realizes a significant positive shift in the reaction onset potential (-0.34 V). Interestingly, despite having increased j_{NH3} at higher overpotentials in alkaline media, the Fe-N-C is observed to have a more positive onset reaction potential in neutral media (0.05M PBS), which could be due to its hyperactivity toward reducing the NO_2^- intermediate in the NO_3RR $2e^- + 6e^-$ transfer pathway, often formed at lower pH, which is suppressed in alkaline media.[110,143] From the LSV the addition of the γ-Fe_2O_3 nanoparticles further shifts the reaction onset potential even more positively to -0.14 V, regardless of either the XC72 or Fe-N-C support. However, as a more cathodic potential is applied, the current response for the γ-Fe_2O_3/Fe-N-C dominates due to

additional activity provided by the active Fe-N_x sites in the Fe-N-C support (and possible, interactions between the γ-Fe_2O_3 nanoparticles and atomically dispersed Fe-N_x sites, creating more favorable adsorption energies). To evaluate the catalytic performance of the supports towards the NO_3RR, chronoamperometry measurements were performed at potentials between -0.20 and -1.20 V as shown in Figure 4-3b. The XC72 support has negligible activity until -0.8 V and reaches a maximum FE_{NH3} of 55%. However, the active Fe-N-C support demonstrates superior activity, holding a FE_{NH3} of *ca.* 80% above -0.20 V, reaching a maximum of 90% at -0.40 V and a maximum $Yield_{NH3}$ of 2.9 $mmol_{NH3}$ hr^{-1} cm^{-2} (j_{NH3} = 620 mA/cm^2 at -1.20 V), surpassing other reported Fe-N-C catalysts for the NO_3RR.[63,64] Figure 4-3c shows that the addition of the γ-Fe_2O_3 nanoparticles enhances the FE_{NH3} (after -0.20 V) and significantly improves the $Yield_{NH3}$ over the potential range reaching a maximum of 6 $mmol_{NH3}$ hr^{-1} cm^{-2} (j_{NH3} = 1,265 mA/cm^2). Furthermore, γ-Fe_2O_3/Fe-N-C demonstrates increased FE_{NH3} and $Yield_{NH3}$ over the potential range compared to γ-Fe_2O_3/XC72. Interestingly, the γ-Fe_2O_3/Fe-N-C can maintain a FE_{NH3} of 90-95% over the potential range, highlighting the catalysts' potential independent NH_3 selectivity, resisting the parasitic HER even at highly cathodic potentials.

Having established the superior performance of the γ-Fe_2O_3/Fe-N-C catalyst, an γ-Fe_2O_3 loading study by adjusting the $Fe(acac)_3$ loading in the catalyst synthesis was performed to further enhance the NO_3RR activity. The TEM images in Figure 4-3d show the impact on the γ-Fe_2O_3 site density and gradual formation of agglomerates (with corresponding XRD patterns in Appendix C.2, suggesting no change in the crystalline structure or phase as precursor loading increases). With a standard 1x γ-Fe_2O_3 (*eg.* 1x$Fe(acac)_3$), a relatively low γ-Fe_2O_3 site density is observed with no agglomerates. The optimal loading appears to be at *ca.* 3x γ-Fe_2O_3 (corresponding to an Fe loading of 42 wt%, determined by TGA, Appendix C.9), in this range,

the γ-Fe_2O_3 site density significantly increases and at 3x γ-Fe_2O_3, slight agglomerate formation begins and by 4x γ-Fe_2O_3, a significant number of agglomerates have formed, reducing the catalytically active surface area. This optimal γ-Fe_2O_3 loading is directly observed in the NO_3RR performance and calculated ECSA (Appendix C.10). The LSV's in Figure 4-3e and chronoamperometry in Figure 3f highlight that 3x γ-Fe_2O_3 is the optimal loading, resulting in both the most positive onset reaction potential and highest current density over the entire potential range. Furthermore, 3x γ-Fe_2O_3/Fe-N-C demonstrates the highest FE_{NH3} maintaining *ca.* 95-100% from -0.40 to -1.20 V, with the highest $Yield_{NH3}$ at all potentials, reaching a maximum of 8.3 $mmol_{NH3}$ hr^{-1} cm^{-2} (j_{NH3} = 1,785 mA/cm^2). 4x γ-Fe_2O_3 suffers from significant agglomerate formation, resulting in a reduced j_{NH3} and FE_{NH3}. To further optimize the catalyst performance and increase j_{NH3}, the optimal catalyst loading on the carbon paper was investigated. The ink volume of 3x γ-Fe_2O_3/Fe-N-C drop cast on the carbon paper electrode was varied to achieve a final catalyst loading between 0.2 – 10.0 mg/cm^2. LSV was performed to screen the activity of different catalyst loadings as shown in Appendix C.11 a-c. Appendix C.11 a-c shows that as the catalyst loading increased from 0.2 – 1.0 mg/cm^2, the maximum current increases and the reaction onset potential shifts positively, with no improvement being observed between 0.5 – 1.0 mg/cm^2. However, after 1.0 mg/cm^2 the catalyst layer becomes too thick, resulting in reduced activity, with 10.0 mg/cm^2 giving the lowest performance. As an activity comparison, Appendix C.11 c shows the reaction onset potential and maximum current at -0.5 V (the maximum potential at which a cathodic energy efficiency of 30% is achieved assuming 100% FE_{NH3}). The optimal catalyst loading is determined to be 0.5 mg/cm^2, which results in an onset potential of *ca.* -0.13 V and a current density of 520 mA/cm^2 at -0.50 V. Therefore, the optimal catalyst is the

3x γ-Fe_2O_3/Fe-N-C with a loading of 0.5 mg/cm^2, and the electrochemical results discussed further in this manuscript utilize these conditions unless explicitly stated.

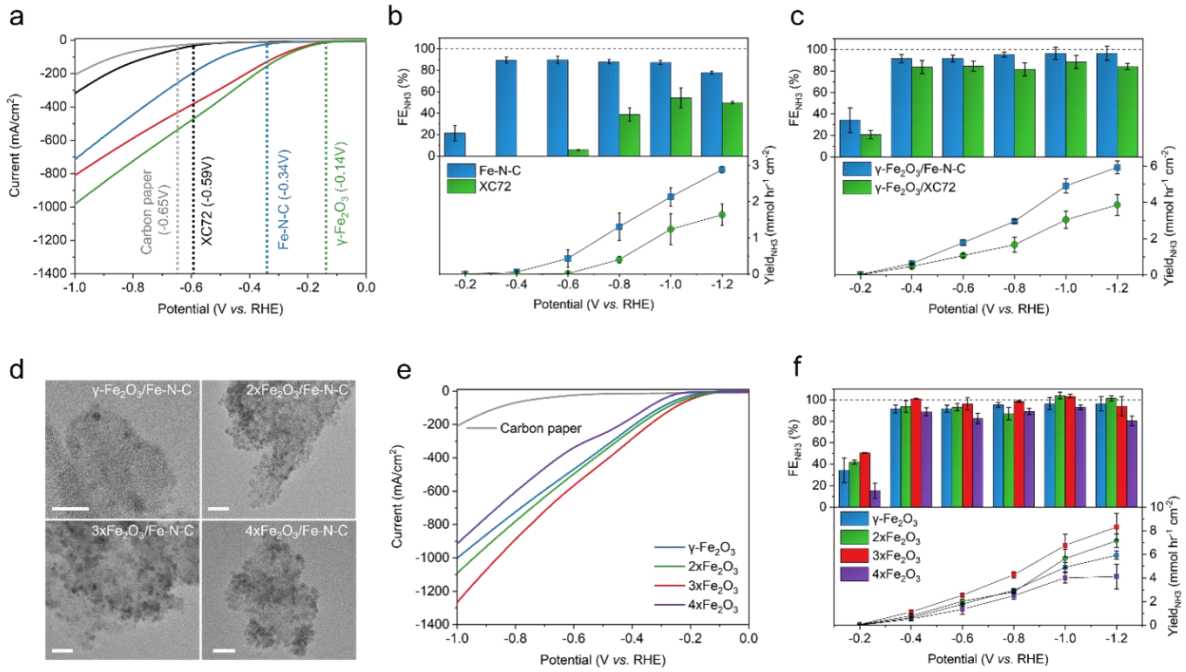

Figure 4-3. Electrochemical NO_3RR performance of γ-Fe_2O_3 based catalysts and supports in 1M KOH + 0.16M KNO_3 electrolyte. (a) Linear sweep voltammetry at a scan rate of 5 mV/s. Chronoamperometry measurements for 15 min at applied potentials from -0.20 to -1.20 V vs. RHE, the red line is γ-Fe_2O_3/XC72 and the green line is γ-Fe_2O_3/Fe-N-C. (b) comparing XC72 vs Fe-N-C catalyst supports, (c) comparing γ-Fe_2O_3/Fe-N-C vs. γ-Fe_2O_3/XC72. (d) TEM images of increasing γ-Fe_2O_3 loadings supported on Fe-N-C, the scale bar is 20 nm. Electrochemical characterization of γ-Fe_2O_3/Fe-N-C with varying γ-Fe_2O_3 loadings, (e) Linear sweep voltammetry at a scan rate of 5 mV/s and (f) Chronoamperometry measurements for 15 min at applied potentials from -0.20 to -1.20V *vs.* RHE with a catalyst loading on the carbon paper of 0.2 mg cm^{-2}. The corresponding chronoamperometry measurements and UV-Vis NH_3 quantification are given in Appendix C.12-17.

With the optimal γ-Fe_2O_3 loading and catalyst loading on the carbon electrode determined, chronoamperometric measurements were performed to evaluate the maximized performance of the 3x γ-Fe_2O_3/Fe-N-C catalyst in an H-cell configuration. Figure 4-4a, shows consistent FE_{NH3} above 95% over the entire -0.40 to -1.20 V potential range, again highlighting its potential independent nature towards NH_3 selectivity. A maximum Yield NH_3 of 9.2 mmol hr^{-1} cm^{-2} is achieved (j_{NH3} = 1,950 mA/cm^2) at *ca.* 100% FE_{NH3}. To confirm the N in the detected NH_3 originates from the nitrate feed and not from contamination or decomposition of the Fe-N-C support, a series of control studies were performed, Appendix C.18. First, constant potential electrolysis in 1M KOH electrolyte (without nitrate) was performed between -0.2 to -1.2 V, after which the electrolyte was sampled and no NH_3 was detected. Additionally, isotopic doping experiments utilizing 1M KOH with 0.16M $K^{15}NO_3$ electrolyte were performed at -1.0 V. ^1H NMR shows only the characteristic doublet of $^{15}NH_3$, with the FE_{NH3} and $Yield_{NH3}$ being consistent between the standard $^{14}NO_3$ (FE_{NH3} 100%, $Yield_{NH3}$ 6.6 mmol hr^{-1} cm^{-2}) and isotopically doped $^{15}NO_3$ (FE_{NH3} 101%, $Yield_{NH3}$ 6.2 mmol hr^{-1} cm^{-2}).

To compare the performance of our γ-3xFe_2O_3/Fe-N-C catalyst to the current NO_3RR literature, Figure 4-4b compares the cathodic energy efficiency, CEE (assuming no over potential for the anodic oxygen evolution reaction) *vs.* the j_{NH3}. The CEE (also called half-cell energy efficiency, is a metric commonly employed in the neighboring CO_2RR to evaluate the half-cell energy efficiency, which is related to half-cell voltage efficiency but incorporates the FE for a species[106,111,151–155]) a function of the FE_{NH3} and applied potential, while the j_{NH3} is a function of the FE_{NH3} and total current, enabling a comparison beyond just the FE_{NH3} or $Yield_{NH3}$, which vary significantly based on the applied potential and reaction conditions. Furthermore, larger

circles indicate higher concentrations of NO_3^-, often resulting in increased performance, while colors are used to designate acidic, neutral, or alkaline media. The contours in Figure 4-4b are composed of the product of (*CEE* x j_{NH3}), giving the effective current towards NH_3, where performance increases across contours, towards the top right corner. From Figure 4-4b, it is apparent that universally, the NO_3RR suffers from relatively low energy efficiencies (maximum 40%) at meaningful j_{NH3}, due to the thermodynamic reaction onset potential (0.69 V *vs.* RHE, pH=14), while more cathodic potentials (*ca.* -0.40 to -0.80 V) are typically required to achieve relevant j_{NH3}. The majority of the NO_3RR performances in the literature report limited j_{NH3}, less than 100 mA/cm^2, or utilize expensive PGM metals to realize higher j_{NH3}, hindering industrial relevance. The γ-3xFe_2O_3/Fe-N-C catalyst system (red circles) enables high current densities even at mildly reductive potentials, 297 mA/cm^2 with a cathodic energy efficiency of *ca.* 33%. The potential independent nature on the NH_3 selectivity, allows the γ-3xFe_2O_3/Fe-N-C system to be operated between -0.40 to -1.20 V at near 100% FE_{NH3}, giving ultra-high j_{NH3} from 297 to 1,950 mA/cm^2, significantly outperforming reported the current NO_3RR literature (see Appendix C.19 for a linear j_{NH3} scale, where the dominating performance of the γ-3xFe_2O_3/Fe-N-C catalyst is more dramatically seen). There is significant ambiguity in determining the optimal cathodic potential to yield both an acceptable energy efficiency and j_{NH3} and depends on many factors including catalyst cost, device costs, CAPEX and OPEX costs, levelized NH_3 costs as j_{NH3} increases and many others. To offer a semi-quantitative optimal tradeoff between energy efficiency and j_{NH3}, Figure 4-4c-e offers a basic economic analysis based off a recent work by Daiyan *et al.*[138] To construct meaningful contours, the levelized cost of NH_3 ($/kg) was determined by considering the CAPEX, OPEX and yield rates of NH_3. These inputs consider the increasing OPEX as the cathodic potential increase, therefore with decreasing energy efficiency,

while also accounting for increased production rates of NH_3. Three scenarios are considered, where the electricity cost varies from standard grid electricity at \$0.07/kWh (4c), idealized renewable energy from solar power at \$0.03/kWh (4d) and with a decreased CAPEX, resulting from reducing electrolyzer stack costs (4e). From these contour plots, it's readily observed that the most effective way to cross contours (until *ca.* 1 A/cm^2) is through increasing the j_{NH3}, rather than achieving low j_{NH3} with increasing energy efficiency. This behavior is supported by the experimental data showing that for both electricity price scenarios, the lowest levelized cost of NH_3 is achieved at the most cathodic potential of -1.2 V, where the ultrahigh current density reaching a j_{NH3} of -1.95 A/cm^2 (-1,950 mA/cm^2) is achieved, despite the lower energy efficiency. Interestingly, the impact of energy efficiency has a minor effect at small j_{NH3} and becomes more effective at higher j_{NH3}, albeit with quickly diminishing returns.

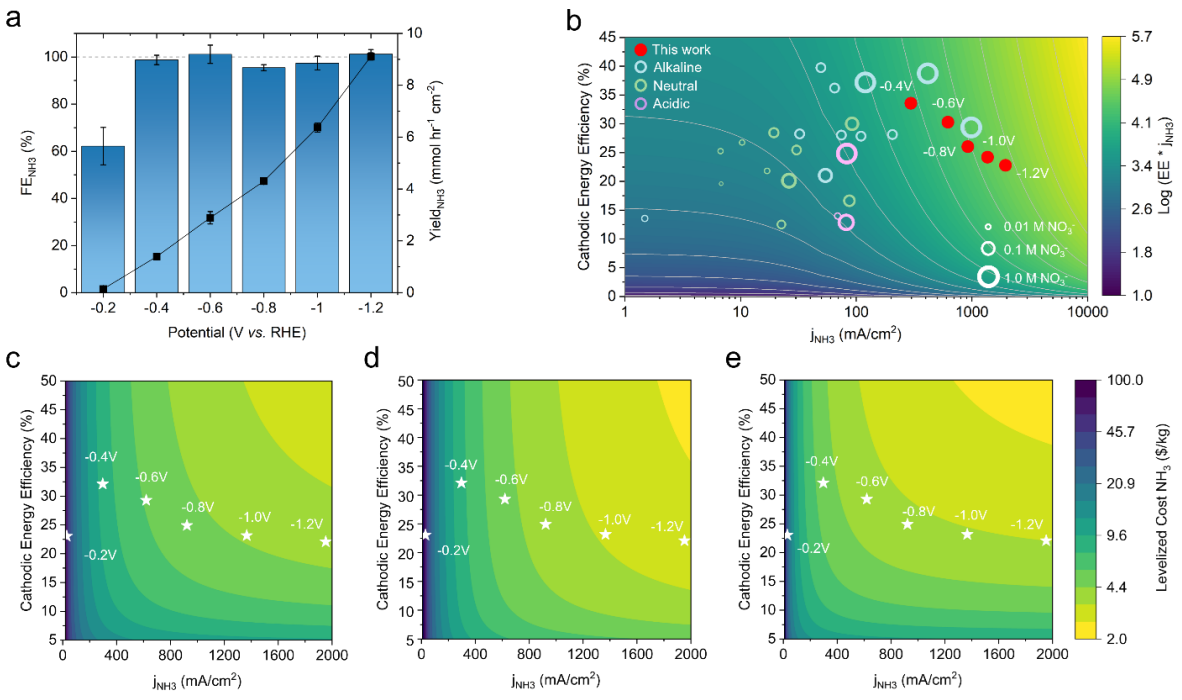

Figure 4-4. Electrochemical NO_3RR performance of the optimized γ-3xFe_2O_3/Fe-N-C catalyst with a 0.5 mg/cm^2 catalyst loading on the carbon paper electrode in a 1M KOH + 0.16M KNO_3

electrolyte. (a) Optimized FE_{NH3} and $Yield_{NH3}$ as a function of applied potential. (b) Comparison of NO_3RR performance in the current literature, evaluating the cathodic energy efficiency vs. j_{NH3}. Full details and references for each reported NO_3RR system are provided in Table 15. Contour plots evaluating the tradeoff of cathodic energy efficiency vs. j_{NH3} on the levelized cost of NH_3 for cases with (c) grid electricity price, (d) idealized cost of renewable energy, and (e) reduced electrolyzer stack cost. Where performance improves across contours towards the top right corner.

4.5 Fe Oxidation State During Activation and Electrolysis & Durability

Prior to the NO_3RR measurements, a pre-reductive activation step was performed and found to significantly improve the activity of the catalyst, as demonstrated through LSV (Appendix C.20). The pre-reduction is performed by applying a highly reductive potential of -1.5 V *vs.* RHE for 90 seconds. To investigate the chemical state of the now highly active catalyst, post-mortem XPS were performed on the catalyst coated electrode after the pre-reduction step. Following the pre-reduction activation step, the electrode was dried under N_2 and stored in a gas-tight vial purged with N_2 for immediate transport to the XPS. To address possible slight re-oxidation of the surface Fe during the transport of the electrode to the XPS, spectra were taken followed by quick (60 sec) Ar^+ ion surface etch and re-sampled. Figure 4-5a looks at the Fe *2p* spectra of the pristine γ-3xFe_2O_3/Fe-N-C catalyst and after the pre-reduction activation step and Figure 4-5b quantifies the Fe species from the corresponding deconvoluted Fe *2p* spectra. The pristine catalyst shows a single peak characteristic of Fe^{3+} (as seen previously in Figure 4-2h). In contrast, as expected, after the pre-reduction activation, the formation of a second peak at lower binding energy (*ca.* 707 eV), for Fe^0 is observed, along with a shift towards lower binding energy in the apex of the Fe *2p* peak, accompanied by peak broadening, indicating a composition

of Fe^{3+} (Fe_2O_3), Fe^{2+} (FeO / $Fe(OH)_2$) and Fe^0.[156] Interestingly, Figure 4-5c, which shows a 24-hour constant potential NO_3RR electrolysis at -1.0 V, with no significant change in the observed current density (or NH_3 selectivity). Post-mortem XPS measurements of the Fe *2p* spectra in Figure 4-5a demonstrate only slight further reduction of the Fe^{3+} (52%) species to more Fe^{2+} (37%) and Fe^0 (11%), where each spectrum has been deconvoluted and quantified in Appendix C.21-22. It has been previously observed and hypothesized that during a cathodic bias (-1V *vs.* RHE), Fe oxides supported on nitrogen doped carbon are not fully reduced to Fe^0, experiencing phase contractions and the insertion of H_2O in the lattice, maintaining a $Fe(OH)_2$ structure, despite being 560 mV lower than thermodynamically expected.[157] Additionally, it has been shown that nitrogen dopants can stabilize Fe^{2+} species, preventing the complete reduction to Fe^0 under a cathodic bias.[158] Therefore, its hypothesized that during the pre-reduction step, surface Fe^{3+} species are reduced to highly active Fe^{2+}/Fe^0, which are maintained as Fe hydroxide species (Fe^{2+}), throughout the NO_3RR electrolysis, maintaining the high NO_3RR activity (Figure 4-5c). Based on this analysis, Fe^{3+} sites while active for the NO_3RR are less active than Fe^{2+}/Fe^0 sites. Therefore, to maximize the NO_3RR performance, a pre-reduction step to reduce Fe^{3+} sites to Fe^{2+}/Fe^0 significantly enhances the activity. In agreement with prior studies demonstrating good activity of lower oxidation state Fe towards the NO_3RR.[159,160]

The ability to maintain the enhanced j_{NH3} over time is critical to the practical implementation of the active catalyst-active support system. A durability study was performed for 24 hours at -1.0 V. To circumvent ultrahigh NH_3 concentrations in the electrolyte and subsequent loss of NH_3 in the gas phase, the electrolysis was performed in eight 3-hour segments. Furthermore, the system was modified such that peristaltic pumps connected an external reservoir to the working chamber, enabling a working electrolyte volume of 250 mL with constant circulation. After a 3-

hour segment, the electrolyte was sampled and refreshed. Figure 4-5c shows the current density, FE_{NH3} and $Yield_{NH3}$ over the 24 hours. Figure 4-5c shows a stable current density of *ca.* -1.3 A/cm^2 at a FE_{NH3} between 90-100% and $Yield_{NH3}$ of *ca.* 6 mmol hr^{-1} cm^{-2}. Demonstrating the ability of the γ-3xFe_2O_3/Fe-N-C catalyst to preserve this ultrahigh NO_3RR performance at a near 100% FE_{NH3}, resisting the HER even at highly reductive potentials.

To investigate changes in the γ-Fe_2O_3 nanoparticle structure and atomically dispersed Fe sites, atomic resolution STEM was performed before and after electrolysis. The pristine catalyst from a catalyst ink, drop cast on the carbon paper electrode, and sonicated off for imaging without electrolysis. From Figure 4-5d, the expected spinel structure of the γ-Fe_2O_3 nanoparticle is observed simultaneously with the atomically dispersed Fe sites in the Fe-N-C. Figure 4-5e shows the post 24 hour electrolysis images of the γ-3xFe_2O_3/Fe-N-C catalyst. A slight coarsening in the γ-Fe_2O_3 nanoparticles is observed (with additional images in Appendix C.23), however, the minor physical change in the catalyst structure does not negatively alter the NO_3RR performance as observed in Figure 4-5c. Additionally, at higher magnification, the coexistence of γ-Fe_2O_3 nanoparticles and atomically dispersed Fe sites are maintained, confirming the durability of both the active γ-Fe_2O_3 nanoparticle catalyst and active Fe-N-C support at highly reductive potentials. For better visualization of the atomically dispersed sites, a Fe-N-C catalyst without γ-Fe_2O_3 nanoparticles after electrolysis was imaged in Appendix C.24. These results are supported by other studies in the literature showing a high stability of the Fe-N-C sites under reductive potentials.[63,64,161]

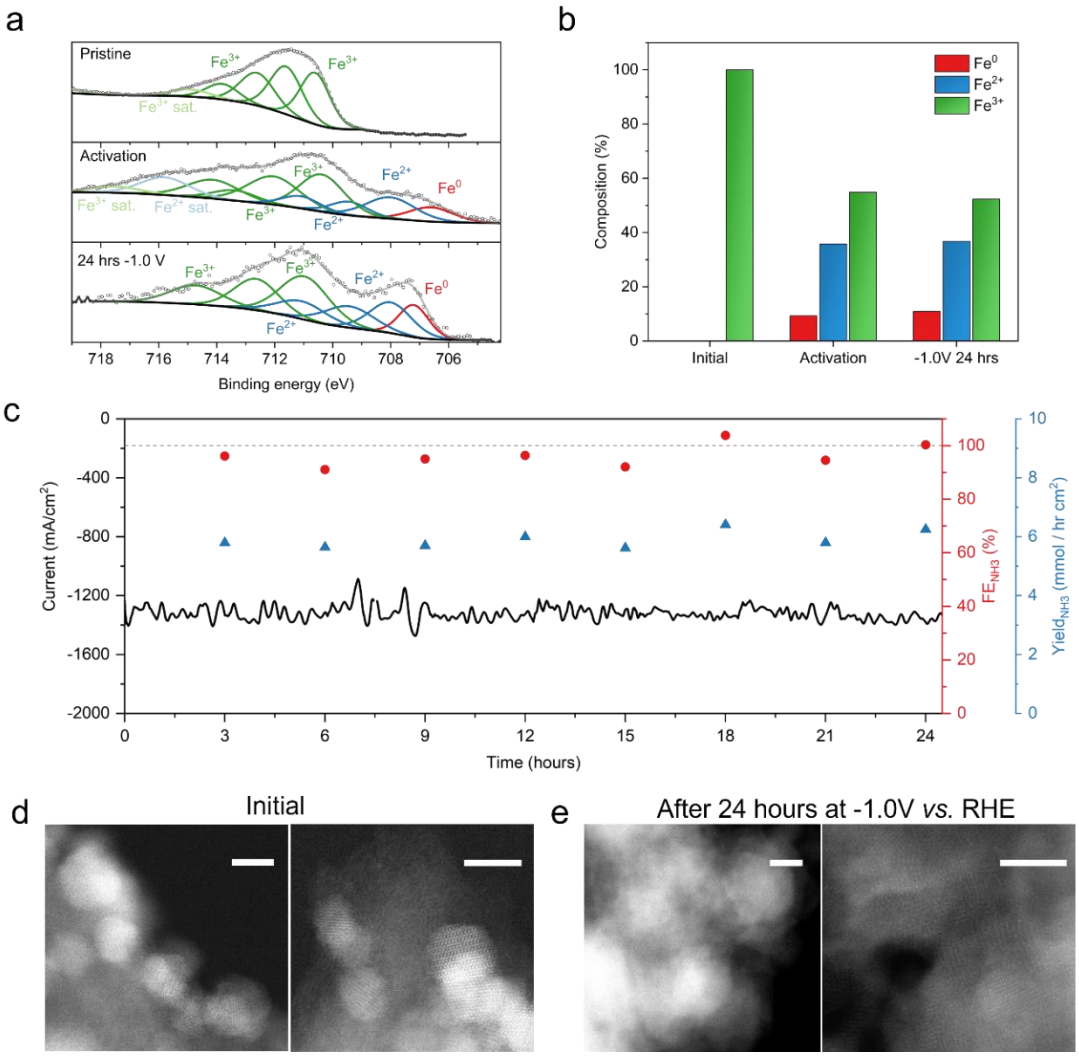

Figure 4-5. Investigation of the electronic state of Fe during the pre-reduction step and electrolysis and durability study of the γ-3xFe_2O_3/Fe-N-C. (a) Fe 2p XPS spectra of the initial catalyst, after the pre-reduction activation and after the 24-hour electrolysis. (b) Quantification of the Fe species from XPS. (c) 24-hour electrolysis at -1.0 V *vs.* RHE in 1M KOH + 0.16M KNO_3 electrolyte. AC-STEM to look at the stability of the γ-Fe_2O_3 nanoparticles and atomically dispersed Fe sites (d) the pristine catalyst (as a catalyst ink, drop cast on a carbon paper electrode) and (e) after the 24-hour electrolysis. All scale bars are 5 nm.

4.6 Conclusions

In summary, we have leveraged the high activity of Fe-based catalysts, both at the nanoparticle and single atom level, towards the selective conversion of NO_3^- to NH_3. We synergized both the nano and atomic scales to synthesize an active particle-active support catalyst system, γ-Fe_2O_3/Fe-N-C. The atomically dispersed Fe-N_x sites of the active Fe-N-C support, Fe-phase, and spinel structure of the γ-Fe_2O_3 nanoparticles was robustly confirmed employing atomic resolution STEM and EELS, XAS and XPS. The optimized γ-3xFe_2O_3/Fe-N-C catalyst demonstrated potential independent NO_3RR activity, even at highly reductive potentials, reaching a high $Yield_{NH3}$ of over 9 mmol hr^{-1} cm^{-2} at a FE_{NH3} of 100%, and a j_{NH3} up to 1.95 A/cm^2. Operando XANES and post-mortem XPS revealed that the reduction of Fe^{3+} surface sites to Fe^{2+}/Fe^0 during the pre-reduction activation step is critical in boosting the NO_3RR performance. A durability study at -1.0 V over 24 hours demonstrated the robustness of both the γ-Fe_2O_3 nanoparticles and single atom Fe-N_x sites, maintaining a current of 1.3 A/cm^2 and a FE_{NH3} of 91-100%. This work introduces a novel active particle-active support catalyst system for the NO_3RR by utilizing a plurality of active sites at both the nanoparticle and single atom scale, to significantly enhance NO_3RR activity, capable of realizing NO_3^- to NH_3 at industrially relevant current densities (1.95 A/cm^2).

Chapter 5

Conclusion and Outlook

5.1 Conclusion

This dissertation elucidated the complex nature of the NO_3RR over atomically dispersed M-N-C catalysts and demonstrated approaches to maximize NH_3 selectivity and perform the NO_3RR at industrial current densities. First, fundamental approaches revealed the almost universal cascade pathway in which NO_3^- is first reduced to NO_2^- and reabsorbed and further reduced to NH_3. Combining lessons from the fundamental studies, an active particle-active support system was synthesized to achieve the NO_3RR to NH_3 at ultrahigh current densities with high NH_3 selectivity. Additionally, although not discussed in this dissertation, several of the systems developed within this dissertation were tailored and applied to neighboring reactions such as the carbon dioxide reduction reaction (CO_2RR) and oxygen reduction reaction (ORR). For the CO_2RR, the bi-metallic FeMo-N-C catalyst was employed with varying ratios of Fe:Mo, such that Fe-N_x will selectively reduce CO_2 to CO, while Mo-N_x will reduce H^+ to H_2. By varying the ratios of Fe:Mo, the ratio of CO/H_2 in the product syngas could be tailored. This work was published in 2022 in ChemElectroChem.[114] The catalyst systems developed in Chapters 3 & 4 were utilized for the ORR. An active catalyst-active support system was developed where the highly ORR active Pt nanoparticles were supported on the library of M-N-C catalyst synthesized. Particle support interactions were demonstrated through CO stripping experiments and ORR performance was evaluated though rotating ring-disk electrode (RRDE) halfwave potentials and through durability studies. The manuscript for this work is in the process of being written and will be published soon.

Chapter 2 synthesized an atomically dispersed bi-metallic FeMo-N-C catalyst inspired from the biological enzymes (nitrogenase / nitrate reductase / nitrite reductase). By combining computational and experimental approaches, it was demonstrated that the NO_3RR could be partitioned into a $2e^- + 6e^-$ transfer cascade pathway and by utilizing a bi-metallic catalyst with catalytic cascade could be optimized. With Mo-N_x sites targeting the dissociation of NO_3^- into NO_2^- and Fe-N_x sites targeting further reduction of NO_2^- to NH_3 at 100% efficiency. By optimizing this catalytic cascade, a NO_3^- to NH_3 efficiency of 94% was obtained and maintained over 60 hours of electrolysis. Critically, a new observation was made demonstrating that Mo-N_x sites could cyclically generate NO_2^- by simultaneously absorbing two intermediates. This revealed that during the NO_3RR, certain atomically dispersed site is present in the oxo-form, where oxygen is bound as a fifth ligand (*O-Mo-N_x), an idea that was further explored in Chapter 3.

In Chapter 3, we noticed that for the NO3RR, atomically dispersed catalyst were largely underexplored, with only Cu, Fe and Mo (with Fe and Mo from our study) being explored experimentally. Over a handful of computational studies looked at developing a variety of activity descriptors for the activity of the NO3RR over a variety of M-Nx sites. However, these descriptors were all developed in the absence of any experimental support. We went beyond just Fe and Mo and synthesized a library of atomically dispersed M-N-C catalysts comprised of 3*d*, 4*d*, 5*d* and *f*-metal catalysts. The atomically dispersed nature and metal-nitrogen coordination was robustly investigated utilizing highly localized single atom EELS measurements combined with synchrotron based XAS measurements. Experimental activity descriptors were developed through NO_3RR and NO_2RR testing, while DFT was employed to develop a set of computational activity descriptors. These experimental and computation descriptors were correlated to reveal

the best set of physically relevant NO_3RR/NO_2RR descriptors over atomically dispersed M-N-C catalysts. Additionally, by correlating experiment and DFT approaches it was revealed that for highly oxyphilic sites, the oxo-form of the M-N-C catalyst must be considered to accurately predict the NO3RR activity. Finally, through isotopic intermediate doping experiments, the $2e^-$ + $6e^-$ transfer cascade pathway was revealed to be universal over M-N-C catalysts and metal-free N-C sites.

Finally, in Chapter 4 we sought to achieve the NO_3RR to NH_3 at industrially relevant current densities. To achieve this, an active particle-active support system was synthesized. Fe-N-C being chosen as the active support due to its NO_3RR activity and ability to selectively adsorb and reduce any generated NO_2^-. The γ-Fe_2O_3/Fe-N-C catalyst system was rigorously characterized to investigate any electronic interactions between the γ-Fe_2O_3 nanoparticles and atomically dispersed Fe-N_x sites. Highly localized single atom EELS measurements and more bulk measurements such as XAS and XPS revealed that when rigorously measured and when the spectra are fit carefully, no meaningful shifts in the energy loss and binding energy are observed. Note that this does not rule out electronic interaction between γ-Fe_2O_3 nanoparticles and Fe-N_x sites, however, they are just not detected with these techniques. To prove these interactions, it is likely necessary to use chemical adsorption/desorption methods. For example, in the ORR, the M-N_x sites do not participate in CO adsorption and subsequent stripping, such that changes in the onset potential for CO stripping can be attributed to changes in the Pt nanoparticles due to interaction with the supporting M-N_x sites. By optimizing the Fe nanoparticle loading in the catalyst and catalyst ink loading on the carbon paper electrode, an ultrahigh NO_3RR, NH_3 partial current density up to 1.95 A/cm^2 was achieved (-1.2 V *vs.* RHE). In the literature it remains ambiguous if it is more optimal to operate at low current density but slightly higher energy

efficiency, or high current density with lower energy efficiency. To account for this, an economic analysis was performed evaluating the levelized cost of NH_3 as a function of the NH_3 partial current density and energy efficiency. This analysis showed that initially the levelized cost of NH_3 is more effectively reduced by increasing the NH_3 partial current density (rather than increasing energy efficiency). However, after approximately 1 A/cm^2, to further reduce the levelized cost of NH_3, it is more effective to increase the energy efficiency (rather than further increase NH_3 partial current density). Durability measurements at -1.0 V *vs.* RHE over 24 hours, demonstrated the ability of the γ-Fe_2O_3/Fe-N-C to maintain a current of 1.3 A/cm^2 at near 100% FE_{NH3}. Critically, post-mortem XPS measurements revealed that during the pre-reduction activation step, the Fe^{3+} is reduced, forming a surface exposed layer of highly active Fe^{2+}/Fe^0, yielding the high NO_3RR observed. During the 24-hour electrolysis, no change in the current or product selectivity is observed, indicating that the Fe^{3+} species that are reduced to Fe^{2+}/Fe^0 are likely subsurface not directly participating in the reaction.

5.2 Outlook

The research in this dissertation has made contributions towards the understanding of atomically dispersed metal-nitrogen-carbon catalysts and the optimization of their synthesis when extending 3*d* metals beyond Fe and into 4*d*, 5*d* and *f*-metals. A deeper understanding of the NO_3RR mechanism was achieved displaying its complex nitrite intermediate cascade pathway and how to tailor active sites to target specific intermediates, resulting in highly efficient NO_3^- to NH_3 reduction. Progress was made in developing computational descriptors with experimental support for NO_3/NO_2RR activities over atomically dispersed M-N-C catalysts, such that a single descriptor can be used to accurately estimate the activity of new M-N_x sites. Finally, progress was made in pushing the limits of maximum achievable partial current density for NH_3 synthesis,

reaching almost 2 A/cm^2, by synthesizing an active catalyst-active support system, synergizing nanoparticles, and single atoms, with a potential independent behavior on the FE_{NH3}, allowing a highly reductive potential of -1.2 V *vs.* RHE to be applied, while maintaining 100% FE_{NH3}. While this dissertation has made significant progress in the electrochemical transformation of nitrogen species to NH_3 over atomically dispersed M-N-C catalysts, significant challenges remain and have been made clear throughout the simultaneous achievements and subsequent limitations of the results herein.

While the electrochemical reduction of NO_3^- to NH_3 is appealing as it is currently the only way to directly electrochemically reduce a nitrogen species to NH_3 (without mediated pathways), ultimately, the electrochemical reduction of N_2 to NH_3 is the holy grail. N_2RR would allow for air to be utilized as a reactant, avoiding the need for NO_3^- generation and significantly reducing energy costs (only $3e^-$ are needed per NH_3 molecule). However, currently the field of N_2RR is plagued with false positives, which were rampant in the literature from 2019-2021. In 2022, there was a break from rapid N_2RR publications as there was a focus on strict control of false positives in the literature. However, it seems this focus has shifted elsewhere and currently there is a rise in false N_2RR reports. The reason for this is quite apparent to the trained electrochemist. N_2RR is the electrochemical reaction with the lowest barriers to entry. No complex equipment is needed for product detection, only an inexpensive UV-Vis. In theory, one could use a glass beaker, potentiostat and a UV-Vis and enter the field of N_2RR. With this in mind, what is published in the field of N_2RR is a focus on “fancy” catalyst systems with equally “fancy” catalyst characterization, employing synchrotron techniques and high-quality imaging. The focus is purely on the physical system, with very low electrochemical rigor. The “fancy” system is enough to carry the manuscript into decent journals. Subsequently, the authors of these false

positive papers are invited to write reviews on the state of N_2RR, which subsequently highlight a host of false N_2RR papers. In order to further the field of N_2RR, we must focus not purely on the material but rather focus on the quality of the electrochemistry. If the paper is being submitted as a N_2RR study, then strict focus should be placed on the electrochemical results. Based on the experience gained during this dissertation, N_2RR needs to be advanced through system developments. We have tested over 20 catalysts (nanoparticles, alloys, hydrides, nitrides, 15 types of M-N-C's, bi-metallic M-N-C's, metal free N-C and Janus particles) with no proof of successful N_2 activation, when tested rigorously (even under increased temperatures). Therefore, to progress N_2RR, it is essential to make system changes, such as increasing the probability of interaction events between N_2 and the surface of the catalyst. Given the ultralow solubility of N_2, the use of gas diffusion electrodes or pressurized systems is required, however, the employment of these systems comes with a whole new set of challenges in maintaining experimental rigor. One should approach N_2RR with the mindset of doing everything they can to not find NH_3, in that way if NH_3 is detected it is likely not the result of non-rigorous experiments. Lastly, I believe in order to publish N_2RR results, given the thousands of false positive reports in the literature, it is imperative to have the results verified by a second independent party.

While the N_2RR is the holy grail of electrochemical nitrogen transformation to NH_3, the NO_3RR provides a number of benefits. Firstly, it allows for ultrahigh current densities to be achieved due to the high solubility of NO_3^- in aqueous electrolytes. Second, independent of the N_2RR, the NO_3RR can be used to reduce waste NO_3^- for water remediation purposes, as a complementary pathway for NH_3 synthesis. Additionally, as will be discussed in the following paragraph, NO_3^- enables a pathway for electrochemical carbon-nitrogen bond formation. Rapid progress has been made with the NO_3RR, where currently several studies can reach high efficiencies for NH_3,

upwards of 90%. However, the current issue is achieving high current densities for NH_3 at high efficiencies, and doing so at low over potentials. In this dissertation we achieved two of these targets, reaching very high current densities and Faradaic efficiencies, however at low energy efficiency (high over potential). In alkaline conditions the thermodynamic potential for the reaction is positive 0.69 V *vs.* RHE, however, typical studies are more reductive than -0.5 V *vs.* RHE to reach low/moderate current densities. The future challenges are in activating NO_3^- at positive potentials, closer to the thermodynamic potential. The most logical pathway to do this is to partition the reaction into two segments are demonstrated in this dissertation, where one active site is selective to the dissociation of NO_3^- into NO_2^- (perhaps through chemical dissociation), then the more active NO_2^- can be reduced at potentials closer to the thermodynamic potential. Examples of this are beginning to be seen in the literature, however, they fail to reach the other objectives (high current density / high FE_{NH3}) at a similar level to the examples in this dissertation. Another challenge with the NO_3RR is decoupling it from the HB process. Currently a large amount of NO_3^- would need to be sourced from wastewater runoffs which originate from fertilizers generated from the HB process. To make the NO_3RR decoupled from the HB process, low energy plasma methods need to be utilized to oxidize inert N_2 into reactive NO_x species, which can easily be reduced to NH_3. Currently, state of the art plasma systems coupled with NO_x reduction can reach energy costs on the level of Li-mediated pathways (Li mediated 12.4 – 25.5 MJ/mol_{NH3}, Plasma assisted 2.1 – 19.1 MJ/mol_{NH3}), making it a promising pathway for decentralized, carbon neutral NH_3 synthesis.[134,162,163] Lastly, the next steps to progressing the NO_3RR are to implement the utilization of flow cells / electrolyzers such that high current densities can be achieved with large scale systems, while maintaining a high selectivity and low cell potential.

NO_3^- offers a pathway for electrochemical synthesis of more complex molecules. NH_3 is typically used as a feedstock chemical in the synthesis of carbon-nitrogen containing molecules, many of which are used in the synthesis of pharmaceutical compounds. Over 80% of produced NH_3 undergoes a second high energy thermal reaction with CO_2 to synthesize urea $(CO(NH_2))_2$ which is then used for fertilizer production. With NO_3^- being highly soluble and reactive, while CO_2/CO is a gaseous species, the use of gas diffusion electrodes readily enables a triple phase boundary where NO_3^- and CO_2/CO can readily meet at the solid surface of the catalyst, allowing the opportunity for C-N bonds to be formed. The electrochemical formation of C-N bonds enables the direct synthesis of urea, methylamine, or other complex, high value products. The difficulty in C-N bond formation is in product selectivity. Often less than 10% current efficiency goes to C-N products, with the remainder going to NH_3 or CO. It was shown in an earlier Nature Chemistry paper than Cu foil could reduce NH_3 and CO into amides.[164] This approach could be utilized such that a Cu based support is used (foam, mesh etc…) to reduce any produced NH_3 into other C-N products to increase overall C-N current efficiency.

Several challenges lie in deciphering the complex reaction mechanism from NO_3^- to urea, being a very complex 16 e^- transfer process when starting with NO_3^-. Currently, the reaction mechanism is largely a black box, in which the carbon-nitrogen formation step varies from study to study and is predicted based on DFT approaches, lacking experimental support. To utilize atomically dispersed M-N-C catalysts, questions regarding the formation of desorbable intermediates needs to be investigated. If no such intermediates exist in the reaction pathway, then the M-N_x site must either simultaneously adsorb a NO_3^- and CO_2/CO or a M-N_x must work with a neighboring metal free N-moiety to achieve C-N bond formation. Additionally, if the M-N_x site can accommodate the simultaneous adsorption of several molecules (such as the Mo-N_x

sites in Chapter 2) and is selective to both carbon and nitrogen species, this could provide a C-N bond forming active site. An alternative approach is bi-metallic M-N-C catalysts, however, the difficulty here is creating coordination bi-metallic sites (M_2-N_6) rather than independent M_1-N_4 and M_2-N_4 sites, where only NO_3^- to NH_3 or CO_2 to CO will take place. Further progress in the synthesis of coordinated bi-metallic sites is needed, along with more rigorous characterization techniques to verify that such sites exist with statistical relevance. An alternative to this is the employment of highly ordered alloys, in which M_1-M_2 sites are periodically ordered and within distances such that adsorbed carbon and nitrogen species could interact.

Given the field of C-N bond formation is so new, studies must be performed to help elucidate reaction pathways. This could involve employing alternative N-sources to monitor C-N products and bond formations. One example would be the use of hydrazine (N_2H_4) as a highly reactive N-source. Currently this has not been explored and could provide information regarding the C-N bond formation pathway as the N_2H_4 molecule is very close to the desired $CO(NH_2)_2$ urea product, or following a different reaction pathway, products such as monomethylhydrazine (used in rocket fuel) could be synthesized electrochemically (which has been achieved in our recent preliminary studies).

One additional study that could be directly investigated utilized the materials systems developed in this thesis involve the evaluation of nitrite stripping for the quantification of atomically disperse sites beyond Fe-N-C. The quantification and utilization factor of atomically dispersed sites in M-N-C catalysts is of great significance and developing active catalysts. Typical M-N_x quantification techniques involve Mossbauer spectroscopy, cryo-CO adsorption, and nitrite stripping. These techniques were classically developed and applied to Fe-N-C catalysts. As new atomically dispersed materials sets are developed (mono and multi-metallics) for applications

beyond the ORR, such as CO_2RR, or nitrogen transformations, the number of active elements significantly expands (beyond Fe and Co for the ORR). Therefore, the ability to quantify the number of active M-Nx sites and active site utilization is of great importance. The set of M-N-C materials developed in this dissertation (mono and bi-metallic) could serve as a screening platform for the feasibility of extending nitrite stripping from Fe-N-C into other metals and multi-metallics. Although nitrite stripping tends to lead to underestimation of active site quantification, it could serve as a valuable baseline, especially considering that popular reactions such as NO_xRR typically take place in the aqueous phase.

Over the past few years there have been significant advances towards the decarbonization of ammonia synthesis through electrochemical nitrogen transformations. This dissertation constitutes a part of this progress, while presenting and highlighting several exciting new challenges that must be explored and tackled as we make progress towards a greener future.

References

(1) Chen, J. G.; Crooks, R. M.; Seefeldt, L. C.; Bren, K. L.; Bullock, R. M.; Darensbourg, M. Y.; Holland, P. L.; Hoffman, B.; Janik, M. J.; Jones, A. K.; Kanatzidis, M. G.; King, P.; Lancaster, K. M.; Lymar, S. V.; Pfromm, P.; Schneider, W. F.; Schrock, R. R. Beyond Fossil Fuel–Driven Nitrogen Transformations. *Science (80-.).* **2018**, *360* (6391). https://doi.org/10.1126/science.aar6611.

(2) Worrel, E.; Phylipsen, D.; Einstein, D.; Martin, N. Energy Use and Energy Intensity of the U.S. Chemical Industry. *Lawrence Berkeley Natl. Lab.* **2000**, *LBNL-44314* (April), 34.

(3) MacFarlane, D. R.; Cherepanov, P. V.; Choi, J.; Suryanto, B. H. R.; Hodgetts, R. Y.; Bakker, J. M.; Ferrero Vallana, F. M.; Simonov, A. N. A Roadmap to the Ammonia Economy. *Joule* **2020**, *0* (0). https://doi.org/10.1016/j.joule.2020.04.004.

(4) Beik, P. H. CHAPTER V. INDUSTRY. In *A Judgment of the Old Régime*; Columbia University Press, 1944; pp 138–160. https://doi.org/10.7312/beik90104-006.

(5) Foster, S. L.; Bakovic, S. I. P.; Duda, R. D.; Maheshwari, S.; Milton, R. D.; Minteer, S. D.; Janik, M. J.; Renner, J. N.; Greenlee, L. F. Catalysts for Nitrogen Reduction to Ammonia. *Nat. Catal.* **2018**, *1* (7), 490–500. https://doi.org/10.1038/s41929-018-0092-7.

(6) Skúlason, E.; Bligaard, T.; Gudmundsdóttir, S.; Studt, F.; Rossmeisl, J.; Abild-Pedersen, F.; Vegge, T.; Jónsson, H.; Nørskov, J. K. A Theoretical Evaluation of Possible Transition Metal Electro-Catalysts for N2 Reduction. *Phys. Chem. Chem. Phys.* **2012**, *14* (3), 1235–1245. https://doi.org/10.1039/c1cp22271f.

(7) Singh, A. R.; Rohr, B. A.; Statt, M. J.; Schwalbe, J. A.; Cargnello, M.; Nørskov, J. K.

Strategies toward Selective Electrochemical Ammonia Synthesis. *ACS Catal.* **2019**, *9* (9), 8316–8324. https://doi.org/10.1021/acscatal.9b02245.

(8) Liu, L.; Corma, A. Metal Catalysts for Heterogeneous Catalysis: From Single Atoms to Nanoclusters and Nanoparticles. *Chem. Rev.* **2018**, *118* (10), 4981–5079. https://doi.org/10.1021/acs.chemrev.7b00776.

(9) Asset, T.; Atanassov, P. Iron-Nitrogen-Carbon Catalysts for Proton Exchange Membrane Fuel Cells. *Joule* **2020**, *4* (1), 33–44. https://doi.org/10.1016/j.joule.2019.12.002.

(10) Kumar, K.; Asset, T.; Li, X.; Liu, Y.; Yan, X.; Chen, Y.; Mermoux, M.; Pan, X.; Atanassov, P.; Maillard, F.; Dubau, L. Fe–N–C Electrocatalysts' Durability: Effects of Single Atoms' Mobility and Clustering. *ACS Catal.* **2021**, *11* (2), 484–494. https://doi.org/10.1021/acscatal.0c04625.

(11) Delafontaine, L.; Asset, T.; Atanassov, P. Metal–Nitrogen–Carbon Electrocatalysts for CO_2 Reduction towards Syngas Generation. *ChemSusChem* **2020**, *13* (7), 1688–1698. https://doi.org/10.1002/cssc.201903281.

(12) Xu, H.; Rebollar, D.; He, H.; Chong, L.; Liu, Y.; Liu, C.; Sun, C.-J.; Li, T.; Muntean, J. V; Winans, R. E.; Liu, D.-J.; Xu, T. Highly Selective Electrocatalytic CO 2 Reduction to Ethanol by Metallic Clusters Dynamically Formed from Atomically Dispersed Copper. *Nat. Energy* **2020**, *5* (8), 623–632. https://doi.org/10.1038/s41560-020-0666-x.

(13) Cai, Y.; Fu, J.; Zhou, Y.; Chang, Y.; Min, Q.; Zhu, J.-J.; Lin, Y.; Zhu, W. Insights on Forming N,O-Coordinated Cu Single-Atom Catalysts for Electrochemical Reduction CO2 to Methane. *Nat. Commun.* **2021**, *12* (1), 586. https://doi.org/10.1038/s41467-020-20769-x.

(14) Kim, D. H.; Ringe, S.; Kim, H.; Kim, S.; Kim, B.; Bae, G.; Oh, H.-S.; Jaouen, F.; Kim, W.; Kim, H.; Choi, C. H. Selective Electrochemical Reduction of Nitric Oxide to Hydroxylamine by Atomically Dispersed Iron Catalyst. *Nat. Commun.* **2021**, *12* (1), 1856. https://doi.org/10.1038/s41467-021-22147-7.

(15) Chen, J. G.; Crooks, R. M.; Seefeldt, L. C.; Bren, K. L.; Bullock, R. M.; Darensbourg, M. Y.; Holland, P. L.; Hoffman, B.; Janik, M. J.; Jones, A. K.; Kanatzidis, M. G.; King, P.; Lancaster, K. M.; Lymar, S. V; Pfromm, P.; Schneider, W. F.; Schrock, R. R. Beyond Fossil Fuel-Driven Nitrogen Transformations. *Science* **2018**, *360* (6391), eaar6611. https://doi.org/10.1126/science.aar6611.

(16) Andersen, S. Z.; Čolić, V.; Yang, S.; Schwalbe, J. A.; Nielander, A. C.; McEnaney, J. M.; Enemark-Rasmussen, K.; Baker, J. G.; Singh, A. R.; Rohr, B. A.; Statt, M. J.; Blair, S. J.; Mezzavilla, S.; Kibsgaard, J.; Vesborg, P. C. K.; Cargnello, M.; Bent, S. F.; Jaramillo, T. F.; Stephens, I. E. L.; Nørskov, J. K.; Chorkendorff, I. A Rigorous Electrochemical Ammonia Synthesis Protocol with Quantitative Isotope Measurements. *Nature* **2019**, *570* (7762), 504–508. https://doi.org/10.1038/s41586-019-1260-x.

(17) Greenlee, L. F.; Renner, J. N.; Foster, S. L. The Use of Controls for Consistent and Accurate Measurements of Electrocatalytic Ammonia Synthesis from Dinitrogen. *ACS Catal.* **2018**, *8* (9), 7820–7827. https://doi.org/10.1021/acscatal.8b02120.

(18) Suryanto, B. H. R.; Du, H.-L.; Wang, D.; Chen, J.; Simonov, A. N.; MacFarlane, D. R. Challenges and Prospects in the Catalysis of Electroreduction of Nitrogen to Ammonia. *Nat. Catal.* **2019**, *2* (4), 290–296. https://doi.org/10.1038/s41929-019-0252-4.

(19) Tang, C.; Qiao, S.-Z. How to Explore Ambient Electrocatalytic Nitrogen Reduction

Reliably and Insightfully. *Chem. Soc. Rev.* **2019**, *48* (12), 3166–3180. https://doi.org/10.1039/C9CS00280D.

(20) Chen, Y.; Liu, H.; Ha, N.; Licht, S.; Gu, S.; Li, W. Revealing Nitrogen-Containing Species in Commercial Catalysts Used for Ammonia Electrosynthesis. *Nat. Catal.* **2020**, *3* (12), 1055–1061. https://doi.org/10.1038/s41929-020-00527-4.

(21) Choi, J.; Suryanto, B. H. R.; Wang, D.; Du, H. L.; Hodgetts, R. Y.; Ferrero Vallana, F. M.; MacFarlane, D. R.; Simonov, A. N. Identification and Elimination of False Positives in Electrochemical Nitrogen Reduction Studies. *Nat. Commun.* **2020**, *11* (1), 1–10. https://doi.org/10.1038/s41467-020-19130-z.

(22) Kibsgaard, J.; Nørskov, J. K.; Chorkendorff, I. The Difficulty of Proving Electrochemical Ammonia Synthesis. *ACS Energy Lett.* **2019**, *4* (12), 2986–2988. https://doi.org/10.1021/acsenergylett.9b02286.

(23) Bao, Y.; Nagasawa, K.; Kuroda, Y.; Mitsushima, S. Current Measurement and Electrochemical Characterization of Gas Evolution Reactions on a Rotating Ring-Disk Electrode. *Electrocatalysis* **2020**, *11* (3), 301–308. https://doi.org/10.1007/s12678-020-00589-9.

(24) Dabundo, R.; Lehmann, M. F.; Treibergs, L.; Tobias, C. R.; Altabet, M. A.; Moisander, P. H.; Granger, J. The Contamination of Commercial 15N2 Gas Stocks with 15N–Labeled Nitrate and Ammonium and Consequences for Nitrogen Fixation Measurements. *PLoS One* **2014**, *9* (10), e110335. https://doi.org/10.1371/journal.pone.0110335.

(25) Licht, S.; Cui, B.; Wang, B.; Li, F.-F.; Lau, J.; Liu, S. (Retracted) Ammonia Synthesis. Ammonia Synthesis by N_2 and Steam Electrolysis in Molten Hydroxide Suspensions of

Nanoscale Fe_2O_3. *Science* **2014**, *345* (6197), 637–640. https://doi.org/10.1126/science.1254234.

(26) Zou, H.; Rong, W.; Wei, S.; Ji, Y.; Duan, L. Regulating Kinetics and Thermodynamics of Electrochemical Nitrogen Reduction with Metal Single-Atom Catalysts in a Pressurized Electrolyser. *Proc. Natl. Acad. Sci. U. S. A.* **2020**, *117* (47), 29462–29468. https://doi.org/10.1073/pnas.2015108117.

(27) Zou, H.; Rong, W.; Wei, S.; Ji, Y.; Duan, L. Regulating Kinetics and Thermodynamics of Electrochemical Nitrogen Reduction with Metal Single-Atom Catalysts in a Pressurized Electrolyser. *Proc. Natl. Acad. Sci.* **2020**, 202015108. https://doi.org/10.1073/pnas.2015108117.

(28) Thorgersen, M. P.; Lancaster, W. A.; Vaccaro, B. J.; Poole, F. L.; Rocha, A. M.; Mehlhorn, T.; Pettenato, A.; Ray, J.; Waters, R. J.; Melnyk, R. A.; Chakraborty, R.; Hazen, T. C.; Deutschbauer, A. M.; Arkin, A. P.; Adams, M. W. W. Molybdenum Availability Is Key to Nitrate Removal in Contaminated Groundwater Environments. *Appl. Environ. Microbiol.* **2015**, *81* (15), 4976–4983. https://doi.org/10.1128/AEM.00917-15.

(29) van Langevelde, P. H.; Katsounaros, I.; Koper, M. T. M. Electrocatalytic Nitrate Reduction for Sustainable Ammonia Production. *Joule* **2021**, *5* (2), 290–294. https://doi.org/10.1016/j.joule.2020.12.025.

(30) Society, R. Ammonia: Zero-Carbon Fertiliser, Fuel and Energy Store. The Royal Society London, UK 2020.

(31) Ren, Y.; Yu, C.; Tan, X.; Huang, H.; Wei, Q.; Qiu, J. Strategies to Suppress Hydrogen

Evolution for Highly Selective Electrocatalytic Nitrogen Reduction: Challenges and Perspectives. *Energy Environ. Sci.* **2021**, *14* (3), 1176–1193. https://doi.org/10.1039/d0ee03596c.

(32) Giddey, S.; Badwal, S. P. S.; Kulkarni, A. Review of Electrochemical Ammonia Production Technologies and Materials. *Int. J. Hydrogen Energy* **2013**, *38* (34), 14576–14594. https://doi.org/10.1016/j.ijhydene.2013.09.054.

(33) Grinberg Dana, A.; Elishav, O.; Bardow, A.; Shter, G. E.; Grader, G. S. Nitrogen-Based Fuels: A Power-to-Fuel-to-Power Analysis. *Angew. Chemie - Int. Ed.* **2016**, *55* (31), 8798–8805. https://doi.org/10.1002/anie.201510618.

(34) Smith, C.; Hill, A. K.; Torrente-Murciano, L. Current and Future Role of Haber-Bosch Ammonia in a Carbon-Free Energy Landscape. *Energy Environ. Sci.* **2020**, *13* (2), 331–344. https://doi.org/10.1039/c9ee02873k.

(35) Klerke, A.; Christensen, C. H.; Nørskov, J. K.; Vegge, T. Ammonia for Hydrogen Storage: Challenges and Opportunities. *J. Mater. Chem.* **2008**, *18* (20), 2304–2310. https://doi.org/10.1039/b720020j.

(36) Norskov, J.; Chen, J. Sustainable Ammonia Synthesis. *Report, DOE Roundtable* **2016**, 1–23.

(37) Tang, C.; Qiao, S. Z. How to Explore Ambient Electrocatalytic Nitrogen Reduction Reliably and Insightfully. *Chem. Soc. Rev.* **2019**, *48* (12), 3166–3180. https://doi.org/10.1039/c9cs00280d.

(38) MacFarlane, D. R.; Cherepanov, P. V.; Choi, J.; Suryanto, B. H. R.; Hodgetts, R. Y.;

Bakker, J. M.; Ferrero Vallana, F. M.; Simonov, A. N. A Roadmap to the Ammonia Economy. *Joule* **2020**, *4* (6), 1186–1205. https://doi.org/10.1016/j.joule.2020.04.004.

(39) Suryanto, B. H. R.; Du, H. L.; Wang, D.; Chen, J.; Simonov, A. N.; MacFarlane, D. R. Challenges and Prospects in the Catalysis of Electroreduction of Nitrogen to Ammonia. *Nat. Catal.* **2019**, *2* (4), 290–296. https://doi.org/10.1038/s41929-019-0252-4.

(40) Katsounaros, I.; Dortsiou, M.; Kyriacou, G. Electrochemical Reduction of Nitrate and Nitrite in Simulated Liquid Nuclear Wastes. *J. Hazard. Mater.* **2009**, *171* (1–3), 323–327. https://doi.org/10.1016/j.jhazmat.2009.06.005.

(41) Chauhan, R.; Srivastava, V. C. Electrochemical Denitrification of Highly Contaminated Actual Nitrate Wastewater by Ti/RuO2 Anode and Iron Cathode. *Chem. Eng. J.* **2020**, *386* (3), 122065. https://doi.org/10.1016/j.cej.2019.122065.

(42) Nguyen, T. T. P.; Do, B. K. D.; Bui, N. N.; Pham, M. A.; Nguyen, T. V. Selectiveness of Copper and Polypyrrole Modified Copper Electrodes for Nitrate Electroreduction: A Comparative Study and Application in Ground Water. *ECS Trans.* **2013**, *53* (16), 41–52. https://doi.org/10.1149/05316.0041ecst.

(43) Xu, D.; Li, Y.; Yin, L.; Ji, Y.; Niu, J.; Yu, Y. Electrochemical Removal of Nitrate in Industrial Wastewater. *Front. Environ. Sci. Eng.* **2018**, *12* (1), 1–14. https://doi.org/10.1007/s11783-018-1033-z.

(44) Mook, W. T.; Chakrabarti, M. H.; Aroua, M. K.; Khan, G. M. A.; Ali, B. S.; Islam, M. S.; Abu Hassan, M. A. Removal of Total Ammonia Nitrogen (TAN), Nitrate and Total Organic Carbon (TOC) from Aquaculture Wastewater Using Electrochemical Technology: A Review. *Desalination* **2012**, *285*, 1–13.

https://doi.org/10.1016/j.desal.2011.09.029.

(45) Su, L.; Han, D.; Zhu, G.; Xu, H.; Luo, W.; Wang, L.; Jiang, W.; Dong, A.; Yang, J. Tailoring the Assembly of Iron Nanoparticles in Carbon Microspheres toward High-Performance Electrocatalytic Denitrification. *Nano Lett.* **2019**, *19* (8), 5423–5430. https://doi.org/10.1021/acs.nanolett.9b01925.

(46) Liu, H.; Park, J.; Chen, Y.; Qiu, Y.; Cheng, Y.; Srivastava, K.; Gu, S.; Shanks, B. H.; Roling, L. T.; Li, W. Electrocatalytic Nitrate Reduction on Oxide-Derived Silver with Tunable Selectivity to Nitrite and Ammonia. *ACS Catal.* **2021**, *2* (3), 8431–8442. https://doi.org/10.1021/acscatal.1c01525.

(47) Martínez, J.; Ortiz, A.; Ortiz, I. State-of-the-Art and Perspectives of the Catalytic and Electrocatalytic Reduction of Aqueous Nitrates. *Appl. Catal. B Environ.* **2017**, *207*, 42–59. https://doi.org/10.1016/j.apcatb.2017.02.016.

(48) De Groot, M. T.; Koper, M. T. M. The Influence of Nitrate Concentration and Acidity on the Electrocatalytic Reduction of Nitrate on Platinum. *J. Electroanal. Chem.* **2004**, *562* (1), 81–94. https://doi.org/10.1016/j.jelechem.2003.08.011.

(49) D'Arino, M.; Pinna, F.; Strukul, G. Nitrate and Nitrite Hydrogenation with Pd and Pt/SnO2 Catalysts: The Effect of the Support Porosity and the Role of Carbon Dioxide in the Control of Selectivity. *Appl. Catal. B Environ.* **2004**, *53* (3), 161–168. https://doi.org/10.1016/j.apcatb.2004.05.015.

(50) Pintar, A.; Batista, J.; Muševič, I. Palladium-Copper and Palladium-Tin Catalysts in the Liquid Phase Nitrate Hydrogenation in a Batch-Recycle Reactor. *Appl. Catal. B Environ.* **2004**, *52* (1), 49–60. https://doi.org/10.1016/j.apcatb.2004.02.019.

(51) Huo, X.; Van Hoomissen, D. J.; Liu, J.; Vyas, S.; Strathmann, T. J. Hydrogenation of Aqueous Nitrate and Nitrite with Ruthenium Catalysts. *Appl. Catal. B Environ.* **2017**, *211*, 188–198. https://doi.org/10.1016/j.apcatb.2017.04.045.

(52) Pizarro, A. H.; Molina, C. B.; Rodriguez, J. J.; Epron, F. Catalytic Reduction of Nitrate and Nitrite with Mono- and Bimetallic Catalysts Supported on Pillared Clays. *J. Environ. Chem. Eng.* **2015**, *3* (4), 2777–2785. https://doi.org/10.1016/j.jece.2015.09.026.

(53) Yamauchi, M.; Abe, R.; Tsukuda, T.; Kato, K.; Takata, M. Highly Selective Ammonia Synthesis from Nitrate with Photocatalytically Generated Hydrogen on CuPd/TiO2. *J. Am. Chem. Soc.* **2011**, *133* (5), 1150–1152. https://doi.org/10.1021/ja106285p.

(54) Pérez-Gallent, E.; Figueiredo, M. C.; Katsounaros, I.; Koper, M. T. M. Electrocatalytic Reduction of Nitrate on Copper Single Crystals in Acidic and Alkaline Solutions. *Electrochim. Acta* **2017**, *227*, 77–84. https://doi.org/10.1016/j.electacta.2016.12.147.

(55) Yang, J.; Sebastian, P.; Duca, M.; Hoogenboom, T.; Koper, M. T. M. PH Dependence of the Electroreduction of Nitrate on Rh and Pt Polycrystalline Electrodes. *Chem. Commun.* **2014**, *50* (17), 2148–2151. https://doi.org/10.1039/c3cc49224a.

(56) Calle-Vallejo, F.; Huang, M.; Henry, J. B.; Koper, M. T. M.; Bandarenka, A. S. Theoretical Design and Experimental Implementation of Ag/Au Electrodes for the Electrochemical Reduction of Nitrate. *Phys. Chem. Chem. Phys.* **2013**, *15* (9), 3196–3202. https://doi.org/10.1039/c2cp44620k.

(57) Wang, Z.; Richards, D.; Singh, N. Recent Discoveries in the Reaction Mechanism of Heterogeneous Electrocatalytic Nitrate Reduction. *Catal. Sci. Technol.* **2021**, *11* (3), 705–725. https://doi.org/10.1039/D0CY02025G.

(58) Zeng, Y.; Priest, C.; Wang, G.; Wu, G. Restoring the Nitrogen Cycle by Electrochemical Reduction of Nitrate: Progress and Prospects. *Small Methods* **2020**, *4* (12), 1–28. https://doi.org/10.1002/smtd.202000672.

(59) Duca, M.; Koper, M. T. M. Powering Denitrification: The Perspectives of Electrocatalytic Nitrate Reduction. *Energy Environ. Sci.* **2012**, *5* (12), 9726–9742. https://doi.org/10.1039/c2ee23062c.

(60) Casey-Stevens, C. A.; Ásmundsson, H.; Skúlason, E.; Garden, A. L. A Density Functional Theory Study of the Mechanism and Onset Potentials for the Major Products of NO Electroreduction on Transition Metal Catalysts. *Appl. Surf. Sci.* **2021**, *552* (February), 149063. https://doi.org/10.1016/j.apsusc.2021.149063.

(61) Chun, H. J.; Apaja, V.; Clayborne, A.; Honkala, K.; Greeley, J. Atomistic Insights into Nitrogen-Cycle Electrochemistry: A Combined DFT and Kinetic Monte Carlo Analysis of NO Electrochemical Reduction on Pt(100). *ACS Catal.* **2017**, *7* (6), 3869–3882. https://doi.org/10.1021/acscatal.7b00547.

(62) Wan, H.; Bagger, A.; Rossmeisl, J. Electrochemical Nitric Oxide Reduction on Metal Surfaces. *Angew. Chemie* **2021**, *133* (40), 22137–22143. https://doi.org/10.1002/ange.202108575.

(63) Wu, Z.; Karamad, M.; Yong, X.; Huang, Q.; Cullen, D. A.; Zhu, P.; Xia, C.; Xiao, Q.; Shakouri, M.; Chen, F.; Kim, J. Y.; Xia, Y.; Heck, K.; Hu, Y.; Wong, M. S.; Li, Q.; Gates, I.; Siahrostami, S.; Wang, H. Electrochemical Ammonia Synthesis via Nitrate Reduction on Fe Single Atom Catalyst. *Nat. Commun.* **2021**, *12* (1), 2870. https://doi.org/10.1038/s41467-021-23115-x.

(64) Li, P.; Jin, Z.; Fang, Z.; Yu, G. A Single-Site Iron Catalyst with Preoccupied Active Centers That Achieves Selective Ammonia Electrosynthesis from Nitrate. *Energy Environ. Sci.* **2021**, *14* (6), 3522–3531. https://doi.org/10.1039/D1EE00545F.

(65) Niu, H.; Zhang, Z.; Wang, X.; Wan, X.; Shao, C.; Guo, Y. Theoretical Insights into the Mechanism of Selective Nitrate-to-Ammonia Electroreduction on Single-Atom Catalysts. *Adv. Funct. Mater.* **2020**, *2008533* (3), 1–8. https://doi.org/10.1002/adfm.202008533.

(66) Wu, J.; Yu, Y. X. Highly Selective Electroreduction of Nitrate to Ammonia on a Ru-Doped Tetragonal Co2P Monolayer with Low-Limiting Overpotential. *Catal. Sci. Technol.* **2021**, *11* (21), 7160–7170. https://doi.org/10.1039/d1cy01217g.

(67) Wu, J.; Li, J. H.; Yu, Y. X. Theoretical Exploration of Electrochemical Nitrate Reduction Reaction Activities on Transition-Metal-Doped h-BP. *J. Phys. Chem. Lett.* **2021**, *12* (16), 3968–3975. https://doi.org/10.1021/acs.jpclett.1c00855.

(68) Milton, R. D.; Minteer, S. D. Enzymatic Bioelectrosynthetic Ammonia Production: Recent Electrochemistry of Nitrogenase, Nitrate Reductase, and Nitrite Reductase. *Chempluschem* **2017**, *82* (4), 513–521. https://doi.org/10.1002/cplu.201600442.

(69) Stein, L. Y.; Klotz, M. G. The Nitrogen Cycle. *Curr. Biol.* **2016**, *26* (3), R94–R98. https://doi.org/10.1016/j.cub.2015.12.021.

(70) Asset, T.; Garcia, S. T.; Herrera, S.; Andersen, N.; Chen, Y.; Peterson, E. J.; Matanovic, I.; Artyushkova, K.; Lee, J.; Minteer, S. D.; Dai, S.; Pan, X.; Chavan, K.; Calabrese Barton, S.; Atanassov, P. Investigating the Nature of the Active Sites for the CO2 Reduction Reaction on Carbon-Based Electrocatalysts. *ACS Catal.* **2019**, *9* (9), 7668–7678. https://doi.org/10.1021/acscatal.9b01513.

(71) Serov, A.; Artyushkova, K.; Andersen, N. I.; Stariha, S.; Atanassov, P. Original Mechanochemical Synthesis of Non-Platinum Group Metals Oxygen Reduction Reaction Catalysts Assisted by Sacrificial Support Method. *Electrochim. Acta* **2015**, *179*, 154–160. https://doi.org/10.1016/j.electacta.2015.02.108.

(72) Zhu, D.; Zhang, L.; Ruther, R. E.; Hamers, R. J. Photo-Illuminated Diamond as a Solid-State Source of Solvated Electrons in Water for Nitrogen Reduction. *Nat. Mater.* **2013**, *12* (9), 836–841. https://doi.org/10.1038/nmat3696.

(73) Blöchl, P. E.; Jepsen, O.; Andersen, O. K. Improved Tetrahedron. *Phys. Rev. B* **1994**, *49* (23), 16223–16233.

(74) Joubert, D. From Ultrasoft Pseudopotentials to the Projector Augmented-Wave Method. *Phys. Rev. B - Condens. Matter Mater. Phys.* **1999**, *59* (3), 1758–1775. https://doi.org/10.1103/PhysRevB.59.1758.

(75) Kresse, G.; Hafner, J. Ab Initio Molecular Dynamics for Liquid Metals. *Phys. Rev. B* **1993**, *47* (1), 558–561. https://doi.org/10.1103/PhysRevB.47.558.

(76) Kresse, G.; Hafner, J. Ab Initio Molecular-Dynamics Simulation of the Liquid-Metalamorphous- Semiconductor Transition in Germanium. *Phys. Rev. B* **1994**, *49* (20), 14251–14269. https://doi.org/10.1103/PhysRevB.49.14251.

(77) Kresse, G.; Furthmüller, J. Efficiency of Ab-Initio Total Energy Calculations for Metals and Semiconductors Using a Plane-Wave Basis Set. *Comput. Mater. Sci.* **1996**, *6* (1), 15–50. https://doi.org/10.1016/0927-0256(96)00008-0.

(78) Dion, M.; Rydberg, H.; Schröder, E.; Langreth, D. C.; Lundqvist, B. I. Van Der Waals

Density Functional for General Geometries. *Phys. Rev. Lett.* **2004**, *92* (24), 22–25. https://doi.org/10.1103/PhysRevLett.92.246401.

(79) Klime, J.; Bowler, D. R.; Michaelides, A. Van Der Waals Density Functionals Applied to Solids. *Phys. Rev. B - Condens. Matter Mater. Phys.* **2011**, *83* (19), 1–13. https://doi.org/10.1103/PhysRevB.83.195131.

(80) Román-Pérez, G.; Soler, J. M. Efficient Implementation of a van Der Waals Density Functional: Application to Double-Wall Carbon Nanotubes. *Phys. Rev. Lett.* **2009**, *103* (9), 1–4. https://doi.org/10.1103/PhysRevLett.103.096102.

(81) Klimeš, J.; Bowler, D. R.; Michaelides, A. Chemical Accuracy for the van Der Waals Density Functional. *J. Phys. Condens. Matter* **2010**, *22* (2), 022201. https://doi.org/10.1088/0953-8984/22/2/022201.

(82) Kattel, S.; Atanassov, P.; Kiefer, B. A Density Functional Theory Study of Oxygen Reduction Reaction on Non-PGM Fe-Nx-C Electrocatalysts. *Phys. Chem. Chem. Phys.* **2014**, *16* (27), 13800–13806. https://doi.org/10.1039/c4cp01634c.

(83) Matanovic, I.; Artyushkova, K.; Atanassov, P. Understanding PGM-Free Catalysts by Linking Density Functional Theory Calculations and Structural Analysis: Perspectives and Challenges. *Curr. Opin. Electrochem.* **2018**, *9*, 137–144. https://doi.org/10.1016/j.coelec.2018.03.009.

(84) Artyushkova, K.; Matanovic, I.; Halevi, B.; Atanassov, P. Oxygen Binding to Active Sites of Fe-N-C ORR Electrocatalysts Observed by Ambient-Pressure XPS. *J. Phys. Chem. C* **2017**, *121* (5), 2836–2843. https://doi.org/10.1021/acs.jpcc.6b11721.

(85) Li, J.; Sougrati, M. T.; Zitolo, A.; Ablett, J. M.; Oğuz, I. C.; Mineva, T.; Matanovic, I.; Atanassov, P.; Huang, Y.; Zenyuk, I.; Di Cicco, A.; Kumar, K.; Dubau, L.; Maillard, F.; Dražić, G.; Jaouen, F. Identification of Durable and Non-Durable FeNx Sites in Fe–N–C Materials for Proton Exchange Membrane Fuel Cells. *Nat. Catal.* **2021**, *4* (1), 10–19. https://doi.org/10.1038/s41929-020-00545-2.

(86) Wang, Y.; Shao, M. Theoretical Screening of Transition Metal–N 4 -Doped Graphene for Electroreduction of Nitrate. *ACS Catal.* **2022**, 5407–5415. https://doi.org/10.1021/acscatal.2c00307.

(87) Chen, G. F.; Yuan, Y.; Jiang, H.; Ren, S. Y.; Ding, L. X.; Ma, L.; Wu, T.; Lu, J.; Wang, H. Electrochemical Reduction of Nitrate to Ammonia via Direct Eight-Electron Transfer Using a Copper–Molecular Solid Catalyst. *Nat. Energy* **2020**, *5* (8), 605–613. https://doi.org/10.1038/s41560-020-0654-1.

(88) McEnaney, J. M.; Blair, S. J.; Nielander, A. C.; Schwalbe, J. A.; Koshy, D. M.; Cargnello, M.; Jaramillo, T. F. Electrolyte Engineering for Efficient Electrochemical Nitrate Reduction to Ammonia on a Titanium Electrode. *ACS Sustain. Chem. Eng.* **2020**, *8* (7), 2672–2681. https://doi.org/10.1021/acssuschemeng.9b05983.

(89) Serov, A.; Artyushkova, K.; Atanassov, P. Fe-N-C Oxygen Reduction Fuel Cell Catalyst Derived from Carbendazim: Synthesis, Structure, and Reactivity. *Adv. Energy Mater.* **2014**, *4* (10), 1301735. https://doi.org/10.1002/aenm.201301735.

(90) Serov, A.; Artyushkova, K.; Niangar, E.; Wang, C.; Dale, N.; Jaouen, F.; Sougrati, M. T.; Jia, Q.; Mukerjee, S.; Atanassov, P. Nano-Structured Non-Platinum Catalysts for Automotive Fuel Cell Application. *Nano Energy* **2015**, *16*, 293–300.

https://doi.org/10.1016/j.nanoen.2015.07.002.

(91) Primbs, M.; Sun, Y.; Roy, A.; Malko, D.; Mehmood, A.; Sougrati, M. T.; Blanchard, P. Y.; Granozzi, G.; Kosmala, T.; Daniel, G.; Atanassov, P.; Sharman, J.; Durante, C.; Kucernak, A.; Jones, D.; Jaouen, F.; Strasser, P. Establishing Reactivity Descriptors for Platinum Group Metal (PGM)-Free Fe-N-C Catalysts for PEM Fuel Cells. *Energy Environ. Sci.* **2020**, *13* (8), 2480–2500. https://doi.org/10.1039/d0ee01013h.

(92) Chen, Y.; Huang, Y.; Xu, M.; Asset, T.; Yan, X.; Artyushkova, K.; Kodali, M.; Murphy, E.; Ly, A.; Pan, X.; Zenyuk, I. V.; Atanassov, P. Catalysts by Pyrolysis: Direct Observation of Transformations during Re-Pyrolysis of Transition Metal-Nitrogen-Carbon Materials Leading to State-of-the-Art Platinum Group Metal-Free Electrocatalyst. *Mater. Today* **2022**, *53* (March), 58–70. https://doi.org/10.1016/j.mattod.2022.01.016.

(93) Tylus, U.; Jia, Q.; Strickland, K.; Ramaswamy, N.; Serov, A.; Atanassov, P.; Mukerjee, S. Elucidating Oxygen Reduction Active Sites in Pyrolyzed Metal-Nitrogen Coordinated Non-Precious-Metal Electrocatalyst Systems. *J. Phys. Chem. C* **2014**, *118* (17), 8999–9008. https://doi.org/10.1021/jp500781v.

(94) Schiffer, Z. J.; Manthiram, K. Electrification and Decarbonization of the Chemical Industry. *Joule* **2017**, *1* (1), 10–14. https://doi.org/10.1016/j.joule.2017.07.008.

(95) van Geem, K. M.; Galvita, V. V.; Marin, G. B. Making Chemicals with Electricity. *Science (80-.).* **2019**, *364* (6442), 734–735. https://doi.org/10.1126/science.aax5179.

(96) Iriawan, H.; Andersen, S. Z.; Zhang, X.; Comer, B. M.; Barrio, J.; Chen, P.; Medford, A. J.; Stephens, I. E. L.; Chorkendorff, I.; Shao-Horn, Y. Methods for Nitrogen Activation by Reduction and Oxidation. *Nat. Rev. Methods Prim.* **2021**, *1* (1).

https://doi.org/10.1038/s43586-021-00053-y.

(97) Wang, Y.; Wang, C.; Li, M.; Yu, Y.; Zhang, B. Nitrate Electroreduction: Mechanism Insight,: In Situ Characterization, Performance Evaluation, and Challenges. *Chem. Soc. Rev.* **2021**, *50* (12), 6720–6733. https://doi.org/10.1039/d1cs00116g.

(98) Ko, B. H.; Hasa, B.; Shin, H.; Zhao, Y.; Jiao, F. Electrochemical Reduction of Gaseous Nitrogen Oxides on Transition Metals at Ambient Conditions. *J. Am. Chem. Soc.* **2022**, *144* (3), 1258–1266. https://doi.org/10.1021/jacs.1c10535.

(99) Long, J.; Chen, S.; Zhang, Y.; Guo, C.; Fu, X.; Deng, D.; Xiao, J. Direct Electrochemical Ammonia Synthesis from Nitric Oxide. *Angew. Chemie - Int. Ed.* **2020**, *59* (24), 9711–9718. https://doi.org/10.1002/anie.202002337.

(100) Sun, J.; Alam, D.; Daiyan, R.; Masood, H.; Zhang, T.; Zhou, R.; Cullen, P. J.; Lovell, E. C.; Jalili, A.; Amal, R. A Hybrid Plasma Electrocatalytic Process for Sustainable Ammonia Production. *Energy Environ. Sci.* **2021**, *14* (2), 865–872. https://doi.org/10.1039/d0ee03769a.

(101) Muzammil, I.; Kim, Y. N.; Kang, H.; Dinh, D. K.; Choi, S.; Jung, C.; Song, Y. H.; Kim, E.; Kim, J. M.; Lee, D. H. Plasma Catalyst-Integrated System for Ammonia Production from H2O and N2at Atmospheric Pressure. *ACS Energy Lett.* **2021**, *6*, 3004–3010. https://doi.org/10.1021/acsenergylett.1c01497.

(102) Ornes, S. Green Ammonia Could Produce Climate-Friendly Ways to Store Energy and Fertilize Farms. *Proc. Natl. Acad. Sci. U. S. A.* **2021**, *118* (49), 1–4. https://doi.org/10.1073/pnas.2119584118.

(103) Wang, Z.; Richards, D.; Singh, N. Recent Discoveries in the Reaction Mechanism of Heterogeneous Electrocatalytic Nitrate Reduction. *Catal. Sci. Technol.* **2021**, *11* (3), 705–725. https://doi.org/10.1039/d0cy02025g.

(104) Liu, J. X.; Richards, D.; Singh, N.; Goldsmith, B. R. Activity and Selectivity Trends in Electrocatalytic Nitrate Reduction on Transition Metals. *ACS Catal.* **2019**, *9* (8), 7052–7064. https://doi.org/10.1021/acscatal.9b02179.

(105) zhao, jingxiang; Yang, M.; Wang, Z.; Jiao, D.; Li, G.; Cai, Q. Tuning Single Metal Atoms Anchored on Graphidyne for Highly Efficient and Selective Nitrate Electroreduction to Ammonia: A Computational Study. *SSRN Electron. J.* **2022**, 1–34. https://doi.org/10.2139/ssrn.4008068.

(106) Wang, Y.; Xu, A.; Wang, Z.; Huang, L.; Li, J.; Li, F.; Wicks, J.; Luo, M.; Nam, D. H.; Tan, C. S.; Ding, Y.; Wu, J.; Lum, Y.; Dinh, C. T.; Sinton, D.; Zheng, G.; Sargent, E. H. Enhanced Nitrate-to-Ammonia Activity on Copper-Nickel Alloys via Tuning of Intermediate Adsorption. *J. Am. Chem. Soc.* **2020**, *142* (12), 5702–5708. https://doi.org/10.1021/jacs.9b13347.

(107) Seraj, S.; Kunal, P.; Li, H.; Henkelman, G.; Humphrey, S. M.; Werth, C. J. PdAu Alloy Nanoparticle Catalysts: Effective Candidates for Nitrite Reduction in Water. *ACS Catal.* **2017**, *7* (5), 3268–3276. https://doi.org/10.1021/acscatal.6b03647.

(108) Wang, Z.; Young, S. D.; Goldsmith, B. R.; Singh, N. Increasing Electrocatalytic Nitrate Reduction Activity by Controlling Adsorption through PtRu Alloying. *J. Catal.* **2021**, *395* (3), 143–154. https://doi.org/10.1016/j.jcat.2020.12.031.

(109) Wang, J.; Feng, T.; Chen, J.; Ramalingam, V.; Li, Z.; Kabtamu, D. M.; He, J. H.; Fang, X.

Electrocatalytic Nitrate/Nitrite Reduction to Ammonia Synthesis Using Metal Nanocatalysts and Bio-Inspired Metalloenzymes. *Nano Energy* **2021**, *86* (March), 106088. https://doi.org/10.1016/j.nanoen.2021.106088.

(110) Murphy, E.; Liu, Y.; Matanovic, I.; Guo, S.; Tieu, P.; Huang, Y.; Ly, A.; Das, S.; Zenyuk, I.; Pan, X.; Spoerke, E.; Atanassov, P. Highly Durable and Selective Fe- and Mo-Based Atomically Dispersed Electrocatalysts for Nitrate Reduction to Ammonia via Distinct and Synergized NO 2 – Pathways . *ACS Catal.* **2022**, *12* (11), 6651–6662. https://doi.org/10.1021/acscatal.2c01367.

(111) He, W.; Zhang, J.; Dieckhöfer, S.; Varhade, S.; Brix, A. C.; Lielpetere, A.; Seisel, S.; Junqueira, J. R. C.; Schuhmann, W. Splicing the Active Phases of Copper/Cobalt-Based Catalysts Achieves High-Rate Tandem Electroreduction of Nitrate to Ammonia. *Nat. Commun.* **2022**, *13* (1), 1–13. https://doi.org/10.1038/s41467-022-28728-4.

(112) Carvalho, O. Q.; Marks, R.; Nguyen, H. K. K.; Vitale-Sullivan, M. E.; Martinez, S. C.; Árnadóttir, L.; Stoerzinger, K. A. Role of Electronic Structure on Nitrate Reduction to Ammonium: A Periodic Journey. *J. Am. Chem. Soc.* **2022**, *144* (32), 14809–14818. https://doi.org/10.1021/jacs.2c05673.

(113) Ju, W.; Bagger, A.; Hao, G. P.; Varela, A. S.; Sinev, I.; Bon, V.; Roldan Cuenya, B.; Kaskel, S.; Rossmeisl, J.; Strasser, P. Understanding Activity and Selectivity of Metal-Nitrogen-Doped Carbon Catalysts for Electrochemical Reduction of CO2. *Nat. Commun.* **2017**, *8* (1), 1–9. https://doi.org/10.1038/s41467-017-01035-z.

(114) Delafontaine, L.; Murphy, E.; Guo, S.; Liu, Y. Synergistic Electrocatalytic Syngas Production from Carbon Dioxide by Bi-Metallic Atomically Dispersed Catalysts. **2022**,

202200647. https://doi.org/10.1002/celc.202200647.

(115) Rojas-Carbonell, S.; Santoro, C.; Serov, A.; Atanassov, P. Transition Metal-Nitrogen-Carbon Catalysts for Oxygen Reduction Reaction in Neutral Electrolyte. *Electrochem. commun.* **2017**, *75*, 38–42. https://doi.org/10.1016/j.elecom.2016.12.011.

(116) Jin, Z.; Li, P.; Meng, Y.; Fang, Z.; Xiao, D.; Yu, G. Understanding the Inter-Site Distance Effect in Single-Atom Catalysts for Oxygen Electroreduction. *Nat. Catal.* **2021**, *4* (7), 615–622. https://doi.org/10.1038/s41929-021-00650-w.

(117) Artyushkova, K.; Serov, A.; Rojas-Carbonell, S.; Atanassov, P. Chemistry of Multitudinous Active Sites for Oxygen Reduction Reaction in Transition Metal-Nitrogen-Carbon Electrocatalysts. *J. Phys. Chem. C* **2015**, *119* (46), 25917–25928. https://doi.org/10.1021/acs.jpcc.5b07653.

(118) Artyushkova, K. Misconceptions in Interpretation of Nitrogen Chemistry from X-Ray Photoelectron Spectra. *J. Vac. Sci. Technol. A* **2020**, *38* (3), 031002. https://doi.org/10.1116/1.5135923.

(119) Ravel, B.; Newville, M. ATHENA, ARTEMIS, HEPHAESTUS: Data Analysis for X-Ray Absorption Spectroscopy Using IFEFFIT. *J. Synchrotron Radiat.* **2005**, *12* (4), 537–541. https://doi.org/10.1107/S0909049505012719.

(120) Ankudinov, A.; Conradson, S.; Mustre de Leon, J. Relativistic XANES Calculations of Pu Hydrates. *Phys. Rev. B - Condens. Matter Mater. Phys.* **1998**, *57* (13), 7518–7525. https://doi.org/10.1103/PhysRevB.57.7518.

(121) Hossen, M. M.; Artyushkova, K.; Atanassov, P.; Serov, A. Synthesis and Characterization

of High Performing Fe-N-C Catalyst for Oxygen Reduction Reaction (ORR) in Alkaline Exchange Membrane Fuel Cells. *J. Power Sources* **2018**, *375*, 214–221. https://doi.org/10.1016/j.jpowsour.2017.08.036.

(122) Serov, A.; Artyushkova, K.; Andersen, N. I.; Stariha, S.; Atanassov, P. Original Mechanochemical Synthesis of Non-Platinum Group Metals Oxygen Reduction Reaction Catalysts Assisted by Sacrificial Support Method. *Electrochim. Acta* **2015**, *179*, 154–160. https://doi.org/10.1016/j.electacta.2015.02.108.

(123) Li, J.; Zhan, G.; Yang, J.; Quan, F.; Mao, C.; Liu, Y.; Wang, B.; Lei, F.; Li, L.; Chan, A. W. M.; Xu, L.; Shi, Y.; Du, Y.; Hao, W.; Wong, P. K.; Wang, J.; Dou, S. X.; Zhang, L.; Yu, J. C. Efficient Ammonia Electrosynthesis from Nitrate on Strained Ruthenium Nanoclusters. *J. Am. Chem. Soc.* **2020**, *142* (15), 7036–7046. https://doi.org/10.1021/jacs.0c00418.

(124) Wang, Y.; Shao, M. Theoretical Screening of Transition Metal-N4-Doped Graphene for Electroreduction of Nitrate. *ACS Catal.* **2022**, *12* (9), 5407–5415. https://doi.org/10.1021/acscatal.2c00307.

(125) Wang, S.; Gao, H.; Li, L.; Hui, K. S.; Dinh, D. A.; Wu, S.; Kumar, S.; Chen, F.; Shao, Z.; Hui, K. N. Jo Rn A. *Nano Energy* **2022**, 107517. https://doi.org/10.1016/j.nanoen.2022.107517.

(126) Wheeldon, I.; Minteer, S. D.; Banta, S.; Barton, S. C.; Atanassov, P.; Sigman, M. Substrate Channelling as an Approach to Cascade Reactions. *Nat. Chem.* **2016**, *8* (4), 299–309. https://doi.org/10.1038/nchem.2459.

(127) Li, J.; Zhang, Y.; Kuruvinashetti, K.; Kornienko, N. Construction of C–N Bonds from

Small-Molecule Precursors through Heterogeneous Electrocatalysis. *Nat. Rev. Chem.* **2022**, *6* (5), 303–319. https://doi.org/10.1038/s41570-022-00379-5.

(128) Wu, Y.; Jiang, Z.; Lin, Z.; Liang, Y.; Wang, H. Direct Electrosynthesis of Methylamine from Carbon Dioxide and Nitrate. *Nat. Sustain.* **2021**, *4* (8), 725–730. https://doi.org/10.1038/s41893-021-00705-7.

(129) Wang, S.; Gao, H.; Li, L.; Hui, K. S.; Dinh, D. A.; Wu, S.; Kumar, S.; Chen, F.; Shao, Z.; Hui, K. N. High-Throughput Identification of Highly Active and Selective Single-Atom Catalysts for Electrochemical Ammonia Synthesis through Nitrate Reduction. *Nano Energy* **2022**, *100* (March), 107517. https://doi.org/10.1016/j.nanoen.2022.107517.

(130) Moltved, K. A.; Kepp, K. P. The Chemical Bond between Transition Metals and Oxygen: Electronegativity, d-Orbital Effects, and Oxophilicity as Descriptors of Metal-Oxygen Interactions. *J. Phys. Chem. C* **2019**, *123* (30), 18432–18444. https://doi.org/10.1021/acs.jpcc.9b04317.

(131) Liang, X.; Zhu, H.; Yang, X.; Xue, S.; Liang, Z. Recent Advances in Designing Ef Fi Cient Electrocatalysts for Electrochemical Nitrate Reduction to Ammonia. **2022**, *2200202*, 1–27. https://doi.org/10.1002/sstr.202200202.

(132) Hu, Q.; Qin, Y.; Wang, X.; Wang, Z.; Huang, X.; Zheng, H.; Gao, K.; Yang, H.; Zhang, P.; Shao, M.; He, C. Reaction Intermediate-Mediated Electrocatalyst Synthesis Favors Specified Facet and Defect Exposure for Efficient Nitrate-Ammonia Conversion. *Energy Environ. Sci.* **2021**, *14* (9), 4989–4997. https://doi.org/10.1039/d1ee01731d.

(133) Katsounaros, I. On the Assessment of Electrocatalysts for Nitrate Reduction. *Curr. Opin. Electrochem.* **2021**, *28*, 100721. https://doi.org/10.1016/j.coelec.2021.100721.

(134) Li, L.; Tang, C.; Cui, X.; Zheng, Y.; Wang, X.; Xu, H.; Zhang, S.; Shao, T.; Davey, K.; Qiao, S. Z. Efficient Nitrogen Fixation to Ammonia through Integration of Plasma Oxidation with Electrocatalytic Reduction. *Angew. Chemie - Int. Ed.* **2021**, *60* (25), 14131–14137. https://doi.org/10.1002/anie.202104394.

(135) Wang, J.; Cai, C.; Wang, Y.; Yang, X.; Wu, D.; Zhu, Y.; Li, M.; Gu, M.; Shao, M. Electrocatalytic Reduction of Nitrate to Ammonia on Low-Cost Ultrathin CoOx Nanosheets. *ACS Catal.* **2021**, *11* (24), 15135–15140. https://doi.org/10.1021/acscatal.1c03918.

(136) Song, Z.; Liu, Y.; Zhong, Y.; Guo, Q.; Zeng, J.; Geng, Z. Efficient Electroreduction of Nitrate into Ammonia at Ultralow Concentrations Via an Enrichment Effect. *Adv. Mater.* **2022**, *34* (36). https://doi.org/10.1002/adma.202204306.

(137) Deng, Z.; Ma, C.; Li, Z.; Luo, Y.; Zhang, L.; Sun, S.; Liu, Q.; Du, J.; Lu, Q.; Zheng, B.; Sun, X. High-Efficiency Electrochemical Nitrate Reduction to Ammonia on a Co3O4Nanoarray Catalyst with Cobalt Vacancies. *ACS Appl. Mater. Interfaces* **2022**. https://doi.org/10.1021/acsami.2c12772.

(138) Daiyan, R.; Tran-Phu, T.; Kumar, P.; Iputera, K.; Tong, Z.; Leverett, J.; Khan, M. H. A.; Asghar Esmailpour, A.; Jalili, A.; Lim, M.; Tricoli, A.; Liu, R. S.; Lu, X.; Lovell, E.; Amal, R. Nitrate Reduction to Ammonium: From CuO Defect Engineering to Waste NOx-to-NH3 Economic Feasibility. *Energy Environ. Sci.* **2021**, *14* (6), 3588–3598. https://doi.org/10.1039/d1ee00594d.

(139) Zhou, F.; Sun, C. Nitrate-to-Ammonia Conversion on Ru/Ni Hydroxide Hybrid through Zinc-Nitrate Fuel Cell. *Small* **2022**, *18* (21). https://doi.org/10.1002/smll.202200436.

(140) Qiao, Z.; Wang, C.; Li, C.; Zeng, Y.; Hwang, S.; Li, B.; Karakalos, S.; Park, J.; Kropf, A. J.; Wegener, E. C.; Gong, Q.; Xu, H.; Wang, G.; Myers, D. J.; Xie, J.; Spendelow, J. S.; Wu, G. Atomically Dispersed Single Iron Sites for Promoting Pt and Pt3Co Fuel Cell Catalysts: Performance and Durability Improvements. *Energy Environ. Sci.* **2021**, *14* (9), 4948–4960. https://doi.org/10.1039/d1ee01675j.

(141) Ly, A.; Wang, H.; Murphy, E.; Huang, Y.; Guo, S.; Liu, Y.; Zenyuk, I. V; Atanassov, P. Electrochemical Trends of Atomically Dispersed Metal-Nitrogen-Carbon Materials As Oxygen Reduction Reaction Catalysts and Active Supports. *ECS Meet. Abstr.* **2022**, *MA2022-01* (35), 1472. https://doi.org/10.1149/MA2022-01351472mtgabs.

(142) Ao, X.; Zhang, W.; Zhao, B.; Ding, Y.; Nam, G.; Soule, L.; Abdelhafiz, A.; Wang, C.; Liu, M. Atomically Dispersed Fe-N-C Decorated with Pt-Alloy Core-Shell Nanoparticles for Improved Activity and Durability towards Oxygen Reduction. *Energy Environ. Sci.* **2020**, *13* (9), 3032–3040. https://doi.org/10.1039/d0ee00832j.

(143) Murphy, E.; Liu, Y.; Matanovic, I.; Huang, Y.; Ly, A.; Guo, S.; Zang, W.; Yan, X.; Zenyuk, I.; Spoerke, E.; Atanassov Plamen. Elucidating Electrochemical Nitrate and Nitrite Reduction over Atomically-Dispersed Transition Metal Sites. *(Submitted)* No. 2.

(144) Vicker, J.; Peterson, D.; Randolph, K. Cost of Electrolytic Hydrogen Production with Existing Technology. *Deparment Energy United Staes Am.* **2020**, 5.

(145) Jiang, K.; Yu, H.; Chen, L.; Fang, M.; Azzi, M.; Cottrell, A.; Li, K. An Advanced, Ammonia-Based Combined NOx/SOx/CO2 Emission Control Process towards a Low-Cost, Clean Coal Technology. *Appl. Energy* **2020**, *260* (x), 114316. https://doi.org/10.1016/j.apenergy.2019.114316.

(146) Tan, H.; Verbeeck, J.; Abakumov, A.; Van Tendeloo, G. Oxidation State and Chemical Shift Investigation in Transition Metal Oxides by EELS. *Ultramicroscopy* **2012**, *116* (2012), 24–33. https://doi.org/10.1016/j.ultramic.2012.03.002.

(147) Liang, L.; Jin, H.; Zhou, H.; Liu, B.; Hu, C.; Chen, D.; Wang, Z.; Hu, Z.; Zhao, Y.; Li, H. W.; He, D.; Mu, S. Cobalt Single Atom Site Isolated Pt Nanoparticles for Efficient ORR and HER in Acid Media. *Nano Energy* **2021**, *88* (May), 106221. https://doi.org/10.1016/j.nanoen.2021.106221.

(148) Gao, J.; Zhou, X.; Wang, Y.; Chen, Y.; Xu, Z.; Qiu, Y.; Yuan, Q.; Lin, X.; Qiu, H. J. Exploiting the Synergistic Electronic Interaction between Pt-Skin Wrapped Intermetallic PtCo Nanoparticles and Co-N-C Support for Efficient ORR/EOR Electrocatalysis in a Direct Ethanol Fuel Cell. *Small* **2022**, *18* (25), 1–9. https://doi.org/10.1002/smll.202202071.

(149) Wang, F.; Liu, X.; Jiang, B.; Zhuo, H.; Chen, W.; Chen, Y.; Li, X. Low-Loading Pt Nanoparticles Combined with the Atomically Dispersed FeN4 Sites Supported by FeSA-N-C for Improved Activity and Stability towards Oxygen Reduction Reaction/Hydrogen Evolution Reaction in Acid and Alkaline Media. *J. Colloid Interface Sci.* **2023**, *635*, 514–523. https://doi.org/10.1016/j.jcis.2022.12.160.

(150) Greczynski, G.; Hultman, L. X-Ray Photoelectron Spectroscopy: Towards Reliable Binding Energy Referencing. *Prog. Mater. Sci.* **2020**, *107* (July 2019), 100591. https://doi.org/10.1016/j.pmatsci.2019.100591.

(151) Gabardo, C. M.; Seifitokaldani, A.; Edwards, J. P.; Dinh, C. T.; Burdyny, T.; Kibria, M. G.; O'Brien, C. P.; Sargent, E. H.; Sinton, D. Combined High Alkalinity and

Pressurization Enable Efficient CO2 Electroreduction to CO. *Energy Environ. Sci.* **2018**, *11* (9), 2531–2539. https://doi.org/10.1039/c8ee01684d.

(152) Wen, G.; Ren, B.; Park, M. G.; Yang, J.; Dou, H.; Zhang, Z.; Deng, Y.; Bai, Z.; Yang, L.; Gostick, J.; Botton, G. A.; Hu, Y.; Chen, Z. Ternary Sn-Ti-O Electrocatalyst Boosts the Stability and Energy Efficiency of CO 2 Reduction . *Angew. Chemie* **2020**, *132* (31), 12960–12967. https://doi.org/10.1002/ange.202004149.

(153) Chen, Y.; Vise, A.; Klein, W. E.; Cetinbas, F. C.; Myers, D. J.; Smith, W. A.; Smith, W. A.; Smith, W. A.; Deutsch, T. G.; Neyerlin, K. C. A Robust, Scalable Platform for the Electrochemical Conversion of CO2to Formate: Identifying Pathways to Higher Energy Efficiencies. *ACS Energy Lett.* **2020**, *5* (6), 1825–1833. https://doi.org/10.1021/acsenergylett.0c00860.

(154) Xie, H.; Zhang, T.; Xie, R.; Hou, Z.; Ji, X.; Pang, Y.; Chen, S.; Titirici, M. M.; Weng, H.; Chai, G. Facet Engineering to Regulate Surface States of Topological Crystalline Insulator Bismuth Rhombic Dodecahedrons for Highly Energy Efficient Electrochemical CO2 Reduction. *Adv. Mater.* **2021**, *33* (31). https://doi.org/10.1002/adma.202008373.

(155) Dinh, C. T.; Burdyny, T.; Kibria, G.; Seifitokaldani, A.; Gabardo, C. M.; Pelayo García De Arquer, F.; Kiani, A.; Edwards, J. P.; De Luna, P.; Bushuyev, O. S.; Zou, C.; Quintero-Bermudez, R.; Pang, Y.; Sinton, D.; Sargent, E. H. CO2 Electroreduction to Ethylene via Hydroxide-Mediated Copper Catalysis at an Abrupt Interface. *Science (80-.).* **2018**, *360* (6390), 783–787. https://doi.org/10.1126/science.aas9100.

(156) Biesinger, M. C.; Payne, B. P.; Grosvenor, A. P.; Lau, L. W. M.; Gerson, A. R.; Smart, R. S. C. Resolving Surface Chemical States in XPS Analysis of First Row Transition Metals,

Oxides and Hydroxides: Cr, Mn, Fe, Co and Ni. *Appl. Surf. Sci.* **2011**, *257* (7), 2717–2730. https://doi.org/10.1016/j.apsusc.2010.10.051.

(157) Li, J.; Zitolo, A.; Garcés-Pineda, F. A.; Asset, T.; Kodali, M.; Tang, P.; Arbiol, J.; Galán-Mascarós, J. R.; Atanassov, P.; Zenyuk, I. V.; Sougrati, M. T.; Jaouen, F. Metal Oxide Clusters on Nitrogen-Doped Carbon Are Highly Selective for CO2Electroreduction to CO. *ACS Catal.* **2021**, *11* (15), 10028–10042. https://doi.org/10.1021/acscatal.1c01702.

(158) Genovese, C.; Schuster, M. E.; Gibson, E. K.; Gianolio, D.; Posligua, V.; Grau-Crespo, R.; Cibin, G.; Wells, P. P.; Garai, D.; Solokha, V.; Krick Calderon, S.; Velasco-Velez, J. J.; Ampelli, C.; Perathoner, S.; Held, G.; Centi, G.; Arrigo, R. Operando Spectroscopy Study of the Carbon Dioxide Electro-Reduction by Iron Species on Nitrogen-Doped Carbon. *Nat. Commun.* **2018**, *9* (1), 1–12. https://doi.org/10.1038/s41467-018-03138-7.

(159) Wagner, K. M.; Karathanasis, T.; Matocha, C. J. Reactivity of Nitrate with Zero-Valent Iron. *Water (Switzerland)* **2022**, *14* (18), 1–15. https://doi.org/10.3390/w14182796.

(160) Teng, W.; Bai, N.; Liu, Y.; Liu, Y.; Fan, J.; Zhang, W. X. Selective Nitrate Reduction to Dinitrogen by Electrocatalysis on Nanoscale Iron Encapsulated in Mesoporous Carbon. *Environ. Sci. Technol.* **2018**, *52* (1), 230–236. https://doi.org/10.1021/acs.est.7b04775.

(161) Lin, L.; Li, H.; Wang, Y.; Li, H.; Wei, P.; Nan, B.; Si, R.; Wang, G.; Bao, X. Temperature-Dependent CO2 Electroreduction over Fe-N-C and Ni-N-C Single-Atom Catalysts. *Angew. Chemie - Int. Ed.* **2021**, *60* (51), 26582–26586. https://doi.org/10.1002/anie.202113135.

(162) Hollevoet, L.; Vervloessem, E.; Gorbanev, Y.; Nikiforov, A.; De Geyter, N.; Bogaerts, A.; Martens, J. A. Energy-Efficient Small-Scale Ammonia Synthesis Process with Plasma-

Enabled Nitrogen Oxidation and Catalytic Reduction of Adsorbed NOx. *ChemSusChem* **2022**, *15* (10). https://doi.org/10.1002/cssc.202102526.

(163) Zheng, J.; Zhang, H.; Lv, J.; Zhang, M.; Wan, J.; Gerrits, N.; Wu, A. Jiageng Zheng, # Hao Zhang, * , # Jiabao Lv, Meng Zhang, Jieying Wan, Nick Gerrits, Angjian Wu, Bingru Lan, Weitao Wang, Shuangyin Wang, * Xin Tu, * Annemie Bogaerts, * and Xiaodong Li. **2023**, No. x. https://doi.org/10.1021/jacsau.3c00087.

(164) Jouny, M.; Lv, J. J.; Cheng, T.; Ko, B. H.; Zhu, J. J.; Goddard, W. A.; Jiao, F. Formation of Carbon–Nitrogen Bonds in Carbon Monoxide Electrolysis. *Nat. Chem.* **2019**, *11* (9), 846–851. https://doi.org/10.1038/s41557-019-0312-z.

(165) Zhu, T.; Chen, Q.; Liao, P.; Duan, W.; Liang, S.; Yan, Z.; Feng, C. Single-Atom Cu Catalysts for Enhanced Electrocatalytic Nitrate Reduction with Significant Alleviation of Nitrite Production. *Small* **2020**, *16* (49), 1–11. https://doi.org/10.1002/smll.202004526.

(166) Wang, Y.; Zhou, W.; Jia, R.; Yu, Y.; Zhang, B. Unveiling the Activity Origin of a Copper-Based Electrocatalyst for Selective Nitrate Reduction to Ammonia. *Angew. Chemie - Int. Ed.* **2020**, *59* (13), 5350–5354. https://doi.org/10.1002/anie.201915992.

(167) Lim, J.; Liu, C.-Y.; Park, J.; Liu, Y.-H.; Senftle, T. P.; Lee, S. W.; Hatzell, M. C. Structure Sensitivity of Pd Facets for Enhanced Electrochemical Nitrate Reduction to Ammonia. *ACS Catal.* **2021**, *11* (12), 7568–7577. https://doi.org/10.1021/acscatal.1c01413.

(168) Jia, R.; Wang, Y.; Wang, C.; Ling, Y.; Yu, Y.; Zhang, B. Boosting Selective Nitrate Electroreduction to Ammonium by Constructing Oxygen Vacancies in TiO2. *ACS Catal.* **2020**, *10* (6), 3533–3540. https://doi.org/10.1021/acscatal.9b05260.

(169) Dean, J. A. Lange's Handbook of Chemistry. *Mater. Manuf. Process* **1990**, *5* (4), 687–688.

(170) Peterson, M. L.; Brown, G. E.; Parks, G. A.; Stein, C. L. Differential Redox and Sorption of Cr(III/VI) on Natural Silicate and Oxide Minerals: EXAFS and XANES Results. *Geochim. Cosmochim. Acta* **1997**, *61* (16), 3399–3412. https://doi.org/10.1016/S0016-7037(97)00165-8.

(171) Li, C.; Ju, W.; Vijay, S.; Timoshenko, J.; Mou, K.; Cullen, D. A.; Yang, J.; Wang, X.; Pachfule, P.; Brückner, S.; Jeon, H. S.; Haase, F. T.; Tsang, S.; Rettenmaier, C.; Chan, K.; Cuenya, B. R.; Thomas, A.; Strasser, P. Covalent Organic Framework (COF) Derived Ni-N-C Catalysts for Electrochemical CO 2 Reduction: Unraveling Fundamental Kinetic and Structural Parameters of the Active Sites . *Angew. Chemie* **2022**, *134* (15). https://doi.org/10.1002/ange.202114707.

(172) Zhou, M.; Jiang, Y.; Wang, G.; Wu, W.; Chen, W.; Yu, P.; Lin, Y.; Mao, J.; Mao, L. Single-Atom Ni-N4 Provides a Robust Cellular NO Sensor. *Nat. Commun.* **2020**, *11* (1), 1–9. https://doi.org/10.1038/s41467-020-17018-6.

(173) Smolders, S.; Lomachenko, K. A.; Bueken, B.; Struyf, A.; Bugaev, A. L.; Atzori, C.; Stock, N.; Lamberti, C.; Roeffaers, M. B. J.; De Vos, D. E. Unravelling the Redox-Catalytic Behavior of Ce4+ Metal–Organic Frameworks by X-Ray Absorption Spectroscopy. *ChemPhysChem* **2018**, *19* (4), 373–378. https://doi.org/10.1002/cphc.201700967.

(174) Asakura, K.; Abe, H.; Kimura, M. The Challenge of Constructing an International XAFS Database. *J. Synchrotron Radiat.* **2018**, *25* (4), 967–971.

https://doi.org/10.1107/S1600577518006963.

(175) Deng, Z.; Ma, C.; Fan, X.; Li, Z.; Luo, Y.; Sun, S.; Zheng, D.; Liu, Q.; Du, J.; Lu, Q.; Zheng, B.; Sun, X. Construction of CoP/TiO2 Nanoarray for Enhanced Electrochemical Nitrate Reduction to Ammonia. *Mater. Today Phys.* **2022**, *28* (August), 100854. https://doi.org/10.1016/j.mtphys.2022.100854.

(176) Wang, J.; Cai, C.; Wang, Y.; Yang, X.; Wu, D.; Zhu, Y.; Li, M.; Gu, M.; Shao, M. Electrocatalytic Reduction of Nitrate to Ammonia on Low-Cost Ultrathin CoO x Nanosheets. *ACS Catal.* **2021**, *11* (24), 15135–15140. https://doi.org/10.1021/acscatal.1c03918.

(177) Yang, J.; Qi, H.; Li, A.; Liu, X.; Yang, X.; Zhang, S.; Zhao, Q.; Jiang, Q.; Su, Y.; Zhang, L.; Li, J.-F.; Tian, Z.-Q.; Liu, W.; Wang, A.; Zhang, T. Potential-Driven Restructuring of Cu Single Atoms to Nanoparticles for Boosting the Electrochemical Reduction of Nitrate to Ammonia. *J. Am. Chem. Soc.* **2022**. https://doi.org/10.1021/jacs.2c02262.

(178) Guo, Y.; Zhang, R.; Zhang, S.; Zhao, Y.; Yang, Q.; Huang, Z.; Dong, B.; Zhi, C. Pd Doping-Weakened Intermediate Adsorption to Promote Electrocatalytic Nitrate Reduction on TiO2nanoarrays for Ammonia Production and Energy Supply with Zinc-Nitrate Batteries. *Energy Environ. Sci.* **2021**, *14* (7), 3938–3944. https://doi.org/10.1039/d1ee00806d.

(179) Xue, Y.; Yu, Q.; Ma, Q.; Chen, Y.; Zhang, C.; Teng, W.; Fan, J.; Zhang, W. X. Electrocatalytic Hydrogenation Boosts Reduction of Nitrate to Ammonia over Single-Atom Cu with Cu(I)-N3C1Sites. *Environ. Sci. Technol.* **2022**, *56* (20), 14797–14807. https://doi.org/10.1021/acs.est.2c04456.

(180) Zheng, W.; Zhu, L.; Yan, Z.; Lin, Z.; Lei, Z.; Zhang, Y.; Xu, H.; Dang, Z.; Wei, C.; Feng, C. Self-Activated Ni Cathode for Electrocatalytic Nitrate Reduction to Ammonia: From Fundamentals to Scale-Up for Treatment of Industrial Wastewater. *Environ. Sci. Technol.* **2021**, *55* (19), 13231–13243. https://doi.org/10.1021/acs.est.1c02278.

(181) Zhang, S.; Li, M.; Li, J.; Song, Q.; Liu, X. High-Ammonia Selective Metal – Organic Framework – Derived Co-Doped Fe / Fe 2 O 3 Catalysts for Electrochemical Nitrate Reduction. **2022**. https://doi.org/10.1073/pnas.2115504119/-/DCSupplemental.Published.

(182) Hong, Q. L.; Zhou, J.; Zhai, Q. G.; Jiang, Y. C.; Hu, M. C.; Xiao, X.; Li, S. N.; Chen, Y. Cobalt Phosphide Nanorings towards Efficient Electrocatalytic Nitrate Reduction to Ammonia. *Chem. Commun.* **2021**, *57* (88), 11621–11624. https://doi.org/10.1039/d1cc04952f.

(183) Kosanke, R. M. 済無No Title No Title No Title. **2019**. https://doi.org/10.1002/adma.202207305.

(184) Li, T.; Tang, C.; Guo, H.; Wu, H.; Duan, C.; Wang, H.; Zhang, F.; Cao, Y.; Yang, G.; Zhou, Y. In Situ Growth of Fe2O3Nanorod Arrays on Carbon Cloth with Rapid Charge Transfer for Efficient Nitrate Electroreduction to Ammonia. *ACS Appl. Mater. Interfaces* **2022**. https://doi.org/10.1021/acsami.2c14215.

(185) Zhu, J. Y.; Xue, Q.; Xue, Y. Y.; Ding, Y.; Li, F. M.; Jin, P.; Chen, P.; Chen, Y. Iridium Nanotubes as Bifunctional Electrocatalysts for Oxygen Evolution and Nitrate Reduction Reactions. *ACS Appl. Mater. Interfaces* **2020**, *12* (12), 14064–14070. https://doi.org/10.1021/acsami.0c01937.

Appendix A - Chapter 2

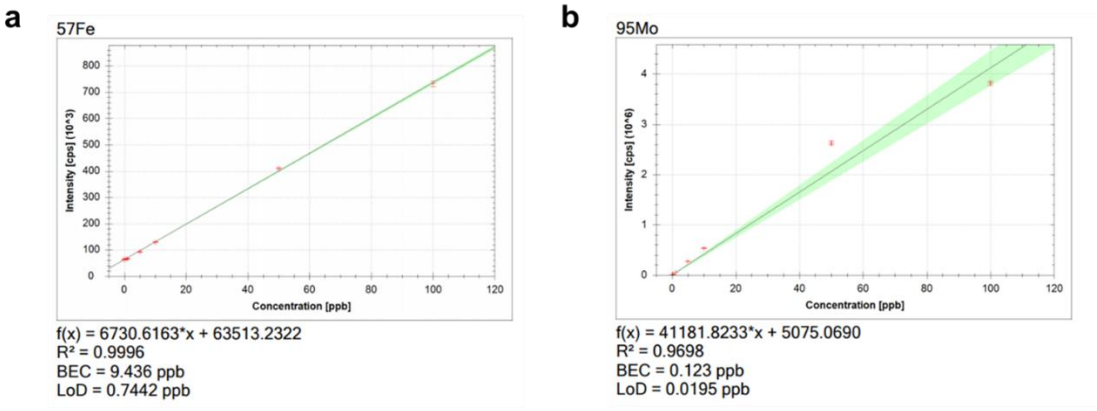

Appendix A.1 ICP-MS calibration curves of a) Fe b) Mo.

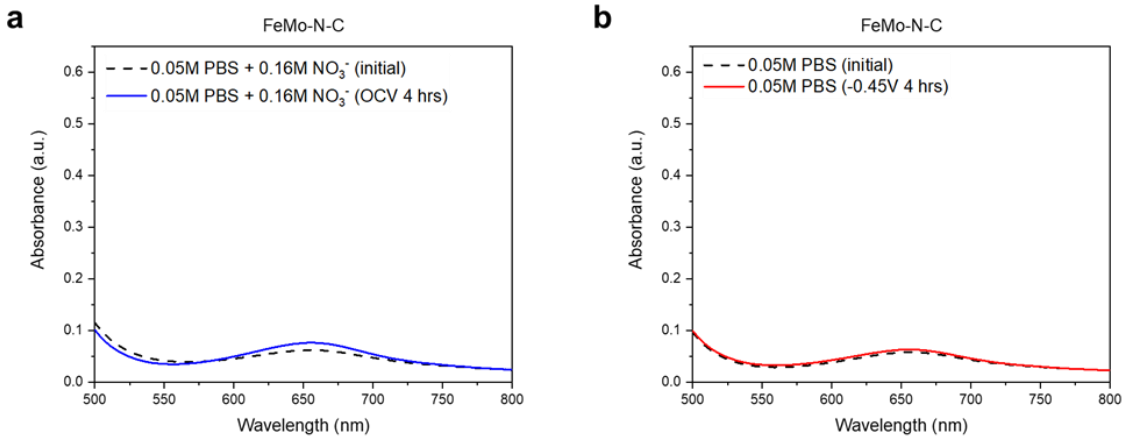

Appendix A.2 NO_3RR control experiments using the bi-metallic FeMo-N-C under a constant N_2 purge of 30 sccm. (a) No applied potential, 4 hours at open circuit voltage (OCV), showing in the absence of an applied potential no increase in ammonia is observed. (b) -0.45 V vs RHE for 4 hours using 0.05M PBS without the addition of NO_3^-, The UV-Vis spectra show no increase in the absorbance at 655 nm, indicating no ammonia is electrochemically produced in the absence of a NO_3^- source, demonstrating the N_2 gas feed is not a participating N-source in the ammonia production. These control

experiments also ruled out the potential ammonia contamination leaching from the pretreated *Nafion* membrane.

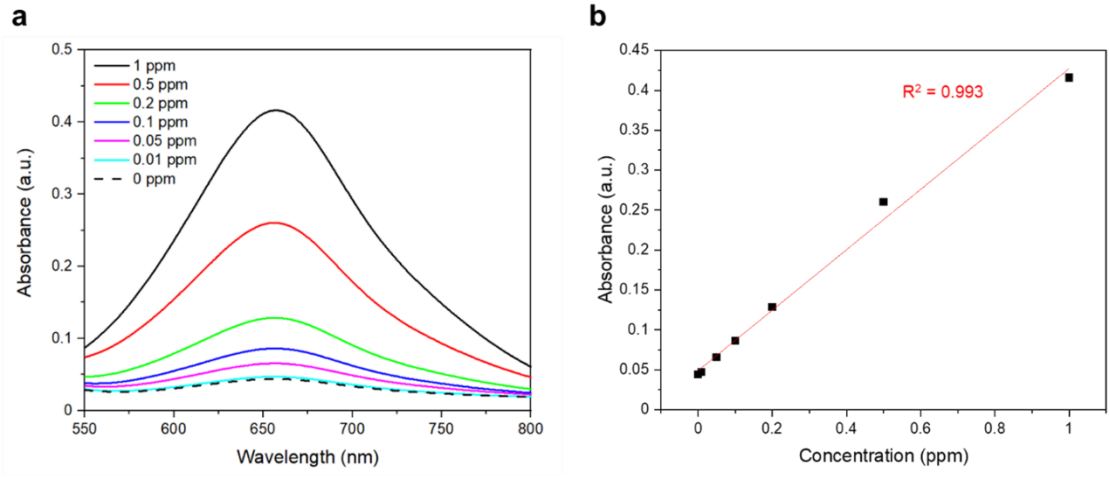

Appendix A.3 Standard calibration curves for UV-Vis detection of NH_3 from the Indophenol blue method (a) raw UV-Vis spectra (b) linear calibration.

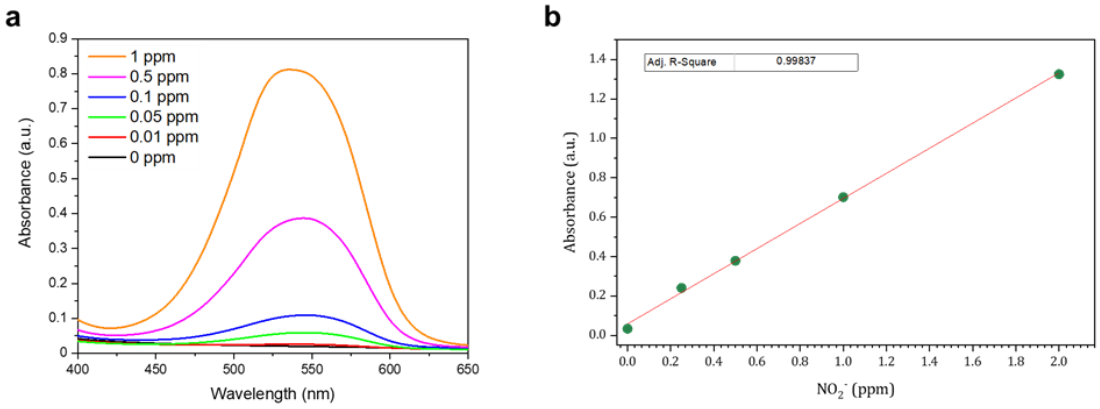

Appendix A.4 Standard calibration curves for UV-Vis detection of NO_2^- from the Griess based test (a) raw UV-Vis spectra (b) linear calibration.

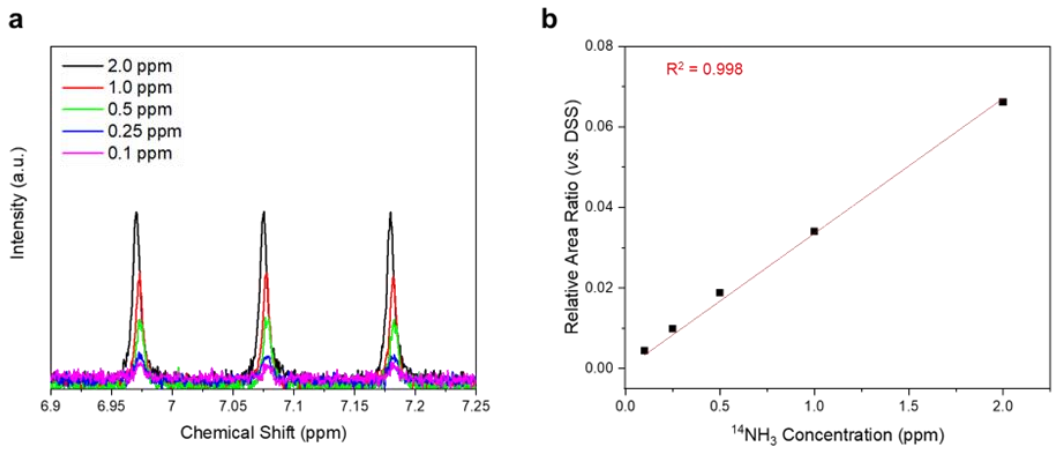

Appendix A.5 Standard ^{1}H NMR calibration curve of standard $^{14}NH_3$. (a) raw NMR chemical shift (b) linear calibration.

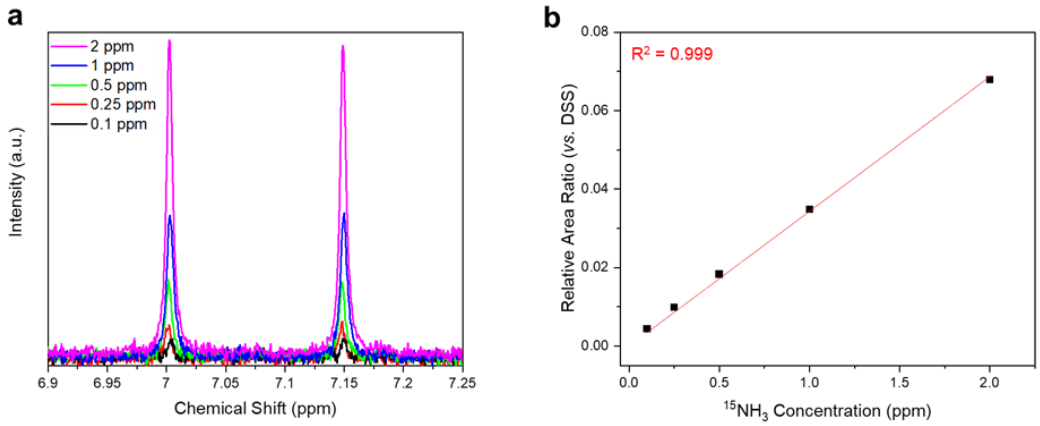

Appendix A.6 ^{1}H NMR calibration curve of isotopic $^{15}NH_3$. (a) raw NMR chemical shift (b) linear calibration.

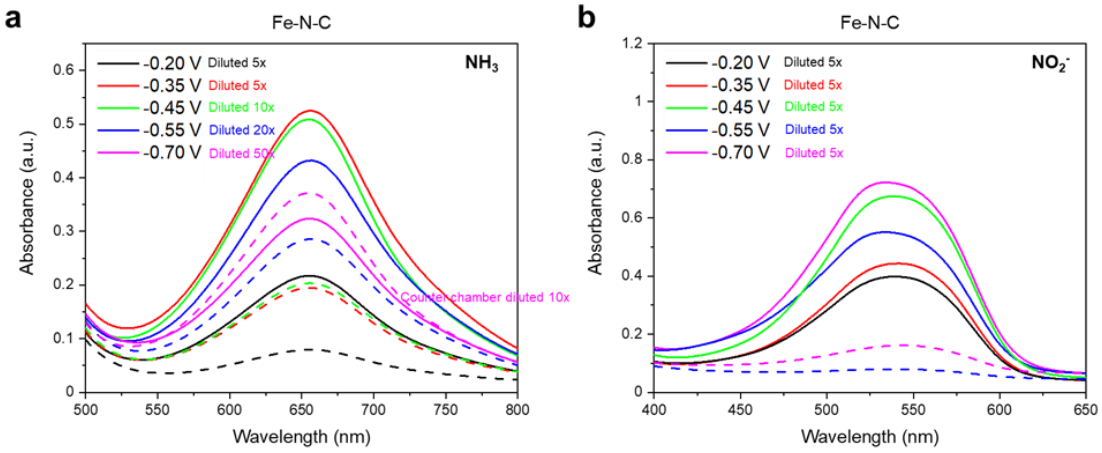

Appendix A.7 UV-Vis spectra for the 24 hour time-course electrolysis at -0.45 V *vs.* RHE (a) NH_3 and (b) NO_2^-, from NO_3RR time course studies on Fe-N-C. Dilutions are applied to bring the NH_3 concentrations within the calibrated range. Dashed lines indicate electrolyte sampled from the counter chamber. An aliquot of the electrolyte was sampled from both the cathodic and anodic chambers and diluted by a predetermined factor prior to the addition of the UV-Vis detection reagents.

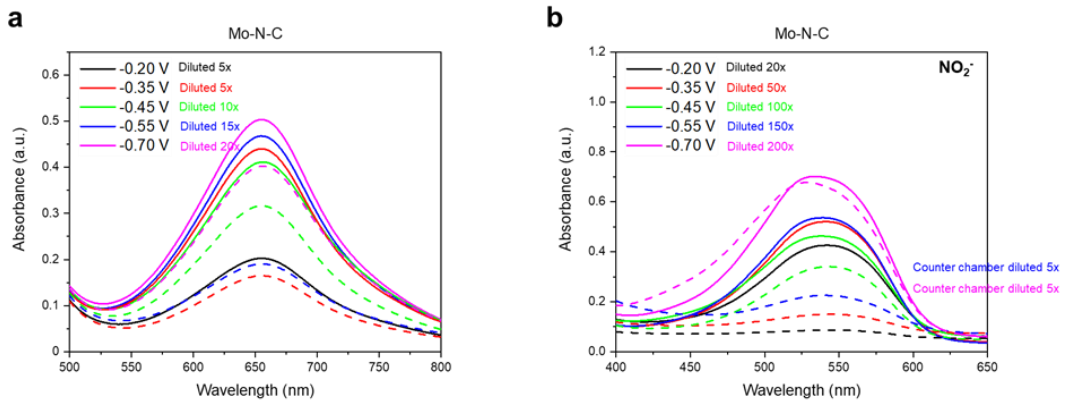

Appendix A.8 UV-Vis spectra for the 24 hour time-course electrolysis at -0.45 V *vs.* RHE (a) NH_3 and (b) NO_2^-, from NO_3RR time course studies on Mo-N-C. Dilutions are applied to bring the NH_3 and NO_2^- concentrations within the calibrated range. Dashed lines indicate electrolyte sampled from the counter chamber. An aliquot of the electrolyte

was sampled from both the cathodic and anodic chambers and diluted by a predetermined factor prior to the addition of the UV-Vis detection reagents.

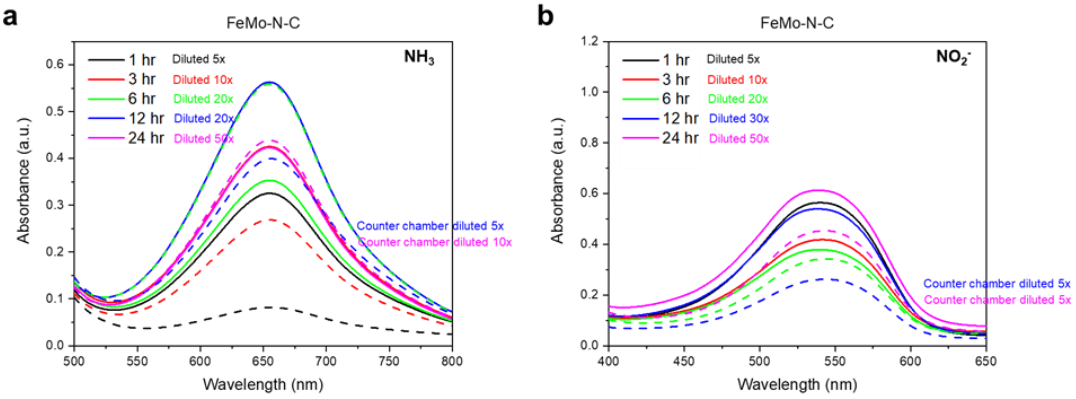

Appendix A.9 UV-Vis spectra for the 24 hour time-course electrolysis at -0.45 V *vs.* RHE (a) NH_3 and (b) NO_2^-, from NO_3RR time course studies on FeMo-N-C. Dilutions are applied to bring the NH_3 and NO_2^- concentrations within the calibrated range. Dashed lines indicate electrolyte sampled from the counter chamber. An aliquot of the electrolyte was sampled from both the cathodic and anodic chambers and diluted by a predetermined factor prior to the addition of the UV-Vis detection reagents.

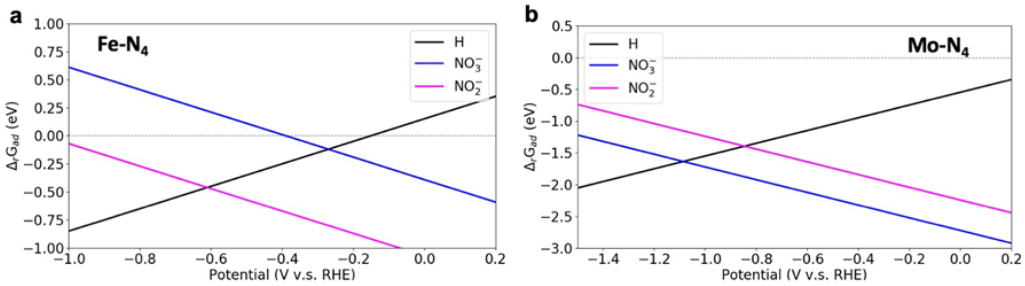

Appendix A.10 The Gibbs free energy of adsorption for NO_3^-, NO_2^- and H adatom *vs.* electrode potential on the (a) Fe-N_4 and (b) Mo-N_4 sites.

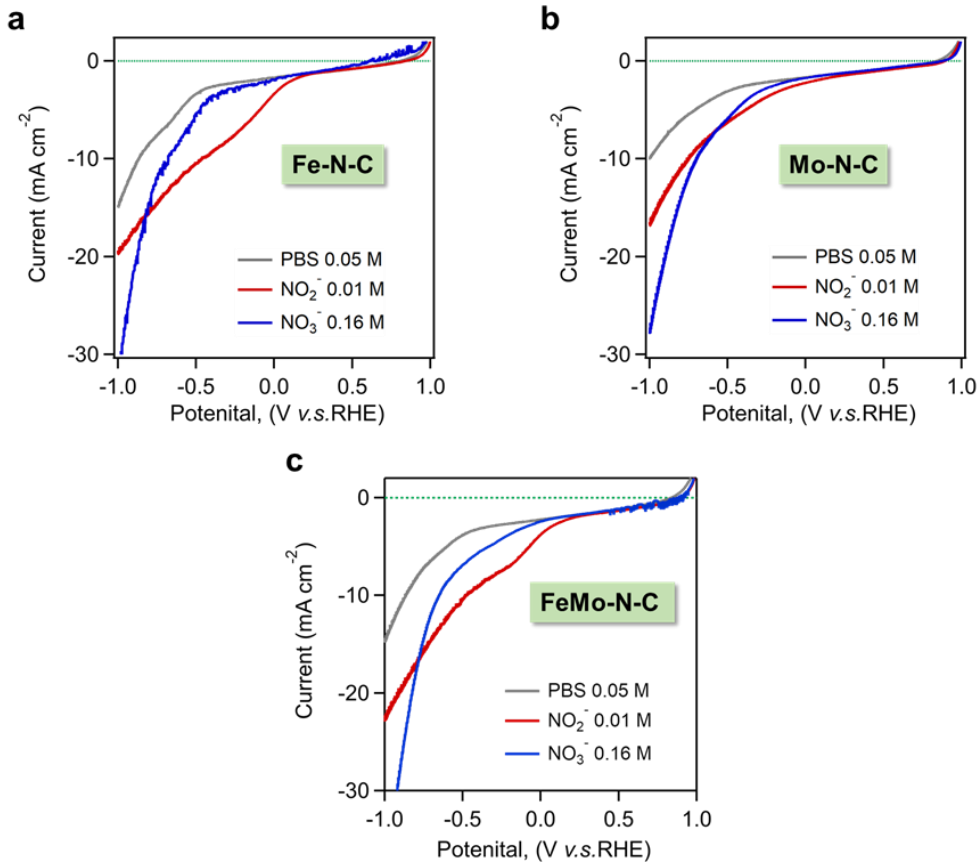

Appendix A.11 Linear sweep voltammetry in 0.05M PBS and 0.05M PBS doped with 0.01M NO_2^- or 0.16M NO_3^- electrolyte on (a) Fe-N-C, (b) Mo-N-C and (c) FeMo-N-C electrocatalysts. 0.5 mg cm^{-2} of catalyst is drop casted on a 0.45 cm^{-2} carbon paper electrode. The cathodic sweep rate is 10 mVs^{-1} and is performed under a constant N_2 purge of 30 sccm.

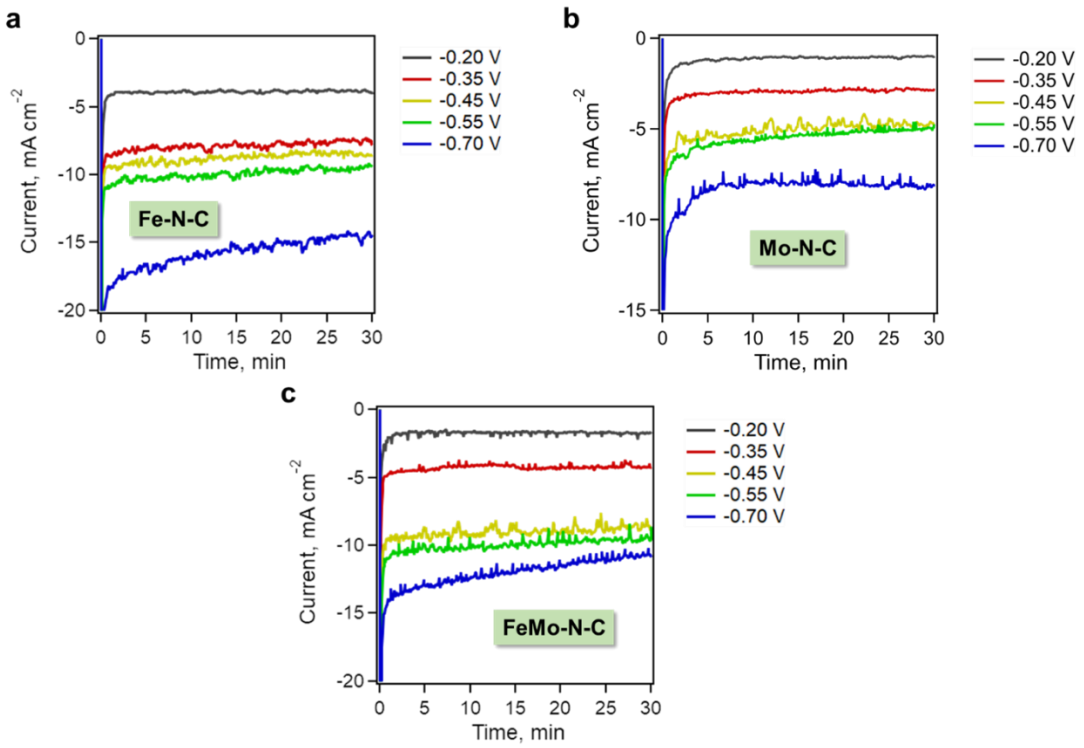

Appendix A.12 NO_2RR chronoamperometry on (a) Fe-N-C, (b) Mo-N-C and (c) FeMo-N-C electrocatalysts. The electrolysis is performed for 30 min in a 0.05M PBS + 0.01M NO_2^- electrolyte, under a constant N_2 purge of 30 sccm. 0.5 mg cm^{-2} of catalyst is drop casted on a 0.45 cm^{-2} carbon paper electrode.

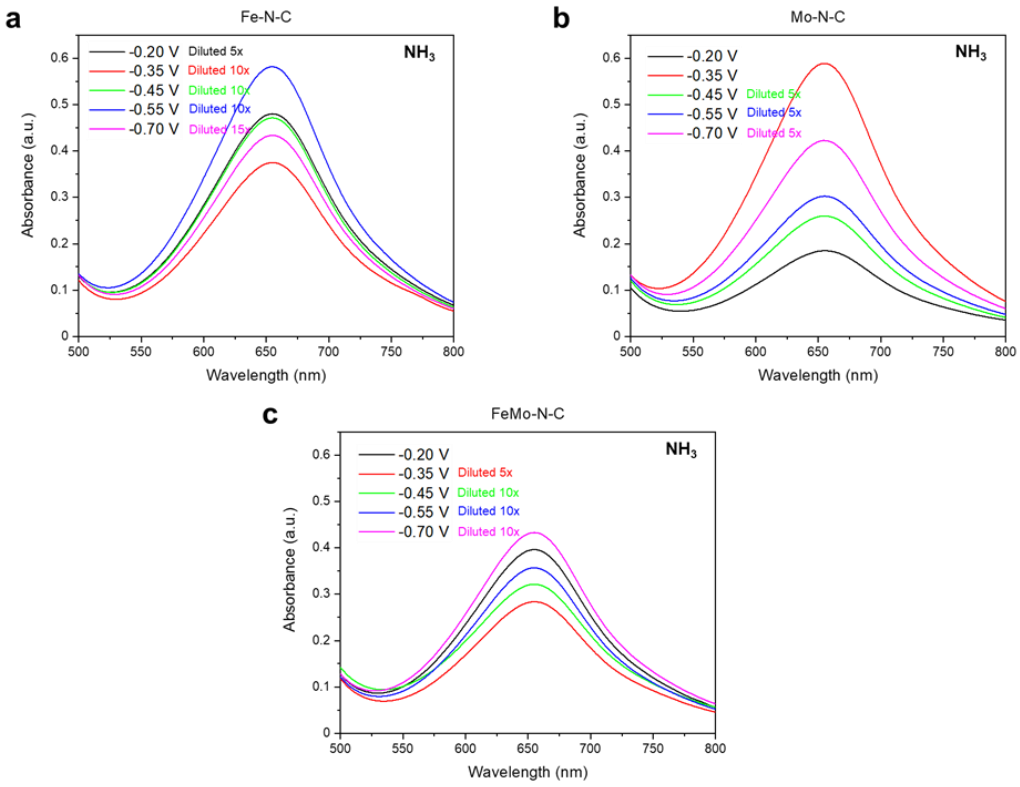

Appendix A.13 UV-Vis spectra for NH_3 from NO_2RR for 30 minutes on (a) Fe-N-C, (b) Mo-N-C and (c) FeMo-N-C electrocatalysts. Dilutions are applied to bring the NH_3 concentration within the calibrated range. An aliquot of the electrolyte was sampled from only the cathodic chamber as no cross over of NH_3 was observed after the 30-minute electrolysis.

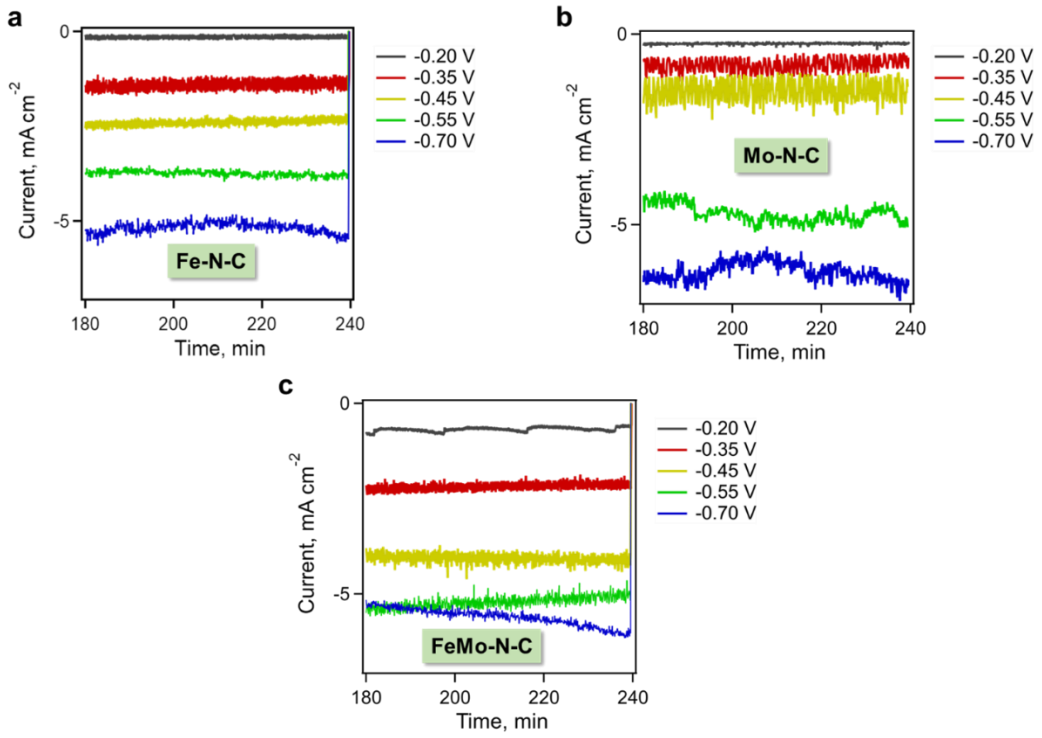

Appendix A.14 NO_3RR chronoamperometry on (a) Fe-N-C, (b) Mo-N-C and (c) FeMo-N-C electrocatalysts. The electrolysis is performed for 4 hours in a 0.05M PBS + 0.16M NO_3^- electrolyte, under a constant N_2 purge of 30 sccm. The 180 – 240-minute time interval is plotted for representation. 0.5 mg cm^{-2} of catalyst is drop casted on a 0.45 cm^{-2} carbon paper electrode.

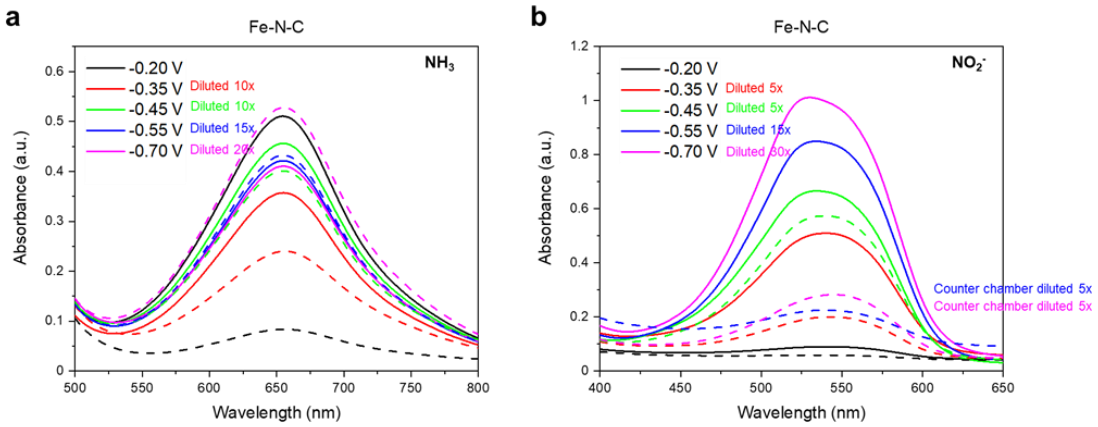

Appendix A.15 NO_3RR for 4-hours on Fe-N-C. UV-Vis detection as a function of potential for (a) NH_3 and (b) NO_2^-. Dilutions are applied to bring the product concentration within the calibrated range. Dashed lines indicate electrolyte sampled from the counter chamber. An aliquot of the electrolyte was sampled from both the cathodic and anodic chambers.

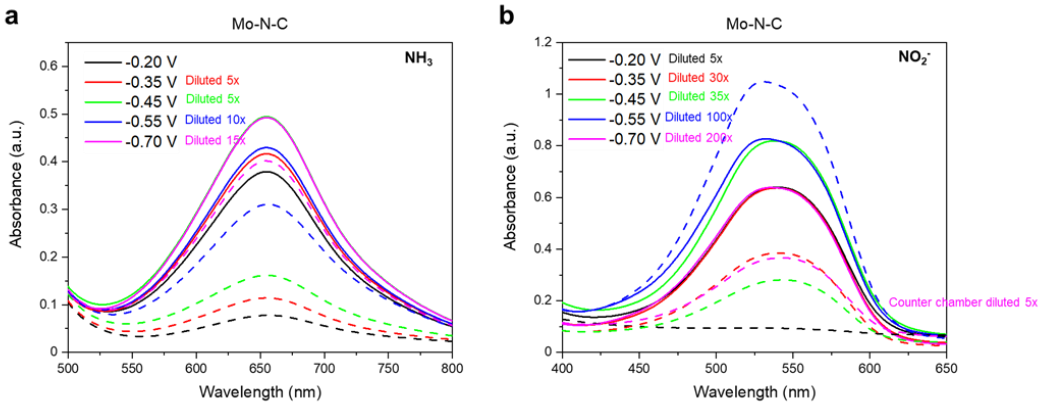

Appendix A.16 NO_3RR for 4-hours on Mo-N-C. UV-Vis detection as a function of potential for (a) NH_3 and (b) NO_2^-. Dilutions are applied to bring the product concentration within the calibrated range. Dashed lines indicate electrolyte sampled from the counter chamber. An aliquot of the electrolyte was sampled from both the cathodic and anodic chambers.

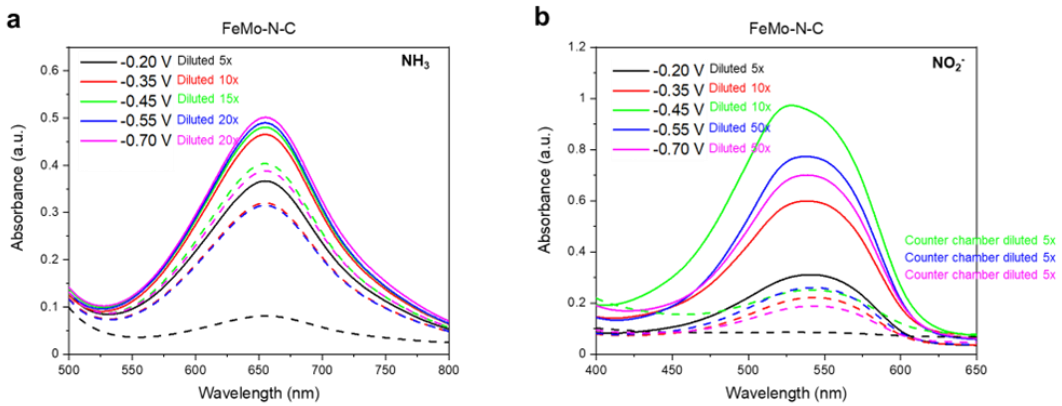

Appendix A.17 NO_3RR for 4-hours on FeMo-N-C. UV-Vis detection as a function of potential for (a) NH_3 and (b) NO_2^-. Dilutions are applied to bring the product concentration within the calibrated range. Dashed lines indicate electrolyte sampled from the counter chamber. An aliquot of the electrolyte was sampled from both the cathodic and anodic chambers.

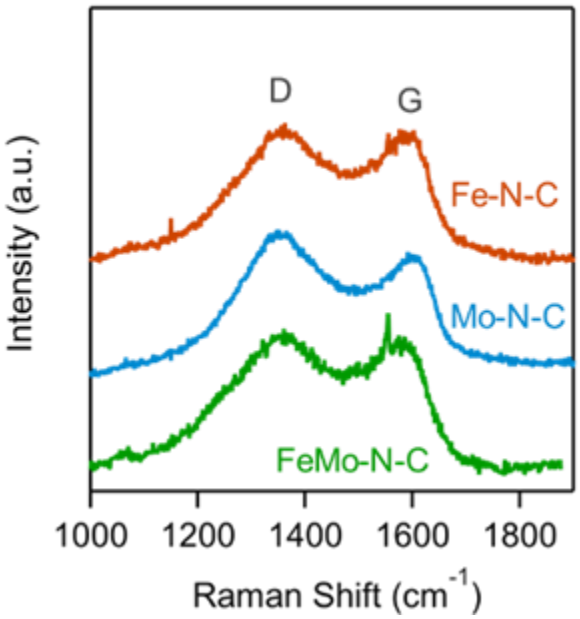

Appendix A.18 Raman spectra for the Fe-N-C, Mo-N-C and FeMo-N-C electrocatalysts. The calculated D/G ratio for Fe-N-C is 2.49, Mo-N-C is 2.15 and FeMo-N-C is 2.45.

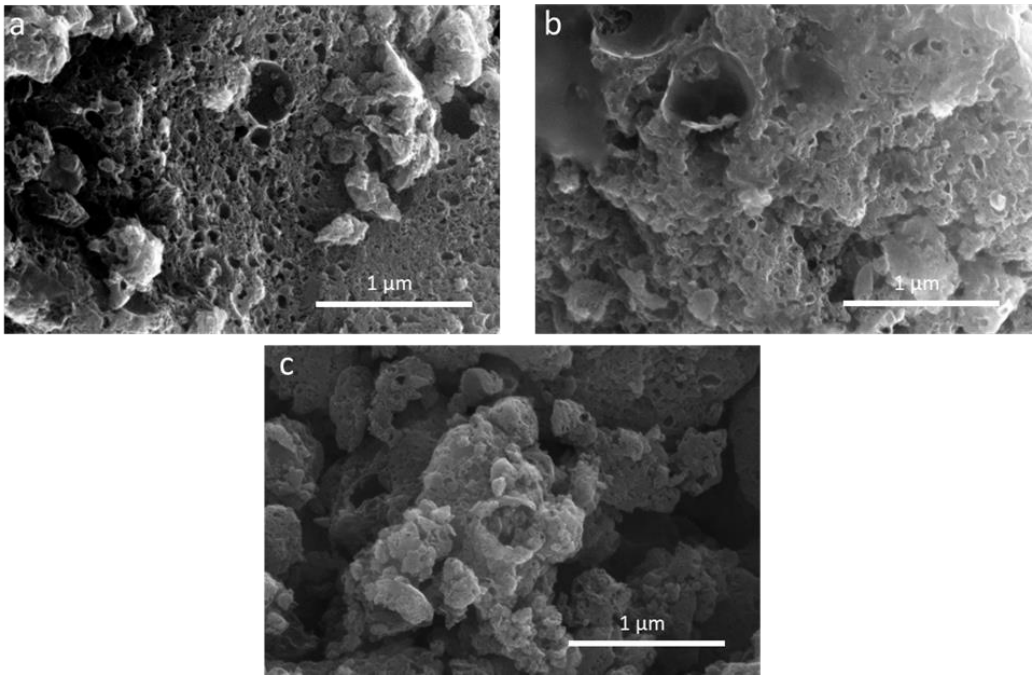

Appendix A.19 SEM images of a) Fe-N-C b) Mo-N-C and c) FeMo-N-C electrocatalysts demonstrating the well-defined hierarchical porous structure formed by the acid etching of the sacrificial silica template.

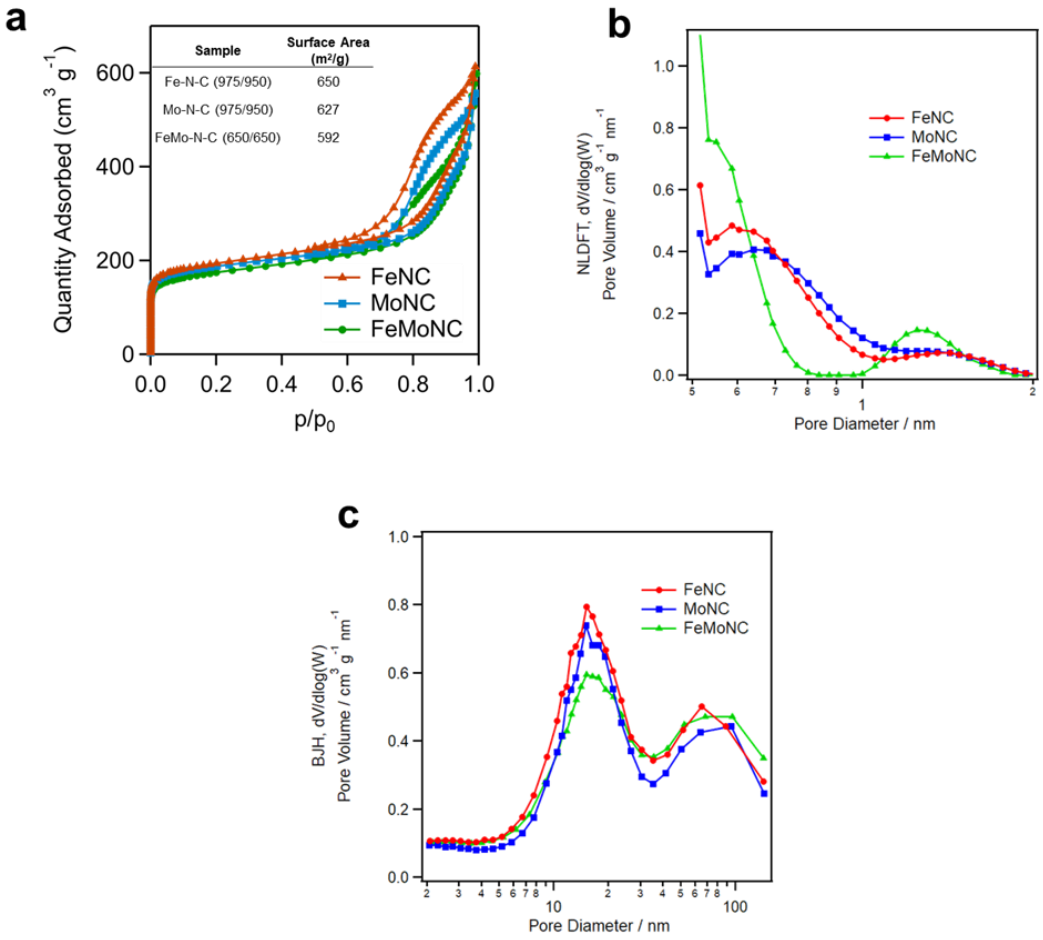

Appendix A.20 a) N_2 sorption isotherm for the Fe-N-C, Mo-N-C and FeMo-N-C electrocatalysts. The BET surface area for Fe-N-C is 650 m^2/g, Mo-N-C is 627 m^2/g and FeMo-N-C is 592 m^2/g. b) Pore size distribution in the microporous range, indicating the presence of microporous. c) Pore size distribution in the meso/macro-porous range, with a distinct mesopore size at ca. 20 nm and micropore size at ca. 90 nm, characteristic to the diameter of the sacrificial porous silica template.

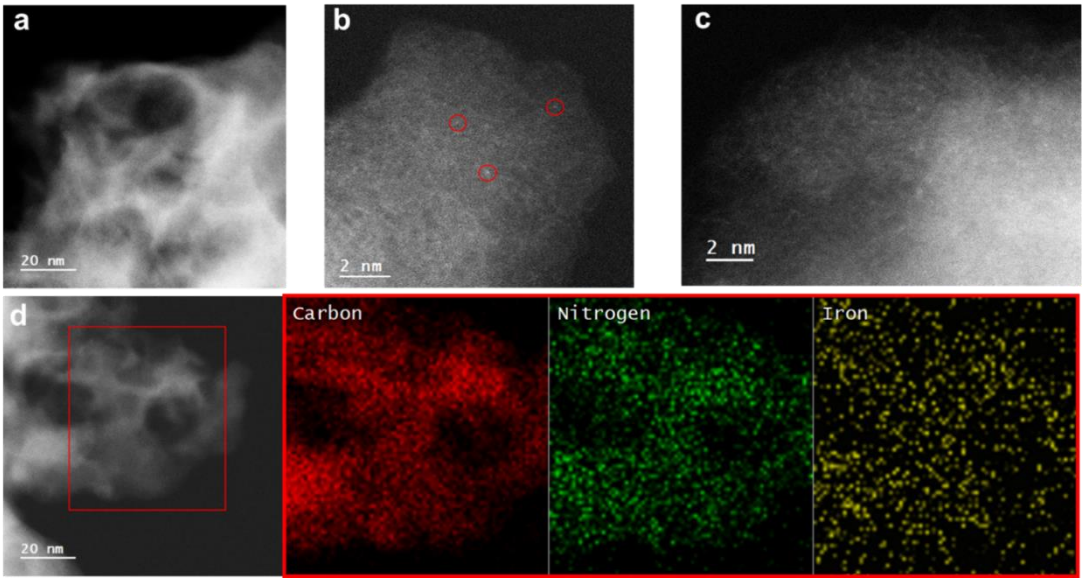

Appendix A.21 a) Low magnification AC-HAADF STEM image of the Fe-N-C catalyst. b-c) Atomic resolution AC-HAADF STEM image, bright spots indicate atomically dispersed Fe sites, red circles are placed to better visualize a few of these single atom sites. (d) AC-HAADF image and EDS mapping of the Fe-N-C catalyst, showing a homogenous dispersion of N-doping and Fe atoms.

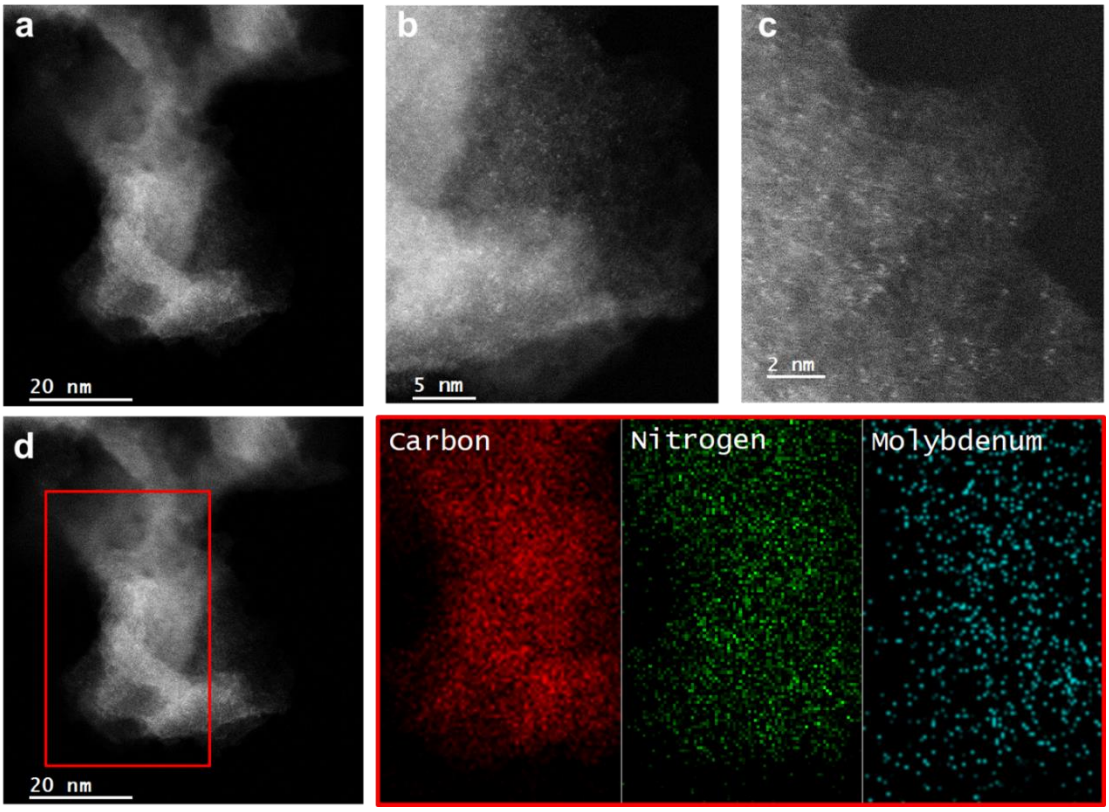

Appendix A.22 a) Low magnification AC-HAADF STEM image of the Mo-N-C catalyst. b-c) Atomic resolution AC-HAADF STEM image, bright spots indicate atomically dispersed Mo sites. (d) AC-HAADF image and EDS mapping of the Mo-N-C catalyst, showing a homogenous dispersion of N-doping and Mo atoms.

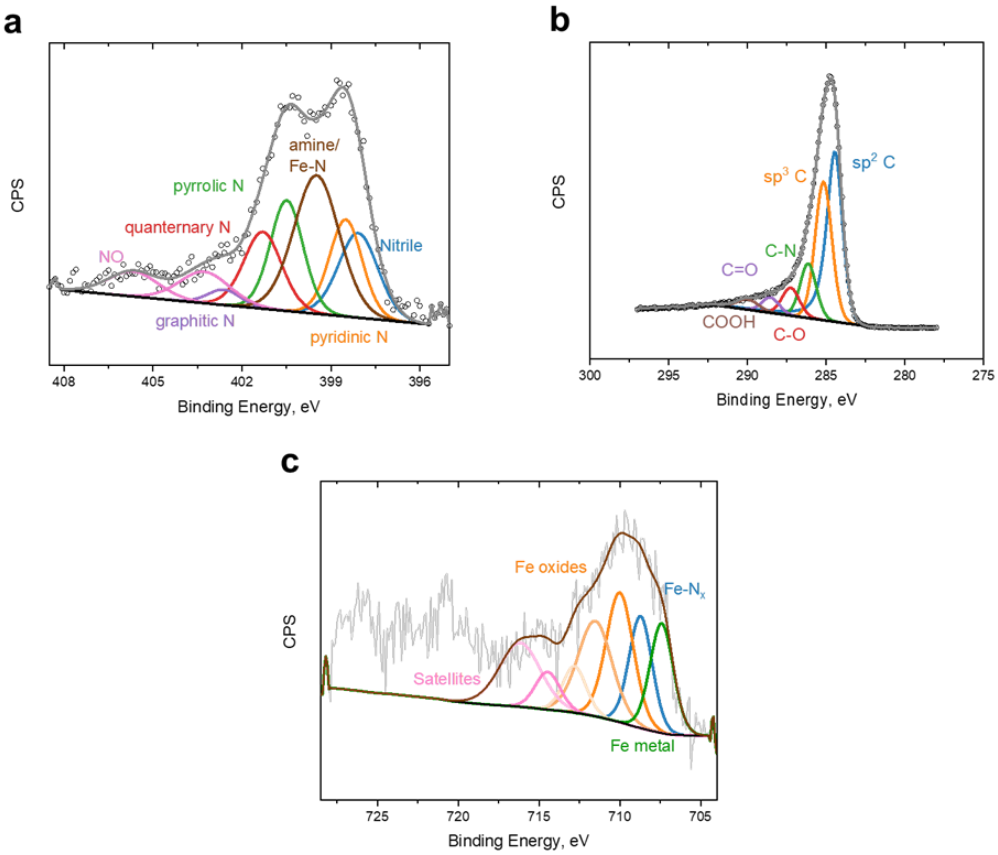

Appendix A.23 XPS spectra of the Fe-N-C catalyst (a) N 1s spectra confirming the formation of M-N_x moieties. (b) C 1s spectra (c) Fe 2p spectra indicating the presence of Fe-N_x sites.

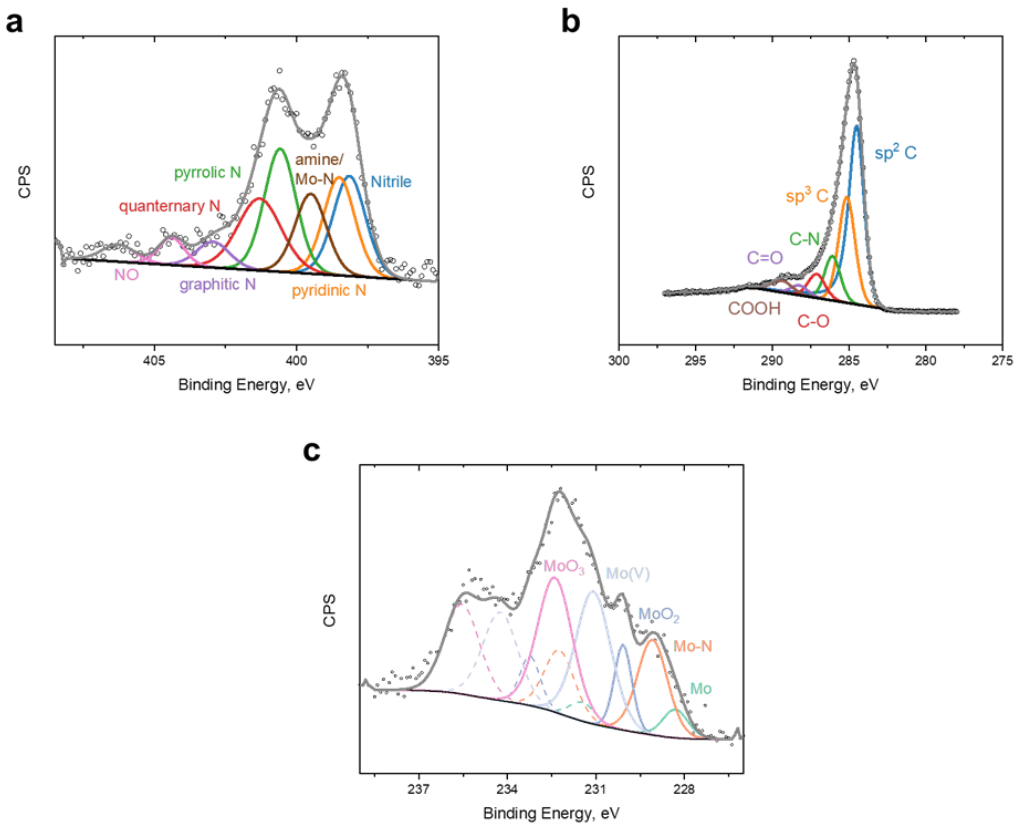

Appendix A.24 XPS spectra of the Mo-N-C catalyst (a) N 1s spectra confirming the formation of M-N_x moieties. (b) C 1s spectra (c) Mo 3d spectra indicating the presence of Mo-N_x sites.

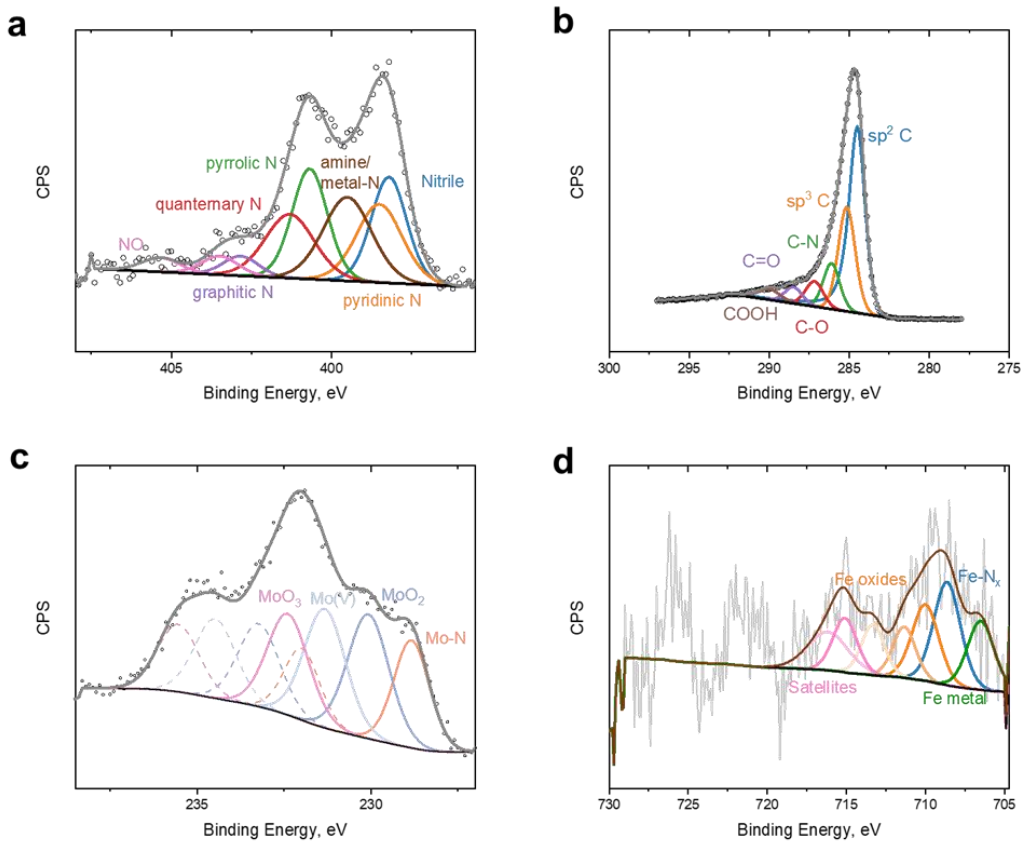

Appendix A.25 XPS spectra of the FeMo-N-C catalyst (a) N 1s spectra confirming the formation of M-N_x moieties. (b) C 1s spectra (c) Mo 3d spectra indicating the presence of Mo-N_x sites (d) Fe 2p spectra inidicating the presence of Fe-N_x sites.

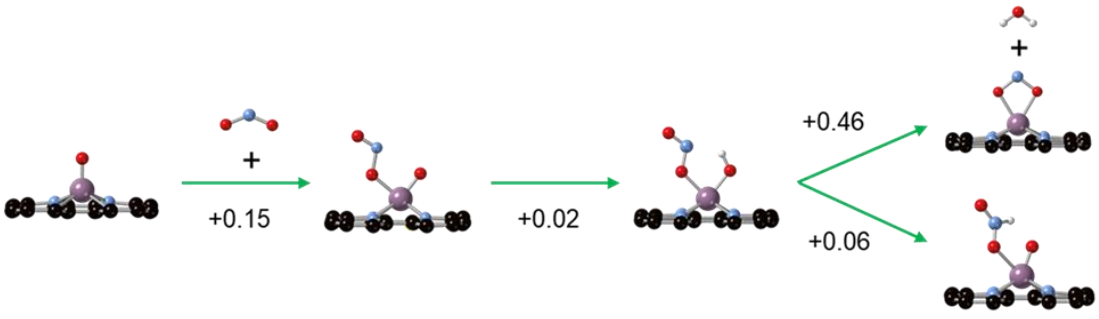

Appendix A.26 Reaction coordinate of the catalytic cycle of NO_2^- generation over the *O-Mo active site, via the adsorption of NO_2^- on the *O-Mo site with DFT calculated Gibbs free energies.

Table 1. DFT calculated electronic energy, zero-point vibrational energies, and the entopic term (T=298.15 K) of gas phase and adsorbed species used for the calculation of the free energy diagrams for NO_3^- to NO_2^- conversion on M-N_4 sites (* denotes M-N_4 site).

Species	E/ eV	ZPE/ eV	TS/ eV
H_2	-6.770	0.27	0.41
N_2	-15.479	0.16	0.59
O_2	-7.939	0.11	0.63
H_2O	-13.196	0.58	0.67
HNO_3	-25.213	0.71	0.83
HNO_2	-20.345	0.55	0.77
*NO_3	-292.239 (Fe-N_4) -294.103 (Mo-N_4)	0.42	0.19
*NO_3H	-295.405 (Fe-N_4) -298.121 (Mo-N_4)	0.65	0.27
*NO_2	-287.679 (Fe-N_4) -289.142 (Mo-N_4)	0.33	0.27
*NO_2H	-291.599 (Fe-N_4) -291.899 (Mo-N_4)	0.61	0.27
*O	-275.230 (Fe-N_4) -278.616 (Mo-N_4)	0.08	0.09
*OH	-279.668 (Fe-N_4) -281.285 (Mo-N_4)	0.35	0.12
*O + *NO_3	-300.676 (Mo-N_4)	0.51	0.27
*OH + *NO_3	-304.098 (Mo-N_4)	0.81	0.31

*OO	-284.222 (Mo-N_4)	0.15	0.16
*O + *OH	-288.052 (Mo-N_4)	0.42	0.20
*H	-273.283 (Fe-N_4)	0.16	0.0
	-273.514 (Mo-N_4)		
*	-269.811 (Fe-N_4)	0	0
	-269.344 (Mo-N_4)		

Table 2. ICP-MS of Fe-N-C, Mo-N-C and FeMo-N-C electrocatalysts.

Catalyst	**Fe (wt%)**	**Mo (wt%)**
Fe-N-C	0.73	0
Mo-N-C	0	1.36
FeMo-N-C	0.38	0.77

Table 3. Comparison of Literature of the NO_3RR for NH_3 synthesis.

Catalyst	**Electrolyte**	**Mass Loading (mg cm^{-2})**	**Yield rate (µg mg^{-1} hr^{-1})**	**Yield rate (µmol cm^{-2} hr^{-1})**	**Yield rate (mmol mg_{metal}^{-1} h^{-1})**	**NH_3 Faradaic Efficiency (%)**	**Stability**	**Reference**
FeMo-N-C (SAC)	0.05M PBS + 0.16M NO_3^-	0.5	602	17.7	3.4	94.7 (-0.45V vs RHE)	90.8% FE over 60 hrs (5x 12 hr cycles)	This Work
Cu-N-C (SAC)	0.05M K_2SO_4 + 50 ppm NO3-	33.5 (7.6 Cu)	1.15	2.27	0.0003	19.5 (-0.945 V vs RHE)	19.5% over 12 hrs	[165]
Cu/Cu2O NWAs	0.5M Na_2SO_4 + 200 ppm NO_3^-	x	x	244.9	x	95.8 (-0.85 V vs RHE)	95% over 12 hrs (6x 2 hr cycles)	[166]
PTCDA/O-Cu	0.1M PBS + 500 ppm NO_3^-	13 (PTCDA) / 0.099 Cu	33.54	25.6	0.13	77 (-0.40 V vs RHE)	85.9% FE over 4 hrs	[87]
Fe-N-C (SAC)	0.1M K_2SO_4 + 0.5M NO_3^-	0.4	5245	123.2	20.53	75 (-0.66 V vs RHE)	75% over 10 hrs (10x 0.5 hr cycles)	[63]

Pd cuboctahedron	0.1M NaOH + 0.02M NO_3^-	x	307	x	0.018	35.1 (-0.20 V vs RHE)	35.1% FE over 4 hrs	[167]
Strained Ru nanoclusters	1.0M KOH + 1M NO_3^-	0.185	23,682	1,029	x	>96 (-0.2 V vs RHE)	>96 over 100 hrs (100x 1 hr cycle)	[123]
TiO2-x	0.5M Na_2SO_4 + 50 ppm NO_3^-	1	766.4	45	0.045	85 (0.97 V vs RHE)	FE not reported for cycles	[168]
Cu-Ni alloy	1.0M KOH + 0.1M NO_3^-	x	x	x	x	99 (-0.15 V vs RHE)	95% (12 hrs)	[106]
Fe-PPy (SAC)	0.1M KOH + 0.1M NO_3^-	0.24	304.6	73.1	12.8	100 (-0.50 V vs RHE)	95% over 4.5 hrs (9x 0.5 hr cycles)	[64]

Table 4. Turn over frequency for NH_3 over the Fe-N-C, Mo-N-C and FeMo-N-C catalysts for the NO_2RR and NO_3RR at -0.45 V *vs.* RHE.

Catalyst	**NO_2RR TOF (s^{-1})**	**NO_3RR TOF (s^{-1})**
Fe-N-C	$1.4*10^{-4}$	$4.1*10^{-5}$
Mo-N-C	$3.6*10^{-5}$	$2.3*10^{-5}$
FeMo-N-C	$9.8*10^{-5}$	$7.2*10^{-5}$

Table 5. XPS atomic concentration of O, C and N in the Fe-N-C, Mo-N-C and FeMo-N-C electrocatalysts, obtained from the O 1s, C 1s and N 1s spectra, respectively.

	Fe-N-C	Mo-N-C	FeMo-N-C
Element	% Atomic Conc.	% Atomic Conc.	% Atomic Conc.
O 1s	1.0	2.7	1.5
C 1s	85.1	86.9	85.7
N 1s	13.9	9.9	11.6

Appendix A.27 Computational Details

To study the activity of the MN_4 sites for NO_3RR, we considered two following paths in the conversion of NO_3^- to NO_2^-.

Pathway *via* associative NO_3^- adsorption:

$$MN_4 + NO_3^- \rightarrow MN_4\text{-}NO_3 + e^-$$

$$MN_4\text{-}NO_3 + 2H^+ + 2e^- \rightarrow MN_4\text{-}NO_2 + H_2O$$

After which NO_2^- can be converted to NH_3 as studied in Refs ([63,65]) or desorb from the catalyst:

$$MN_4\text{-}NO_2 + e^- \rightarrow MN_4 + NO_2^-$$

In the alternative path, the adsorption of NO_3^- is dissociative forming adsorbed *O and NO_2^-. Adsorbed *O can be removed from MN_4 sites by reducing the adsorbed *O to form H_2O.

Pathway *via* dissociative NO_3^- adsorption:

$$MN_4 + NO_3^- \rightarrow MN_4\text{-}O + NO_2^-$$

$$MN_4\text{-}O + 2H^+ + 2e^- \rightarrow MN_4 + H_2O$$

Free energy diagrams for the above reactions at pH = 7 were calculated using the following formula:

$$\Delta_{\mathrm{r}}G = \Delta E + \Delta\mathrm{ZPE} - T\Delta S + n_{H+}0.059p\mathrm{H}$$

where ΔE is the change in the electronic energy during the considered reaction, ΔZPE is the change in the zero-point energy, ΔS is the change in the entropy, and $n_{\mathrm{H+}}$ is the number of exchanged protons. ZPE values and ΔS values are tabulated in **TableDFT_S1**. ZPE values were evaluated from the DFT calculated vibrational frequencies and entropy changes were obtained from standard molecular tables.[169] Using the standard hydrogen electrode, the chemical potential for the proton/electron pair is related to that of the $H^+ + e^- = 1/2H_2$.

Using the approach by Calle-Vallejo in Ref. [56], the DFT binding energies of NO_3^-/NO_2^- were calculated with respect to H_2 and HNO_3/HNO_2 acid in the gas phase. The choice of a gas reference based on H_2 and HNO_3/HNO_2 instead of using dissolved NO_3^-/NO_2^- is due to the difficulties of DFT to describe accurately the electronic energies and solvation of NO_3^-/NO_2^- ions. Gibbs free energy for the reaction

(PA) $MN_4 + NO_3^- \rightarrow MN_4\text{-}NO_3 + e^-$

was, therefore, calculated from the Gibbs free energies for reactions (PAa) and (PAb)

(PAa) $HNO_3\ (g) \rightarrow H^+ + NO_3^-$

(PAb) $MN_4 + HNO_3\ (g) \rightarrow MN_4\text{-}NO_3 + H^+ + e^-$

using

$$\Delta G(\mathrm{PA}) = \Delta G(\mathrm{PAb}) - \Delta G(\mathrm{PAa}) = \Delta G(\mathrm{PAb}) + 0.392$$

Equivalently, for the NO_2^- desorption, Gibbs free energy for the reaction

(PD) $MN_4\text{-}NO_2 + e^- \rightarrow MN_4 + NO_2^-$

was calculated from Gibbs free energies for the reactions (PDa) and (PDb)

(PDa) $HNO_2\ (g) \rightarrow H^+ + NO_2^-$

(PDb) $MN_4 + HNO_2\ (g) \rightarrow MN_4\text{-}NO_2 + H^+ + e^-$

using

$$\Delta G(\mathrm{PD}) = \Delta G(\mathrm{PDa}) - \Delta G(\mathrm{PDb}) = 0.007 - \Delta G(\mathrm{PDb})$$

Experimental values of were taken for reaction (PAa) and (PDa) in the value of -0.392 and 0.007 eV, while the Gibbs free energy for reaction (PAb) and (PDb) were calculated with DFT. In addition, DFT calculated Gibbs free energy for the formation of HNO_3 and HNO_2 were corrected for the difference between DFT-calculated and experimental formation energies of HNO_3/HNO_2, which for the optB86b-vdW functional were calculated as -0.46 eV and -0.30 eV. Namely, DFT calculated formation energies of HNO_3 and HNO_2 are overestimated within DFT i.e., they are calculated as -1.24 eV and -0.76 eV, while the experimental values are -0.77 eV and -0.46 eV for HNO_3 and HNO_2, respectively.[169]

Appendix B - Chapter 3

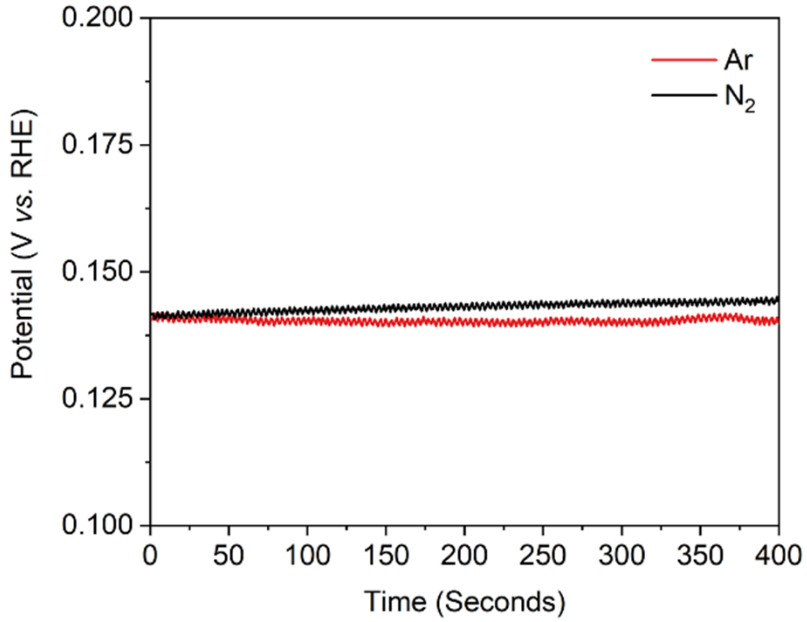

Appendix B.1 Open circuit voltage (OCV) measurements when the electrolyte is saturated in N_2 or Ar. The negligible difference in the OCV suggests that the use of either N_2 or Ar does not alter the equilibrium potentials of the NO_3RR process.

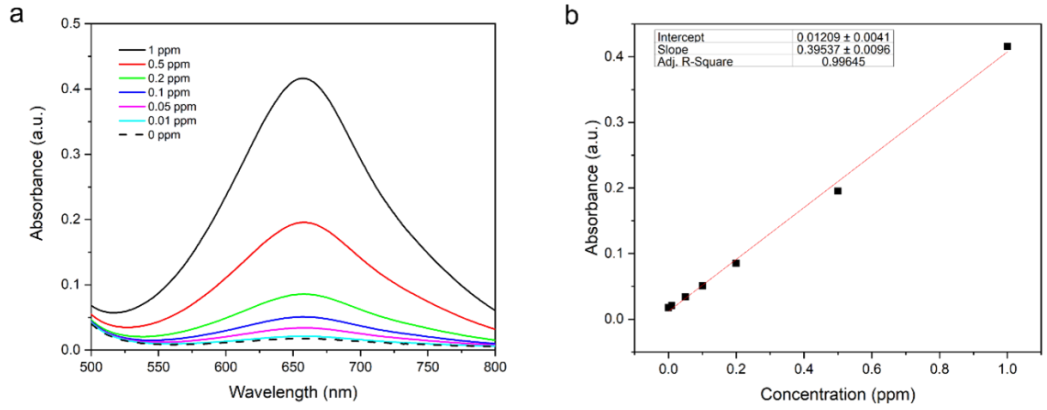

Appendix B.2 Calibration curves for the Indophenol blue method for NH_3 detection in 0.05M PBS electrolyte. (a) Raw UV-Vis curves and (b) linear calibration.

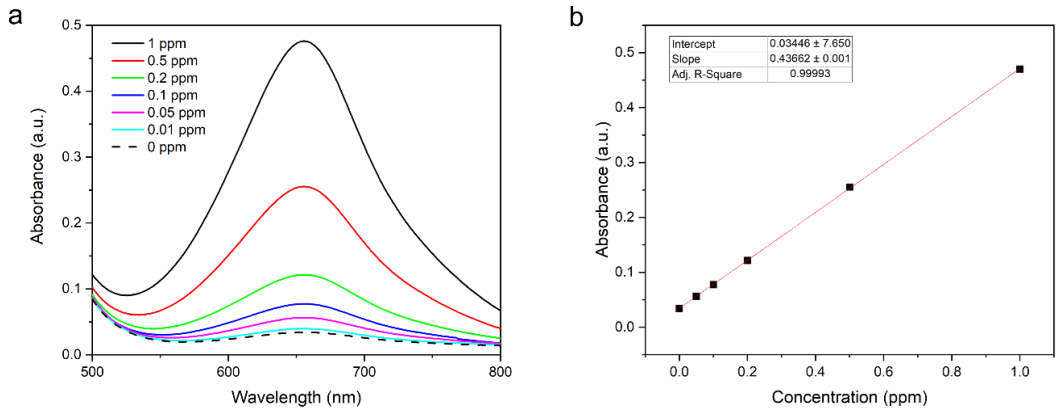

Appendix B.3 Calibration curves for the Indophenol blue method for NH_3 detection in 1M KOH electrolyte. (a) Raw UV-Vis curves and (b) linear calibration.

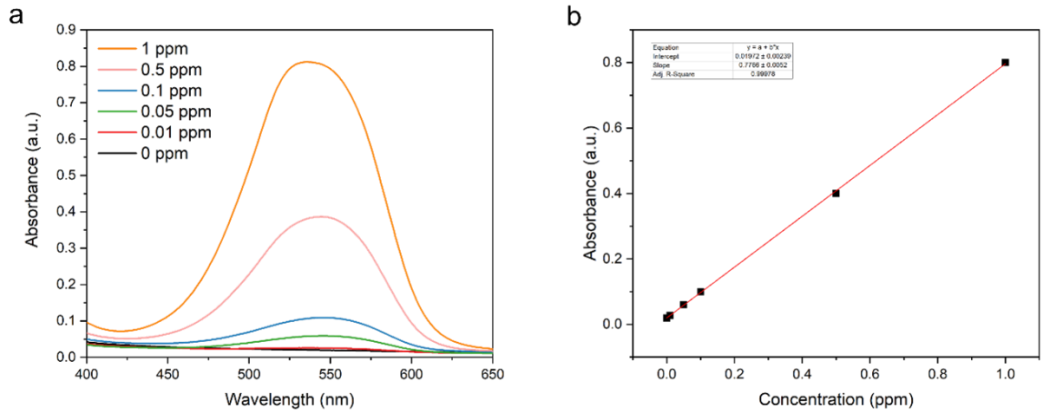

Appendix B.4 Calibration curves for the Griess method for NO_2^- detection in 0.05M PBS electrolyte . (a) Raw UV-Vis curves and (b) linear calibration.

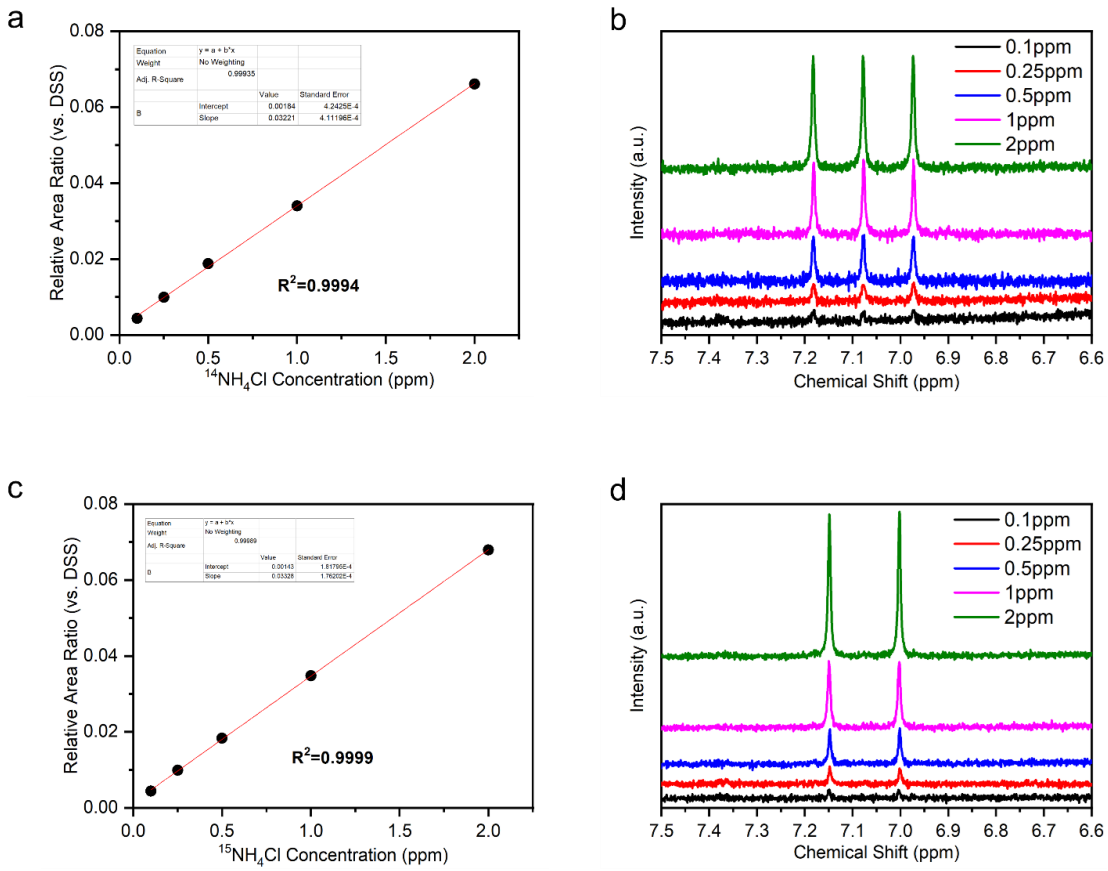

Appendix B.5 Calibration curves for the detection of NH_3 with ^1H NMR. (a) Linear calibration for the detection of $^{14}NH_4$, (b) ^1H NMR spectra for $^{14}NH_4$, (c) Linear calibration for the detection of isotopic $^{15}NH_4$, (d) ^1H NMR spectra for $^{15}NH_4$.

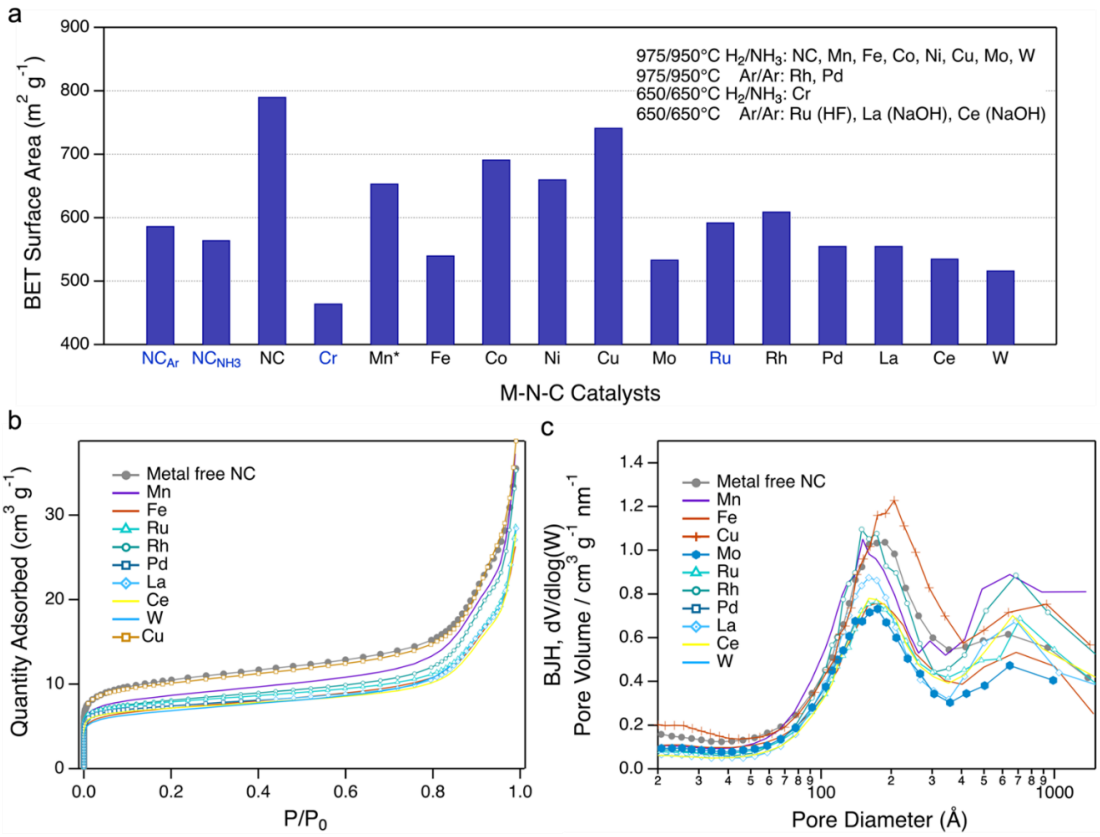

Appendix B.6 (a) BET surface area of the metal free N-C and M-N-C catalysts. The surface area of all M-N-C catalysts falls between 550 and 750 m^2/g. (b) N_2 sorption isotherm for the metal free N-C and M-N-C Catalysts. (c) pore size distribution in the meso/macro-porous range, showing distinct microporosity at *ca.* 20 nm and *ca.* 80 nm for all M-N-C catalysts, characteristic of the diameter of the sacrificial silica template.

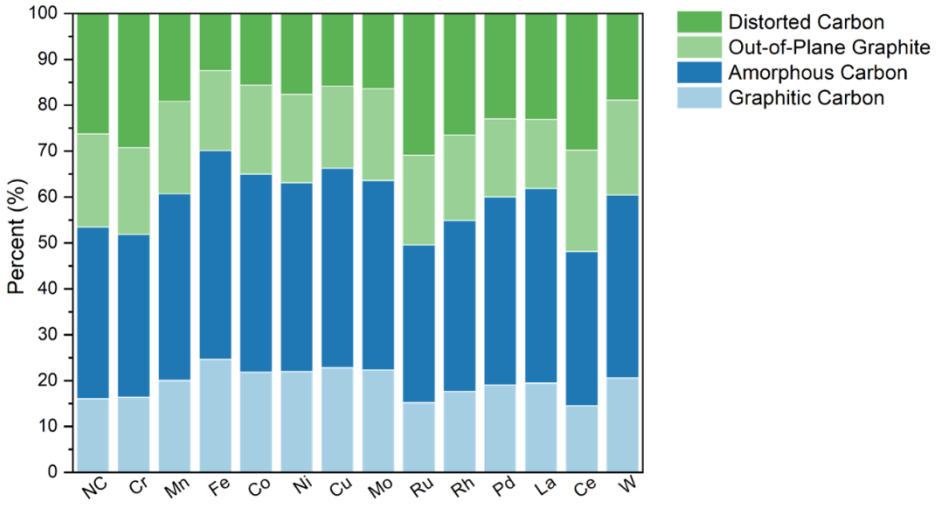

Appendix B.7 Carbon composition of the M-N-C catalysts as determined by deconvoluted Raman spectra of the D and G bands. Demonstrating similar carbon composition of all the M-N-C catalysts.

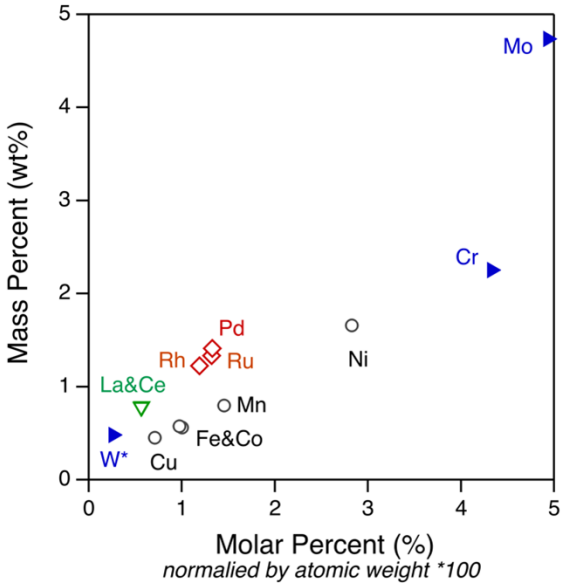

Appendix B.8 Metal loading of M-N-C catalysts determined by ICP-MS. The Y-axis is the mass percent as determined by the ICP-MS, while the X-axis is normalized by the molar mass of the metal element.

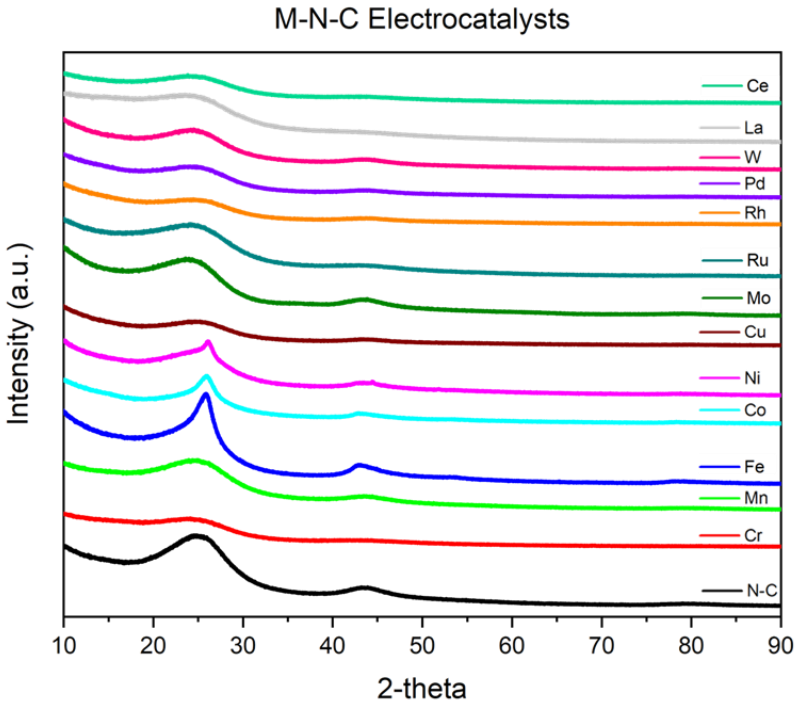

Appendix B.9 X-ray diffraction patterns of the metal free N-C and M-N-C catalysts. All materials show only the (002) and (100) graphitic peaks, indicating the absence of any metallic crystalline phases in the materials, characteristic of atomically dispersed materials.

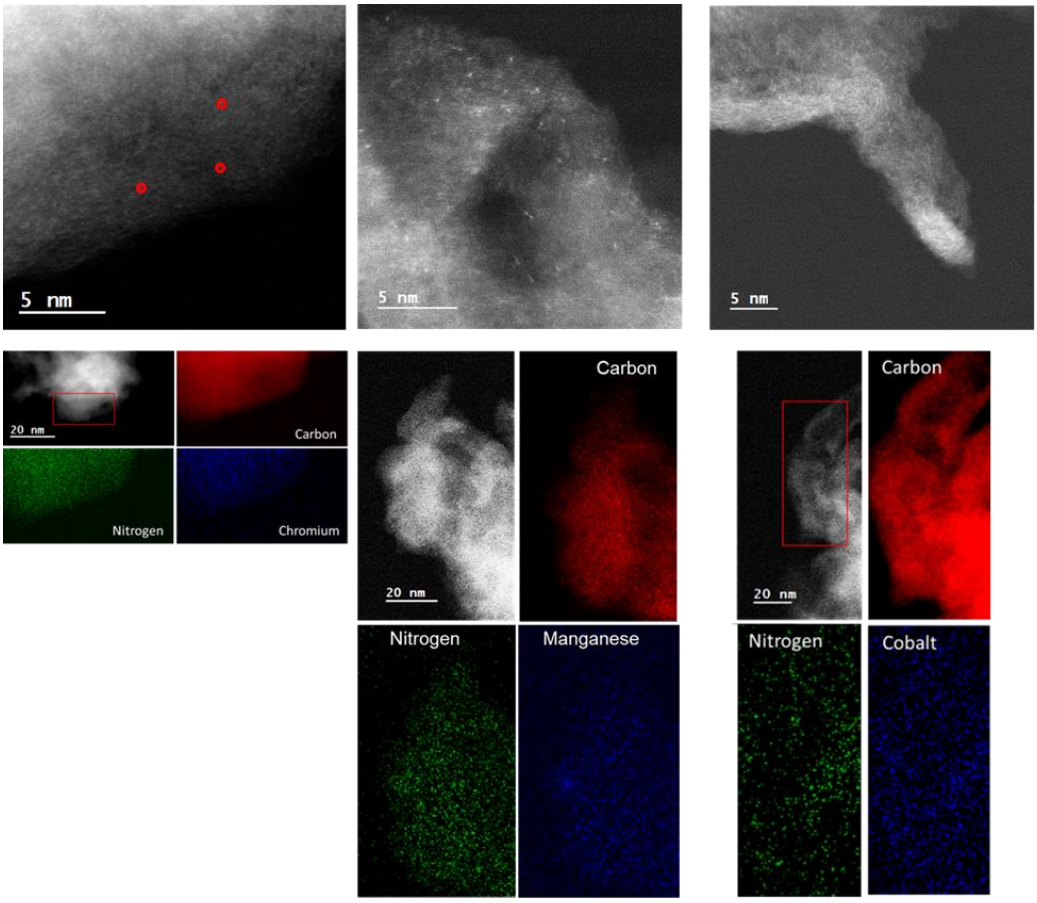

Appendix B.10 AC-HAADF STEM images and corresponding EDS mapping of the carbon, nitrogen and metal elements for the (a) Cr-N-C (b) Mn-N-C and (c) Co-N-C catalysts. Demonstrating the atomically dispersed metal sites and homogenous distribution of C, N and metal in the materials.

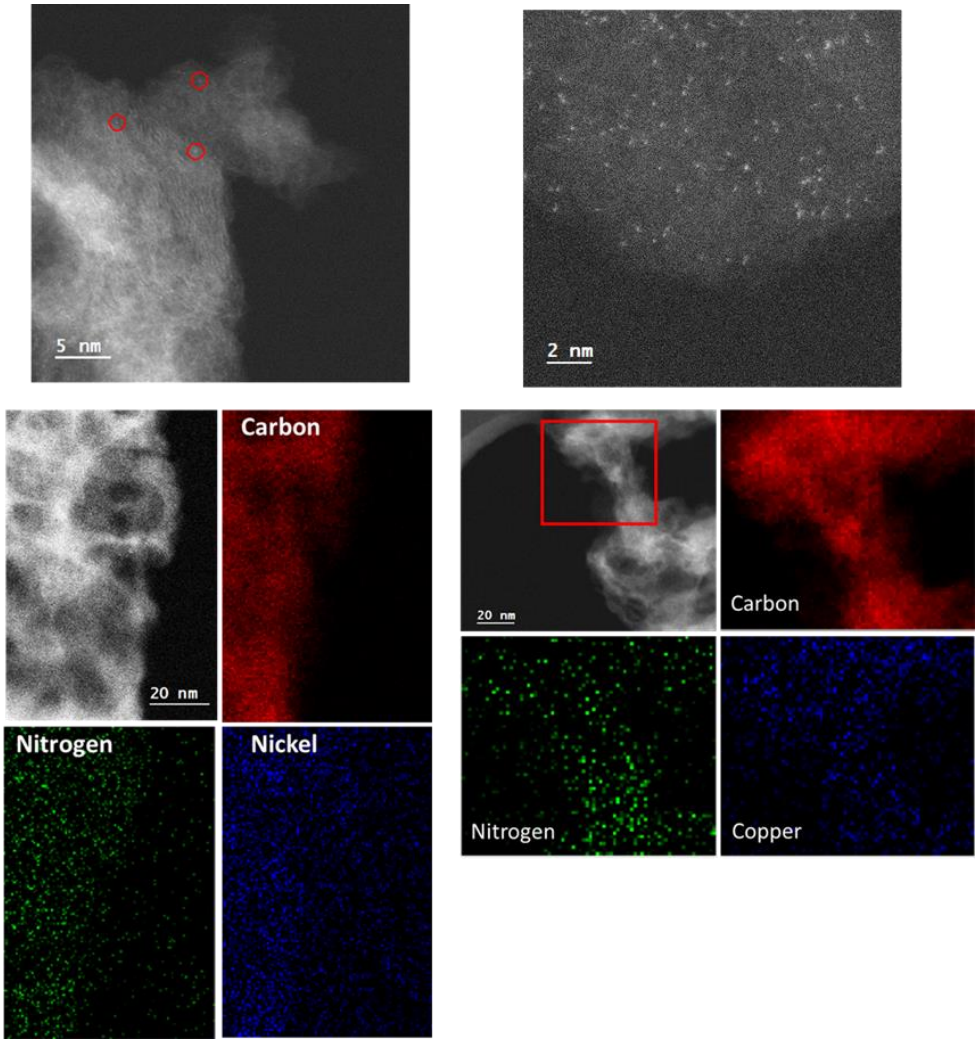

Appendix B.11 AC-HAADF STEM images and corresponding EDS mapping of the carbon, nitrogen and metal elements for the (a) Ni-N-C and (b) Cu-N-C. Demonstrating the atomically dispersed metal sites and homogenous distribution of C, N and metal in the materials.

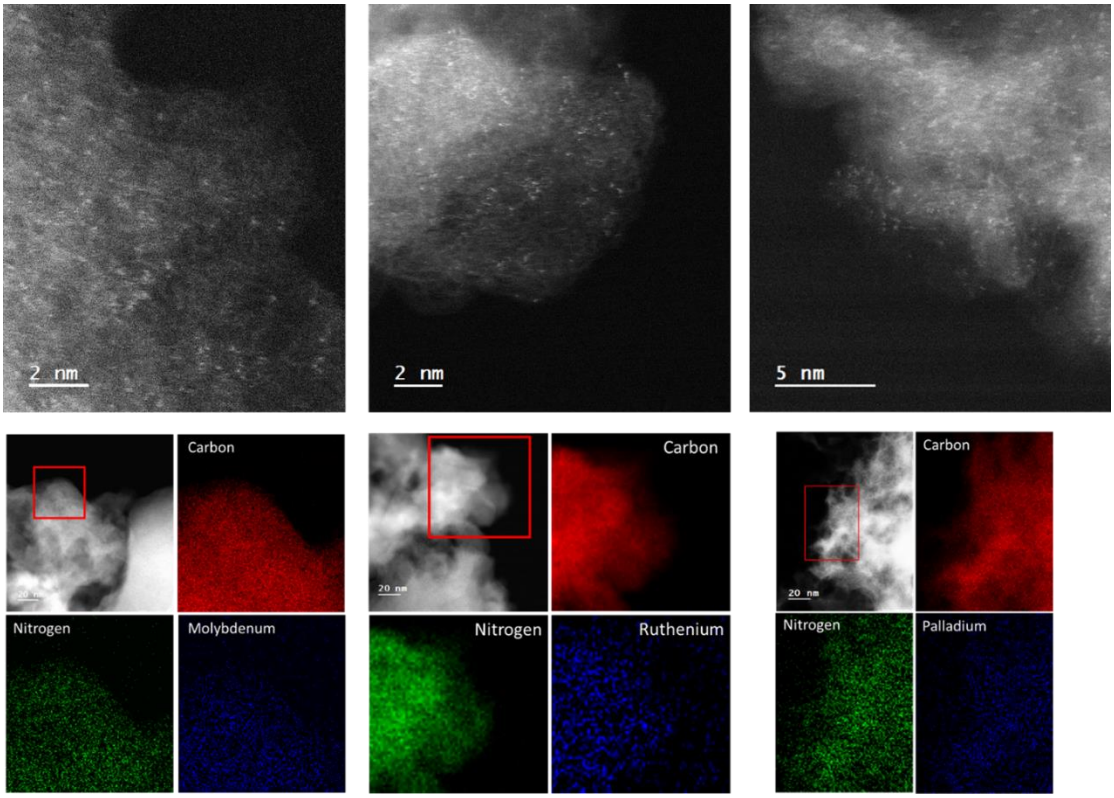

Appendix B.12 AC-HAADF STEM images and corresponding EDS mapping of the carbon, nitrogen and metal elements for the (a) Mo-N-C (b) Ru-N-C and (c) Pd-N-C. Demonstrating the atomically dispersed metal sites and homogenous distribution of C, N and metal in the materials.

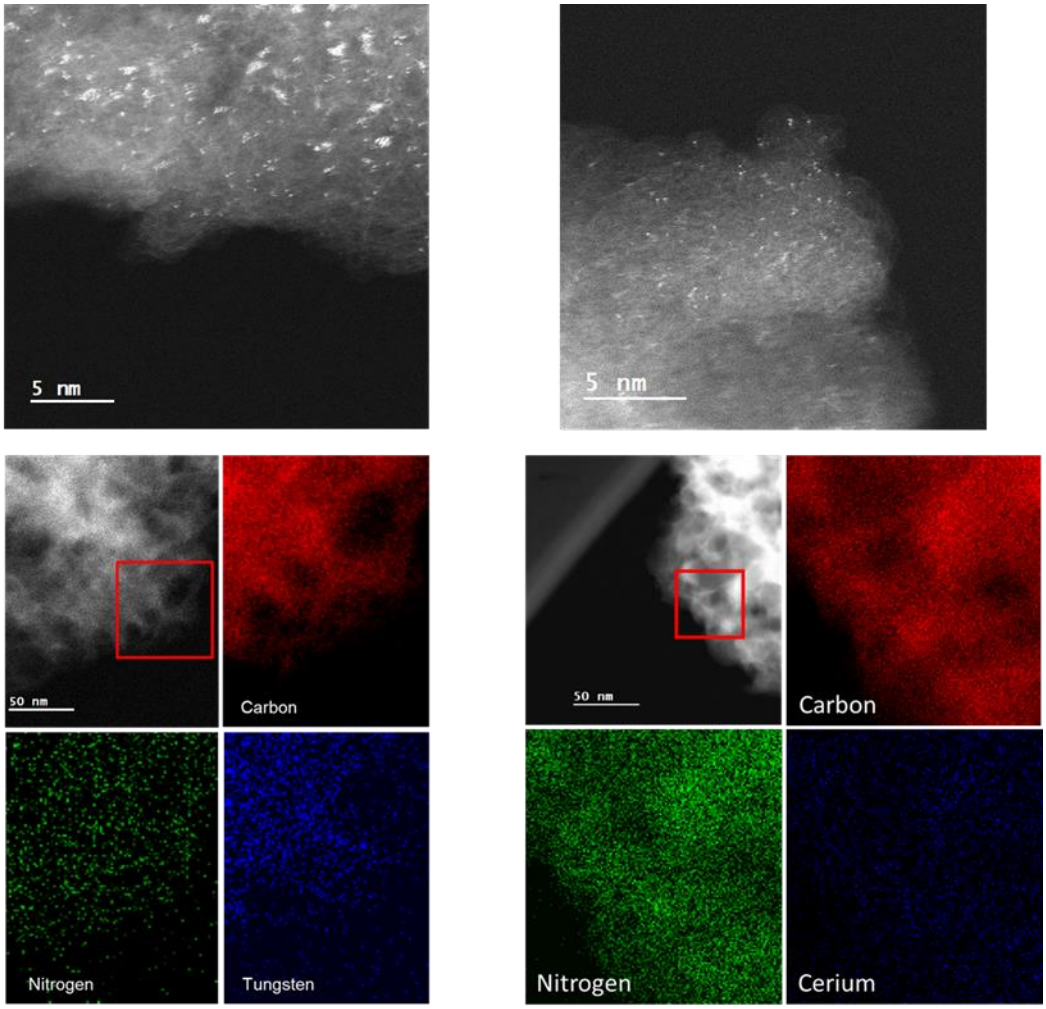

Appendix B.13 AC-HAADF STEM images and corresponding EDS mapping of the carbon, nitrogen and metal elements for the (a) W-N-C and (b) Ce-N-C. It can be seen that for W-N-C, while isolated atomically dispersed sites are present, the formation of 2-D nanoclusters are also present.

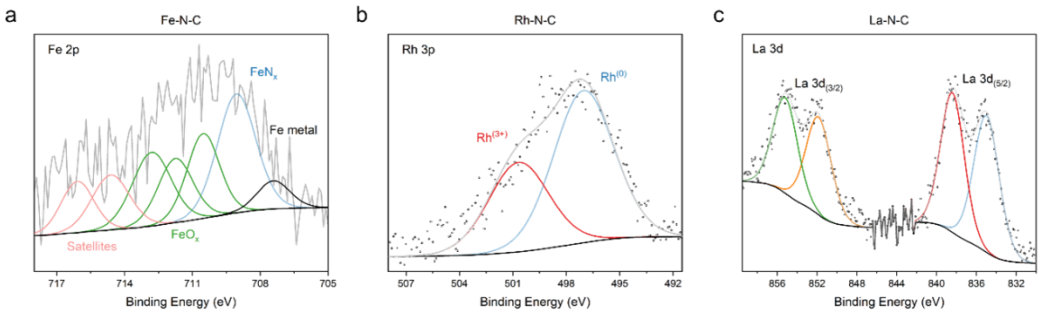

Appendix B.14 Deconvoluted XPS spectra for (a) Fe-N-C, showing a mixed oxidation state characteristic of Fe^{2+} and Fe^{3+}. (b) Rh-N-C, showing a mix between Rh^{0} and Rh^{3+}, equating to an oxidation state of ca. $Rh^{1.7+}$. (c) La-N-C, showing an oxidation state of La^{3+}.

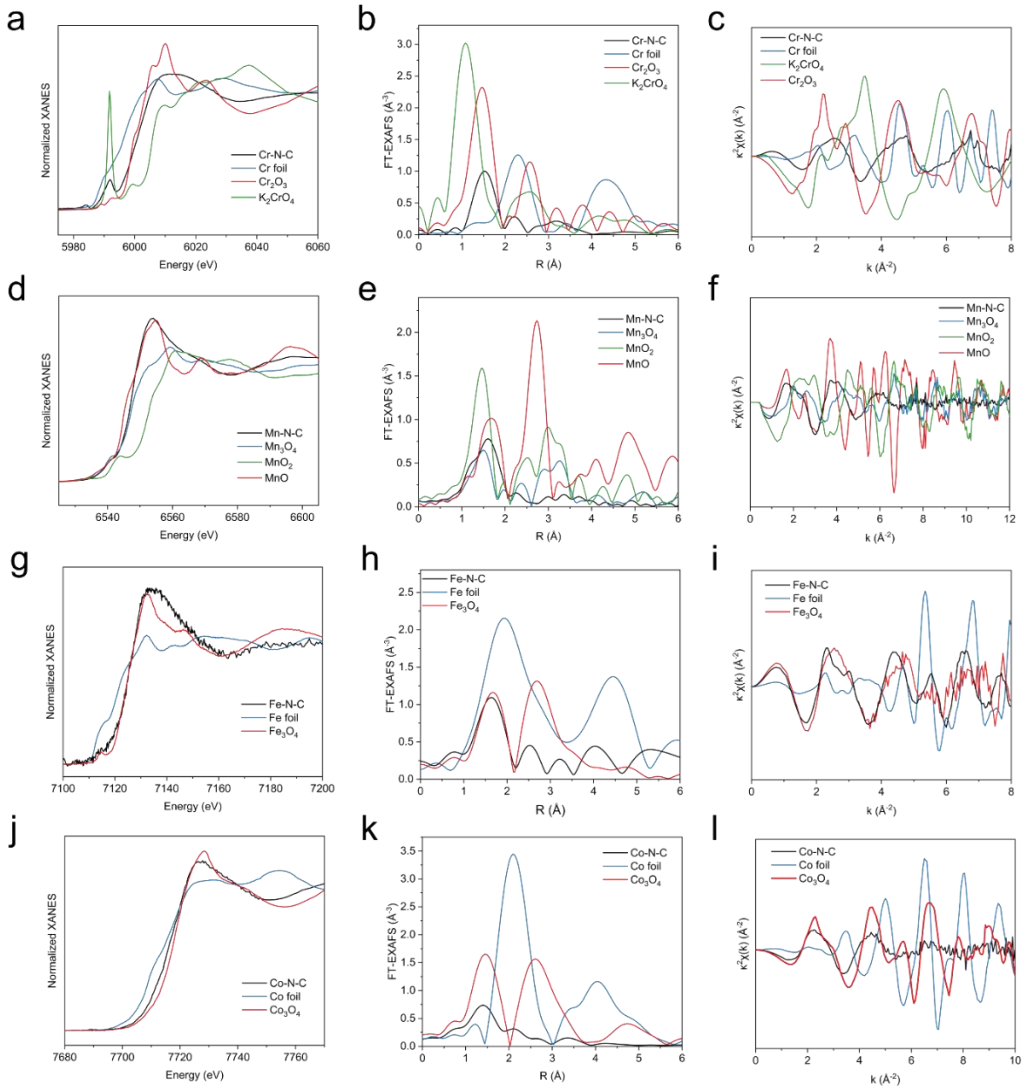

Appendix B.15 XANES, FT-EXAFS and EXAFS spectra for the *3d* metals (a-c) Cr-K edge in Cr-N-C, (d-f) Mn-K edge in Mn-N-C, (g-i) Fe-K edge in Fe-N-C and (j-l) Co-K edge in Co-N-C. See Supplementary note 1 for a full discussion on the XANES interpretation and determination of metal oxidation states and Supplementary Table 2 and Supplementary note 3 for a full discussion on the EXAFS analysis.

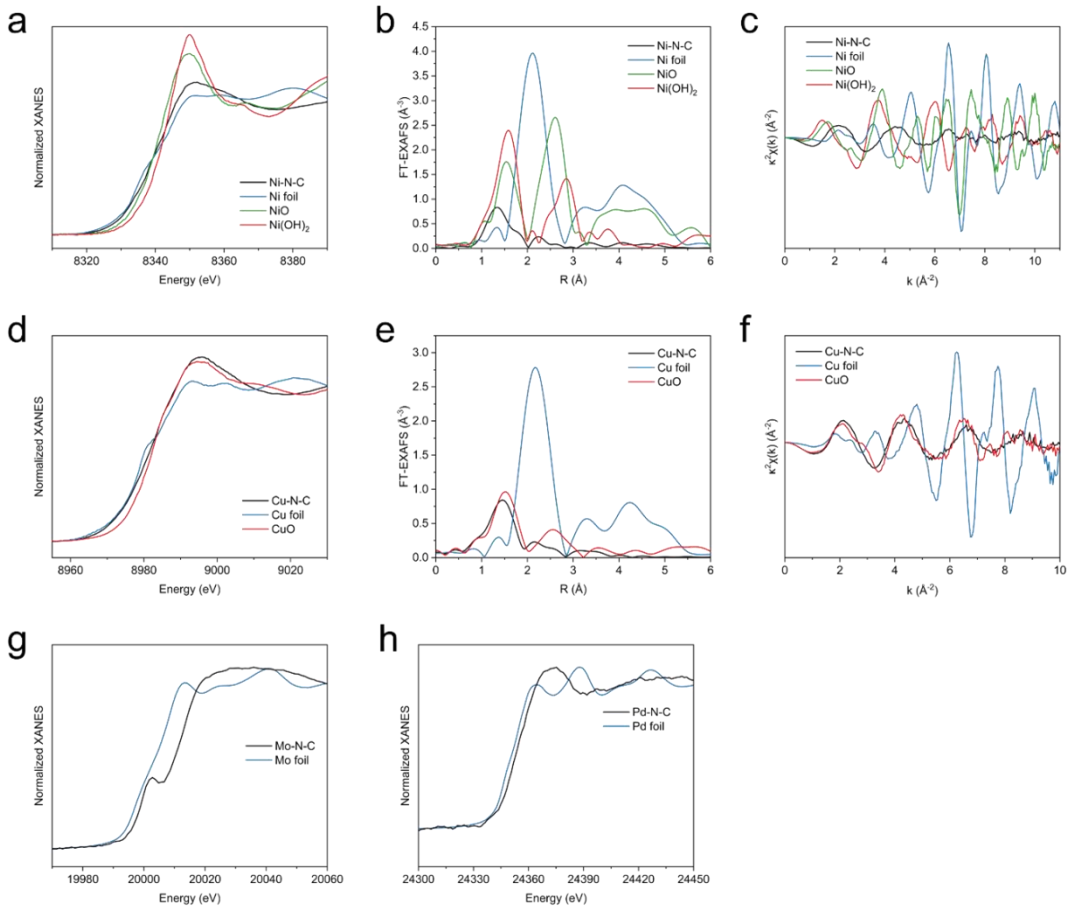

Appendix B.16 XANES, FT-EXAFS and EXAFS spectra *3d* metals (a-c) Ni-K edge in Ni-N-C and (d-f) Cu-K edge in Cu-N-C and XANES spectra for *4d* metals (g) Mo-K edge in Mo-N-C and (h) Pd-K edge in Pd-N-C. See Supplementary note 1 for a full discussion on the XANES interpretation and determination of metal oxidation states and Supplementary Table 2 and Supplementary note 3 for a full discussion on the EXAFS analysis.

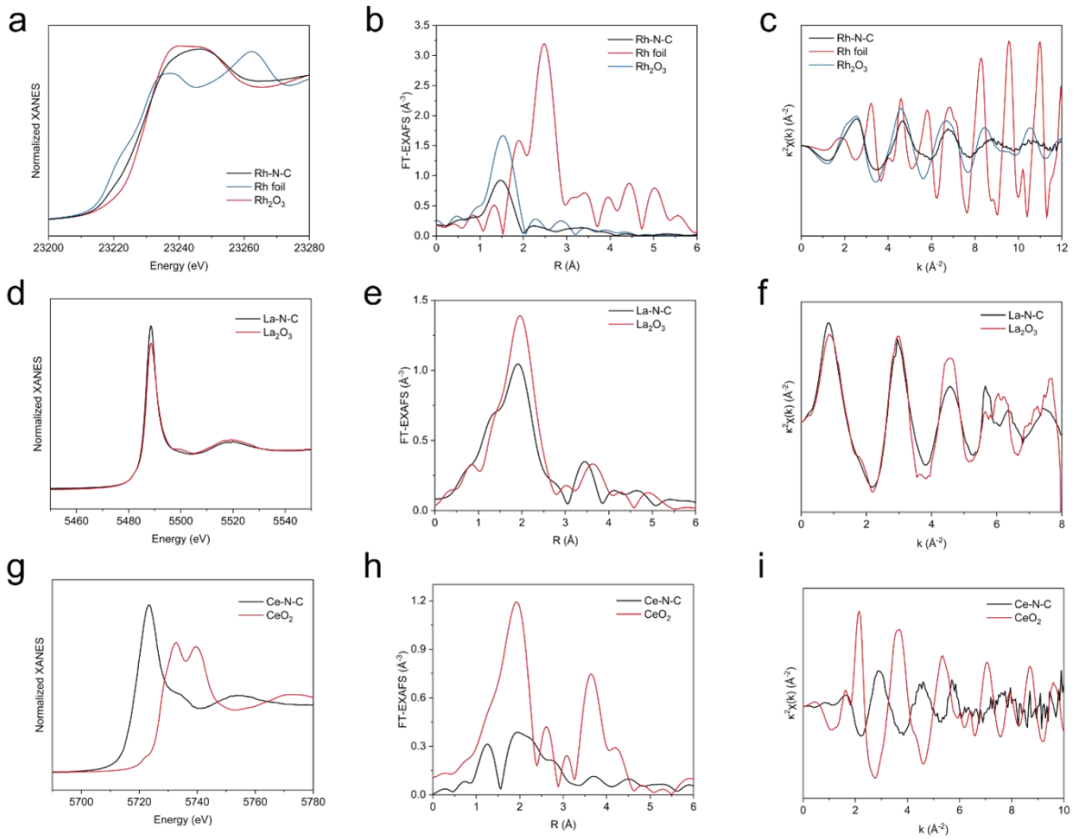

Appendix B.17 XANES, FT-EXAFS and EXAFS spectra for *4d* and *f*-metals (a-c) Rh-K edge in Rh-N-C, (d-f) La-L edge in La-N-C and (g-i) Ce-L edge in Ce-N-C. See Supplementary note 1 for a full discussion on the XANES interpretation and determination of metal oxidation states and Supplementary Table 2 and Supplementary note 3 for a full discussion on the EXAFS analysis.

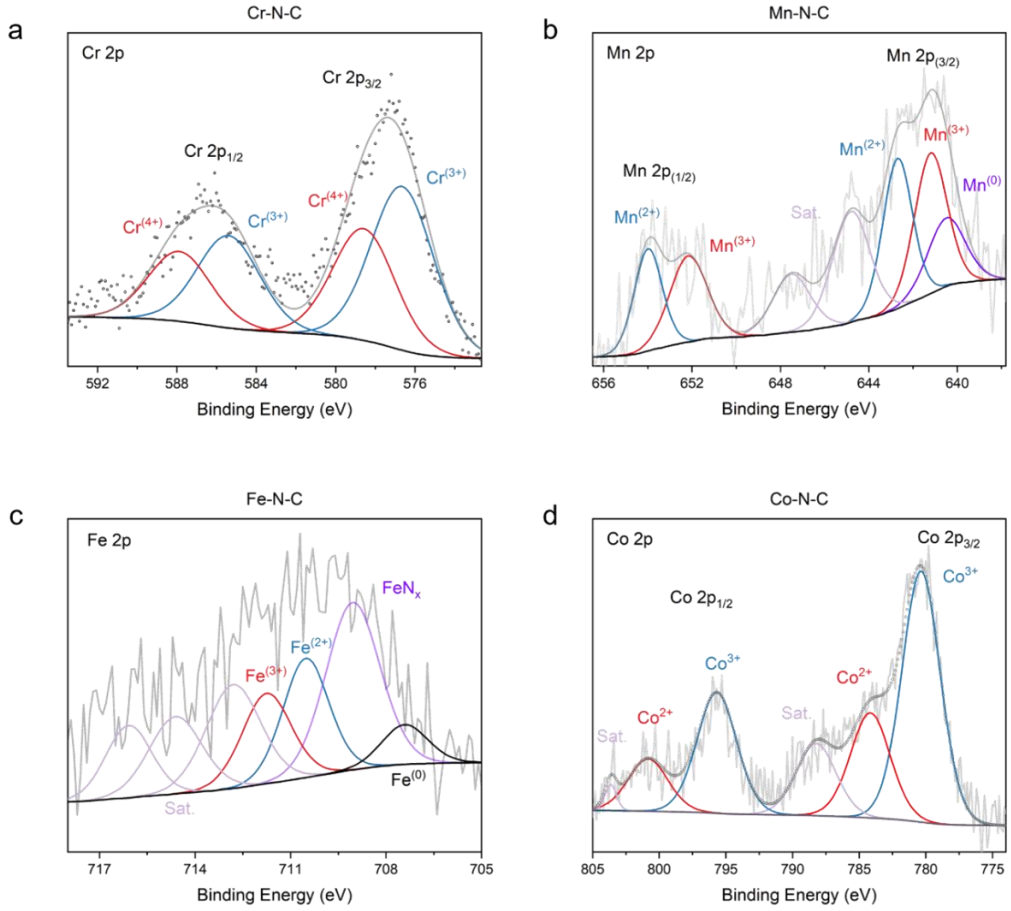

Appendix B.18 Deconvoluted XPS spectra for 3d metals (a) Cr-N-C, Cr 2p spectra showing a mixed oxidation state of Cr^{3+} and Cr^{4+}. (b) Mn-N-C, Mn 2p spectra showing a mix between Mn^{0} and Mn^{3+}. (c) Fe-N-C, Fe 2p spectra showing a mixed metal oxidation state between Fe^{0} and Fe^{3+}. (d) Co-N-C, Co 2p spectra showing a mixed metal oxidation state between Co^{2+} and Co^{3+}.

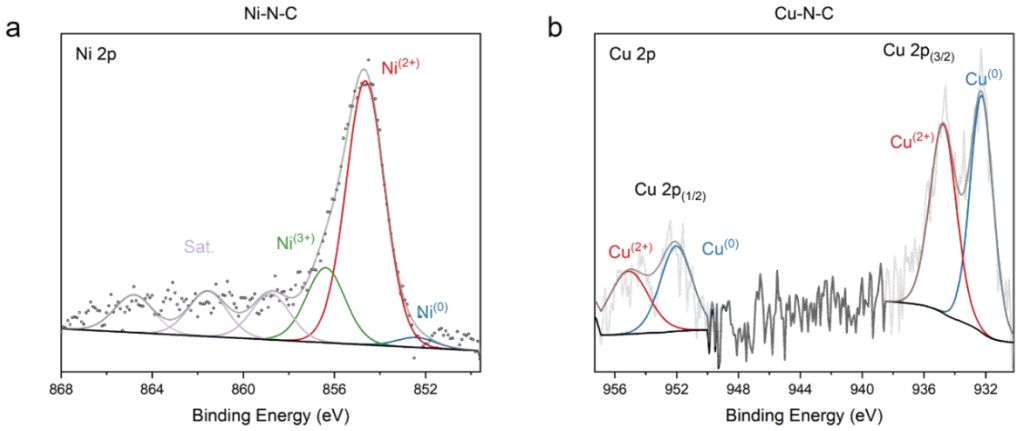

Appendix B.19 Deconvoluted XPS spectra for 3d metals (a) Ni-N-C, Ni 2p spectra showing a metal oxidation state between $Ni^{(0)}$ and Ni^{3+}. (b) Cu-N-C, Cu 2p spectra showing a metal oxidation state between $Cu^{(0)}$ and $Cu^{(2+)}$.

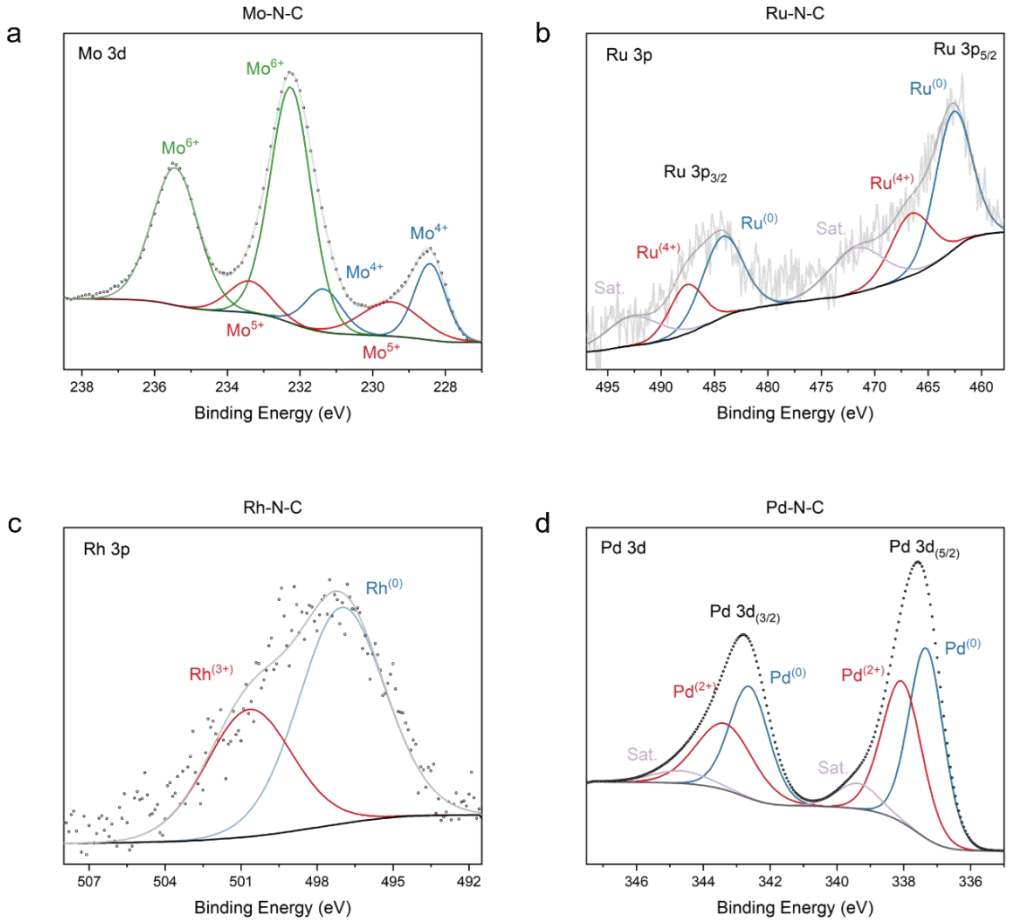

Appendix B.20 Deconvoluted XPS spectra for 4 d metals (a) Mo-N-C, Mo 3d spectra showing a metal oxidation state between Mo^{4+} and Mo^{6+}. (b) Ru-N-C, Ru 3p spectra showing a metal oxidation state between Ru^{0} and Ru^{4+}. (c) Rh-N-C, Rh 3p spectra showing a metal oxidation state between $Rh^{(0)}$ and $Rh^{(3+)}$. (d) Pd-N-C, Pd 3d spectra showing a metal oxidation state between $Pd^{(0)}$ and $Pd^{(2+)}$.

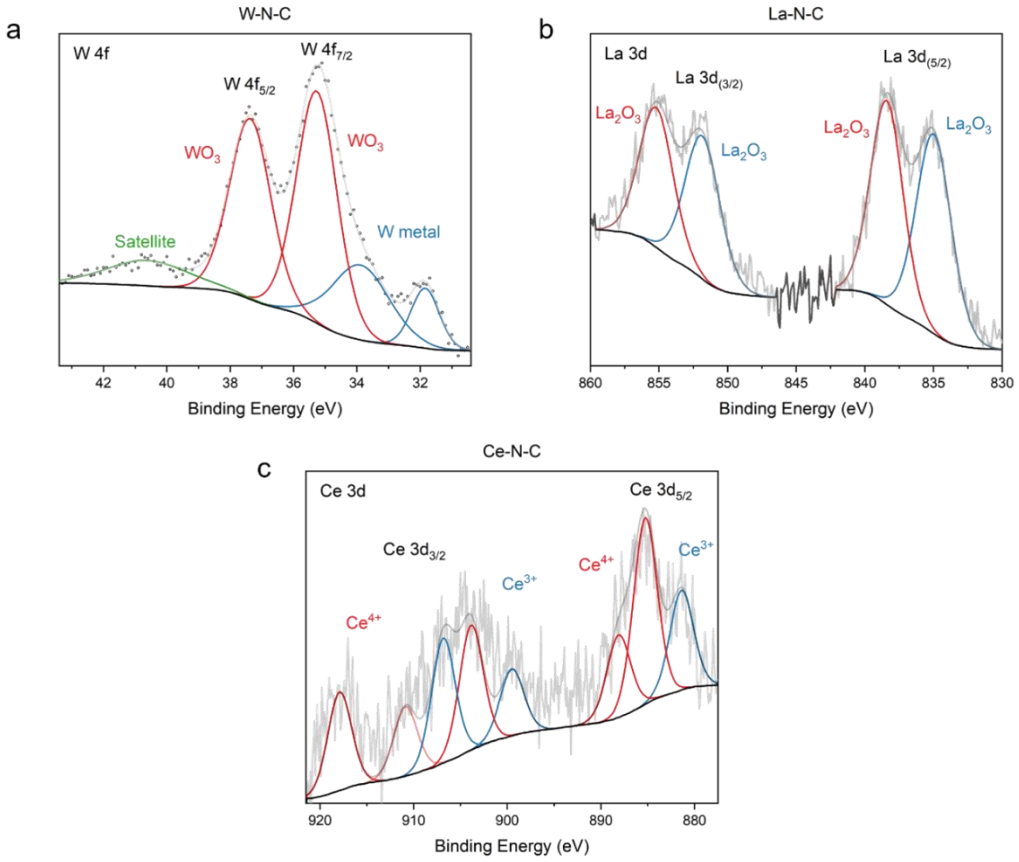

Appendix B.21 Deconvoluted XPS spectra for 5 d and f metals (a) W-N-C, W 4f spectra showing a metal oxidation state between $W^{(0)}$ and $W^{(6+)}$. (b) La-N-C, La 3d spectra showing a metal oxidation state of $La^{(3+)}$. (c) Ce-N-C, Ce 3d spectra showing a metal oxidation state between $Ce^{(3+)}$ and $Ce^{(4+)}$.

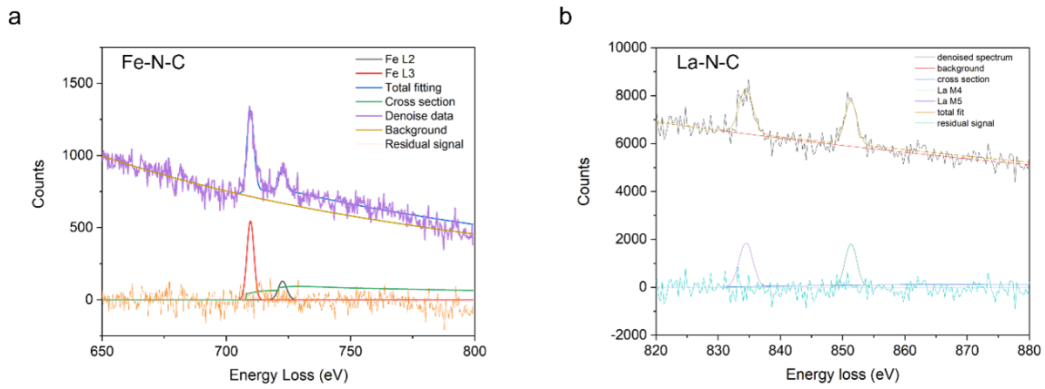

Appendix B.22 EELS valence state analysis. a) Fe-N-C, the Fe L_3/L_2 intensity ratio is 4.2, $L_2 - L_3$ separation distance is 12.9 eV, according to the literature this suggests a valance state of Fe close to Fe^{2+}. b) La-N-C, the La M_5/M_4 intensity ratio is 0.97, being close to a standard La_2O_3 sample, suggesting a La valence state close to La^{3+}.

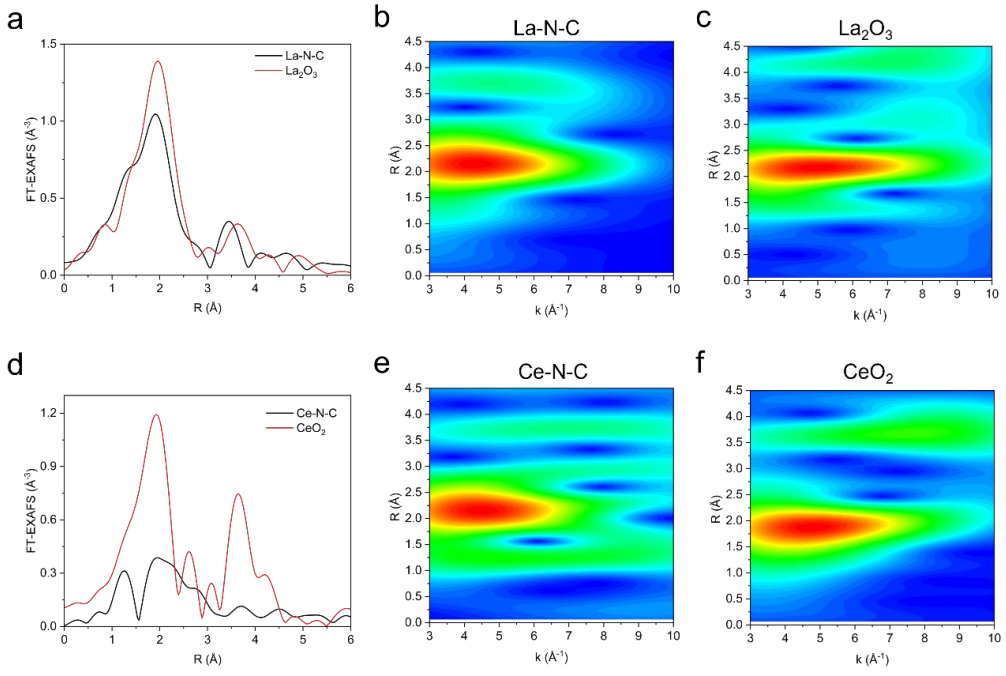

Appendix B.23 FT-EXAFS and wavelet transformation (WT) for *f*-metals (a-c) La-N-C and the corresponding La_2O_3 standard and (d-f) Ce-N-C and the corresponding CeO_2 standard. In the WT-EXAFS, in addition to the peak intensity observed at *ca.* 2.1 Å at low k-values, an additional peak is present at *ca.* 3.7 Å again at low k-values, indicating interactions with only low Z-number neighbors, in particular La-C. For Ce-N-C, the WT-EXAFS shows two features located at *ca.* 1.5 Å and 2 Å, both located at low k-values (*ca.* 4-5 $Å^{-1}$), matching the Ce-O intensity in the CeO_2 WT-EXAFS, indicating the split peaks for Ce-N-C constitute interactions between Ce and low Z number neighbors (C, N or O atoms). While an additional feature at 3.7 Å is also observed at higher k-number (7 $Å^{-1}$), suggesting that in addition to atomically dispersed Ce-N_x sites, the formation of small oxide clusters can coexist.

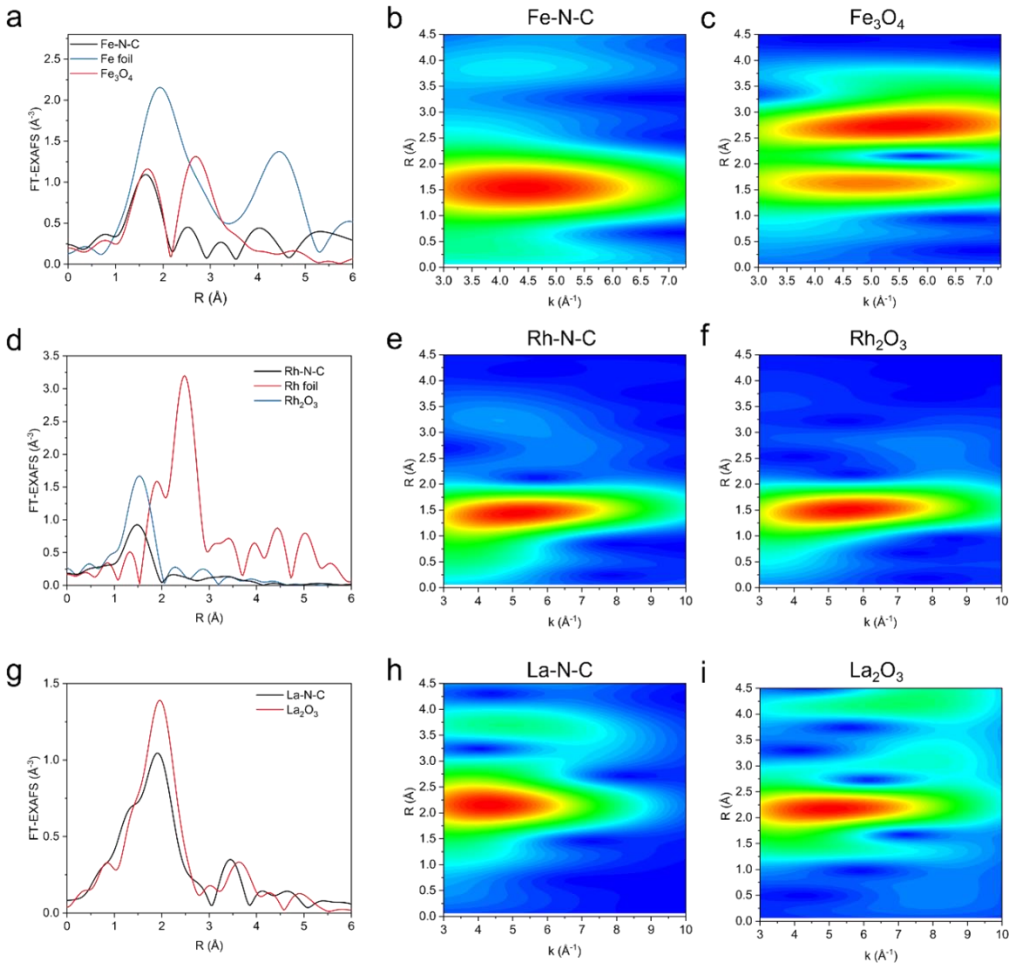

Appendix B.24 FT-EXAFS and WT-EXAFS for (a-c) Fe-N-C and the corresponding Fe_3O_4 standard, (d-f) Rh-N-C and the corresponding Rh_2O_3 standard (g-i) La-N-C with the corresponding La_2O_3 standard.

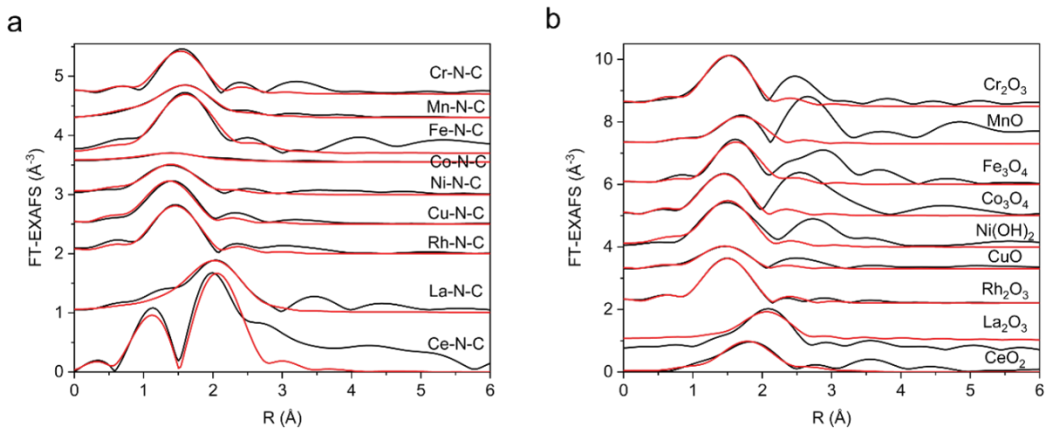

Appendix B.25 Fitting of the Fourier-transformed experimental (black lines) and fitted (red lines) EXAFS spectra for the M-N-C catalysts, where only contributions from the first coordination shell were considered. Note that for Ce-N-C two different paths were included in the fit, to describe the split distributions of bond-lengths to neighboring atoms due to the displacement of Ce from the center of Ce-N_4 unit.

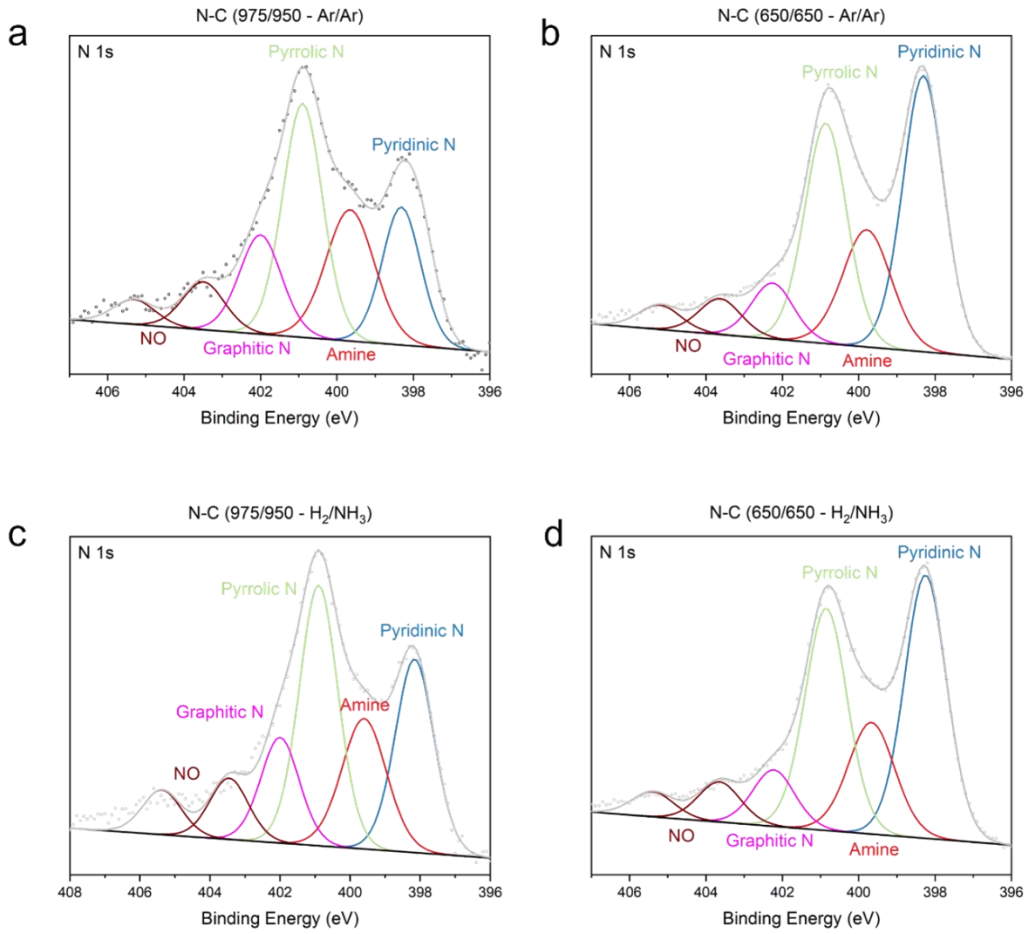

Appendix B.26 Deconvoluted N 1s XPS spectra for the metal free N-C synthesized under varying conditions. a) N-C (975-Ar / 950-Ar), b) N-C (650-Ar / 650-Ar), c) N-C (975-H_2 / 950-NH_3) and d) N-C (650- H_2 / 650- NH_3).

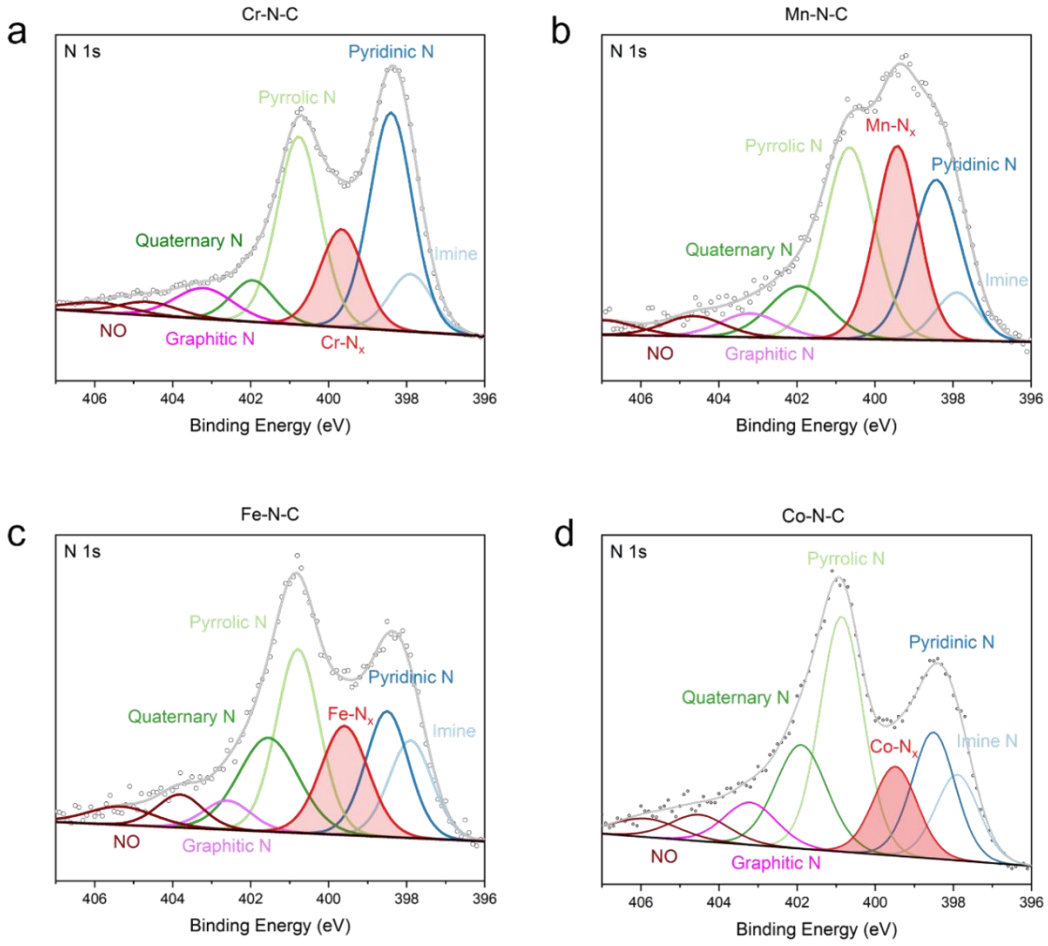

Appendix B.27 Deconvoluted N 1s XPS spectra for the 3d metal; Cr-, Mn-, Fe- and Co-N-C catalysts.

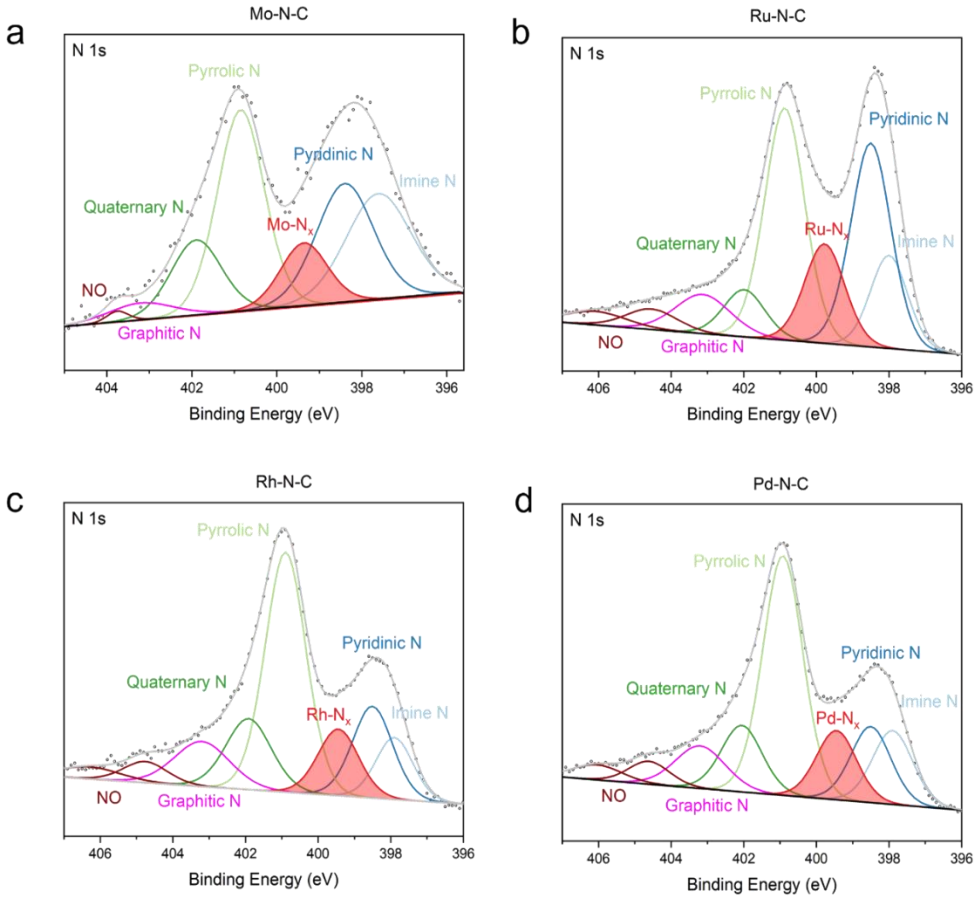

Appendix B.28 Deconvoluted N 1s XPS spectra for the 4d metal; Mo, Ru, Rh and Pd-N-C catalysts.

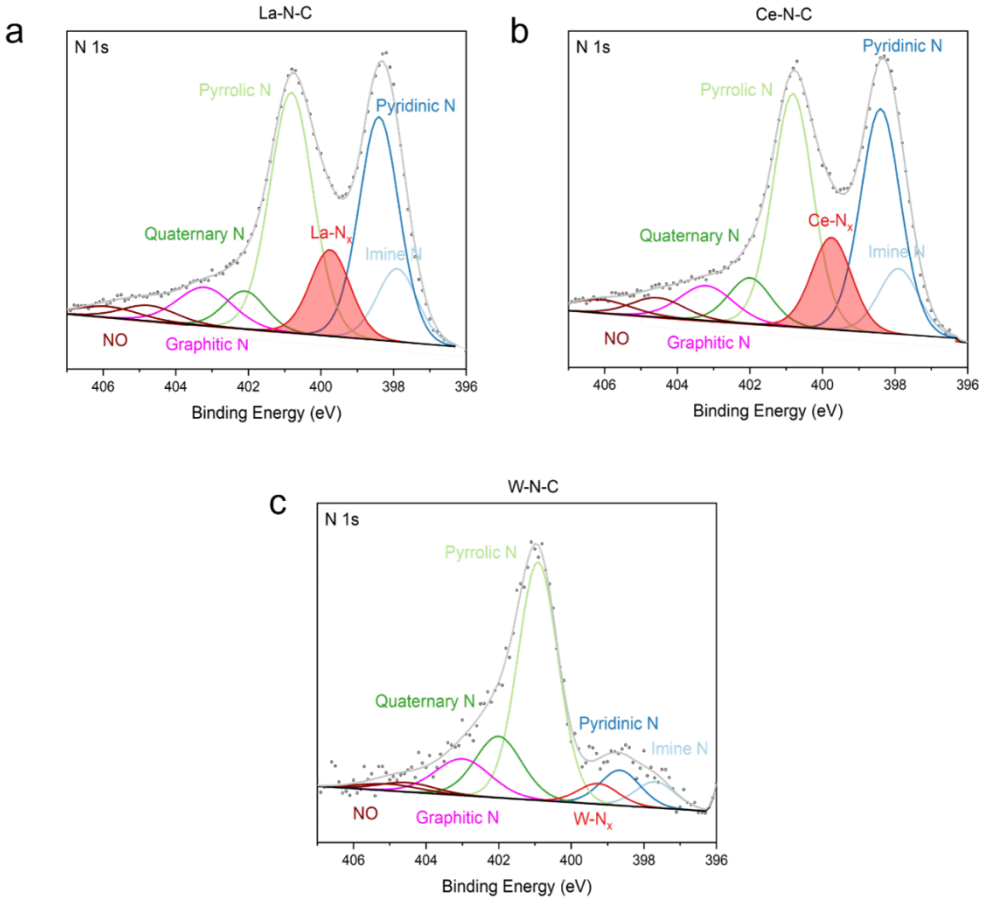

Appendix B.29 Deconvoluted N 1s XPS spectra for the 5d and f metal; La, Ce and W-N-C catalysts.

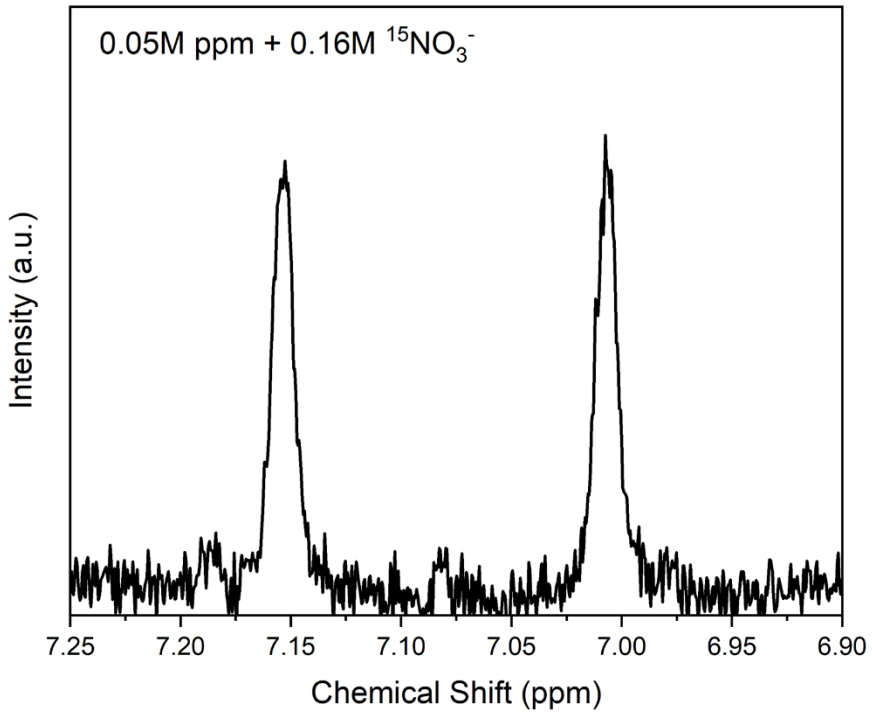

Appendix B.30 Isotopically labeled NO_3RR with 0.05M PBS + 0.16M $K^{15}NO_3^-$ electrolyte for metal-free N-C catalyst. Electrolysis is performed for 4 hours at -0.40 V *vs.* RHE to ensure a reliable amount of $^{15}NH_3$ had been produced. The typical doublet is observed for $^{15}NH_3$. The FE for $^{15}NH_3$ is 36% with a $^{15}NH_3$ yield rate of 1.14 μmol h^{-1} cm^{-2}, agreeing with the non-isotopic NO_3RR for N-C (975-H_2 / 950-NH_3) with a FE of 40% and a yield rate of 1.32 μmol h^{-1} cm^{-2}. This confirms both that the metal free N-C is active for the NO_3RR and that the NH_3 produced originates from the nitrate salt rather than catalyst degradation from the N-C support or other contamination.

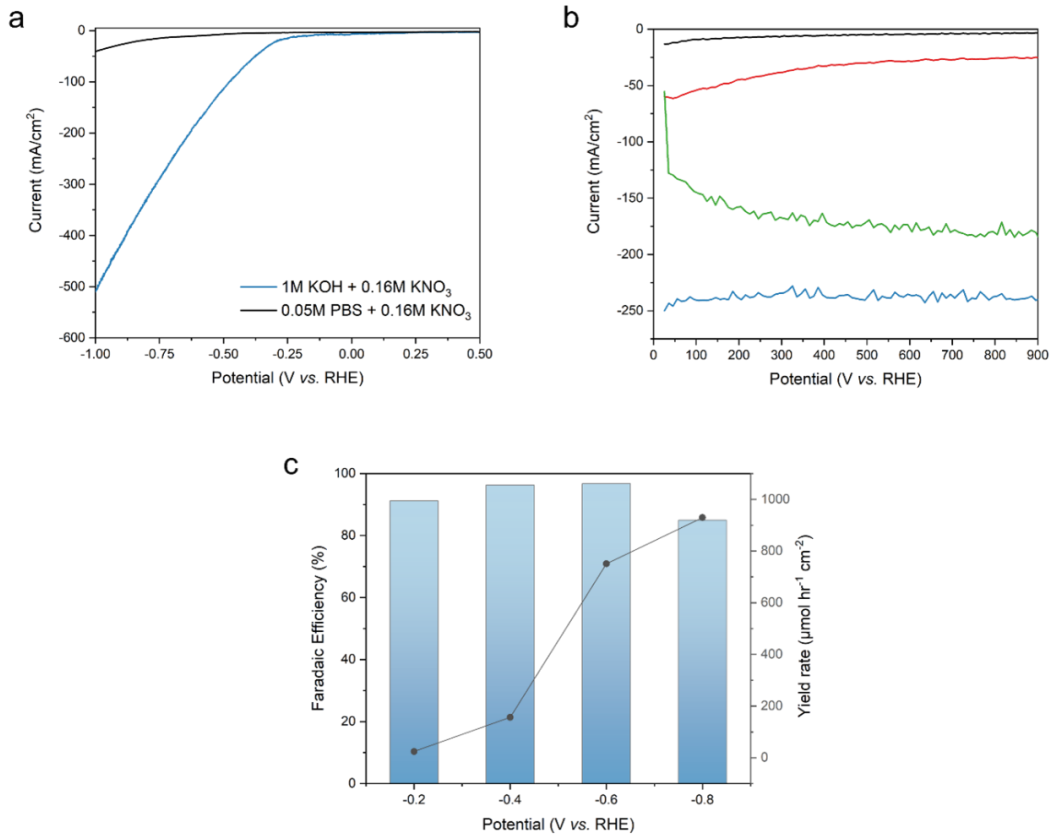

Appendix B.31 NO_3RR electrolysis for the Fe-N-C catalyst in a static cell with alkaline electrolyte (1M KOH, pH = 14). a) LSV comparing 0.05M PBS (pH = 7) with 0.16M KNO_3 and 1M KOH (pH = 14) with 0.16M KNO_3. b) Chronoamperometry in 1M KOH + 0.16M KNO_3 electrolyte at -0.2 to -0.8 V *vs.* RHE. c) Faradaic efficiency for NH_3 (left) and NH_3 yield rate per geometric surface area (right) as a function of applied potential.

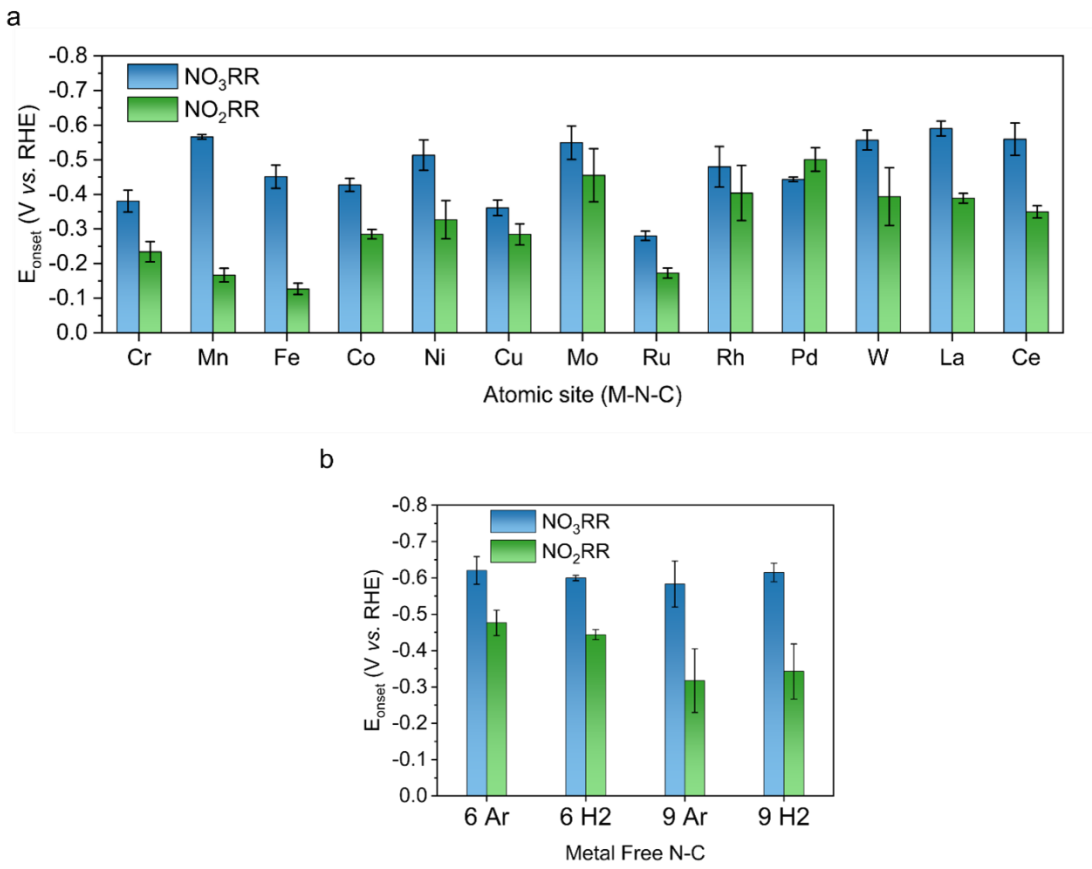

Appendix B.32 Onset potential of the (a) M-N-C and (b) metal-free N-C catalysts for the NO_2RR and NO_3RR. The onset potentials were determined at a current density of -1.0 mA/cm^2. Cr- and Cu-N-C exhibit the lowest onset potentials for the NO_3RR, while Fe-N-C demonstrates the lowest onset potential for the NO_2RR. Note that Ru-N-C exhibits an early onset potential for both the NO_3 and NO_2RR, however, the NO_3 and NO_2RR electrolysis results in Figure 3d and 4d suggest activity is largely attributed to the HER. Figure b suggests that over the metal free N-C catalysts the onset potential for the NO_3RR not impacted by the varying pyrolysis conditions, while for the NO_2RR, a slightly earlier onset potential is shown for the NO_2RR.

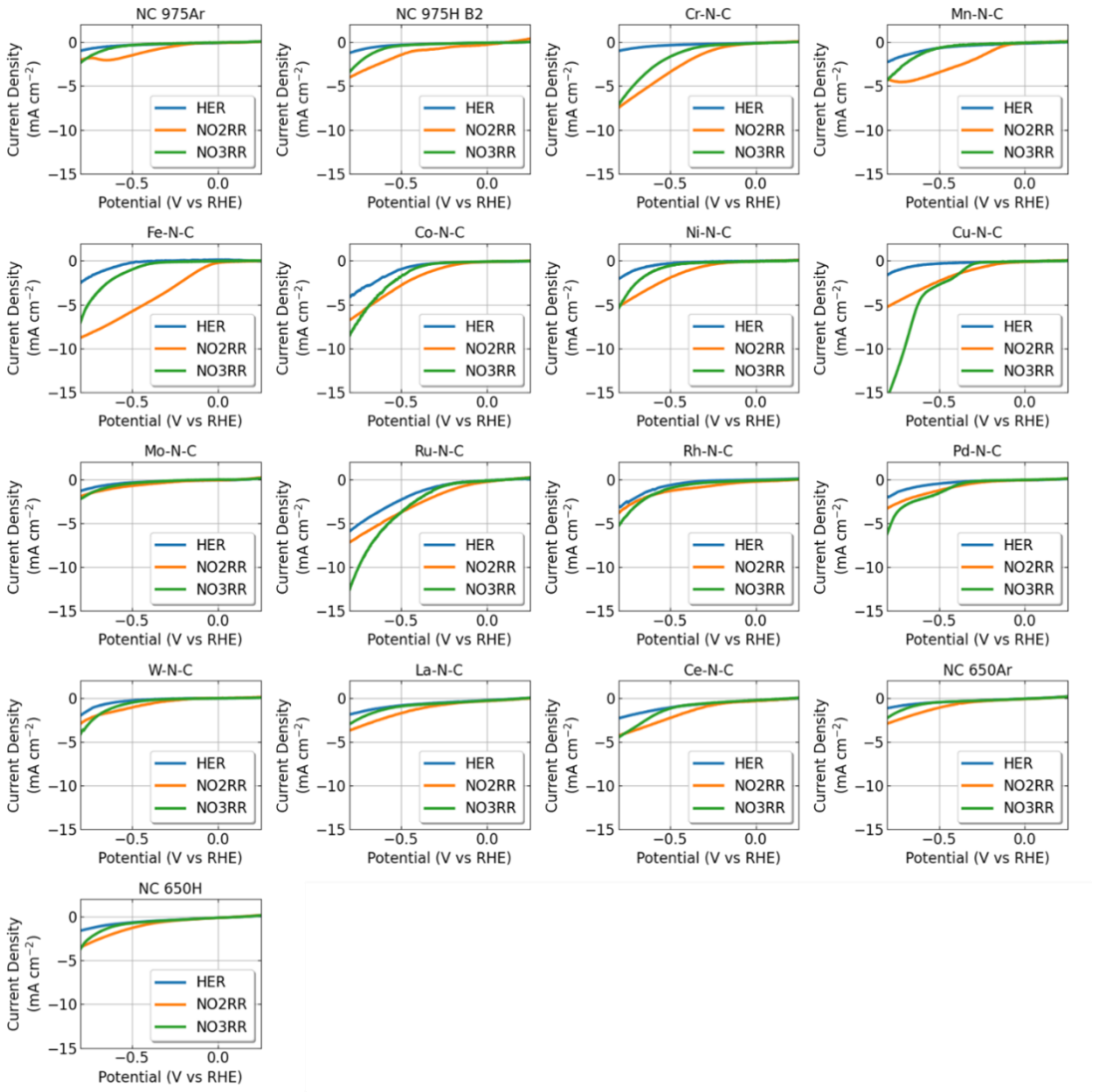

Appendix B.33 Linear sweep voltammetry in 0.05M PBS (HER), 0.01M KNO_2 (NO_2RR) and 0.16M KNO_3 (NO_3RR) for all metal free N-C and M-N-C catalysts.

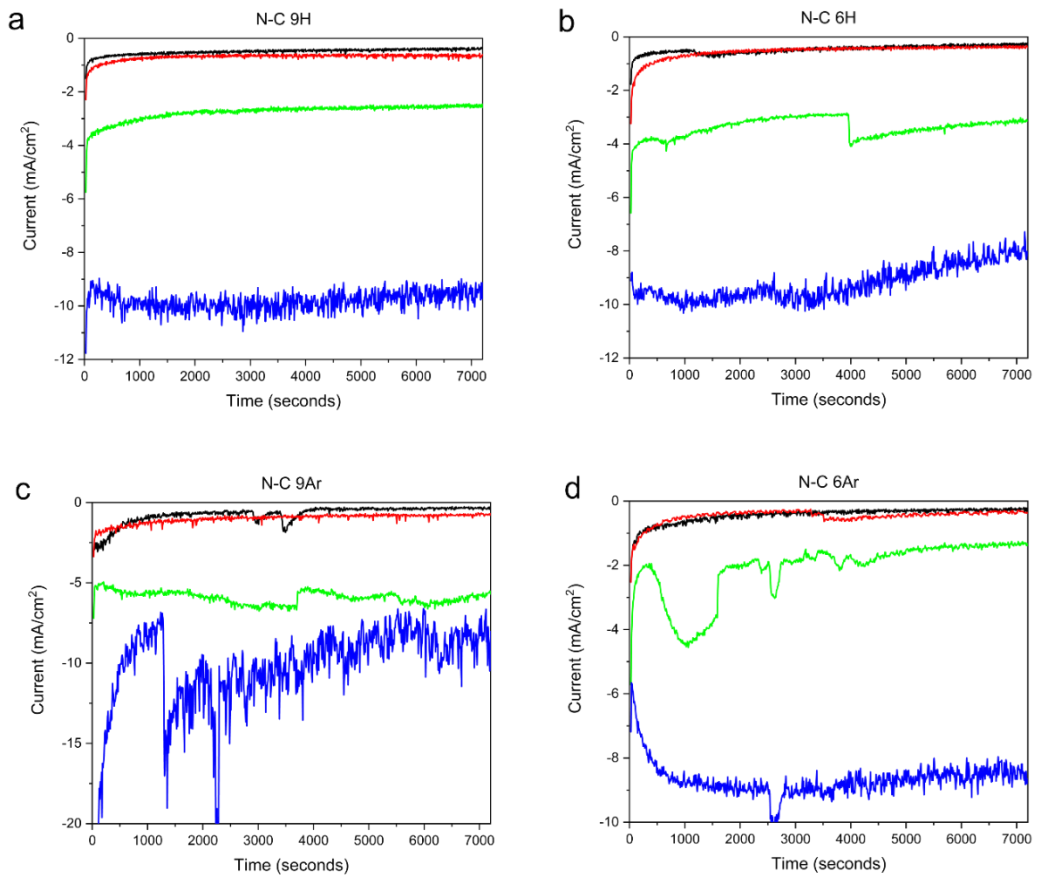

Appendix B.34 NO_3RR chronoamperometry on (a) N-C (975 H_2 / 950 Ar), (b) N-C (650 H_2 / 650 Ar), (c) N-C (975 Ar / 950 Ar) and (d) N-C (650 Ar / 650 Ar) catalysts. NO_3RR electrolysis is performed for 2 hours in a 0.05M PBS + 0.16M NO_3^- electrolyte. The black, red, green and blue curves correspond to applied potentials of -0.20, -0.40, -0.60 and -0.80 V *vs.* RHE, respectively.

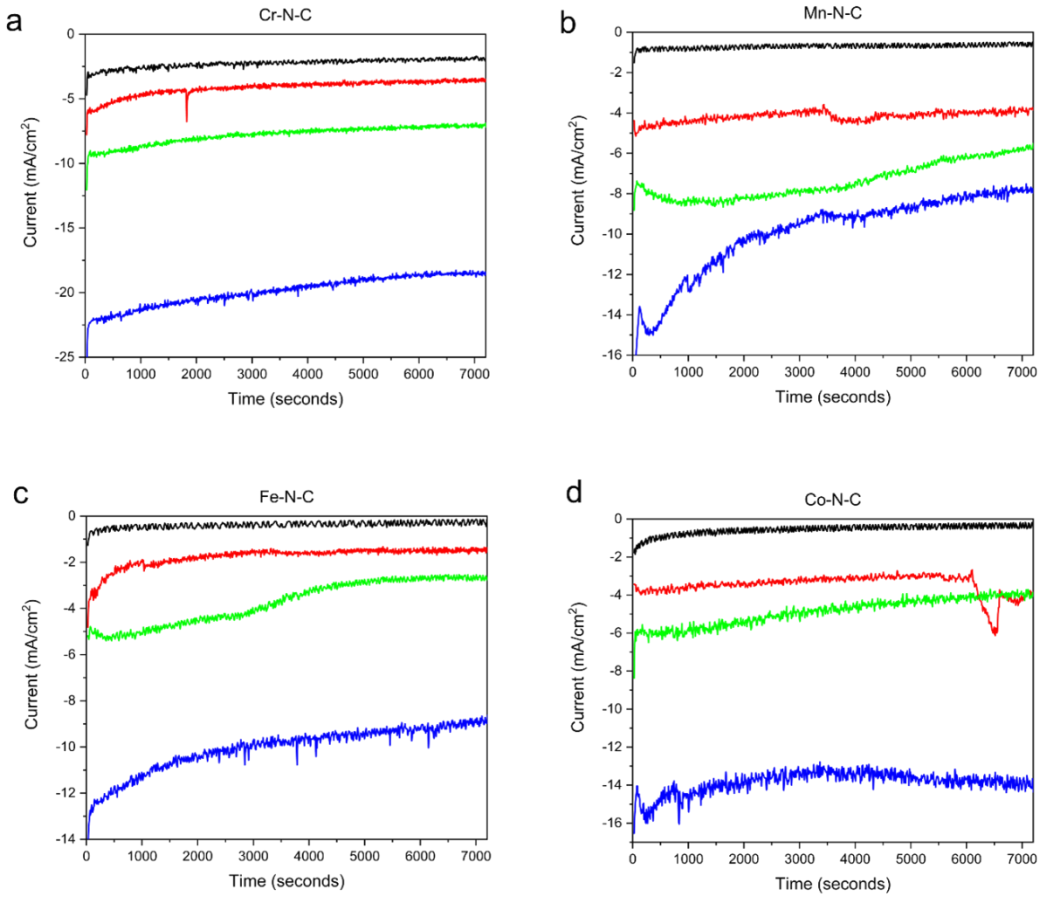

Appendix B.35 NO_3RR chronoamperometry on (a) Cr-N-C, (b) Mn-N-C, (c) Fe-N-C and (d) Co-N-C catalysts. NO_3RR electrolysis is performed for 2 hours in a 0.05M PBS + 0.16M NO_3^- electrolyte. The black, red, green and blue curves correspond to applied potentials of -0.20, -0.40, -0.60 and -0.80 V *vs.* RHE, respectively.

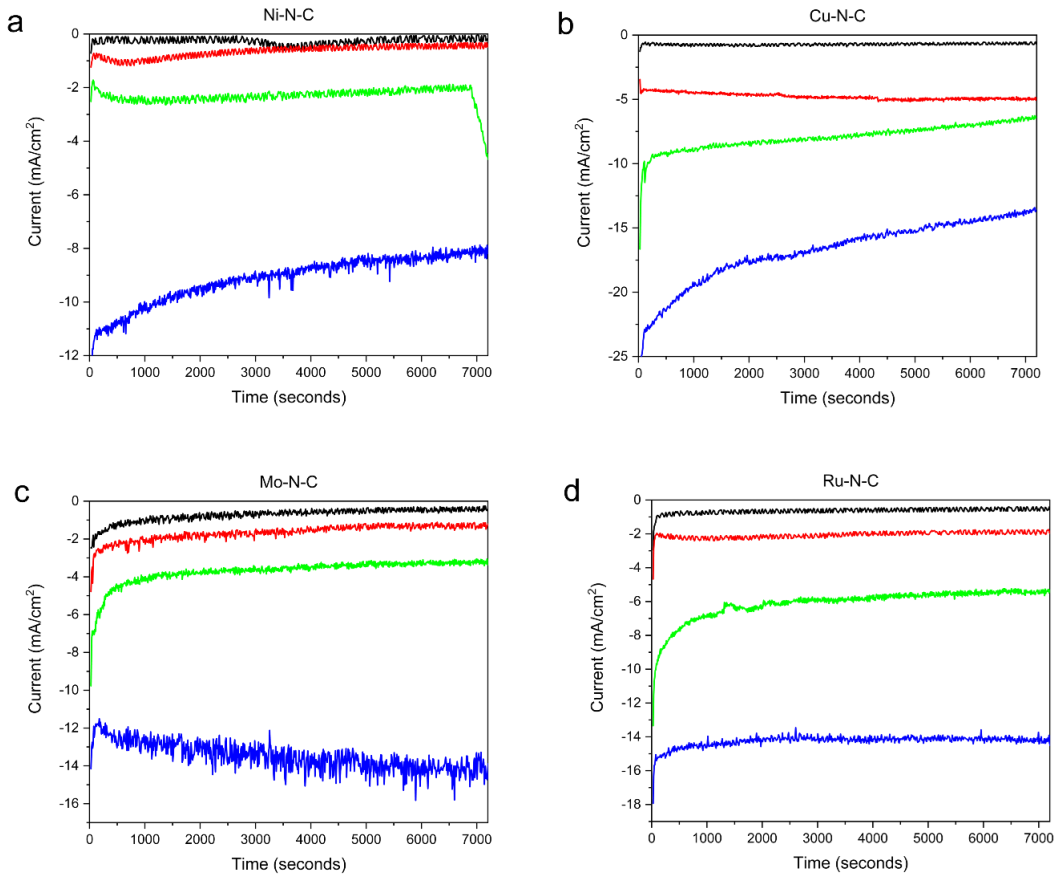

Appendix B.36 NO_3RR chronoamperometry on (a) Ni-N-C, (b) Cu-N-C, (c) Mo-N-C and (d) Ru-N-C catalysts. NO_3RR electrolysis is performed for 2 hours in a 0.05M PBS + 0.16M NO_3^- electrolyte. The black, red, green and blue curves correspond to applied potentials of -0.20, -0.40, -0.60 and -0.80 V *vs.* RHE, respectively.

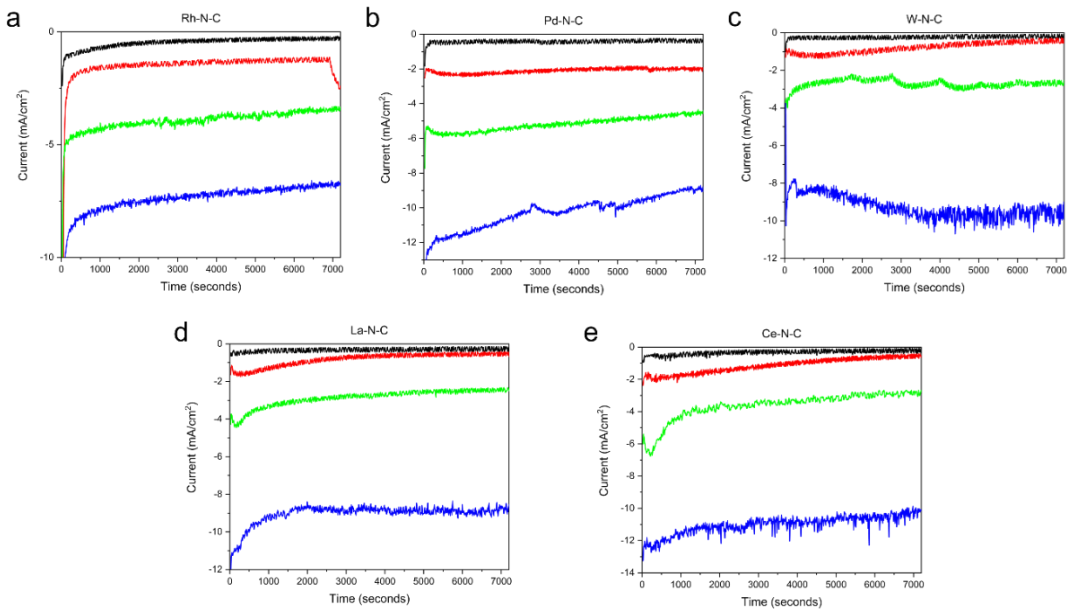

Appendix B.37 NO_3RR chronoamperometry on (a) Rh-N-C, (b) Pd-N-C, (c) W-N-C, (d) La-N-C and (e) Ce-N-C catalysts. NO_3RR electrolysis is performed for 2 hours in a 0.05M PBS + 0.16M NO_3^- electrolyte. The black, red, green and blue curves correspond to applied potentials of -0.20, -0.40, -0.60 and -0.80 V *vs.* RHE, respectively.

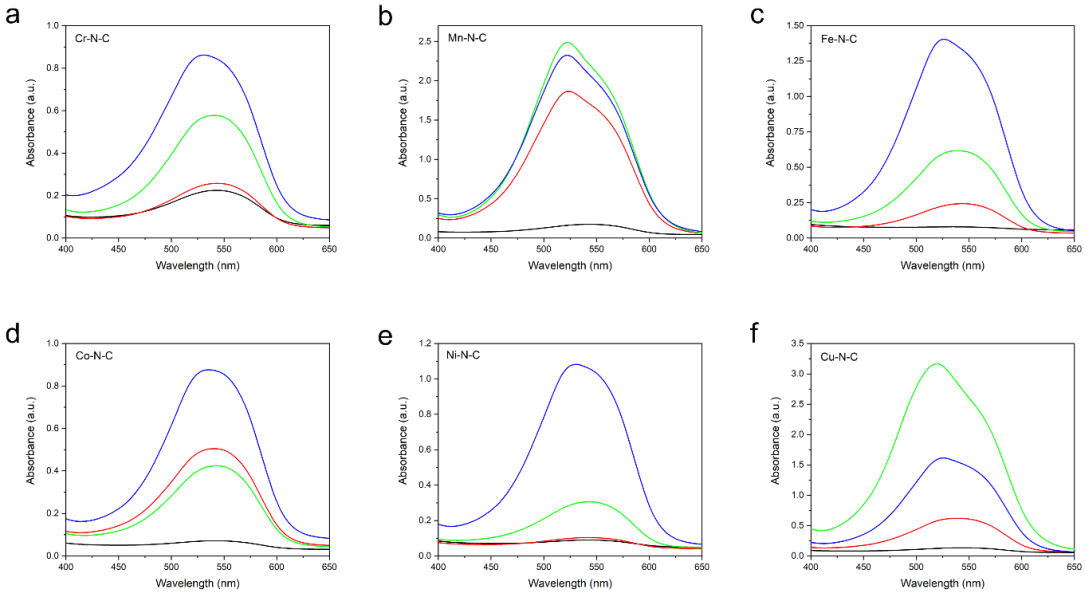

Appendix B.38 NO_3RR UV Vis detection of NO_2^- for (a) Cr-N-C and (b) Mn-N-C (c) Fe-N-C, (d) Co-N-C, (e) Ni-N-C and (f) Cu-N-C for 2 hr electrolysis at an applied potential of -0.20 V (black), -0.40 V (red), -0.60 V (green) and -0.80 V *vs.* RHE (blue). Dashed curves are spectra from electrolyte in the counter chamber. Dilutions have been applied to obtain a NH_3 concentration in the calibration range.

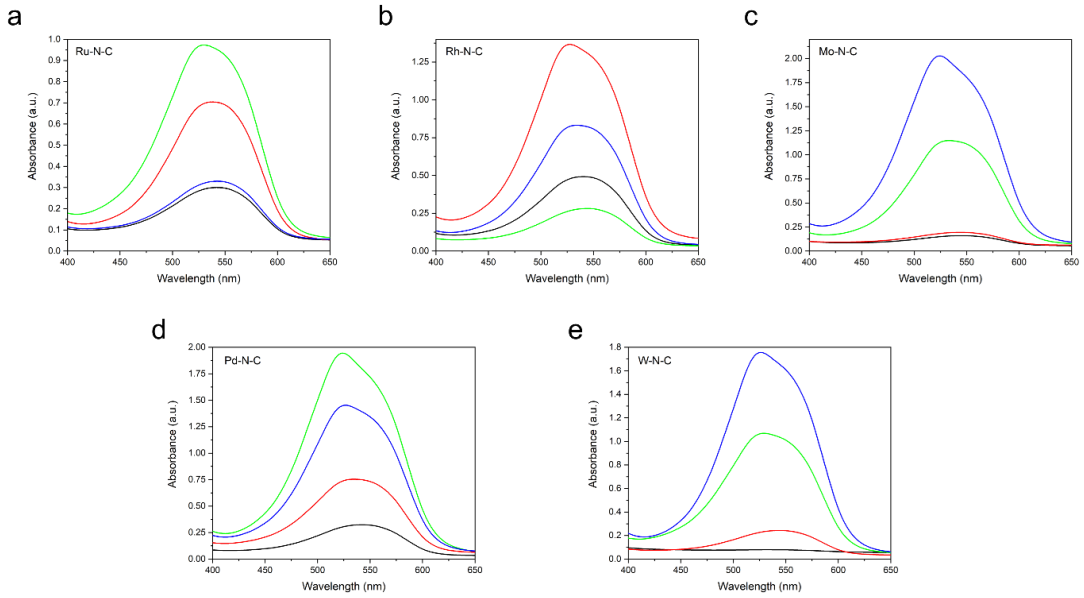

Appendix B.39 NO_3RR UV Vis detection of NO_2^- for (a) Mo-N-C and (b) Ru-N-C (c) Rh-N-C, (d) Pd-N-C and (e) W-N-C for 2 hr electrolysis at an applied potential of -0.20 V (black), -0.40 V (red), -0.60 V (green) and -0.80 V *vs.* RHE (blue). Dashed curves are spectra from electrolyte in the counter chamber. Dilutions have been applied to obtain a NH_3 concentration in the calibration range.

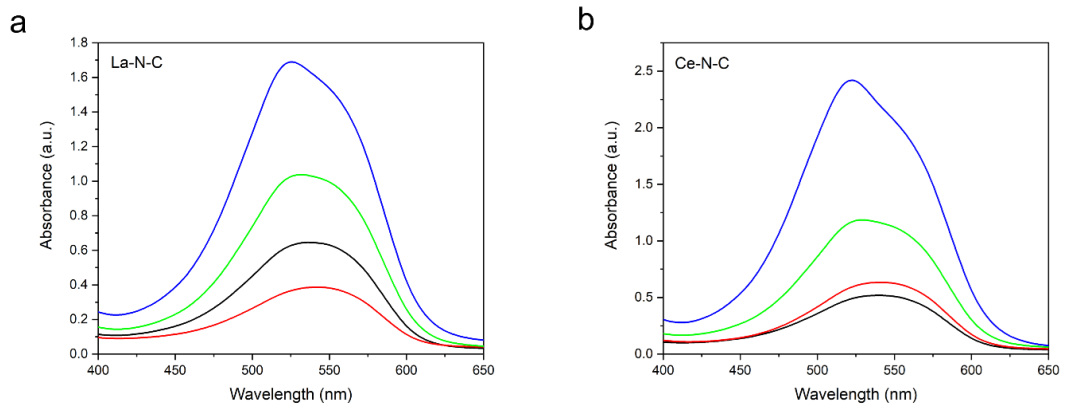

Appendix B.40 NO_3RR UV Vis detection of NO_2^- for (a) La-N-C and (b) Ce-N-C for 2 hr electrolysis at an applied potential of -0.20 V (black), -0.40 V (red), -0.60 V (green) and -0.80 V *vs.* RHE (blue). Dashed curves are spectra from electrolyte in the counter chamber. Dilutions have been applied to obtain a NH_3 concentration in the calibration range.

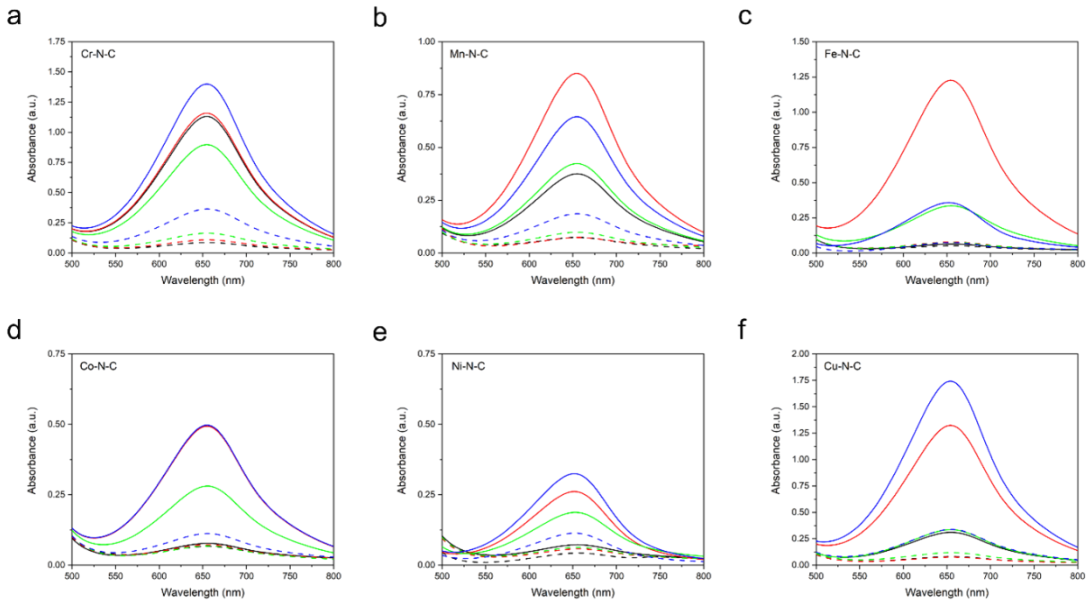

Appendix B.41 NO_3RR UV Vis detection of NH_3 for (a) Cr-N-C and (b) Mn-N-C (c) Fe-N-C, (d) Co-N-C, (e) Ni-N-C and (f) Cu-N-C for 2 hr electrolysis at an applied potential of -0.20 V (black), -0.40 V (red), -0.60 V (green) and -0.80 V *vs.* RHE (blue). Dashed curves are spectra from electrolyte in the counter chamber. Dilutions have been applied to obtain a NH_3 concentration in the calibration range.

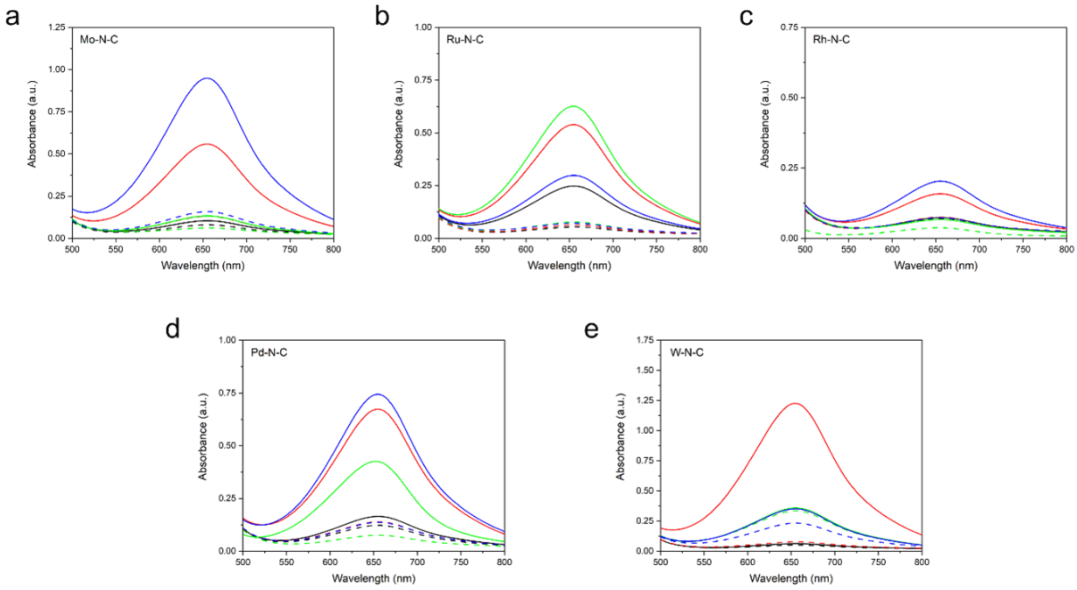

Appendix B.42 NO_3RR UV Vis detection of NH_3 for (a) Mo-N-C and (b) Ru-N-C (c) Rh-N-C, (d) Pd-N-C and (e) W-N-C for 2 hr electrolysis at an applied potential of -0.20 V (black), -0.40 V (red), -0.60 V (green) and -0.80 V *vs.* RHE (blue). Dashed curves are spectra from electrolyte in the counter chamber. Dilutions have been applied to obtain a NH_3 concentration in the calibration range.

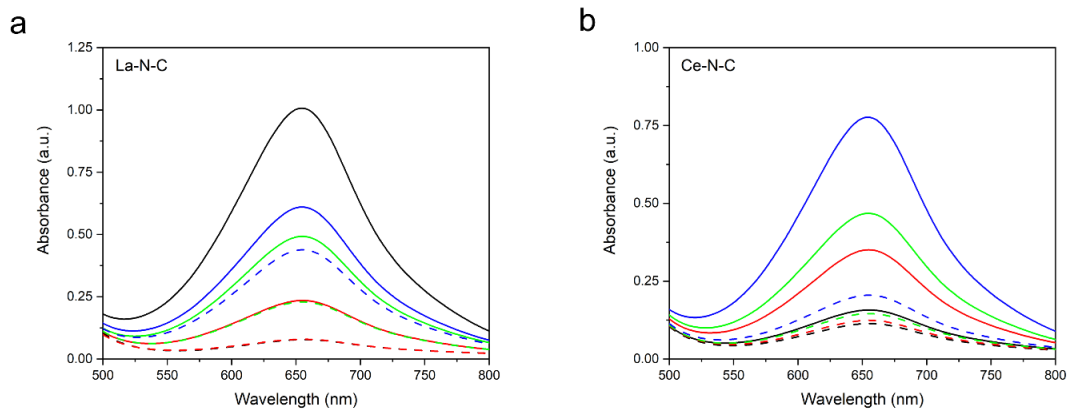

Appendix B.43 NO_3RR UV Vis detection of NH_3 for (a) La-N-C and (b) Ce-N-C for 2 hr electrolysis at an applied potential of -0.20 V (black), -0.40 V (red), -0.60 V (green) and -0.80 V *vs.* RHE (blue). Dashed curves are spectra from electrolyte in the counter chamber. Dilutions have been applied to obtain a NH_3 concentration in the calibration range.

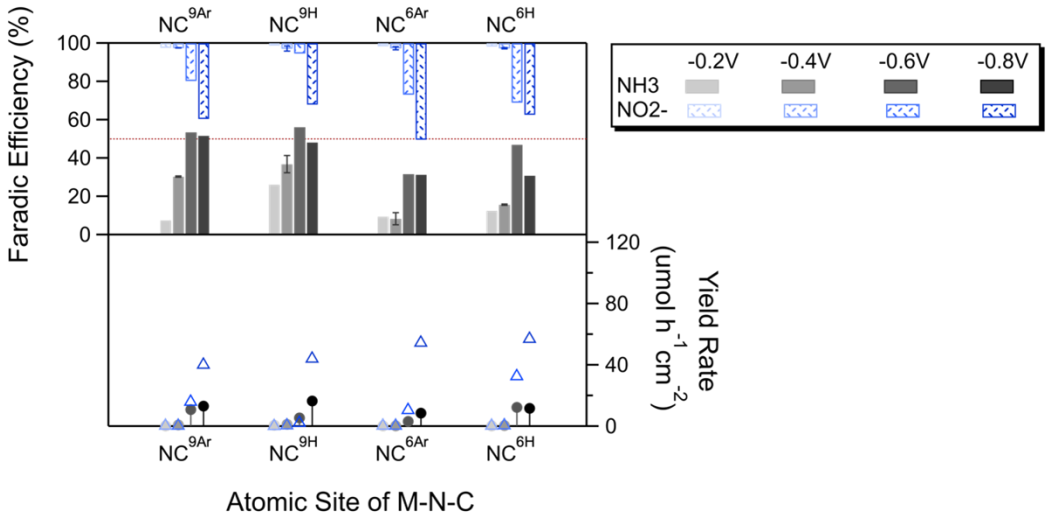

Appendix B.44 Electrochemical NO_3RR for metal free N-C catalysts in 0.05M PBS + 0.16M KNO_3 for 2 hours at an applied potential of -0.20 to -0.80 V *vs.* RHE. The top

section of the figure shows the Faradic efficiency for NO_2^- (blue; top-down) and NH_3 (gray; bottom-up) A red line is set an efficiency of 50% to guide the eye. The bottom section of the figure shows the corresponding yield rate (μmol h^{-1} cm^{-2}) for NO_2^- (blue; triangle) and NH_3 (gray; circle) as a function of the applied potential.

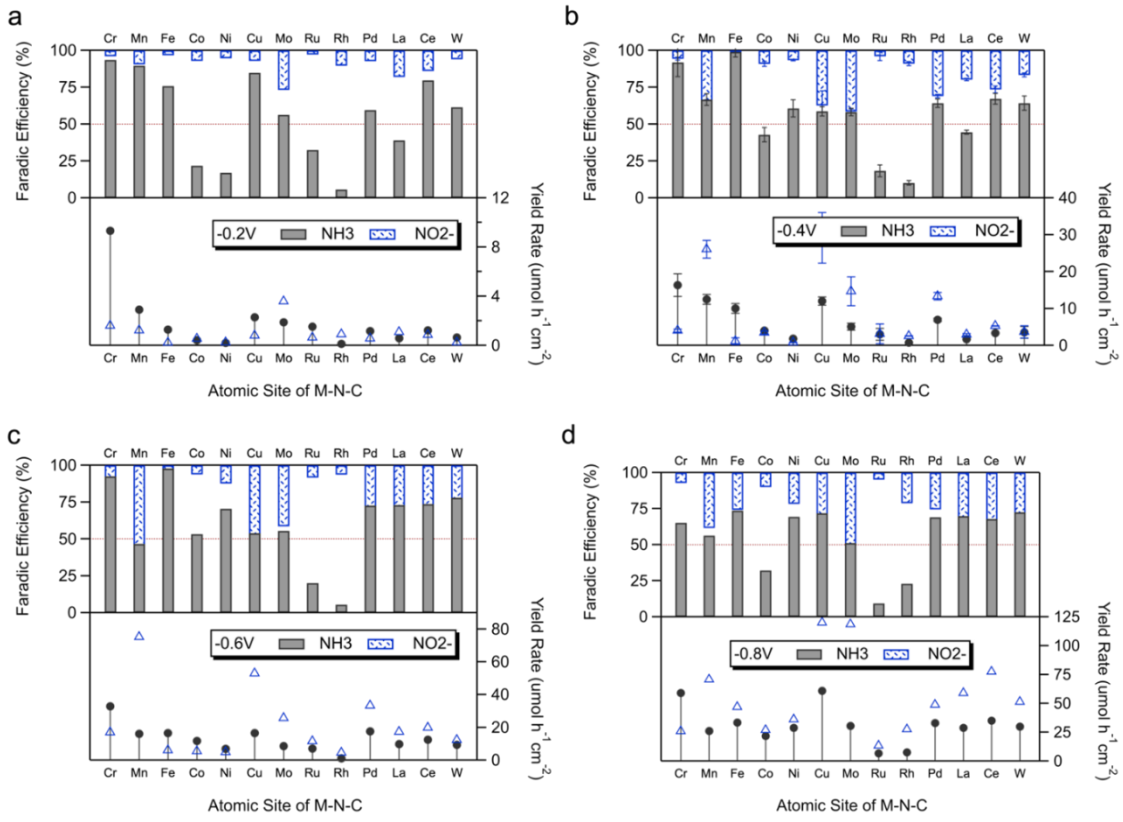

Appendix B.45 Electrochemical NO_3RR for all M-N-C catalysts in 0.05M PBS + 0.16M KNO_3 for 2 hours at each applied potential of (a) -0.20 V, (b) -0.40 V, (c) -0.60 V and (d) -0.80 V v.s. RHE. The top section of the figure shows the Faradic efficiency for NO_2^- (blue; top-down) and NH_3 (gray; bottom-up) A red line is set an efficiency of 50% to guide the eye. The bottom section of the figure shows the corresponding yield rate (μmol h^{-1} cm^{-2}) for NO_2^- (blue; triangle) and NH_3 (gray; circle).

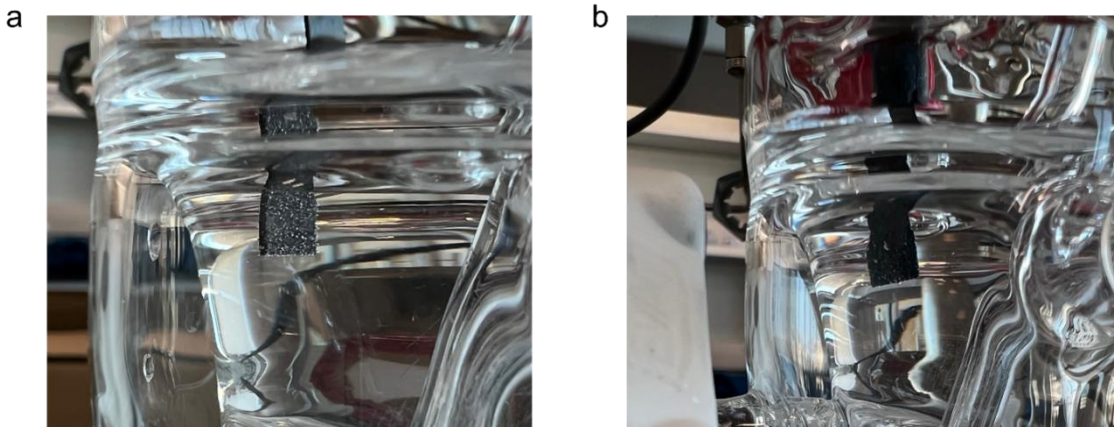

Appendix B.46 NO_3RR electrolysis over (a) Ru-N-C and (b) Rh-N-C, showing gaseous bubbles produced on the working electrode. Demonstrating the Ru/Rh-N-C catalysts being out competed by the HER, yielding a large gap in the GAP of Figure 4 and Figure S 38.

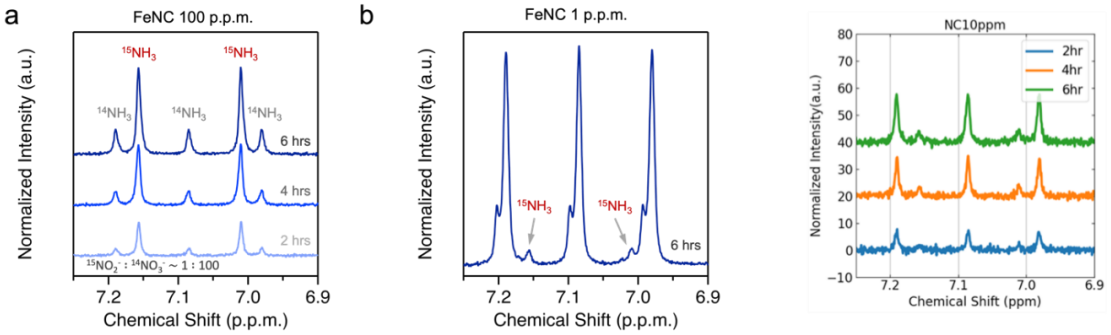

Appendix B.47 Competing NO_2RR in concentrated NO_3^-. NO_3RR electrolysis with isotopically labeled $^{15}NO_2^-$ in concentrated $^{14}NO_3^-$. This figure is correlated to Figure 4 in the main text. (a) NMR curves for NH_3 produced during electrolysis of 100 ppm of doped $^{15}NO_2^-$ at -0.40V *vs.* RHE over an Fe-N-C catalyst. (b) 1 ppm of doped $^{15}NO_2^-$. (c) 10 ppm of doped $^{15}NO_2^-$ over a metal free N-C catalyst.

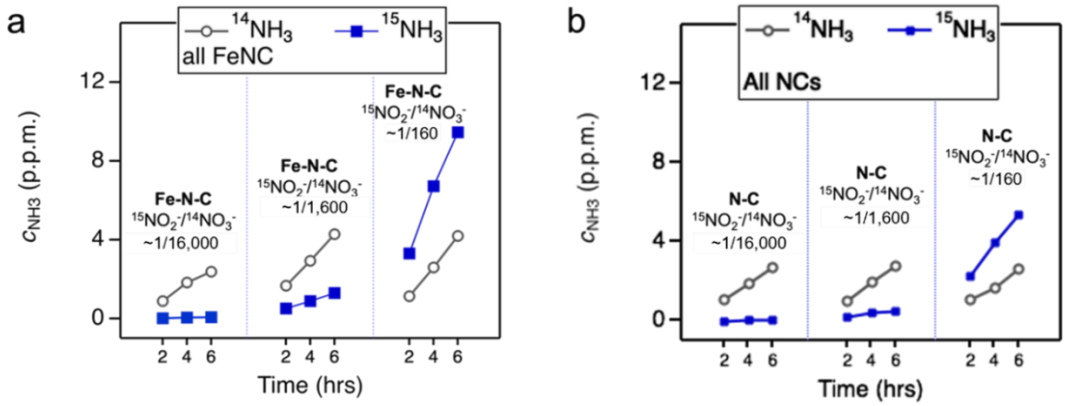

Appendix B.48 Time course of $^{15}NH_3$ in the electrolysis with concentrated $^{14}NO_3^-$ doped with small amount $^{15}NO_2^-$. (a) FeNC catalysts. (b) Metal free NC catalyst.

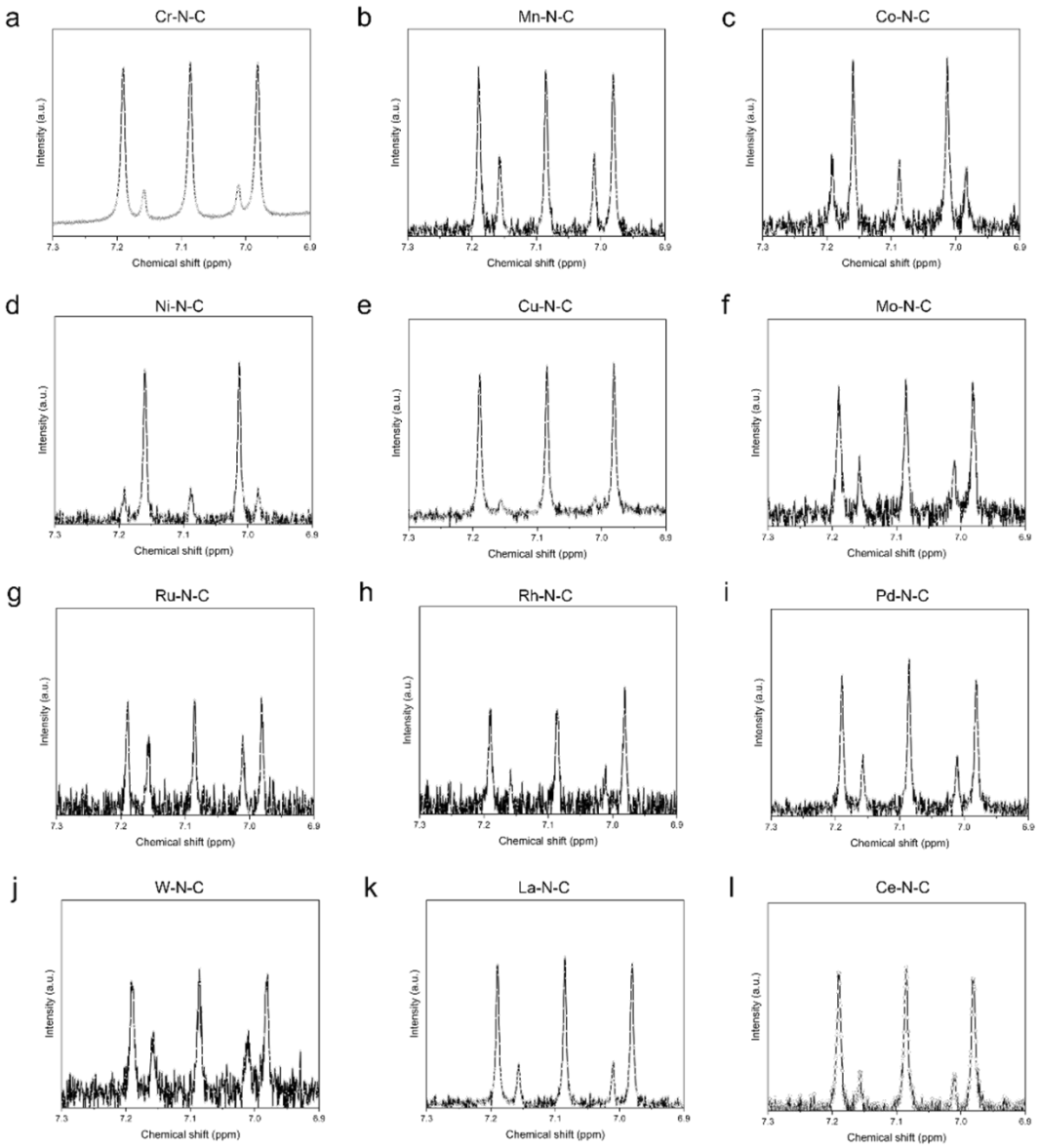

Appendix B.49 Competing NO_2RR in concentrated NO_3^-. NO_3RR electrolysis with isotopically labeled $^{15}NO_2^-$ in concentrated $^{14}NO_3^-$ for all M-N-C catalysts. All electrolysis is performed at -0.40 V *vs.* RHE for 2 hours. The electrolyte consists of 0.16M $K^{14}NO_3$ and 10 ppm of isotopically labeled nitrite, $K^{15}NO_2$. For all catalysts (except Co & Ni) there is a dominating triplet indicative of the reduction of the $K^{14}NO_3$ to standard $^{14}NH_3$, with a smaller doublet peak for isotopic $^{15}NH_3$. For Co and Ni, very

unique behavior is observed in that these atomically dispersed metal centers show poor activity for the NO_3RR, but are highly active for the reduction of NO_2^-, as shown by the dominating doublet for $^{15}NH_3$.

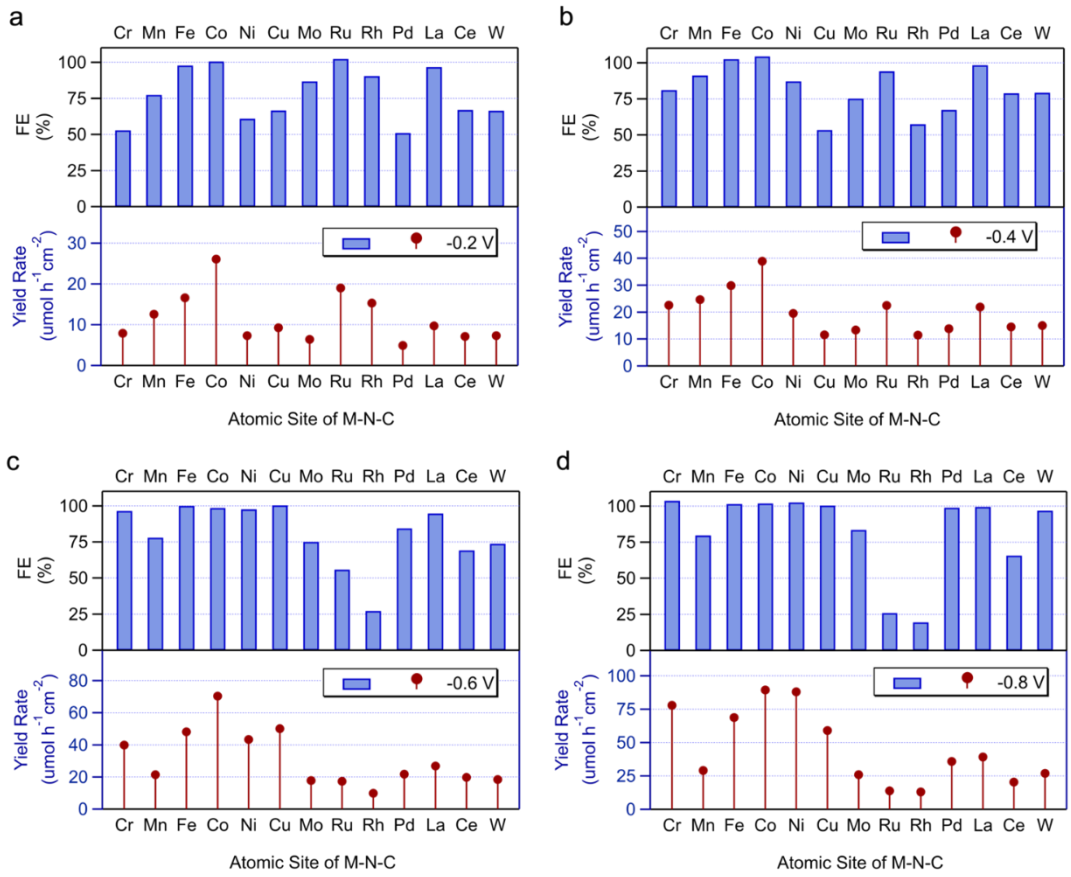

Appendix B.50 Electrochemical NO_2RR for all M-N-C catalysts in 0.05M PBS + 0.01M KNO_2 for 30 min at each applied potential of (a) -0.20 V, (b) -0.40 V, (c) -0.60 V and (d) -0.80 V *vs.* RHE. The top section of the figure shows the Faradic efficiency for NO_2^- (blue; top-down) and NH_3 (gray; bottom-up). The bottom section of the figure shows the corresponding yield rate (μmol h^{-1} cm^{-2}) for NH_3.

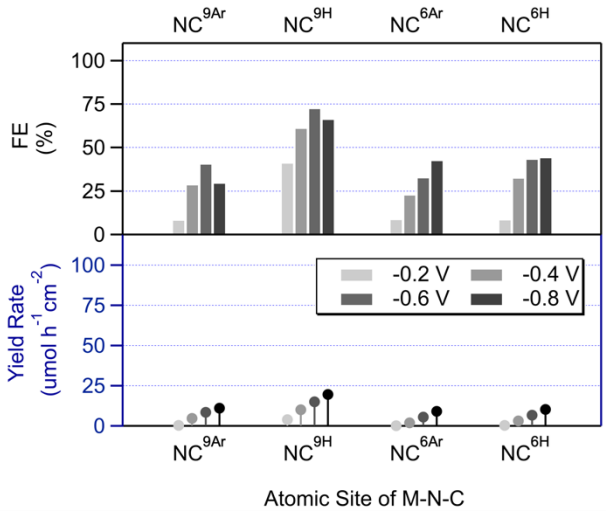

Appendix B.51 Electrochemical NO_2RR for metal free N-C catalysts in 0.05M PBS + 0.01M KNO_3 for 30 min at an applied potential of -0.20 to -0.80 V *vs.* RHE. The top section of the figure shows the Faradic efficiency for NO_2^- (blue; top-down) and NH_3 (gray; bottom-up). The bottom section of the figure shows the corresponding yield rate ($\mu mol\ h^{-1}\ cm^{-2}$) for NH_3 as a function of the applied potential.

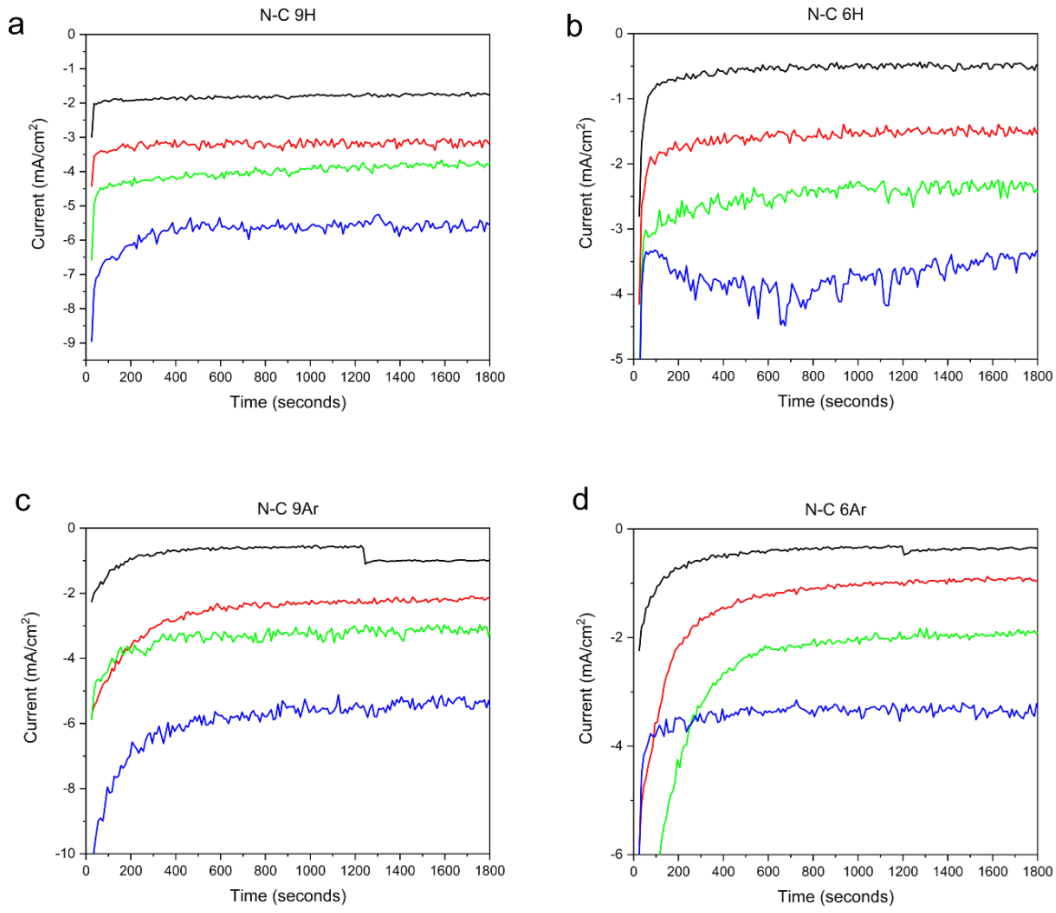

Appendix B.52 NO_2RR chronoamperometry on (a) N-C (975 H_2 / 950 Ar), (b) N-C (650 H_2 / 650 Ar), (c) N-C (975 Ar / 950 Ar) and (d) N-C (650 Ar / 650 Ar) catalysts. NO_2RR electrolysis is performed for 0.5 hours in a 0.05M PBS + 0.01M NO_2^- electrolyte. The black, red, green and blue curves correspond to applied potentials of -0.20, -0.40, -0.60 and -0.80 V *vs.* RHE, respectively.

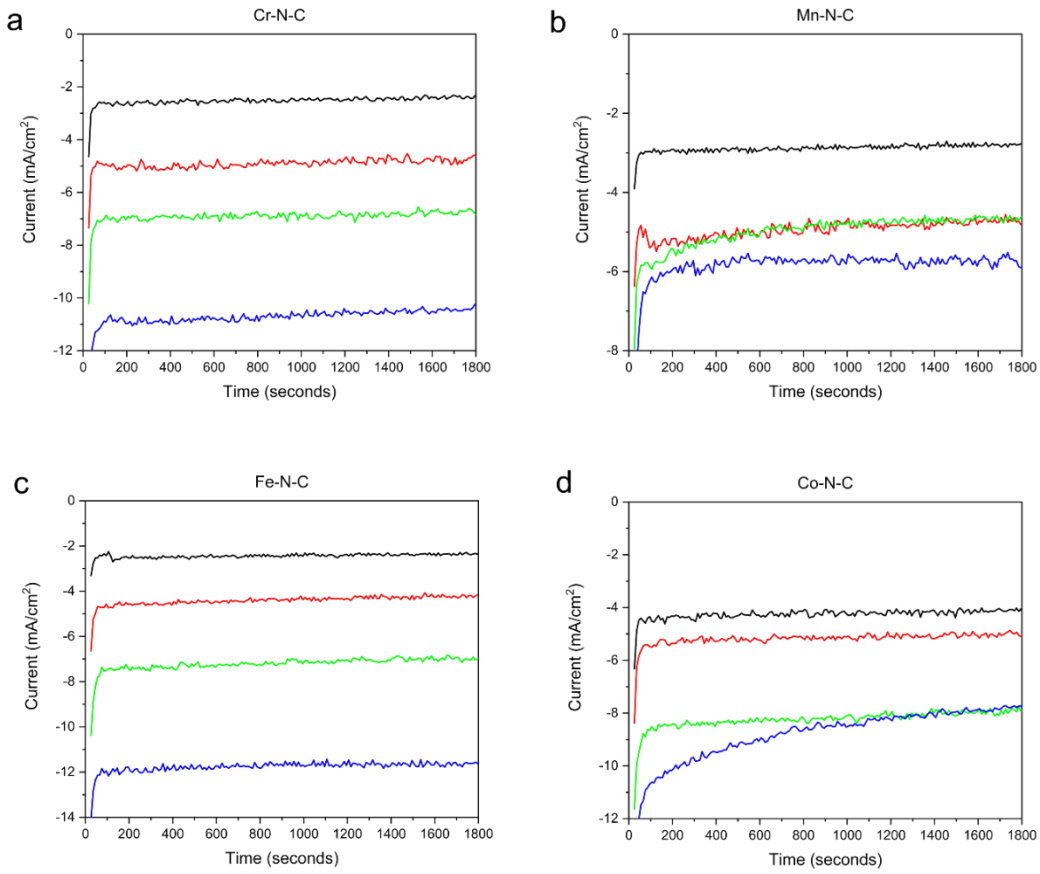

Appendix B.53 NO_2RR chronoamperometry on (a) Cr-N-C, (b) Mn-N-C, (c) Fe-N-C and (d) Co-N-C catalysts. NO_2RR electrolysis is performed for 0.5 hours in a 0.05M PBS + 0.01M NO_2^- electrolyte. The black, red, green and blue curves correspond to applied potentials of -0.20, -0.40, -0.60 and -0.80 V *vs.* RHE, respectively.

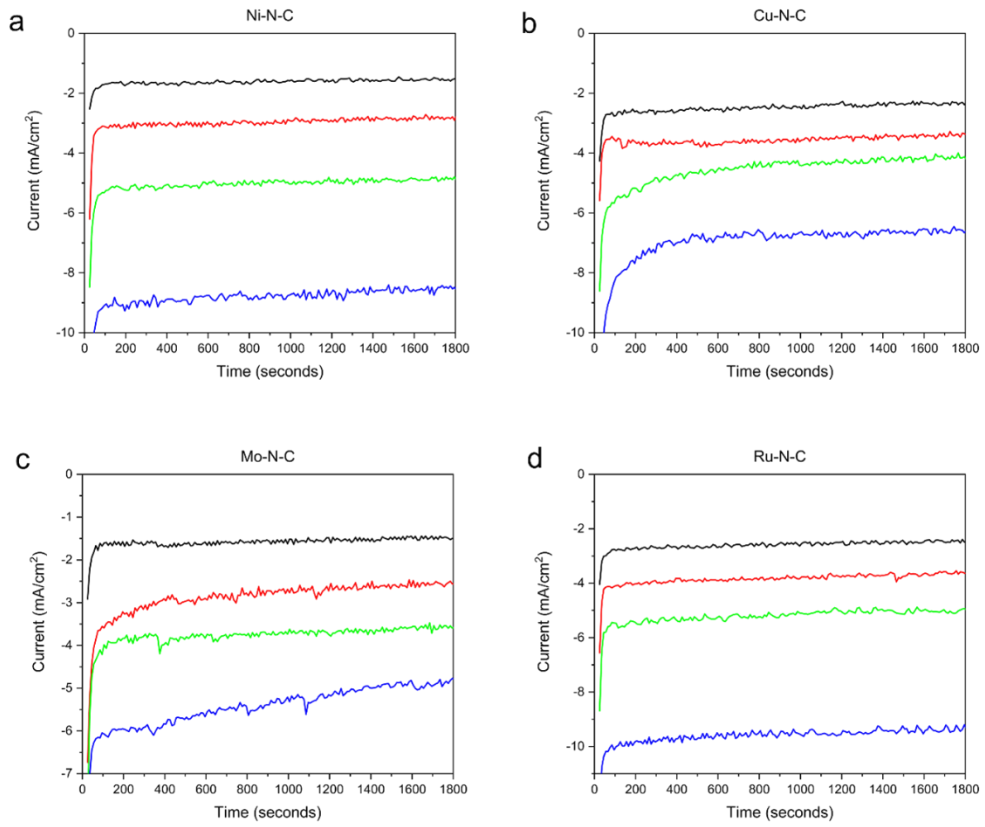

Appendix B.54 NO_2RR chronoamperometry on (a) Ni-N-C, (b) Cu-N-C, (c) Mo-N-C and (d) Ru-N-C catalysts. NO_2RR electrolysis is performed for 0.5 hours in a 0.05M PBS + 0.01M NO_2^- electrolyte. The black, red, green and blue curves correspond to applied potentials of -0.20, -0.40, -0.60 and -0.80 V *vs.* RHE, respectively.

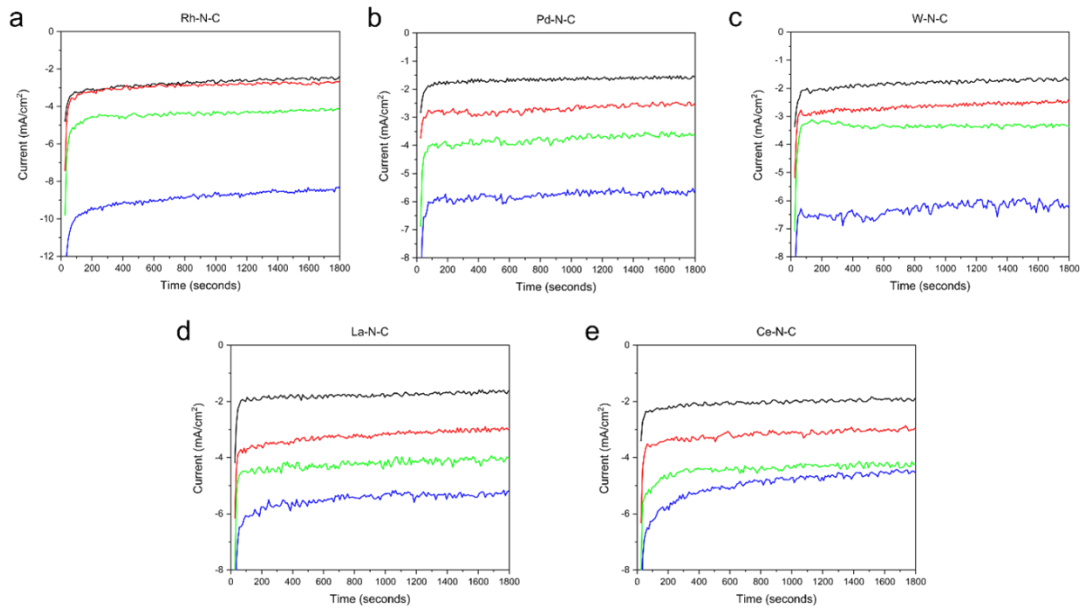

Appendix B.55 NO_2RR chronoamperometry on (a) Rh-N-C, (b) Pd-N-C, (c) W-N-C, (d) La-N-C and (e) Ce-N-C catalysts. NO_2RR electrolysis is performed for 0.5 hours in a 0.05M PBS + 0.01M NO_2^- electrolyte. The black, red, green and blue curves correspond to applied potentials of -0.20, -0.40, -0.60 and -0.80 V *vs.* RHE, respectively.

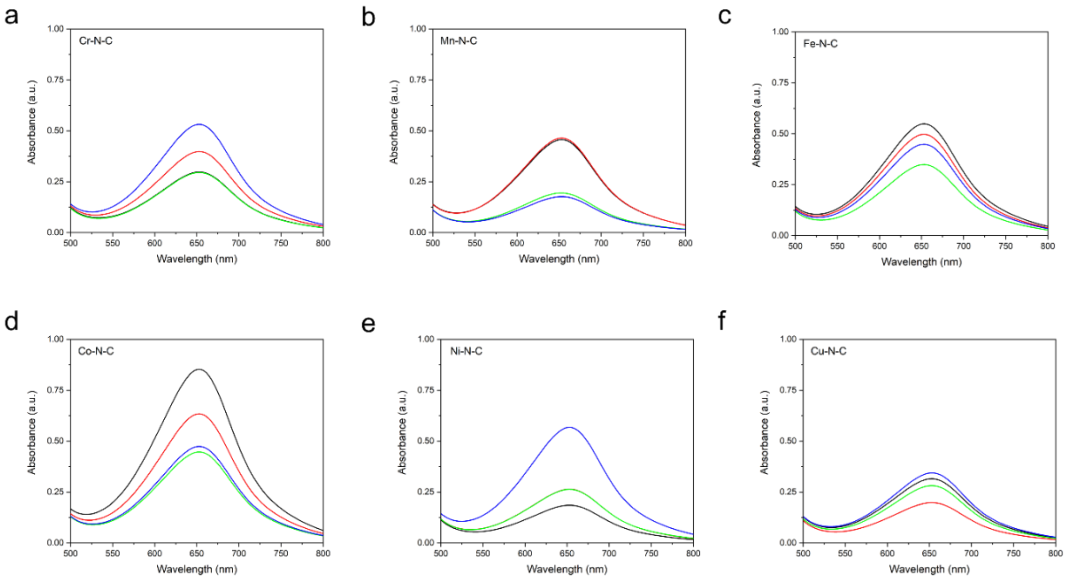

Appendix B.56 NO_2RR UV Vis detection of NH_3 for (a) Cr-N-C, (b) Mn-N-C, (c) Fe-N-C, (d) Co-N-C, (e) Ni-N-C and (f) Cu-N-C for 0.5 hr electrolysis at an applied potential of -0.20 V (black), -0.40 V (red), -0.60 V (green) and -0.80 V *vs.* RHE (blue). Dashed curves are spectra from electrolyte in the counter chamber. Dilutions have been applied to obtain a NH_3 concentration in the calibration range.

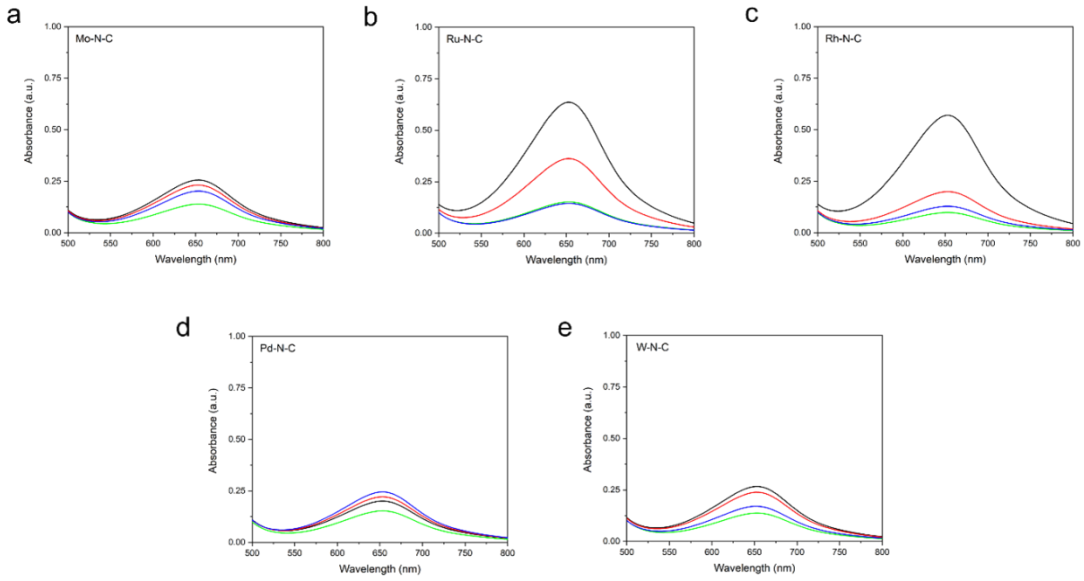

Appendix B.57 NO_2RR UV Vis detection of NH_3 for (a) Mo-N-C, (b) Ru-N-C, (c) Rh-N-C, (d) Pd-N-C and (e) W-N-C for 0.5 hr electrolysis at an applied potential of -0.20 V (black), -0.40 V (red), -0.60 V (green) and -0.80 V *vs.* RHE (blue). Dashed curves are spectra from electrolyte in the counter chamber. Dilutions have been applied to obtain a NH_3 concentration in the calibration range.

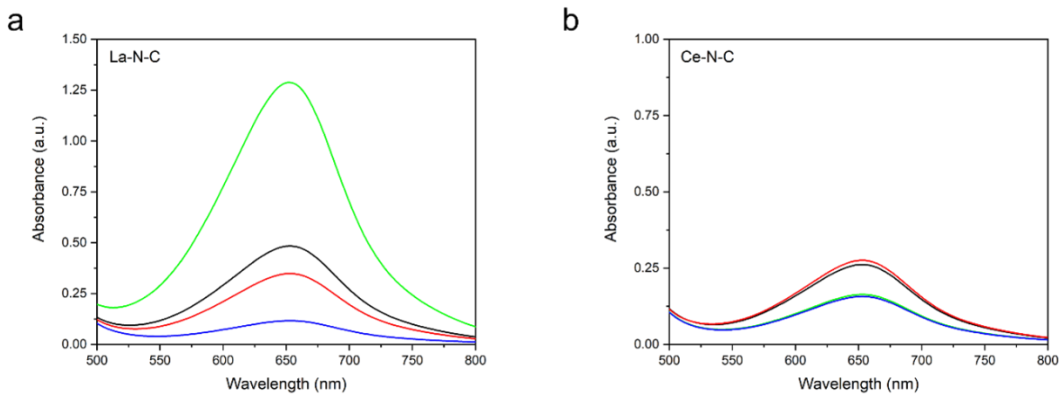

Appendix B.58 NO_2RR UV Vis detection of NH_3 for (a) La-N-C and (b) Ce-N-C for 0.5 hr electrolysis at an applied potential of -0.20 V (black), -0.40 V (red), -0.60 V (green) and -0.80 V *vs.* RHE (blue). Dashed curves are spectra from electrolyte in the counter chamber. Dilutions have been applied to obtain a NH_3 concentration in the calibration range.

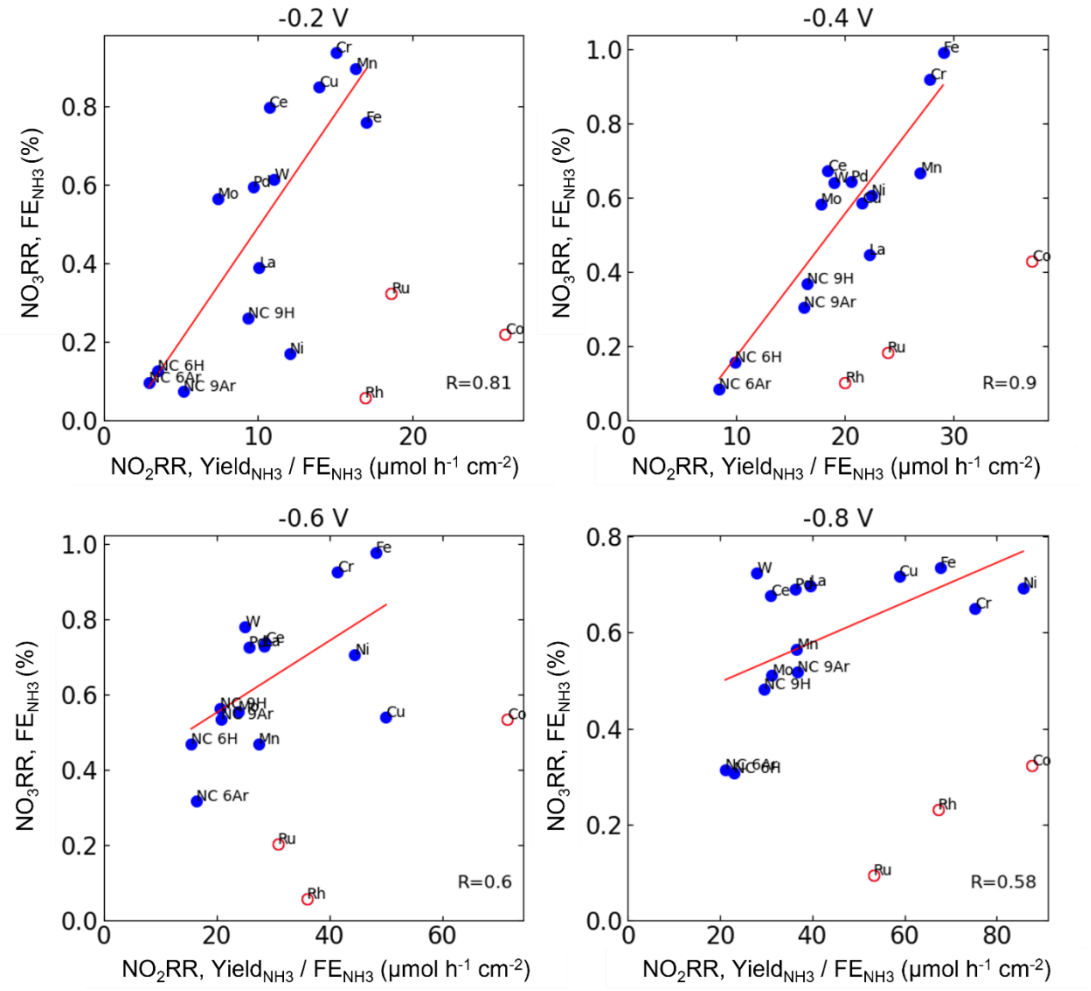

Appendix B.59 Correlations between the NO_3RR FE_{NH3} and the NO_2RR dividend of the NH_3 yield rate and NO_2RR FE_{NH3} at cathodic potentials of -0.2 V, -0.4 V, -0.6 V and -0.8V vs. RHE. R values represent the linearity of the blue points (also shown in Figure 5g). Red points (Co, Ru, Rh) represent the outliers due to dominant gaseous products (Figure 4 and Figure 5d), and were not included in the linear fitting. The linearity gradually dropped with increasing overpotentials, as the reaction is forcibly driven over various active sites, convoluting the electrolysis.

note: The R values of the linear fitting decreased at more reductive potentials, as at very reductive potentials, the reaction can be forcefully driven over most active sites convoluting the intrinsic activity of the M-Nx site.

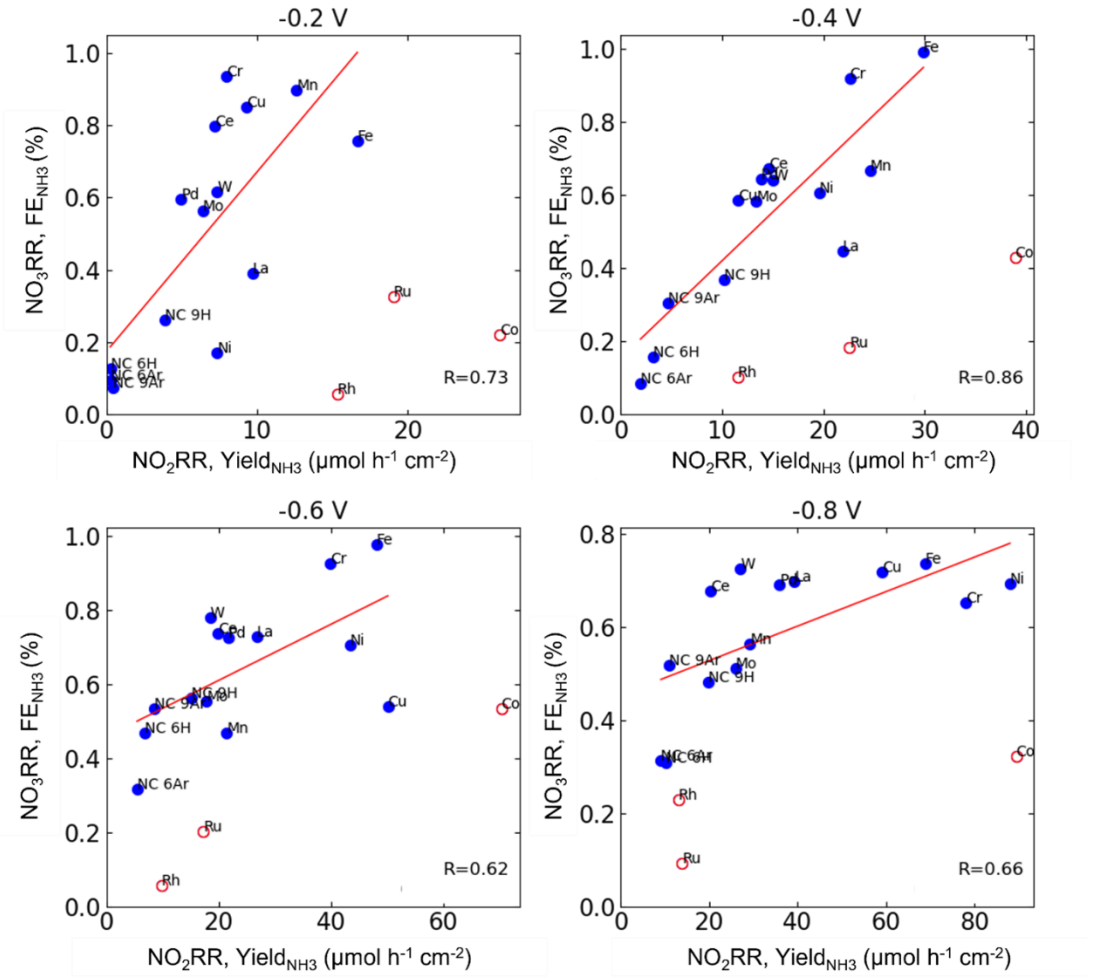

Appendix B.60 Correlations between the NO_3RR FE_{NH3} and the NO_2RR NH_3 yield rate at cathodic potentials of -0.2 V, -0.4 V, -0.6 V and -0.8V *vs.* RHE. R values represent the linearity of the blue points. Red points (Co, Ru, Rh) represent the outliers due to

dominant gaseous products (Figure 4 and Figure 5d), and were not included in the linear fitting.

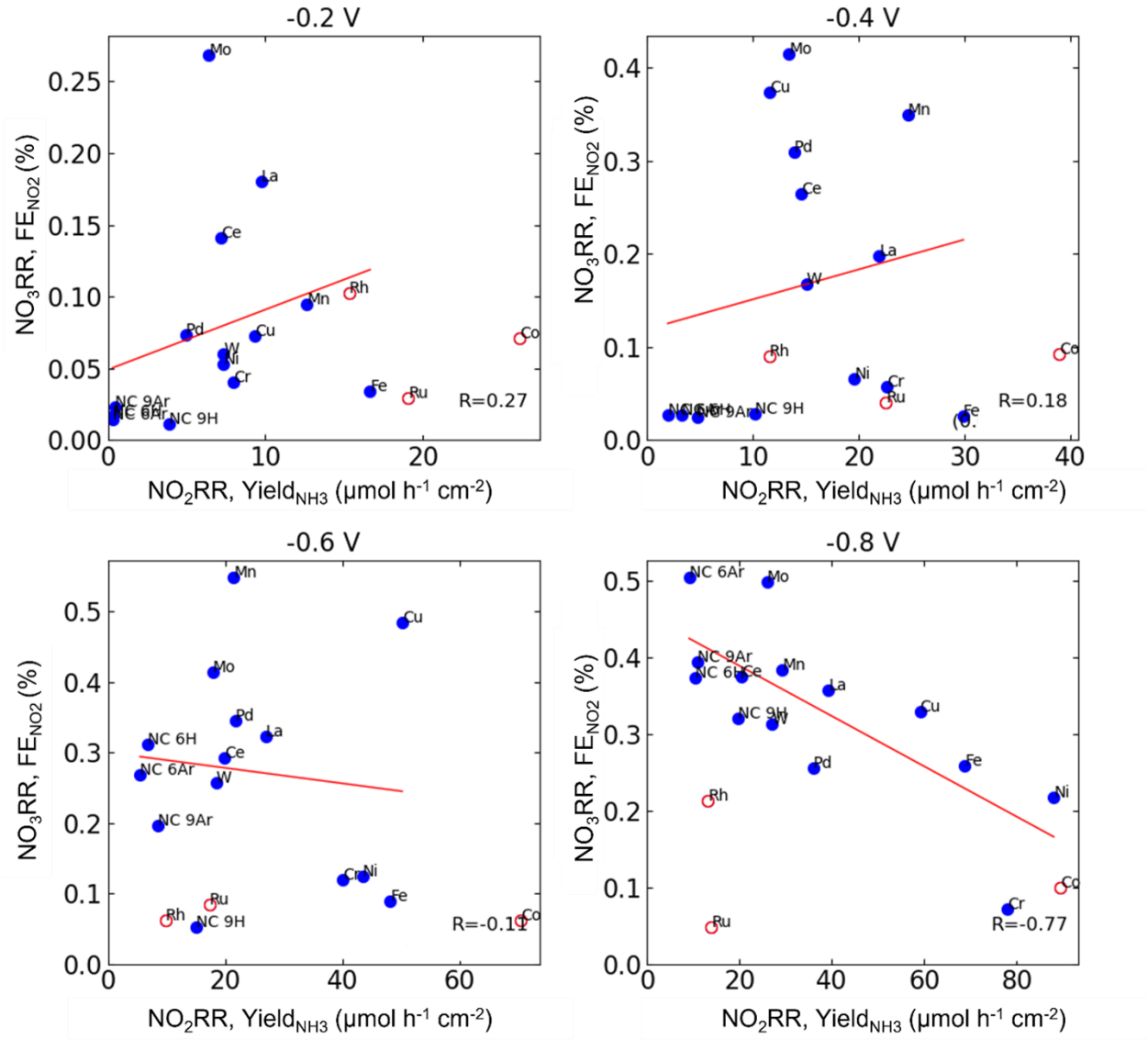

Appendix B.61 Correlations between the NO_3RR FE_{NO2} and the NO_2RR NH_3 yield rate at cathodic potentials of -0.2 V, -0.4 V, -0.6 V and -0.8V *vs.* RHE. R values represent the linearity of the blue points (also shown in Figure 5g). Red points (Co, Ru, Rh) represent

the outliers due to dominant gaseous products (Figure 4 and Figure 5d), and were not included in the linear fitting.

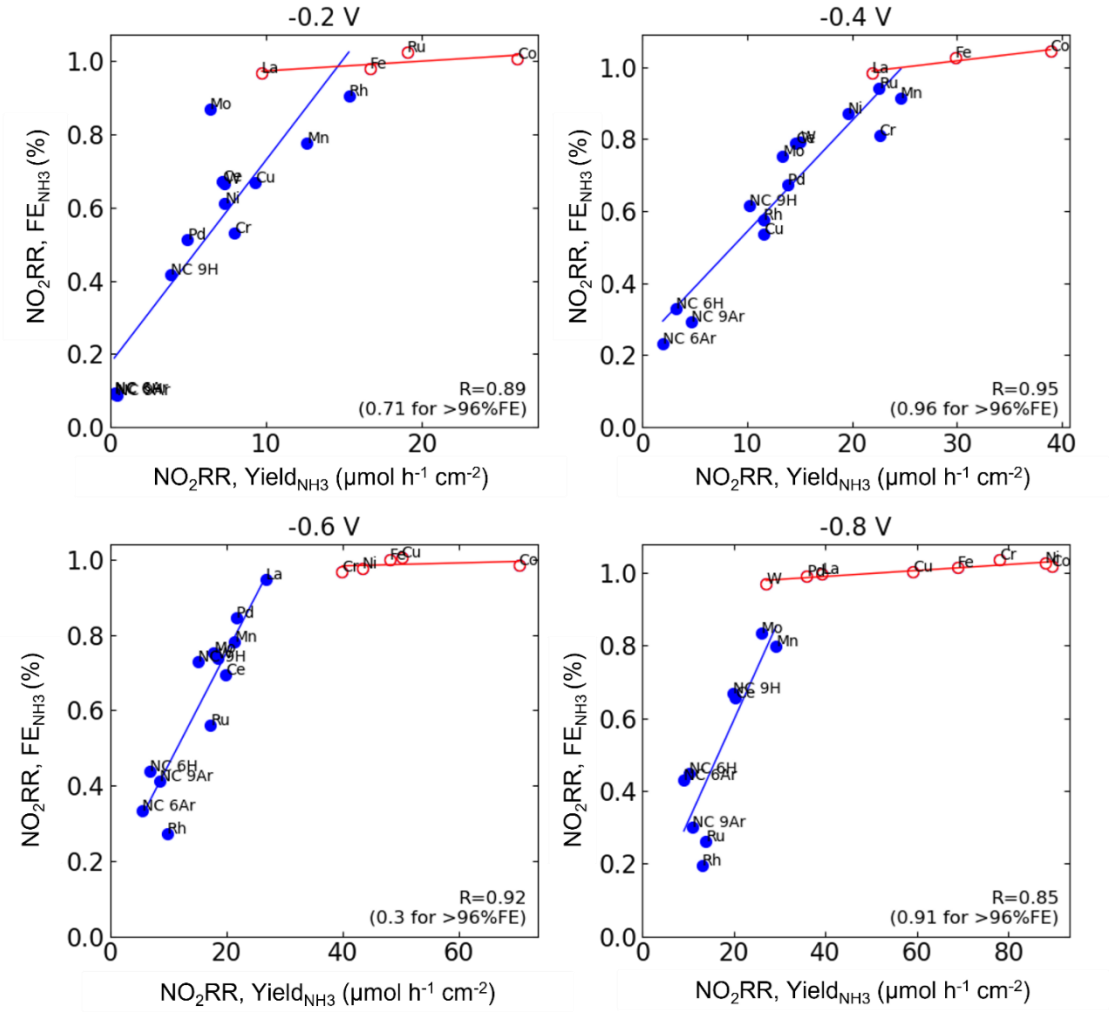

Appendix B.62 Correlations between the NO_2RR FE_{NH3} and the NO_2RR NH_3 yield rate at cathodic potentials of -0.2 V, -0.4 V, -0.6 V and -0.8V *vs.* RHE. R values represent the linearity of the blue points (also shown in Figure 5g). Red points represent the catalysts reaching 100% FE at each potential, and were not included in the linear fitting.

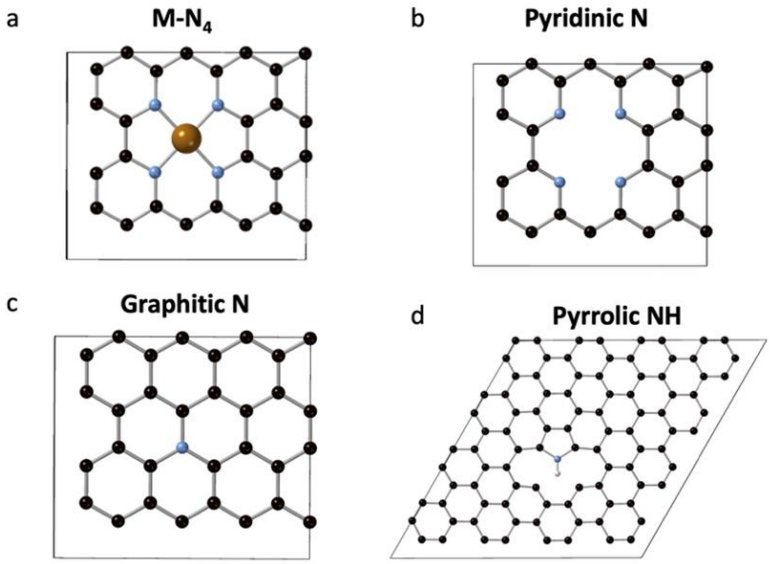

Appendix B.63 Active sites used in the DFT calculation of reactivity descriptors for the NO_3RR and the NO_2RR. a) $M\text{-}N_4$ site, b) pyridinic N, c) graphitic N, and d) pyrrolic NH. Atoms belonging to one unit cell are shown. Black – C, blue – N, white – H, tan – metal atom.

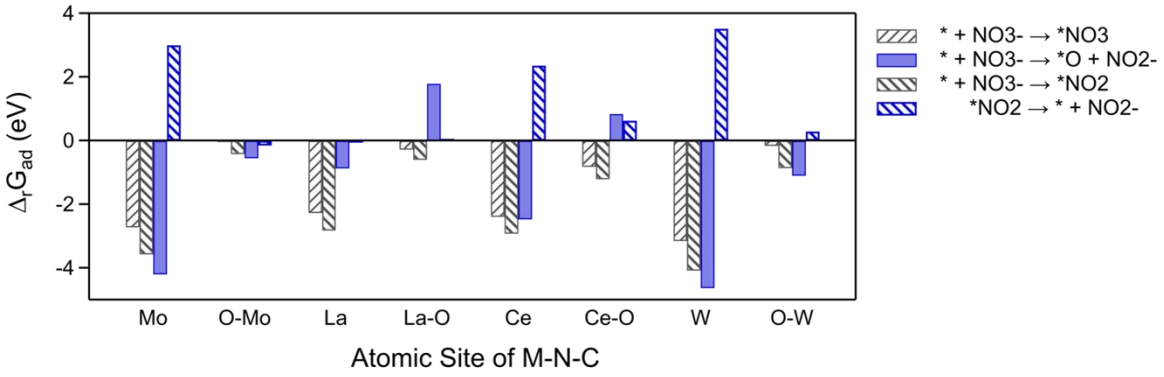

Appendix B.64 DFT-derived free energies on Mo-, La-, Ce- and W-N-C sites and their oxygenated (O-M) states.

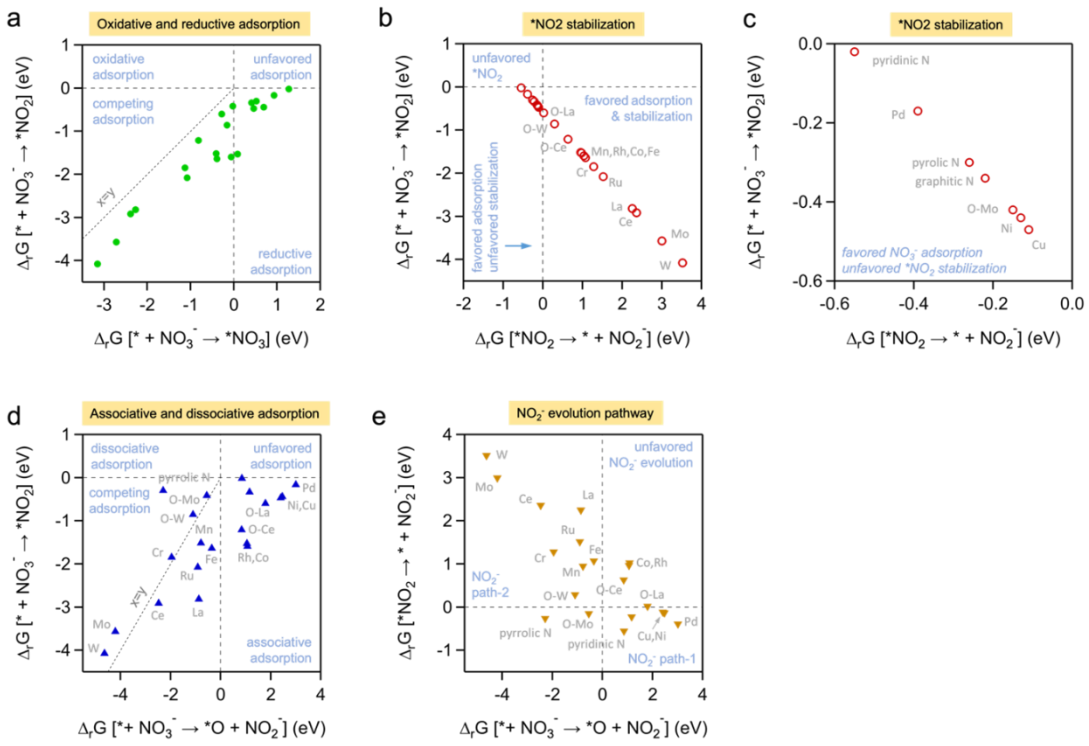

Appendix B.65 Correlations between various DFT-derived free energies ($\Delta_r G$) in Figure 5a. It should be noted that $\Delta_r G[\ ^*{+}NO_3^- \rightarrow\ ^*NO_2]$ and $\Delta_r G[\ ^*NO_2 \rightarrow\ ^*{+}NO_2^-]$ were dependent terms, given the fact that they shared same surface intermediate species $^*NO_2^-$ and all other species in these two reaction coordinates were bulk items

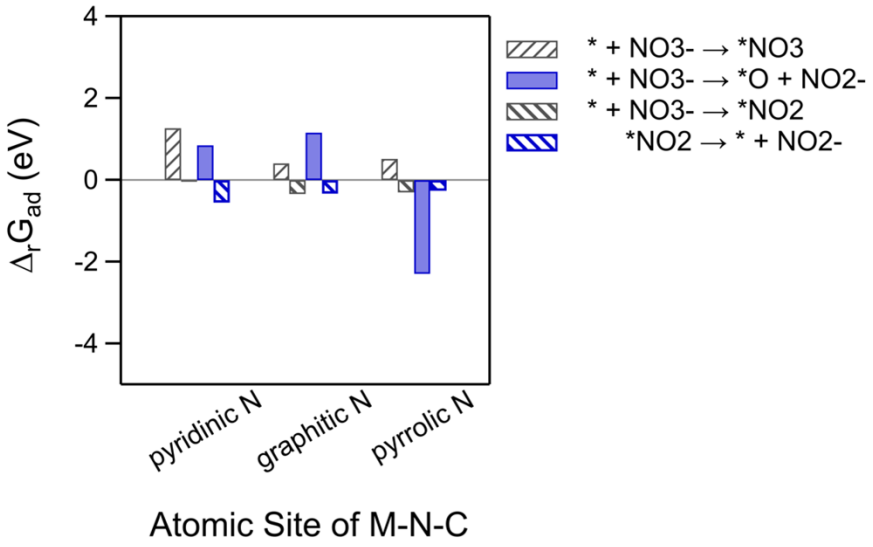

Appendix B.66 DFT-derived adsorption/desorption energies on different nitrogen moieties.

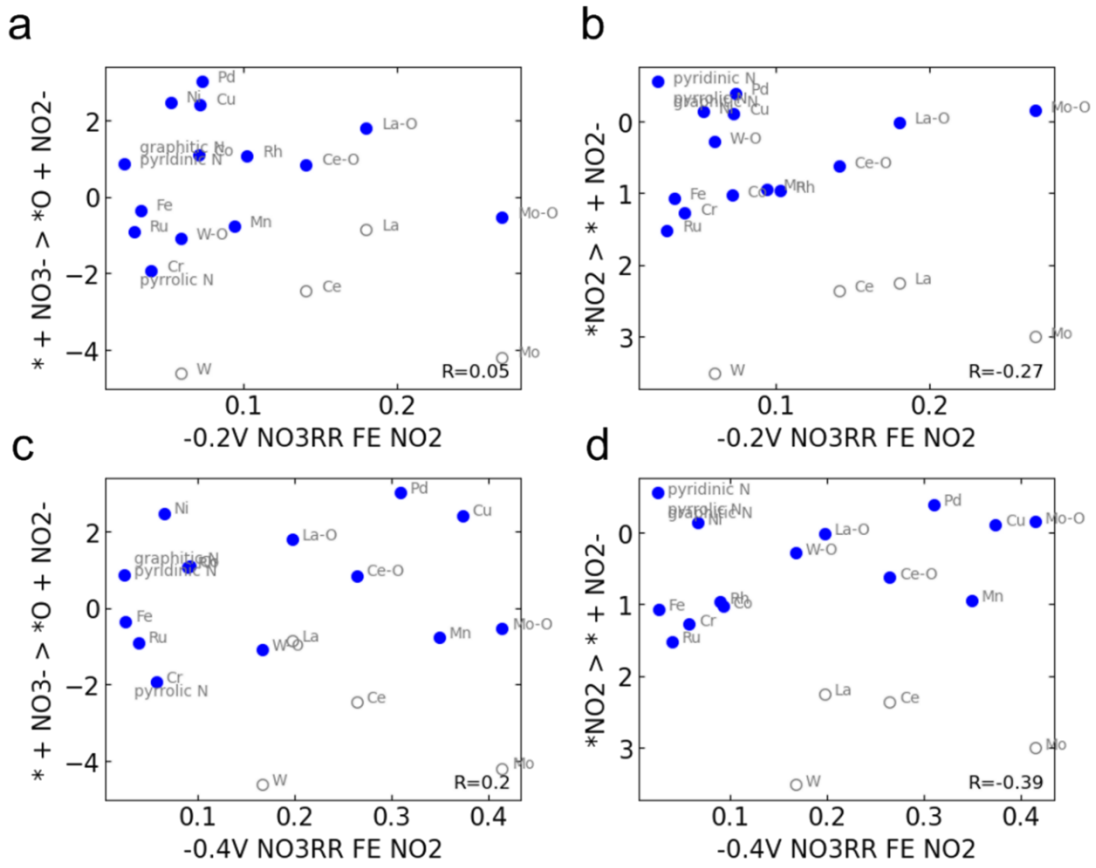

Appendix B.67 Correlations between various DFT-derived descriptors $\Delta_r G$ [$^*NO_2 \rightarrow {}^* + NO_2^-$] or $\Delta_r G$ [$^* + NO_3^- \rightarrow {}^*O + NO_2^-$], and the NO_3RR FE_{NO2-} at (a) -0.20, (b) -0.40, (c) -0.60, (d) -0.80 V *vs.* RHE.

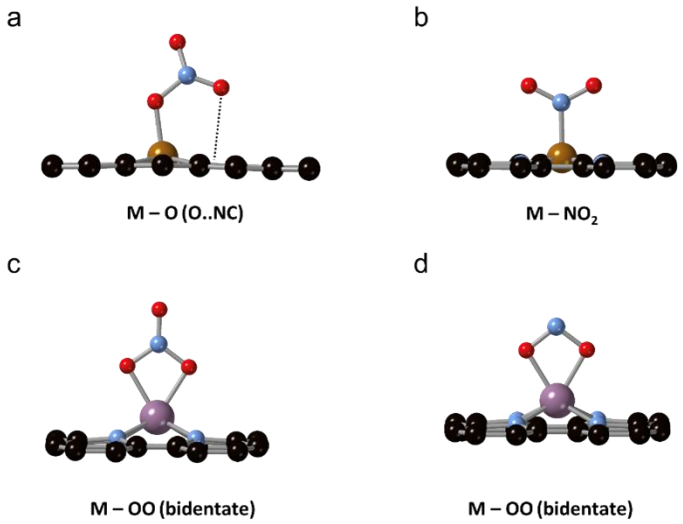

Schematically represented DFT determined *NO_3 and *NO_2 preferred orientations on different in-plane and out-of-plane M-N_4 sites (See table S9).

Table 6. Summary of optimized synthesis conditions to obtain atomically dispersed metal sites with a variety of M-N-C catalysts. See supplementary note 2 for a discussion on tuning the synthesis parameters to maintain an atomic dispersion of the metal species.

Catalyst	Pyrolysis 1 Temperature	Pyrolysis 1 Environment	Pyrolysis 2 Temperature	Pyrolysis 2 Environment	Etching Media
Cr-N-C	650 ˚C	8% H_2 / 92% Ar	650 ˚C	10% NH_3 / 90% N_2	HF
Mn-, Fe-, Ni-, Co-, Cu-, Mo-, W-N-C	975 ˚C	8% H_2 / 92% Ar	950 ˚C	10% NH_3 / 90% N_2	HF
Ru-N-C	650 ˚C	Ar	650 ˚C	Ar	HF
Rh-, Pd-N-C	975 ˚C	Ar	950 ˚C	Ar	HF
La-, Ce-N-C	650 ˚C	Ar	650 ˚C	Ar	NaOH - 80˚C

Table 7. Structure parameters from the EXAFS fittings for the M-N-C catalysts including coordination number, interatomic distances (Metal-Oxygen, R_{M-O} and Metal-Nitrogen, R_{M-N}) and disorder factor σ^2. See supplementary note 3 for a discussion regarding the EXAFS fitting results and coordination numbers.

Sample	S_0^2 factor	Coordination number	$R_{M-N / M-O}$ (Å)	$\sigma^2_{M-N / M-O}$ (Å^2)	ΔE_0 (eV)	R factor
Cr-N-C		2.4 ± 0.3	1.97 ± 0.001	0 ± 0.003	5.31 ± 2.8	0.81%
Cr_2O_3	0.56	6	1.96 ± 0.01	0.002 ± 0.002	4.18 ± 1.1	0.13%
Mn-N-C		7.9 ± 1.4	2.12 ± 0.1	0.017 ± 0.001	-5.52 ± 0.7	0.01%
MnO	0.48	6	2.2 ± 0.03	0.002 ± 0.003	-5.08 ± 2.1	0.46%
Fe-N-C		5.98 ± 1.1	2.12 ± 0.1	0.009 ± 0.005	8.49 ± 1.6	0.37%
Fe_3O_4	0.53	5.3	2.03 ± 0.1	0.005 ± 0.005	8.56 ± 1.3	0.25%
Co-N-C		8.4 ± 0.9	1.92 ± 0.02	0.021 ± 0.002	-5.82 ± 1.1	0.46%
Co_3O_4	0.54	5.3	1.91 ± 0.02	0 ± 0.005	-6.41 ± 3.4	0.90%
Ni-N-C		1.8 ± 0.3	1.89 ± 0.2	0.01 ± 0.003	-7.58 ± 1.7	0.21%
$Ni(OH)_2$	0.99	6	2.08 ± 0.06	0.006 ± 0.004	-11.41 ± 2.9	0.60%
Cu-N-C		5.2 ± 0.4	1.9 ± 0.06	0.005 ± 0.001	-5.84 ± 1.0	0.07%
CuO	0.41	4	1.94 ± 0.02	0.001 ± 0.002	-4.5 ± 1.2	0.11%
Rh-N-C		4.1 ± 0.6	1.99 ± 0.05	0.004 ± 0.002	-1.31 ± 1.8	0.26%
Rh_2O_3	0.67	6	2.02 ± 0.02	0 ± 0.001	-0.57 ± 0.8	0.05%
La-N-C		8.2 ± 1.4	2.61 ± 0.3	0.03 ± 0.006	5.77 ± 1.0	1.74%
La_2O_3	1.4	7	2.6 ± 0.2	0.015 ± 0.003	5.57 ± 0.6	0.56%
Ce-N-C		0.35 ± 0.1 / 5.5 ± 0.6	1.65 ± 0.7 / 2.60 ± 0.2	0.00 ± 0.04 / 0.015 ± 0.02	1.29 ± 5.7	0.91%
CeO_2	0.70	8	2.27 ± 0.1	0.011 ± 0.004	5.97 ± 1.7	1.58%

Table 8. Summary of total nitrogen and oxygen content for all metal free N-C catalysts

Catalyst	Total N (At %)	Total O (At %)
N-C (650-H_2 / 650-NH_3)	11.13%	3.25%
N-C (975-H_2 / 950-NH_3)	3.22%	6.87%
N-C (650-Ar / 650-Ar)	12.48%	3.13%
N-C (975-Ar / 950-Ar)	3.18%	7.48%

Table 9. Summary of the total nitrogen and oxygen content for all M-N-C catalysts

Catalyst	Total N (At %)	Total O (At %)
Cr	12.10%	3.71%
Mn	2.86%	10.65%
Fe	2.71%	5.40%
Co	3.60%	1.79%
Ni	2.61%	2.04%
Cu	4.23%	3.20%
Mo	1.07%	2.70%
Ru	12.12%	3.61%
Rh	5.55%	2.90%
Pd	5.91%	2.55%
W	1.64%	3.08%
La	11.65%	3.81%
Ce	11.26%	4.22%

Table 10. Quantification of specific N-moieties; pyridinic, pyrrolic and graphitic and amine, for all metal free N-C catalysts

Catalyst	pyridinic N (At %)	pyrrolic (At %)	graphitic (At %)	Metal-N_x (At %)
N-C (650-H_2 / 650-NH_3)	3.95%	3.35%	0.87%	2.03%
N-C (975-H_2 / 950-NH_3)	0.77%	1.03%	0.42%	0.59%
N-C (650-Ar / 650-Ar)	4.65%	3.59%	0.91%	2.16%
N-C (975-Ar / 950-Ar)	0.56%	0.96%	0.44%	0.67%

Table 11. Quantification of specific N-moieties; pyridinic, pyrrolic and graphitic and $M\text{-}N_x$, for all M-N-C catalysts.

Catalyst	pyridinic N (At %)	pyrrolic (At %)	graphitic (At %)	Metal-N_x (At %)
Cr	3.88%	3.36%	0.75%	1.75%
Mn	0.65%	0.79%	0.12%	0.69%
Fe	0.45%	0.66%	0.11%	0.43%
Co	0.58%	1.09%	0.24%	0.42%
Ni	0.55%	0.94%	0.22%	0.32%
Cu	0.77%	1.07%	0.38%	0.50%
Mo	0.23%	0.32%	0.04%	0.10%
Ru	3.21%	3.74%	0.89%	1.46%
Rh	0.75%	2.05%	0.55%	0.59%
Pd	0.72%	2.28%	0.51%	0.66%
W	0.12%	0.84%	0.18%	0.07%
La	3.37%	3.91%	0.80%	1.30%
Ce	3.34%	3.47%	0.69%	1.37%

Table 12. DFT calculated Gibbs free energy changes for reactions on Appendix B.55 (in eV) on different M-N_4 sites.

	Descriptors for NH_3 formation (in NO_3RR)		**Descriptors for NO_2^- formation (in NO_3RR) /NH_3 formation (in NO_2RR)**	
site	* + NO_3^- > *NO_3 + e^-	* + NO_3^- + $2H^+$ + e^- > *NO_2 + H_2O	*+ NO_3^- > *O + NO_2^-	*NO_2 + e^- > * + NO_2^-
	$\triangle_r G$ [eV]	$\triangle_r G$ [eV]	$\triangle_r G$ [eV]	$\triangle_r G$ [eV]
FeN_4	-0.39	-1.64	-0.35	+1.07
MoN_4	-2.72	-3.57	-4.20*	+3.0
MoN_4-O	-0.02	-0.42	-0.55	-0.15
CuN_4	+0.46	-0.47	+2.41	-0.11
NiN_4	+0.69	-0.44	+2.47	-0.13
CoN_4	-0.06	-1.60	+1.08	+1.03
MnN_4	-0.41	-1.52	-0.78	+0.95
PdN_4	+0.93	-0.17	+3.01	-0.39
RuN_4	-1.08	-2.08	-0.91	+1.52
RhN_4	+0.09	+0.19	+1.05	+0.97
CrN_4	-1.13	-1.85	-1.95	+1.28
WN_4	-3.15	-4.08	-4.63*	+3.52
WN_4-O	-0.16	-0.86	-1.10	+0.29
LaN4	-2.27	-2.82	-0.87	+2.25
LaN_4-O	-0.28	-0.60	1.79	0.02
CeN4	-2.39	-2.92	-2.47	+2.36
CeN_4-O	-0.82	-1.21	0.84	0.63
pyridinic N	+1.27	-0.02	+0.85	-0.55
graphitic N	+0.41	-0.34	+1.16	-0.33
pyrrolic NH	+0.52	-0.30	-2.29	-0.26

Table 13. Fitting parameters for the EXAFS spectra χ(k)k2 in R-space and Fourier transform k range

	R min (Å)	R max (Å)	kmin ($Å^{-1}$)	k max ($Å^{-1}$)
Cr-N-C	1	2	2	8
Mn-N-C	1	2	3	8
Co-N-C	1	2	3	8
Ni-N-C	1	2	3	8
Cu-N-C	1	2	3	8
Rh-N-C	1	2	3	8
La-N-C	0.8	2.5	3	8
Ce-N-C	0.8	2.5	3	8
Fe-N-C	1	2	3	7.3

Table 14. DFT determined preferred *NO_3 and *NO_2 orientations on different M-N_4 sites.

	*NO_3	*NO_2
FeN_4	M-O (O…NC)	M-NO_2
MoN_4	M-OO (bidentate)	M-OO (bidentate)
MoN_4-O	M-OO (bidentate)	M-O (monodentate)
CuN_4	M-O (O…NC)	M-NO_2
NiN_4	M-O (O…NC)	M-NO_2
CoN_4	M-O (O…NC)	M-NO_2
MnN_4	M-OO (bidentate)	M-NO_2
PdN_4	M-O (O…NC)	M-NO_2
RuN_4	M-OO (bidentate)	M-NO_2
RhN_4	M-O (O…NC)	M-NO_2
CrN_4	M-OO (bidentate)	M-NO_2
WN_4	M-OO (bidentate)	M-OO (bidentate)
WN_4-O	M-OO (bidentate)	M-O (monodentate)
LaN4	M-OO (bidentate)	M-OO (bidentate)
CeN4	M-OO (bidentate)	M-OO (bidentate)
pyridinic N	CNC-OO (bidentate)	N-NO_2
graphitic N	CNC-NO_3 parallel	CC-OO (bidentate)
pyrrolic NH	NH-O (monodentate)	NH-O (monodentate)

Appendix B.68 XANES Analysis

For Cr-N-C, the XANES spectrum of the Cr K-edge exhibits a feature in the pre-edge at *ca.* 5994 eV, which strongly resembles the pre-edge of the K_2CrO_3 reference, a $Cr6^+$ compound. This feature arises due to the excitation of a photoelectron from the 1*s* state to the 3*d* state (such a transition is forbidden in Cr_2O_3).[170] The Cr oxidation state can be inferred by the relative

intensity of this feature and can be used to quantify the ratio between Cr^{6+} (20-30%) and Cr^{3+} (70-80%).

For Mn-N-C, the XANES spectrum of the Mn K-edge the position and intensity of the main features closely resemble those in the MnO reference spectrum. Indicating Mn is in a Mn^{2+} oxidation state.

The Fe K-edge XANES spectrum for the Fe-N-C aligns well with the Fe_3O_4 reference spectrum, suggesting that Fe-N-C is in a *ca.* $Fe^{2.6+}$ oxidation state. While the Fe-N-C spectrum differs from Fe_3O_4 indicating a dissimilar local environment.

For Co-N-C, the XANES spectrum of the Co K-edge closely resembles that of the Co_3O_4 reference, which has an oxidation state of $Co^{2.6+}$. However, the Co-N-C is shifted to lower energies, indicating a slightly reduced oxidation state.

While the position of the Ni-N-C, Ni K-edge matches well with the Ni^{2+} reference, the white line intensity is reduced compared to the oxide reference. This behavior has also been observed for other atomically dispersed Ni-based catalysts containing a planar geometry with $Ni-N_4$ moieties.[171,172]

For Cu-N-C, the XANES spectrum of the Cu K-edge resembles the CuO reference spectrum, suggesting that Cu is in a Cu^{2+} oxidation state, exhibiting a 4-coordination or strongly disordered 6-coordination local environment.

For Mo-N-C, the XANES spectrum of the Mo K-edge is shifted to significantly higher energies than the Mo foil reference, suggesting a highly oxidized Mo state. Where the deconvoluted XPS spectrum supports Mo species present at high oxidation states, comprising a mixture of Mo^{6+}, Mo^{5+} and Mo^{4+}.

For Rh-N-C, the Rh-K edge XANES spectrum is very similar to the Rh_2O_3 reference both in the shape and intensity of the white line feature, indicating a Rh^{3+} oxidation state.

The Pd-N-C, the XANES spectrum of the Pd K-edge is shifted to higher energies than the Pd reference foil suggesting the Pd-N-C is in an oxidized state. Where the deconvoluted XPS spectrum suggests a mixture of Pd^{2+} and Pd^0.

For La-N-C, the XANES spectrum of the La L_3-edge is similar to that of the amorphous La_2O_3 reference, suggesting a La oxidation state of La^{3+}. The energy calibration was done by collecting the V K-edge spectrum for a vanadium foil as a reference, which was measured simultaneously with the La-N-C sample.

For Ce-N-C, the XANES spectrum of the Ce L_3-edge differs strongly from the CeO_2 reference spectrum. However, the Ce-N-C spectrum is very similar to Ce^{3+} compounds in the literature, for example, cerium nitrate, $Ce(NO_3)_3$.[173] Therefore suggesting the Ce-N-C catalyst is in a *ca.* Ce^{3+} oxidation state.

Note several references were acquired from XAS databases.

Cr : K_2CrO_3 and Cr_2O_3 references are extracted from the Hokkaido university XAS database.[174]

La: The La_2O_3 reference data was extracted from the Farrel Lytle XAS data base. (http://ixs.iit.edu/database/data/Farrel_Lytle_data/RAW/index.html)

Ce: The CeO_2 reference was taken from the HEPHAESTUS data base.[119]

Note that due to some problems with the optics at the beamline, the optimal energy resolution was not obtained at the KMC-3 beamline (BESSY), which can lead to some distortions in the spectra. The samples measured at BESSY include Cr-, Mn-, Co-, Ni-, Cu- and Ce-N-C.

However, corresponding reference foils and compounds were measured for energy calibrations and comparison of features. The XANES spectra for Mo-N-C and Pd-N-C and corresponding reference metal foils were measured on the 10-BM beamline of the Advanced Photon Source are Argonne National Laboratory.

Supplementary note 2: Optimization of catalyst synthesis conditions

To accurately evaluate the NO_2RR/NO_3RR activity and selectivity of single-atom centers, synthesis parameters were optimized to ensure the exclusive formation of $M\text{-}N_x$ sites, especially in metals difficult to disperse atomically, such as 4d noble metals (Ru, Rh and Pd) and rare earth elements (La and Ce) (Table S1). Therefore, control experiments to deconvolute the contributions of the metal-free N-C supports for the NO_3RR and NO_2RR revealed similar activity between all metal free N-C's, regardless of the pyrolyzing conditions (Figure S39 and S46), indicating the minimum impact on the NO_3RR and NO_2RR activity by the non-metal-associated N-moieties, as discussed in more detail in the main text.

Appendix B.69 EXAFS Analysis – coordination of M-N-C catalysts

The observed coordination number for the M-N-C catalysts varies between *ca.* 1.8 to 8.4. While Rh-N-C displays a coordination number of 4 (that anticipated for $M\text{-}N_4$ motifs), for Fe- and Cu-N-C, it is likely that in addition to the M-N bonds, some additional M-O bonds are present, leading to a slightly increased coordination number. For Ni-N-C, the low coordination number could be attributed to the large structural disorder due to the off-center displacement of the Ni for the center of the $Ni\text{-}N_4$ moiety (as indicated by the XANES features). Additionally, Ce-N-C, in addition to the M-N feature at low bond distance, the wavelet transformations of the EXAFS data

also show an additional wave peak at higher R- and k-values, indicating small oxide clusters not detected by other techniques may co-exist.

Appendix C - Chapter 4

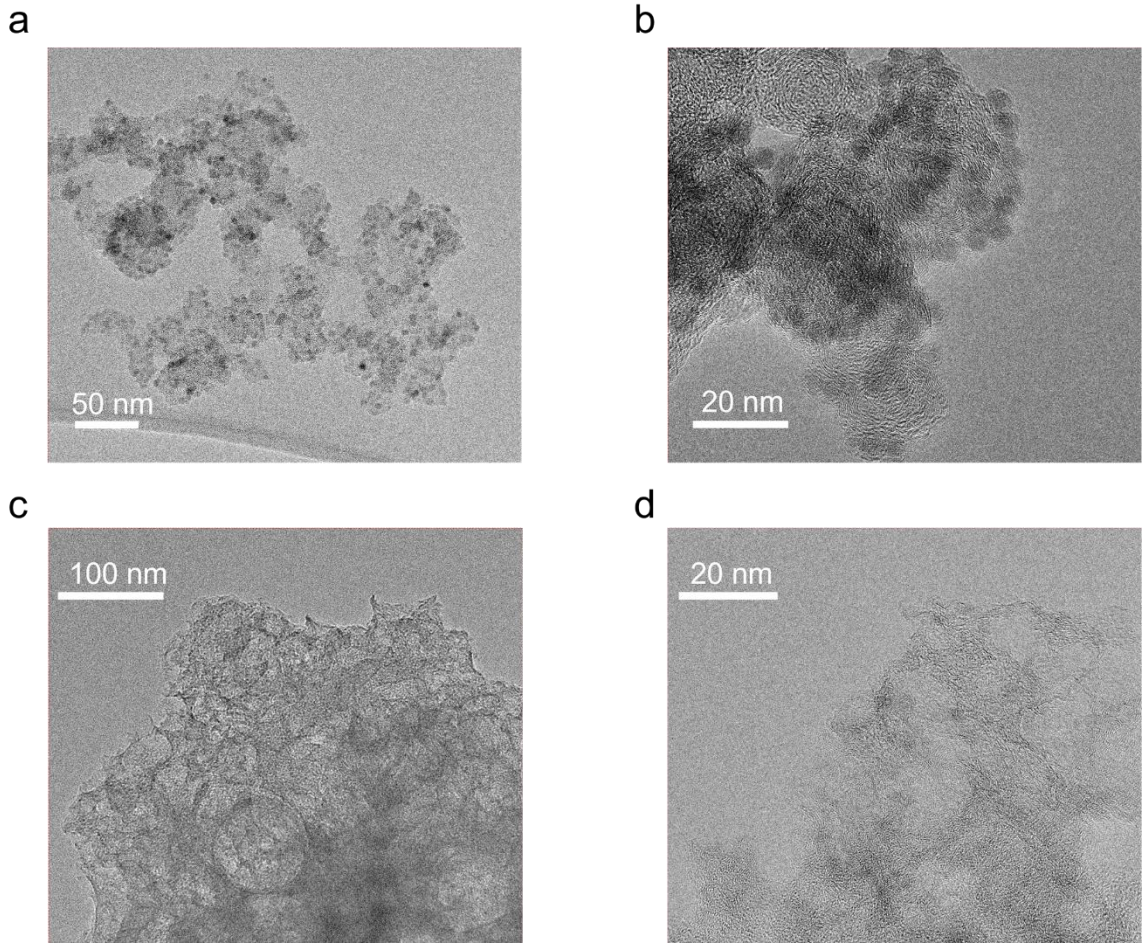

Appendix C.1 TEM images of the γ-Fe_2O_3 nanoparticles supported on (a) Fe-N-C and (b) XC72-Vulcan carbon. Showing a well-controlled sub-5 nm particle size and homogenous distribution of the γ-Fe_2O_3 nanoparticles.

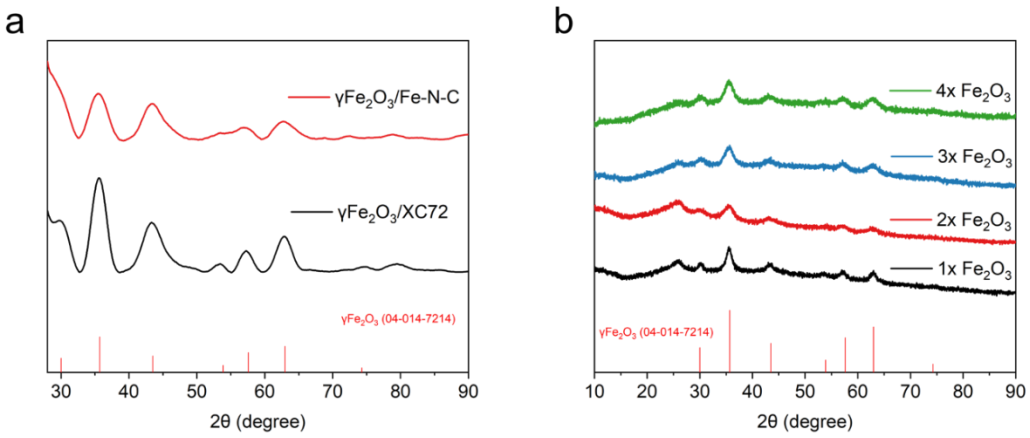

Appendix C.2 XRD pattern of the γ-Fe_2O_3 nanoparticles. (a) γ-Fe_2O_3 supported on Fe-N-C (red) and XC72 (black), where the spectra match closely to the γ-Fe_2O_3 reference spectra. (b) XRD pattern of the γ-Fe_2O_3 with varying precursor loadings.

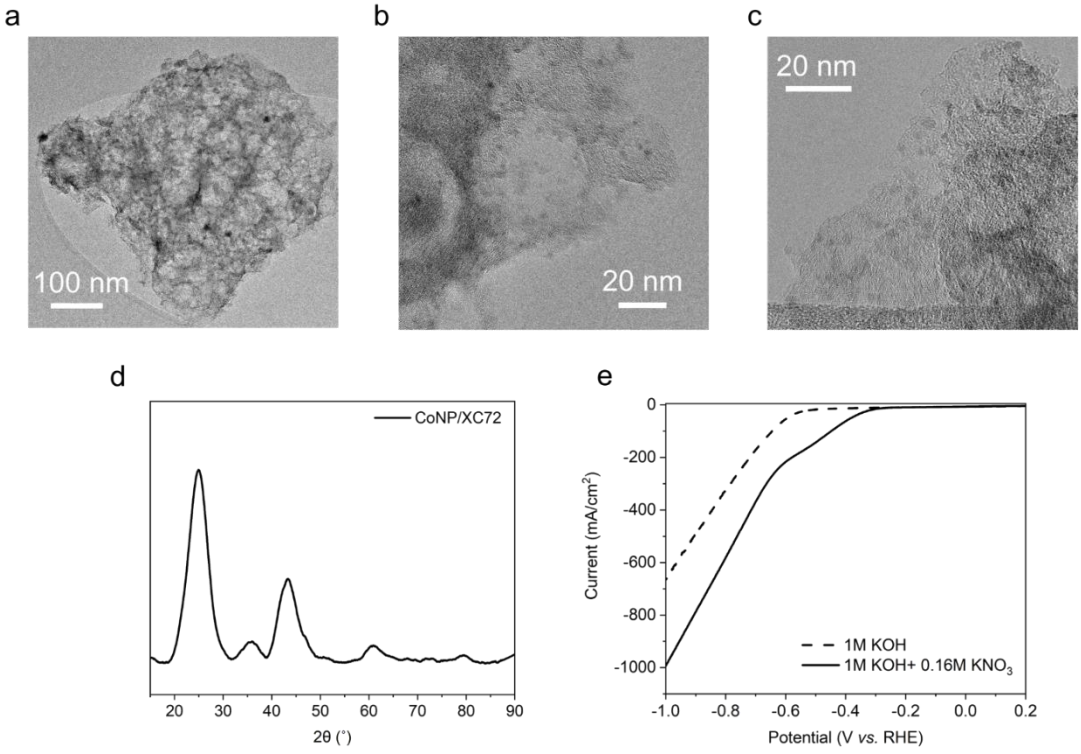

Appendix C.3 Physical and electrochemical characterization of Co_2O_3/Fe-N-C. (a-c) TEM images from low mag to high mag showing the successful incorporation of Co_2O_3 nanoparticles on Fe-N-C, showing the characteristic hierarchical porous structure of the Fe-N-C support and *ca.* 2-5 nm Co_2O_3 nanoparticles. (d) XRD pattern of the Co_2O_3/Fe-N-C, matching well with the Co_2O_3 reference. (e) LSV of the Co_2O_3/Fe-N-C in both 1M KOH and 1M KOH with 0.16M KNO_3 from 0.2 to -1.0 V *vs.* RHE. An onset potential of ca. -0.3 V *vs.* RHE is observed (indicating a delayed onset potential compared to γ-Fe_2O_3/Fe-N-C).

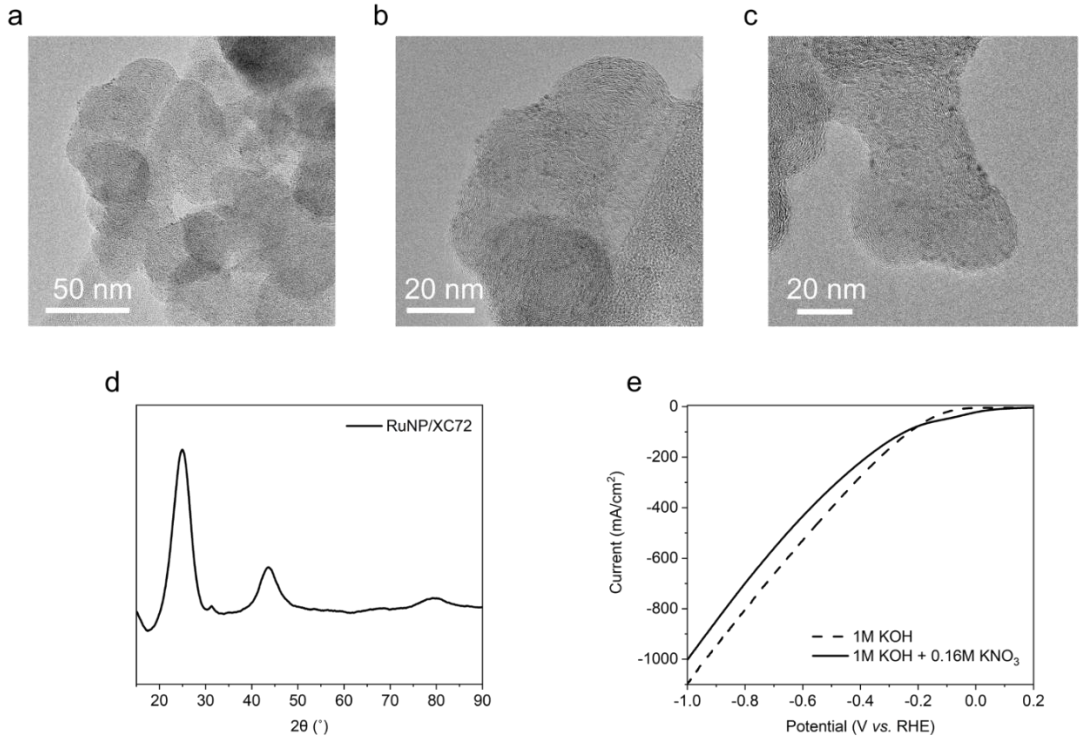

Appendix C.4 Physical and electrochemical characterization of RuO_x/XC72. (a-c) TEM images from low mag to high mag showing the successful incorporation of RuO_x nanoparticles on XC72, showing the formation of *ca.* 2-3 nm RuO_x nanoparticles. (d) XRD pattern of RuO_x nanoparticles, matching well with the Ru reference. (e) LSV of the RuO_x/XC72 in both 1M KOH and 1M KOH with 0.16M

KNO_3 from 0.2 to -1.0 V *vs.* RHE. An early onset potential is observed at *ca.* 0.05 V *vs.* RHE (earlier than either γ-Fe_2O_3 or Co_2O_3), however, the RuO_x is quickly out competed by the HER (with significant bubble formation observed during the reductive sweep).

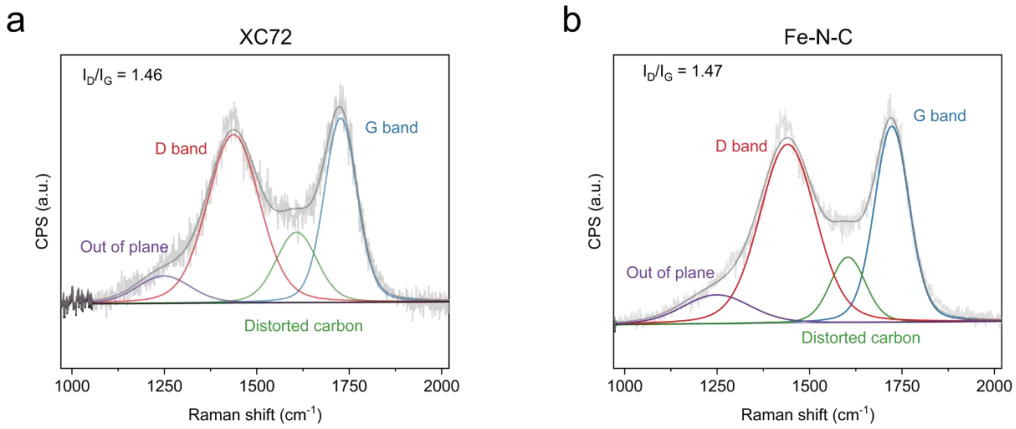

Appendix C.5 Raman spectra and deconvolution for the catalyst supports (a) XC72 and (b) Fe-N-C, with the calculated I_D/I_G ratio.

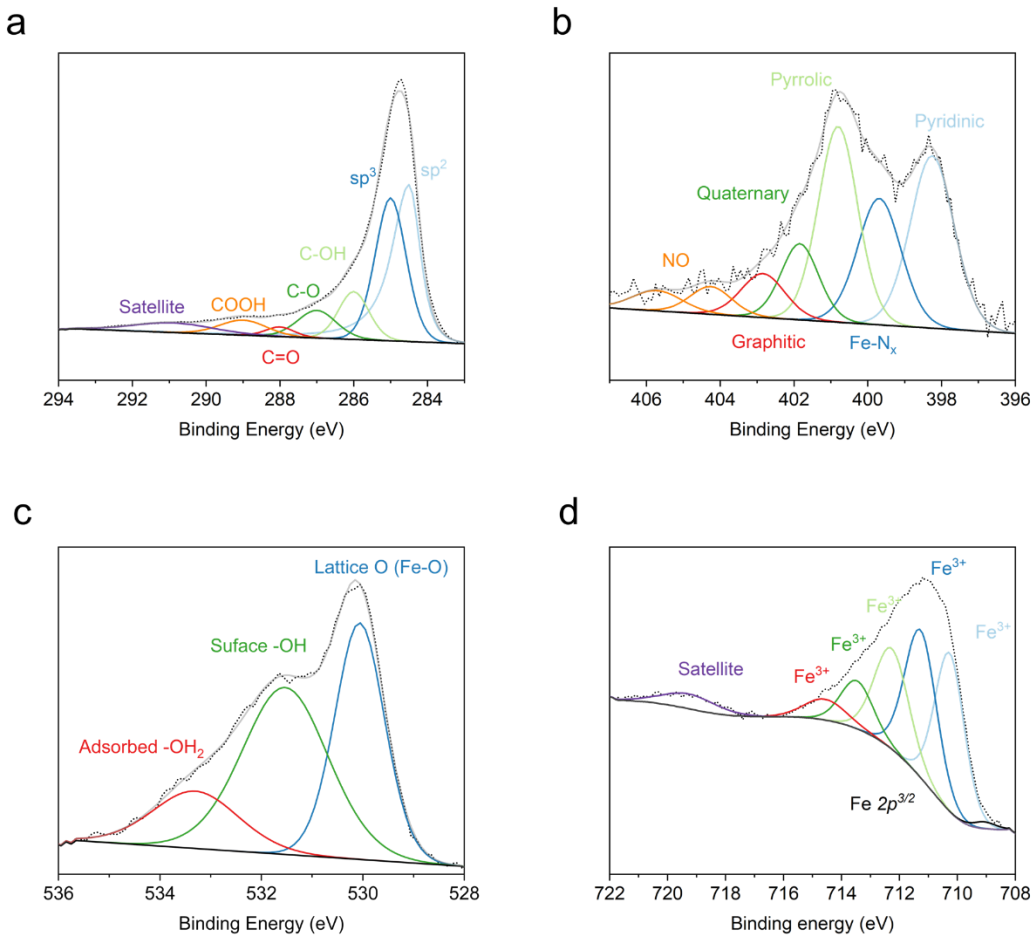

Appendix C.6 Deconvoluted XPS spectra for γ-Fe_2O_3/Fe-N-C, (a) C *1s*, (b) N *1s*, (c) O *1s* and (d) Fe *2p*. The C *1s* spectrum demonstrates the presence of both graphitic and amorphous carbon in almost equal proportions (similarly observed in the corresponding Raman spectrum Figure Sx). The N *1s* spectrum agrees strongly with the N *1s* spectra from the bare Fe-N-C support, confirming Fe-N_x moieties remain after the reduction of Fe_2O_3 nanoparticles onto the support. The O *1s* spectrum indicates the presence of lattice O, as expected in the formation of Fe_2O_3 nanoparticles (Fe-O). The Fe *2p*

spectrum indicates Fe present in a Fe^{3+} oxidation state.

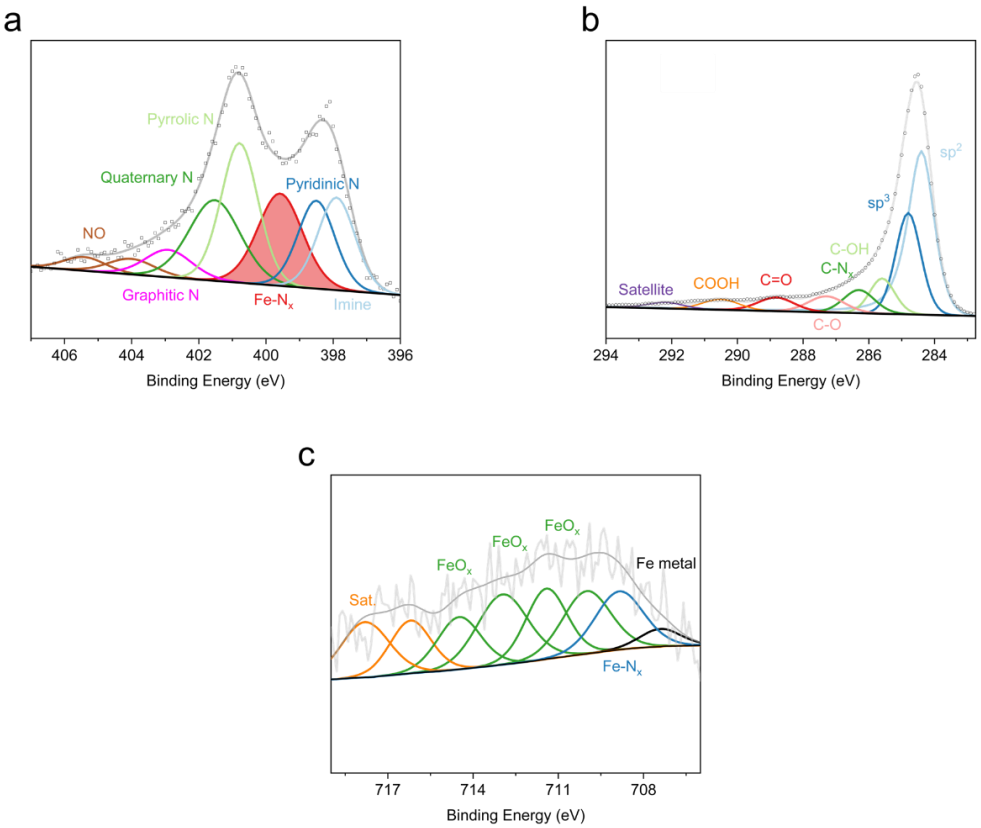

Appendix C.7 XPS of the Fe-N-C support. (a) Deconvoluted N *1s* spectrum showing the presence of the nitrogen moieties and formation of the Fe-N_x moiety. (b) C *1s* spectrum showing the formation of C-Nx species and a mixture of sp^2 and sp^3 carbon. (c) Fe *2p*

spectrum showing the presence of Fe-N_x and oxidized nitrogen species**.**

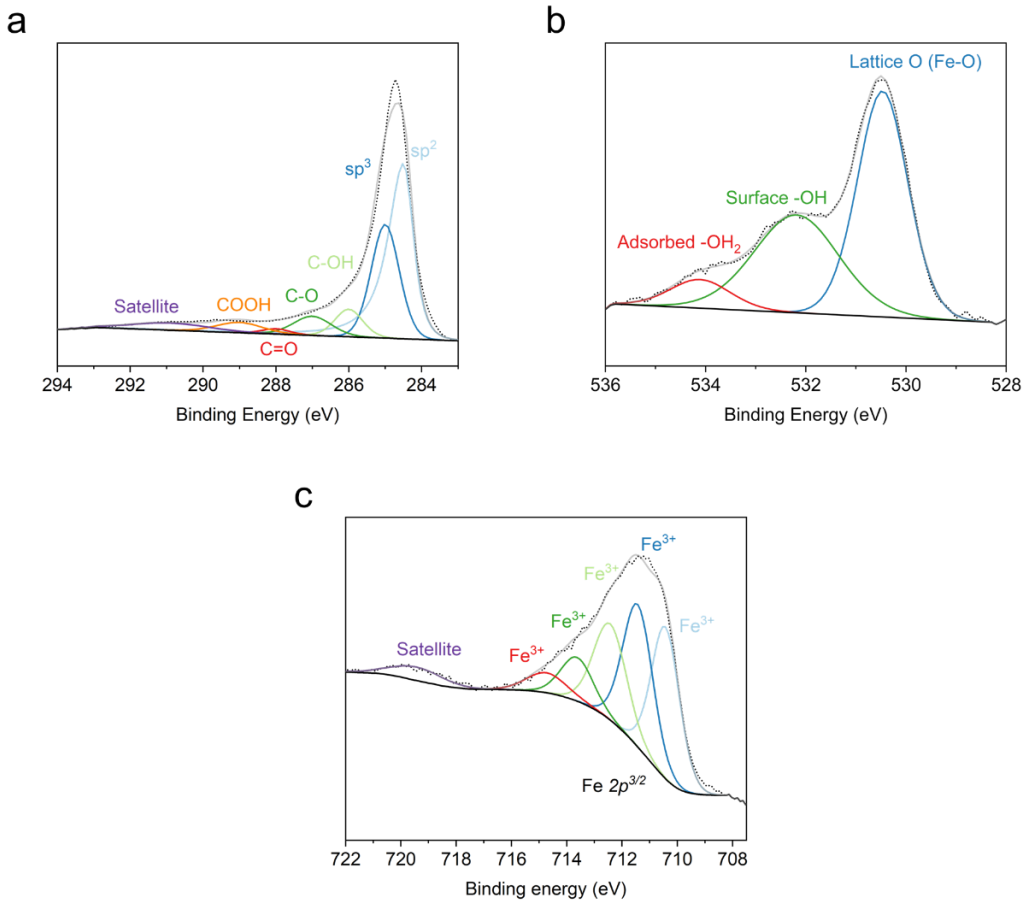

Appendix C.8 Deconvoluted XPS spectra for γ-Fe_2O_3/XC72, (a) C *1s*, (b) O *1s* and (c) Fe *2p*. The C *1s* spectrum demonstrates a more graphitic structure as compared to the Fe-N-C support. The O *1s* spectrum indicates the presence of lattice O, as expected in the formation of Fe_2O_3 nanoparticles (Fe-O). The Fe *2p* spectrum indicates Fe present in a

Fe^{3+} oxidation state.

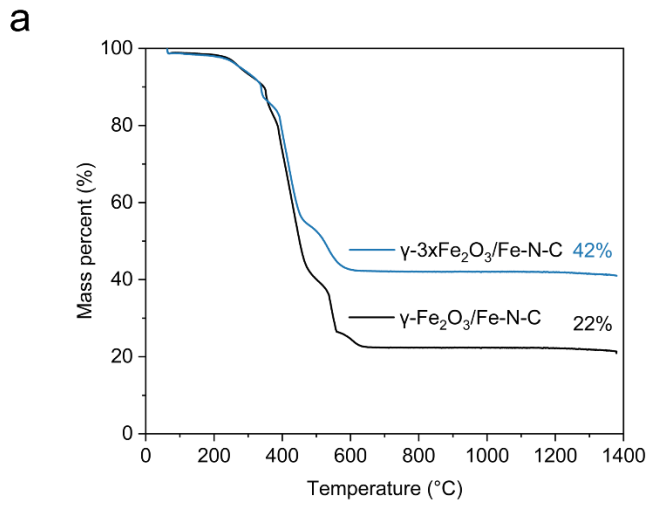

Appendix C.9 TGA evaluation of the weight percent of Fe when changing the $Fe(acac)_3$ precursor in the synthesis, 1x and 3x precursor loading.

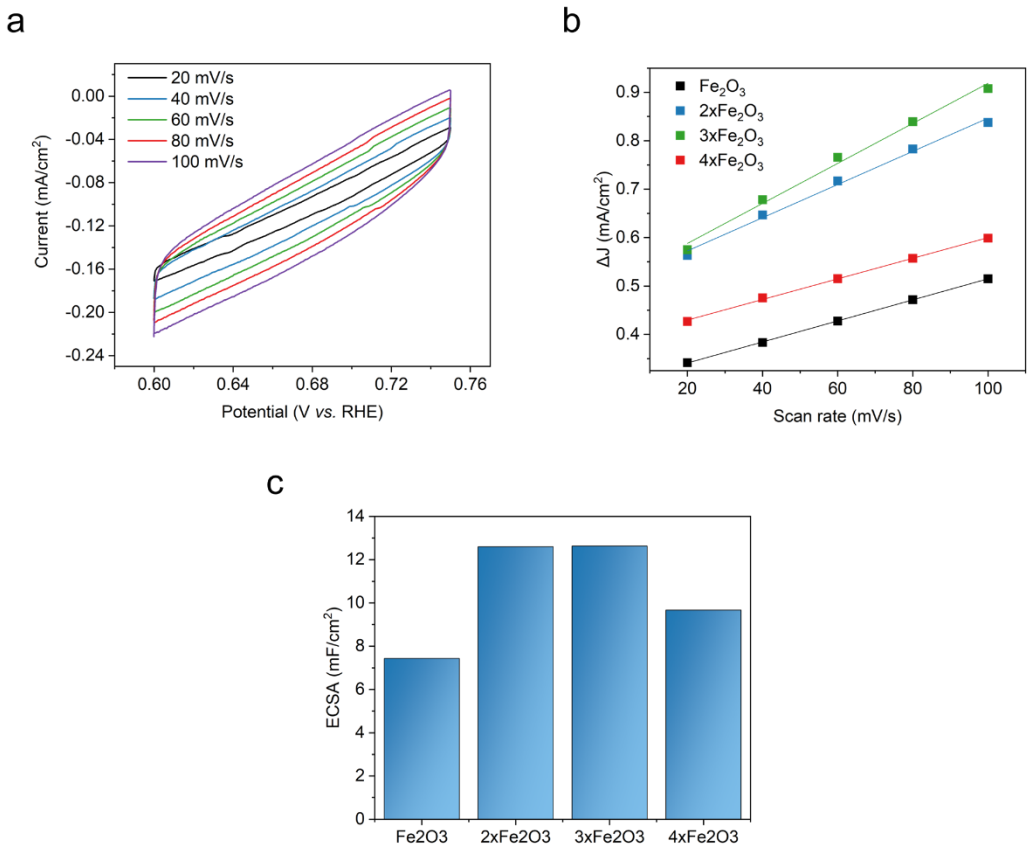

Appendix C.10 Determination of the electrochemically active surface area (ECSA) for the γ-Fe_2O_3 with increasing Fe precursor loading, via capacitance measurements. (a) CV as a function of scan rate from 20 mV/s and 100 mV/s between 0.6 and 0.76 V *vs.* RHE. (b) Current differences as a function of scan rate. (c) ECSA for the γ-Fe_2O_3 nanoparticles by Fe precursor loading.

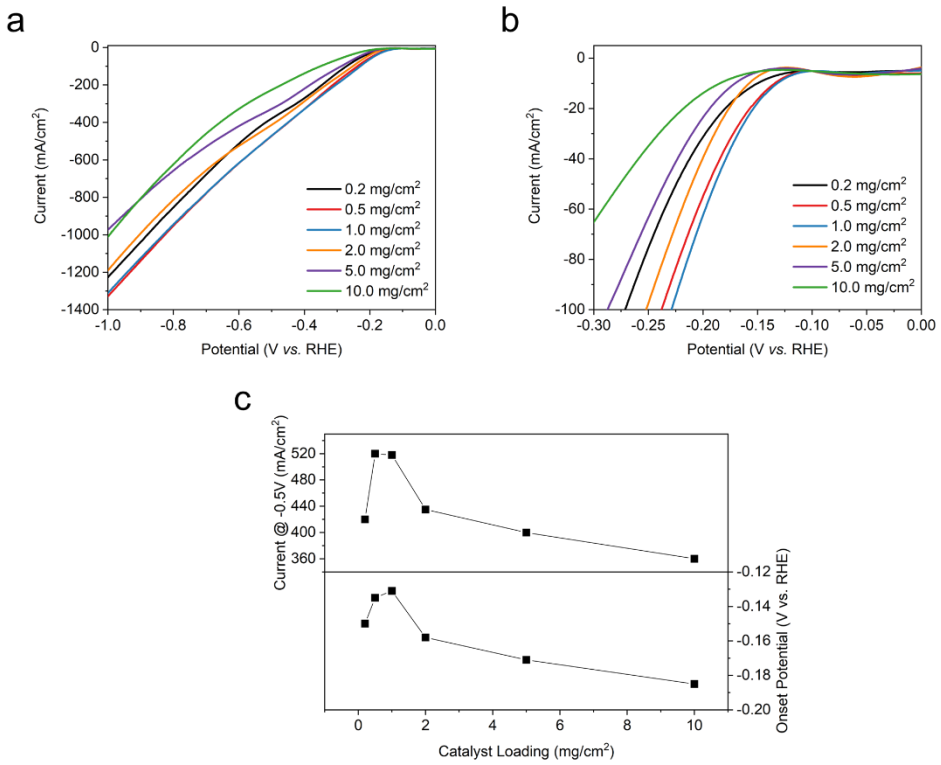

Appendix C.11 Optimizing the γ-3xFe_2O_3/Fe-N-C catalyst loading on the carbon paper electrode. (a) LSV of the catalyst loadings between 0.2 – 10 mg/cm^2 from 0 to -1.0 V *vs.* RHE, evaluating the observed current response (b) zoomed region between 0 and -0.3 V *vs.* RHE looking at the reaction onset potential. From the LSV, the catalyst loadings of 0.5 and 1.0 mg/cm^2 achieve the highest current response and earlier reaction onset potential. (c) Maximum current at a potential of -0.5 V *vs.* RHE and reaction onset potential as a function of catalyst loading. A potential of -0.5 V *vs.* RHE is the maximum potential at which a cathodic energy efficiency of 30% could be achieved (assuming 100% FE_{NH3}). Where again the top performing loadings are 0.5 and 1.0 mg/cm^2.

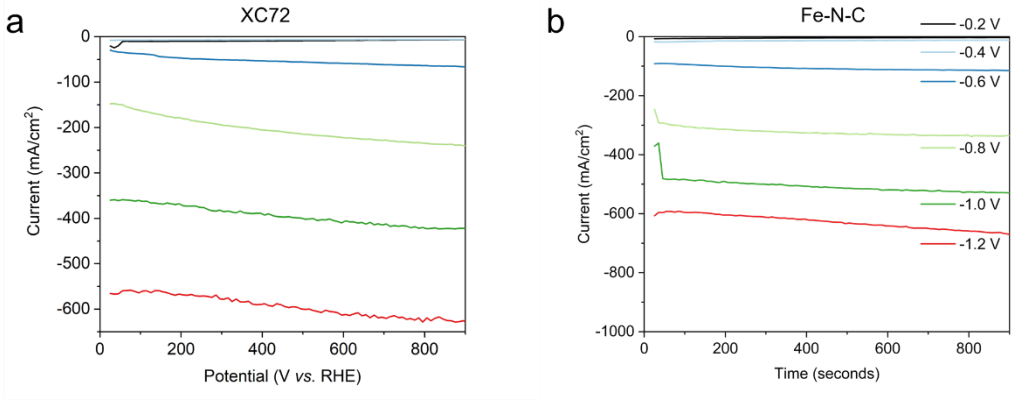

Appendix C.12 Constant potential electrolysis on the support materials. (a) XC72 and (b) Fe-N-C in 1M KOH + 0.16M KNO_3 at potentials of -0.2 to -1.2 V *vs.* RHE for 15 min each.

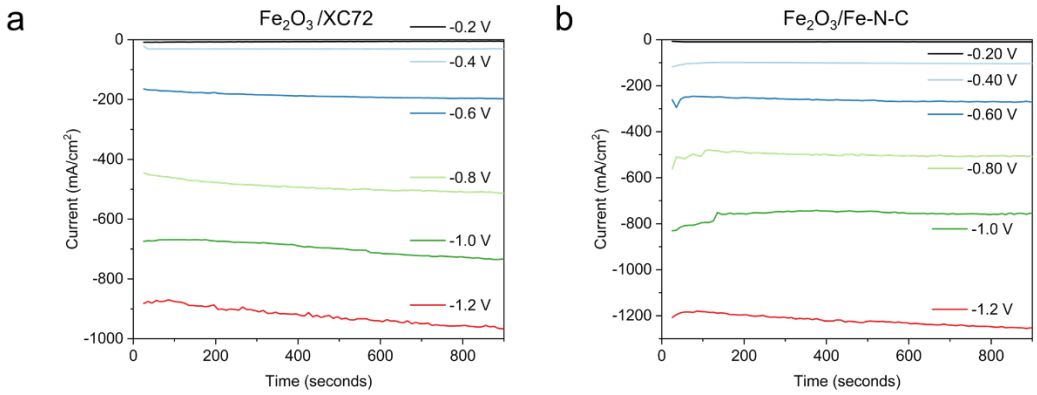

Appendix C.13 Constant potential electrolysis on the support materials. (a) γFe_2O_3/XC72 and (b) γFe_2O_3/Fe-N-C in 1M KOH + 0.16M KNO_3 at potentials of -0.2 to -1.2 V *vs.* RHE for 15 min each.

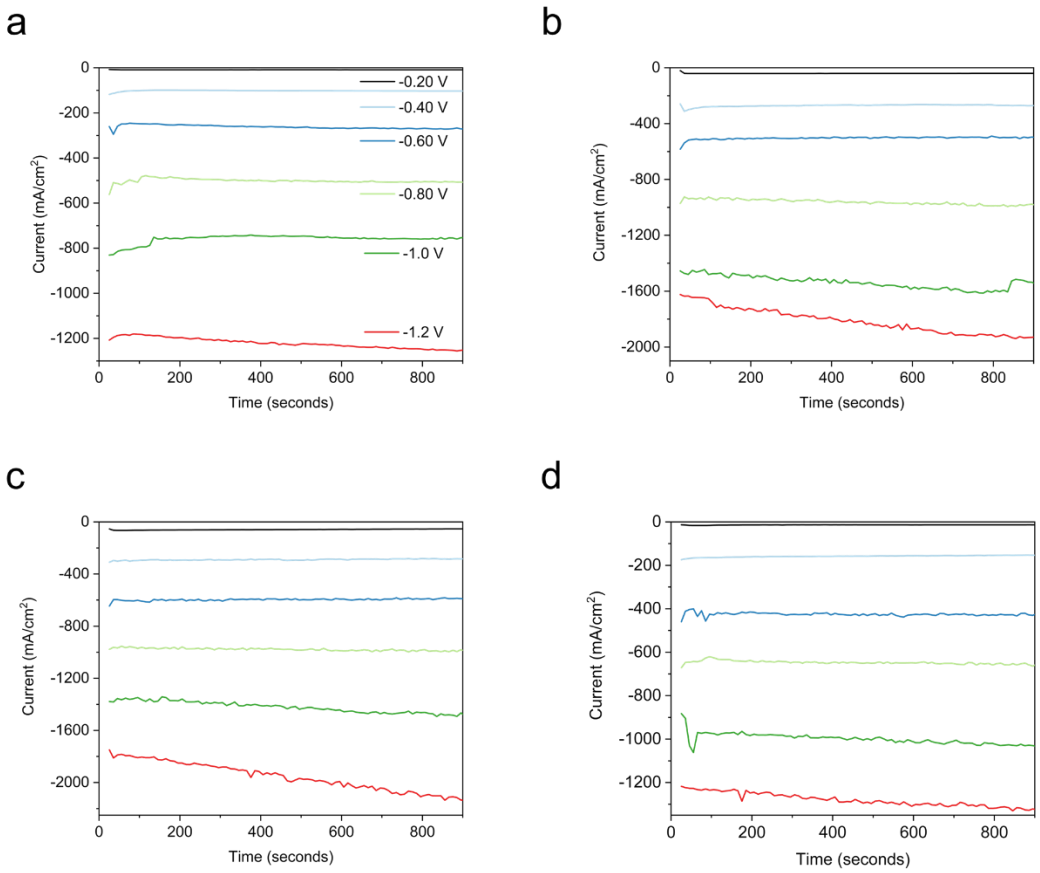

Appendix C.14 Constant potential electrolysis on γ-Fe_2O_3/Fe-N-C with different γFe_2O_3 loadings. (a) γ-Fe_2O_3/Fe-N-C and (b) γ-2xFe_2O_3/Fe-N-C, (c) γ-3xFe_2O_3/Fe-N-C and (d) γ-4xFe_2O_3/Fe-N-C in 1M KOH + 0.16M KNO_3 at potentials of -0.2 to -1.2 V *vs.* RHE for 15 min each.

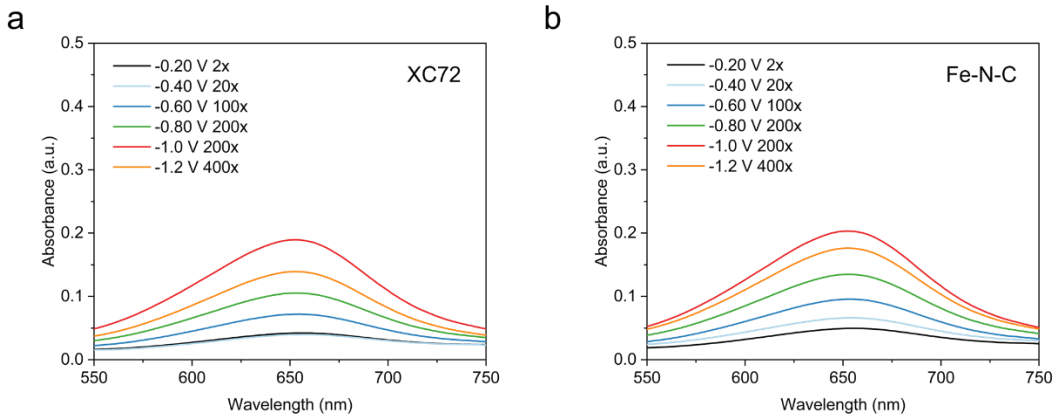

Appendix C.15 UV-Vis curves for the detection of NH_3 (*ca.* 655 nm) for the constant potential NO_3RR electrolysis in 1M KOH + 0.16M KNO_3 over (a) XC72 and (b) Fe-N-C at potentials of 0.2 V to -1.2 V *vs.* RHE for 15 min each. Samples were diluted to fall within the calibration curves.

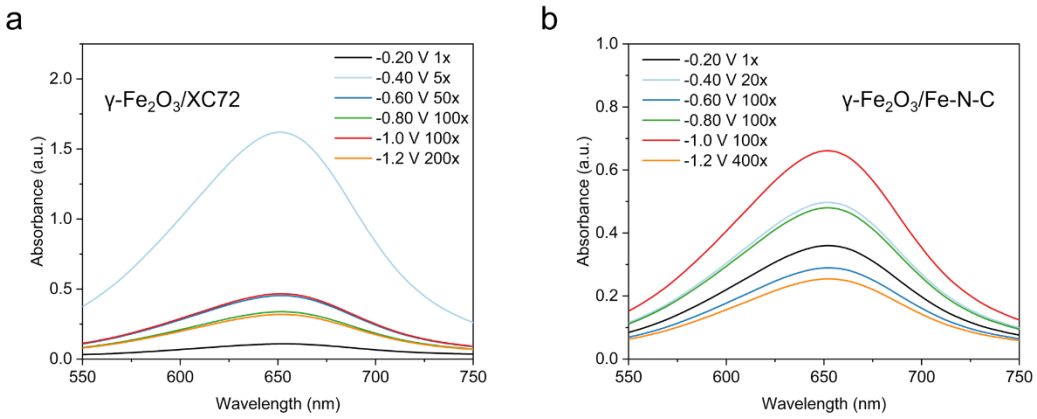

Appendix C.16 UV-Vis curves for the detection of NH_3 (*ca.* 655 nm) for the constant potential NO_3RR electrolysis in 1M KOH + 0.16M KNO_3 over (a) γFe_2O_3/XC72 and (b) γFe_2O_3/Fe-N-C at potentials of 0.2 V to -1.2 V *vs.* RHE for 15 min each. Samples were diluted to fall within the calibration curves.

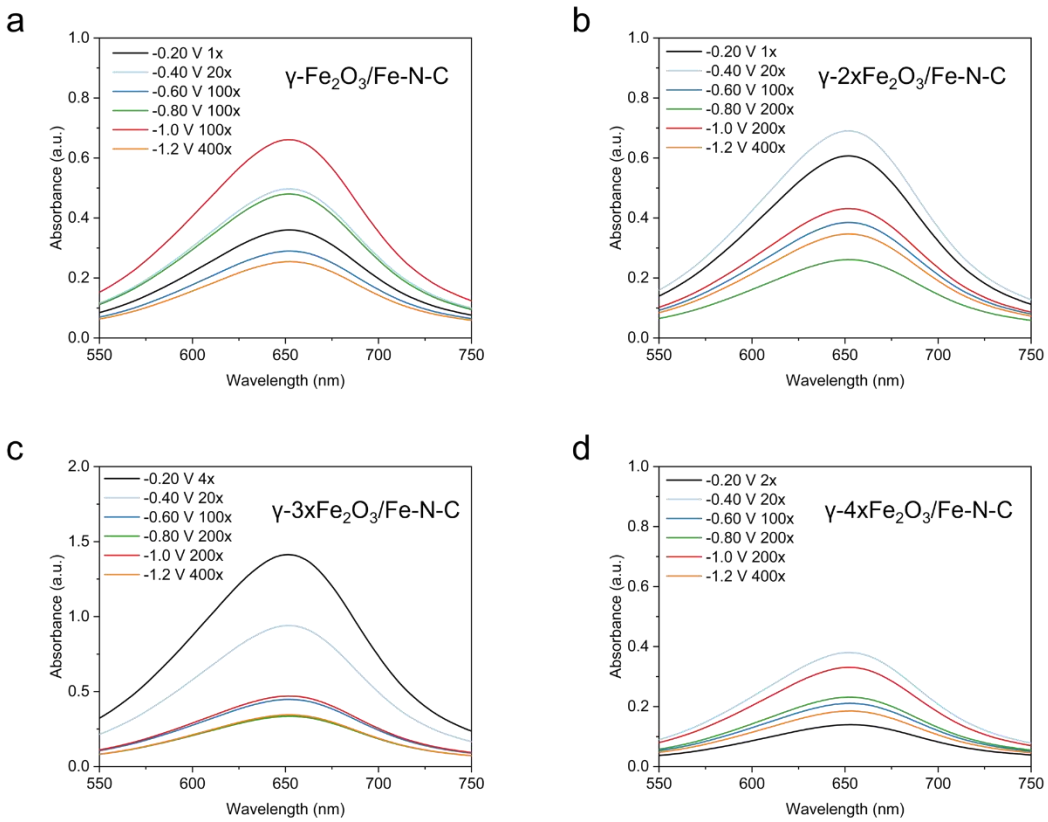

Appendix C.17 UV-Vis curves for the detection of NH_3 (*ca.* 655 nm) for the constant potential NO_3RR electrolysis in 1M KOH + 0.16M KNO_3 over (a) γFe_2O_3/Fe-N-C and (b) γ-2xFe_2O_3/Fe-N-C, (c) γ-3xFe_2O_3/Fe-N-C and (d) γ-4xFe_2O_3/Fe-N-C at potentials of 0.2 V to -1.2 V *vs.* RHE for 15 min each. Samples were diluted to fall within the calibration curves.

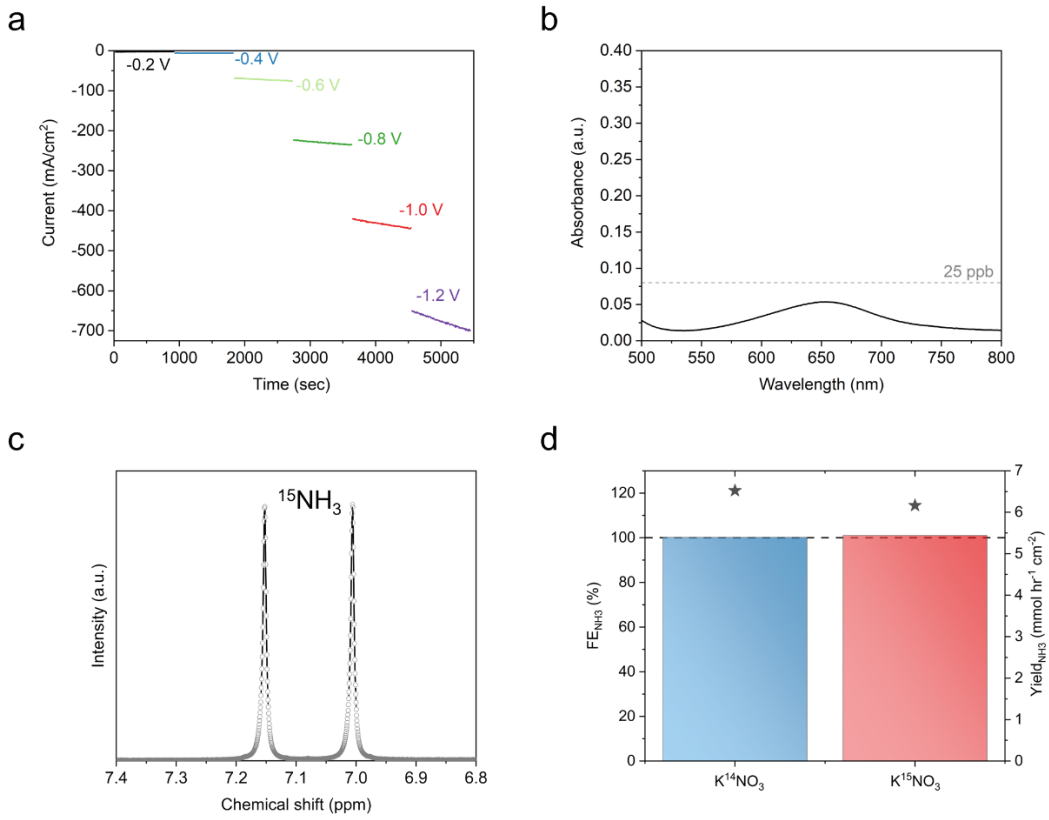

Appendix C.18 **A** Control studies to confirm the origin of the N in the detected NH_3 originates from the nitrate feed and not from contamination or decomposition of the Fe-N-C support, utilizing the optimized γ-3xFe_2O_3/Fe-N-C catalyst (a) Constant potential electrolysis in 1M KOH without the addition of nitrate from -0.2 to -1.2 V *vs.* RHE. (b) UV-Vis detection of the electrolyte after electrolysis over all potentials, showing the absence of NH_3. (c) ^1H NMR spectra showing the presence of only $^{15}NH_3$ after electrolysis with 1M KOH and 0.16M isotopically labeled $K^{15}NO_3$ at -1.0 V *vs.* RHE for 15 min. (d) FE_{NH3} and $Yield_{NH3}$ for standard $K^{14}NO_3$ (blue) and isotopic $K^{15}NO_3$ (red) feed.

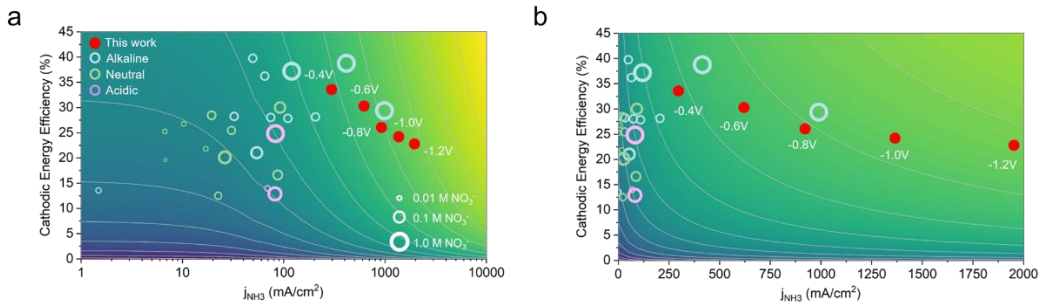

Appendix C.19 Comparison of NO_3RR performance from the literature and this work. (a) log scale of ammonia partial current density (j_{NH3}) and (b) linear scale of j_{NH3}. The performance reported in this work is indicated by the red circles. The performance increases to the right and up and the contours are determined as the log of the j_{NH3} and cathodic energy efficiency (CEE).

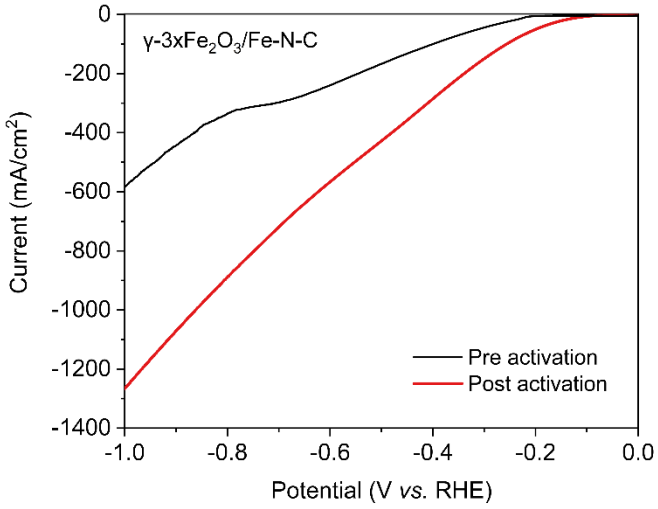

Appendix C.20 LSV of the optimized γ-3xFe_2O_3/Fe-N-C catalyst before and after the pre-reduction activation step, holding at -1.5 V *vs.* RHE for 90 seconds. A clear enhancement of both the reaction onset potential and maximum current density achieved after the pre-

reduction step, forming surface Fe^{2+}/Fe^{0} species.

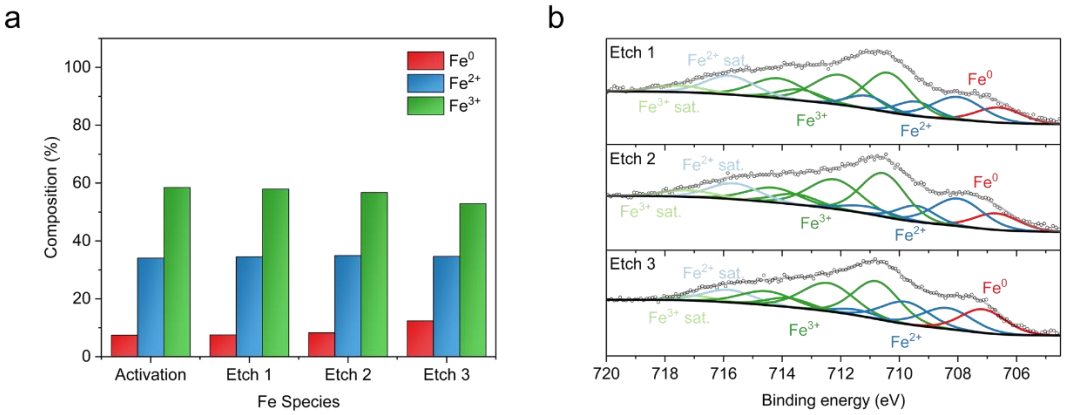

Appendix C.21 XPS of γ-3xFe_2O_3/Fe-N-C after the pre-reduction activation step at -1.5 V *vs.* RHE. for 90 seconds (a) Quantification of the Fe species based on deconvolution of the Fe *2p* spectra as a function of Ar^+ ion etching. (b) Deconvoluted Fe *2p* spectra after each 60 second Ar^+ ion etch. Interestingly, the different Fe species remain stable after the activation and through the first 2 Ar^+ ion etches. Therefore, the Fe speciation was analyzed from the first Ar^+ ion etch.

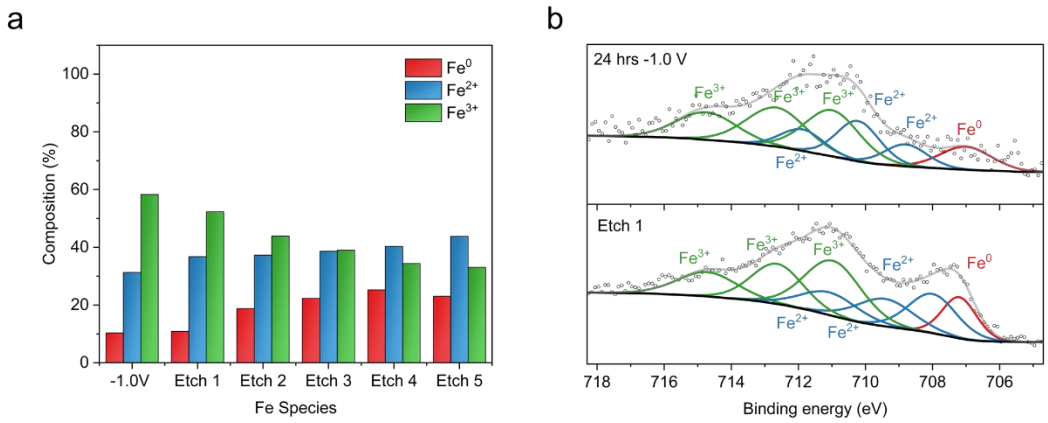

Appendix C.22 A XPS of γ-3xFe_2O_3/Fe-N-C after the 24-hour electrolysis at -1.0 V *vs.* RHE. (a) Quantification of the Fe species based on deconvolution of the Fe *2p* spectra as a function of Ar^+ ion etching. (b) Deconvoluted Fe *2p* spectra of the catalyst after the 24-hour electrolysis and after one 60 second Ar^+ ion etch. Therefore, data from the first etch have been selected for use in analyzing the oxidation state of Fe after the 24-hour electrolysis. It can be seen after the second etching, a significant amount of higher oxidation state Fe has been reduced to Fe0, which further increased as more etching steps are performed.

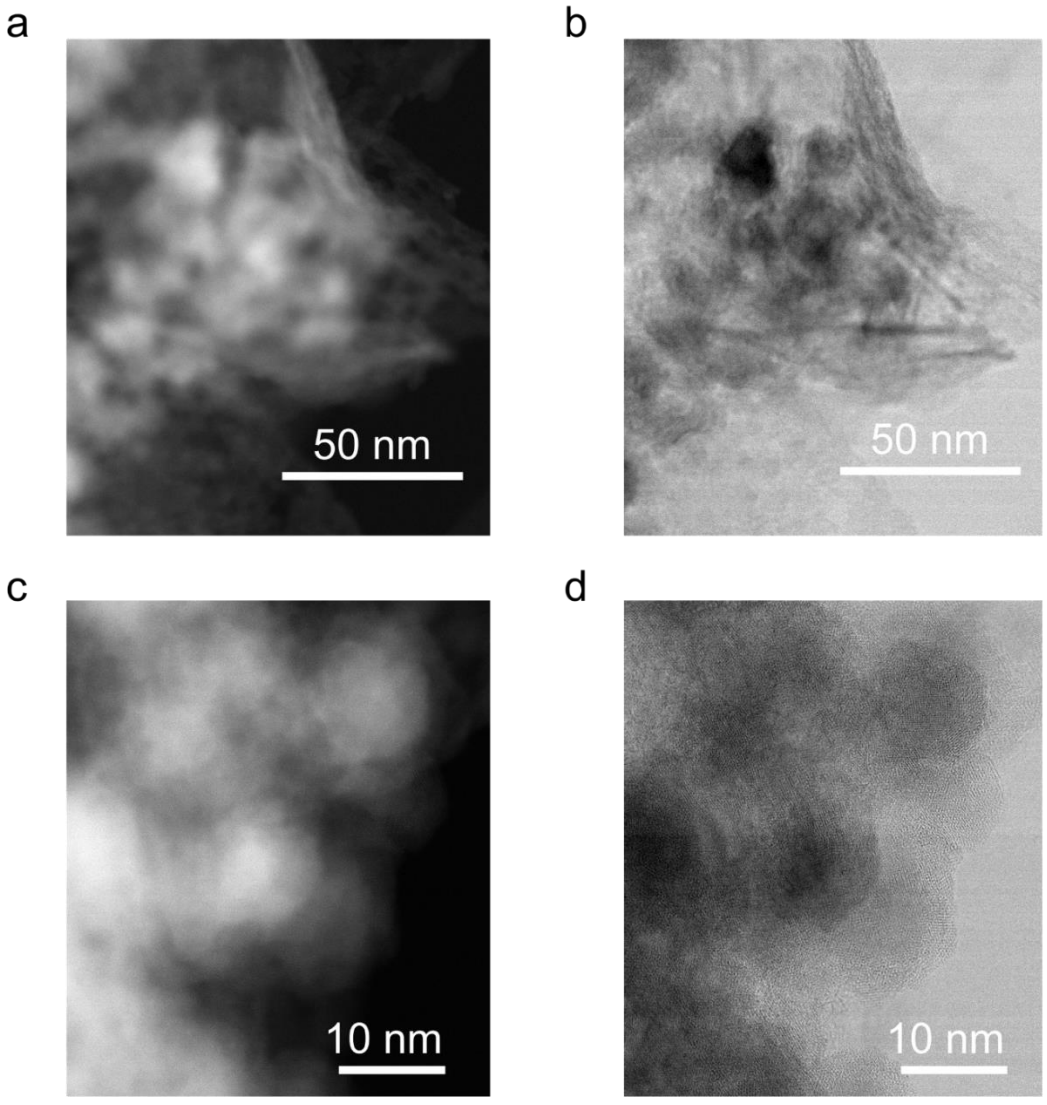

Appendix C.23 Darkfield and corresponding brightfield STEM images of the γ-3xFe_2O_3/Fe-N-C after the durability test at -1.0 V *vs.* RHE for 24 hours. After the electrolysis, slight coarsening of the iron nanoparticles is observed. The used catalyst loaded carbon paper electrode was sonicated in IPA to remove some of the catalyst for

imaging.

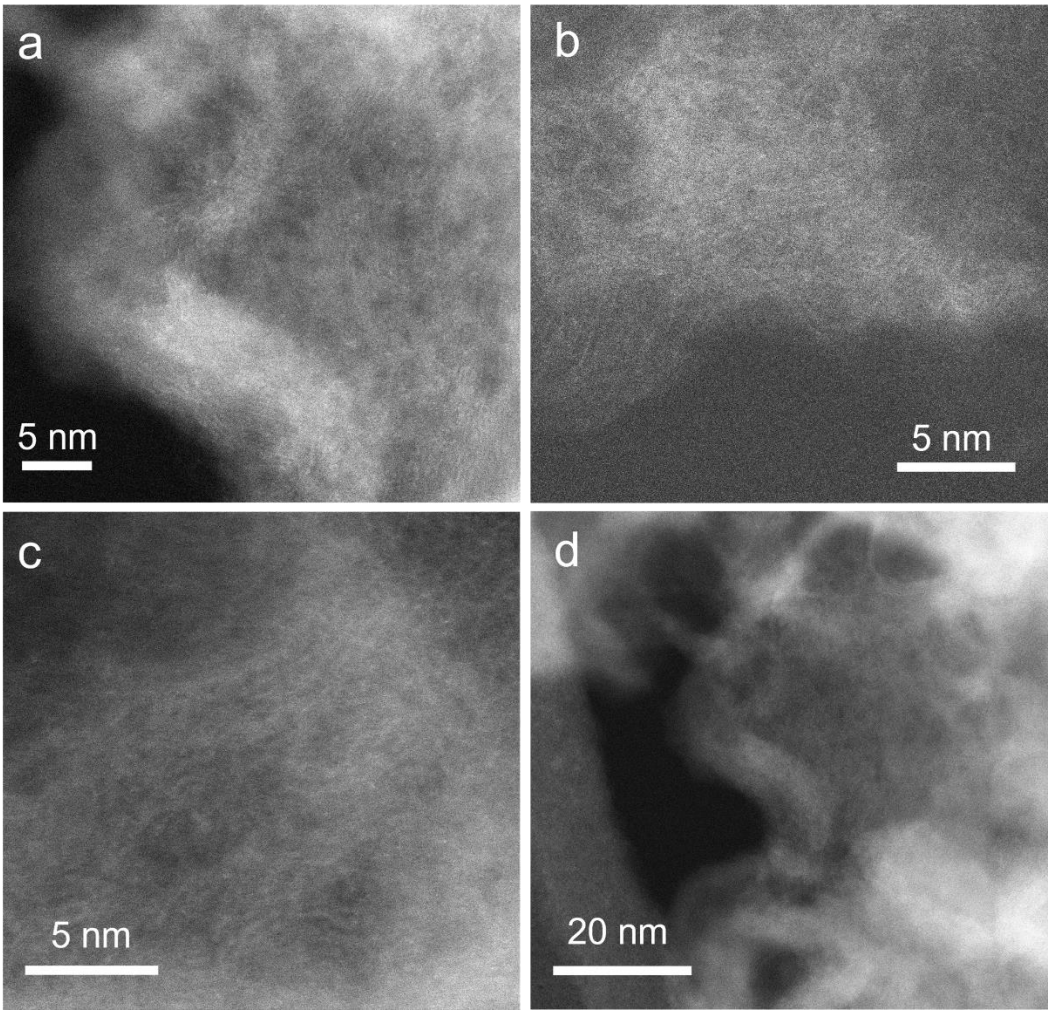

Appendix C.24 Darkfield STEM images of the atomically dispersed Fe-N-C catalyst after NO3RR electrolysis at potentials from -0.2 to -1.2 V vs. RHE. Iron remains atomically dispersed as observed in the high magnification images (a - c), while the absence of metallic nanoparticles is observed in the lower magnification image (d). Showing the robust nature of the atomically dispersed Fe sites under reductive potentials.

Table 15. Literature summary of NO_3RR performance. Reports in alkaline, neutral and acidic media are shaded in blue, green and orange, respectively.

Catalyst	pH	[NO_3^-] (M)	FE_{NH3} (%)	I (mA/ cm^2)	j_{NH3} (mA/cm^2)	Potential (V *vs.* RHE)	CEE (%)	Reference
RuNi/NF	14	1.000	97.0	1020	989.4	-0.60	29%	139
RuNi/NF	14	1.000	100.0	415	415.0	-0.20	39%	139
CuNi Alloy	14	0.100	99.0	50	49.5	-0.15	40%	106
Ru nanocluster	14	1.000	96.0	125	120.0	-0.20	37%	123
Cu@C	14	0.100	98.0	210	205.8	-0.70	28%	136
Cu-NBs-100	14	0.100	95.0	303	288.0	-0.15	38%	132
γ-Fe_2O_3/Fe-N-C	14	0.160	98.7	301	297.0	-0.40	34%	This work
γ-Fe_2O_3/Fe-N-C	14	0.160	100.0	620	620.0	-0.60	30%	This work
γ-Fe_2O_3/Fe-N-C	14	0.160	95.5	966	922.0	-0.80	26%	This work
γ-Fe_2O_3/Fe-N-C	14	0.160	97.4	1402	1366.0	-1.00	24%	This work
γ-Fe_2O_3/Fe-N-C	14	0.160	100.0	1953	1952.8	-1.20	23%	This work
Fe-N-C	13	0.100	98.4	33	32.5	-0.70	28%	64
CoP/TiO_2 nanoarray	13	0.100	87.5	85	74.4	-0.50	28%	175
Pd nanoparticles	13	0.020	35.0	4	1.5	-0.20	14%	167
CoOx nanosheets	13	0.100	93.4	3	2.8	-0.30	34%	176
Ni3B@NiB2.74	13	0.100	100.0	65	65.0	-0.30	36%	134
Co_3O_4 - CoVac	13	0.100	92.0	130	110.0	-0.60	28%	137
Cu-N-C	13	0.100	84.7	64	54.2	-1.00	21%	177
Pd/TiO_2	7 (LiCl)	0.250	92.1	15	13.8	-0.70	30%	178
Cu(I)-N3C1	7	0.036	93.9	33	30.5	-0.64	25%	179
$Ni(OH)_2$	7	0.024	90.4	25	22.6	3.67 V (Cell)	13%	180
Co doped Fe/Fe_2O_3	7	0.006	85.0	20	17.0	-0.75	22%	181
CoP nanorings	7	0.050	97.1	20	19.4	-0.50	28%	182
Fe-N-C	7	0.500	75.0	35	26.3	-0.66	20%	63
O-Cu-PTCDA	7	0.005	86.0	12	10.3	-0.40	27%	87
TiO_2-OV	7	0.001	85.0	8	6.8	-0.97	20%	168
PdX-NCs	7	0.005	96.1	7	6.7	-0.70	25%	183
Fe_2O_3 NA	7	0.100	69.8	125	87.2	-0.90	17%	184
Ir nanotubes	1.1	1.000	83.0	3	2.3	0.06	25%	185
pCuO-10	1	0.050	69.0	140	96.6	-0.50	14%	138
TiO_2	0.77	0.400	82.0	27	22.0	-1.00	13%	88